

# Biomechanical Response of Human Skin: A Hierarchical Porous Media Framework.

Thomas Jeffrey Hugo Marc LAVIGNE

---

Defence held on 24 June 2025 in Esch-sur-Alzette to obtain the degree of

Docteur de l'Université du Luxembourg en sciences de l'ingénieur,  
spécialisé en *Computational Mechanics*

and

Docteur de l'École Nationale Supérieure d'Arts et Métiers en sciences de l'ingénieur,  
spécialisé en *Biomécanique et Ingénierie de la santé*.



PhD-FSTM-2025-058

École Doctorale n° 432 (SMI)

Faculty of Science, Technology and Medicine    École Nationale Supérieure d'Arts et Métiers

## DISSERTATION

Defence held on 24 June 2025 in Esch-sur-Alzette  
to obtain the degree of

DOCTEUR DE L'UNIVERSITÉ DU LUXEMBOURG EN SCIENCES  
DE L'INGÉNIEUR

AND

DOCTEUR DE L'ÉCOLE NATIONALE SUPÉRIEURE D'ARTS ET  
MÉTIERS EN SCIENCES DE L'INGÉNIEUR

by

**Thomas Jeffrey Hugo Marc LAVIGNE**

Born on 8 August 1998 in Paris (France)

Biomechanical Response of Human Skin: A Hierarchical Porous Media  
Framework.

### Dissertation defence committee

Prof. Dr Stéphane BORDAS,

Supervisor

*Full Prof., Université du Luxembourg, Esch-sur-Alzette, Luxembourg*

Dr. Pierre-Yves ROHAN,

Co-Supervisor

*HDR., Institut de Biomécanique Humaine Georges Charpak, Paris, France*

Dr. Giuseppe SCIUME,

Co-Supervisor

*HDR., Institut de Mécanique et d'Ingénierie, Bordeaux, France*

Prof. Christian VINCENOT,

Chair

*Full Prof., Université du Luxembourg, Esch-sur-Alzette, Luxembourg*

Prof. Yohan PAYAN,

Vice-Chair

*Full Prof., Université Grenoble-Alpes, Grenoble, France*

Prof. Stéphane AVRIL,

Member

*Full Prof., École des Mines Saint-Étienne, Saint-Étienne, France*



*To Célestine Petit, Monique Petit,*

*and Solange Lavigne,*



# Acknowledgments

First and foremost, I express my deepest gratitude to the *Fonds National de la Recherche (FNR)* for funding this research project and making this work possible. This research was funded by the *Luxembourg National Research Fund (FNR)*, grant reference No. 17013182. For the purpose of open access, a Creative Commons Attribution 4.0 International (CC BY 4.0) licence to any Author Accepted Manuscript version arising from this PhD work is applicable.

I extend my heartfelt thanks to my supervisors, PY Rohan, G. Sciumè, and S.P.A. Bordas, for their invaluable guidance, unwavering support, and constant encouragement throughout this journey. Their expertise and mentorship have been instrumental in shaping both this work and my growth as a researcher. I am also deeply grateful to S. Laporte and J. Hale for the invaluable expertise and insights they contributed to this PhD.

To my esteemed collaborators — F. Hild, B. Smaniotto, E. Jacquet, J. Chambert, A. Elouneg, G. Dubois, B. Fromy, A. Josset-Lamaugarny, D. Baroli, and S. Budday — thank you for the fruitful exchanges, innovative ideas, and dedication to pushing the boundaries of my work. It has been an absolute privilege to work alongside such brilliant minds.

A special acknowledgment goes to the administrative support team, without whom research would be considerably more complicated. My sincere thanks to O. Marois, W. Titcheu Yamdje, I. Majerus, C. Davrainville, and M. Ezan-Bore for the invaluable assistance and guidance in administrative tasks. Similarly, I extend my gratitude to the IT team, whose support made my multi-site and computational workload manageable. Thank you, A. Zoccollo, J. Tessier, B. Piotrowski, T. Gross, and C. Burton, for the kindness, availability, and unwavering assistance.

To my officemates, colleagues, and friends — thank you for the *camaraderie*, stimulating discussions, and shared moments that enriched this experience and made it

## *Acknowledgments*

more fulfilling. Your support has meant the world to me and made long days more pleasant. In particular, I am grateful to A. Mazier, O. Francis, A. Obeidat, M. Abbad Andaloussi, S. Desphande, Z. Shen, C. Suarez Afanador, A. Kerachni, R. Collet, and M. Amigo for the countless moments of kindness and support in Luxembourg. In Paris, I am deeply thankful to C. Bosio, M. Geoffreoy, J. Péladeau, T. Daney, M. Matray, M. Krombi, C. Dendale and many others for making my stay at IBHGC a cherished memory. A special thank you to M. Le Moing and A. Lagache — our coffee breaks and shared laughter will be dearly missed. I am also grateful to C. Génibre, G. Rio, A. Mounier, and L. Haddadj for their unwavering support over the years.

I would like to take a moment to specifically express my heartfelt gratitude to O. Marois. Your presence, kindness, and warm welcome in Luxembourg and within your family have meant so much to me. I truly cherish our shared time and hope we will continue to stay connected. A special thanks also to A. Perney, C. Suarez Afanador and J. Lengiewicz for their incredible support and companionship. I eagerly look forward to more bike rides together. Thank you, B. Sauty, for our weekly calls, whether for work, discussion or video games—your friendship has been invaluable.

S. Urcun, you deserve a special mention, despite your reluctance for it. Thank you for everything you have brought into my life, both professionally and personally. Your support has helped me grow, and I greatly value our shared moments. I sincerely hope we will continue to meet often and perhaps collaborate further in the future.

To my family — my grandmother, my father, my mother, Mathieu, Lucie, and Una — thank you for your unwavering love, encouragement, and belief in me. Your support has been my foundation and my driving force throughout this journey. My heartfelt thanks also go to T. Thomas (you made the end of this journey lighter) and O. Otillon for being there for me.

Finally, I extend my gratitude to all those who could not be individually named but have contributed to this work in some way, whether through direct collaboration, insightful conversations, or moral support. Your contributions, big or small, have left an indelible mark on this project.

Thank you all for being part of this journey.

# Résumé

Les tissus vivants, tels que la peau, sont particulièrement sensibles aux altérations mécaniques et physiologiques, pouvant conduire à l'apparition de lésions, de rougeurs inflammatoires ou de plaies ouvertes. Ces altérations, regroupées sous le terme d'« endommagement tissulaire », désignent toute dégradation de la structure ou de la fonction du tissu. Elles peuvent survenir dans des conditions physiologiques normales ou résulter de contraintes mécaniques externes, telles qu'une pression modérée mais prolongée, ou au contraire, une charge intense appliquée brutalement. Ces situations sont fréquentes chez les patients hospitalisés, les personnes en situation d'immobilité prolongée, alitées ou en fauteuil roulant, et peuvent conduire à des complications graves. Ces lésions, accentuées par le vieillissement démographique et les habitudes sédentaires, constituent un enjeu majeur de santé publique. Leur prévention et leur prise en charge reposent sur une meilleure compréhension des mécanismes sous-jacents, afin d'anticiper leur survenue et de développer des stratégies personnalisées de soin.

L'apparition de lésions tissulaires résulte d'un enchevêtrement de facteurs mécaniques, biologiques et individuels. Les études animales ont mis en évidence un lien entre le chargement mécanique des tissus, la privation d'oxygène (ischémie) et la mort cellulaire, cette dernière survenant notamment lorsque la déformation mécanique dépasse un seuil critique, en compression ou en cisaillement. De plus, plusieurs travaux ont montré que les effets mécaniques et ischémiques agissent de manière synergique pour initier et propager les lésions. Toutefois, les modèles mathématiques actuels traitent encore trop souvent ces dimensions de manière séparée, sans intégrer explicitement les interactions dynamiques entre contraintes mécaniques, déformation du tissu, microcirculation et réponse biologique. Ce cloisonnement constitue une limite importante à la prédictivité et à la transférabilité de ces modèles. Par ailleurs, la majorité des données utilisées pour calibrer ces modèles provient d'animaux, rendant difficile leur application directe à la peau humaine et, a fortiori, leur adaptation à la variabilité interindividuelle des patients.

## Résumé

L'hypothèse centrale de ce travail est qu'un cadre de modélisation poromécanique, multi-phasique et multi-échelle, intégrant les composantes structurelles, fluidiques et biologiques du tissu, permettrait de mieux caractériser le couplage entre chargement mécanique et réponse microvasculaire.

La stratégie mise en œuvre combine étroitement modélisation mathématique et validation expérimentale (en conditions physiologiques). Une formulation poromécanique intégrant la phase solide du tissu cutané, l'interstitium (incluant fluide interstitiel et cellules mobiles), ainsi que la microcirculation vasculaire, a été implémentée dans le logiciel open-source FEniCSx. Des données expérimentales d'essais d'extension *in vivo* sur peau humaine ont permis de valider la capacité du modèle à reproduire la réponse temporelle du tissu cutané soumis à une sollicitation mécanique. Puis une étude expérimentale réalisée au cours de cette thèse, reposant sur l'indentation de la peau couplée à une mesure de la perfusion par sonde laser Doppler, a été conduite pour caractériser la réponse microcirculatoire sous chargement externe. Le modèle a été enrichi pour intégrer le réseau vasculaire et la possibilité d'incorporer des processus biologiques tels que la diffusion d'oxygène.

Ce travail propose ainsi une approche pour étudier l'interaction entre les mécanismes d'endommagement cutané sous contrainte, en s'appuyant sur une modélisation couplée des processus mécaniques et biologiques. En offrant un outil capable de prendre en compte la complexité multi-échelle du tissu humain et sa variabilité interindividuelle, cette recherche pourrait inspirer de meilleures stratégies de prévention et de traitement personnalisés, en particulier dans le cadre des escarres, des ulcères et des lésions associées aux dispositifs médicaux.

## Mots-clés :

Peau humaine, Poromécanique, Multi-compartiment, Micro-circulation, FEniCSx

# Abstract

Living tissues, such as skin, are particularly sensitive to mechanical and physiological alterations, which can cause lesions, inflammatory redness, or open wounds. These alterations, collectively referred to as tissue damage, encompass any degradation of the structure or function of the tissue. Damage may arise under normal physiological conditions or result from external mechanical stress, such as moderate but prolonged pressure or intense sudden loading. Such situations are common among hospitalised patients or individuals with prolonged immobility - bedridden or wheelchair-bound - and can lead to serious complications such as pressure ulcers. With an ageing population and an increase in chronic diseases and sedentary lifestyles, these injuries represent a major public health challenge. Prevention and management are based on a better understanding of the underlying mechanisms to anticipate their occurrence and develop personalised care strategies.

Tissue lesions are the result of a complex interplay of mechanical, biological, and individual factors. Animal studies have demonstrated a link between mechanical loading, oxygen deprivation (ischaemia), and cell death, particularly when mechanical deformation exceeds a critical threshold, whether through compression or shear. Furthermore, mechanical and ischaemic effects have been shown to act synergistically in initiating and propagating tissue damage. However, current mathematical models often treat these aspects separately, failing to explicitly account for the dynamic interactions between mechanical stress, tissue deformation, micro-circulation, and biological responses. This compartmentalisation limits the predictive power and applicability of these models. In addition, most calibration data come from animal studies, which hampers their direct applicability to human skin and their adaptation to patient-specific variability.

The central hypothesis of this work is that a poromechanical, multiphasic and multi-scale modelling framework, one that integrates the structural, fluidic, and biological components of tissue, can better characterise the critical conditions leading to skin

## *Abstract*

damage. This approach also provides a promising tool for identifying susceptibility biomarkers, thus contributing to the development of personalised preventive care.

The main objective of this thesis is therefore to develop a hierarchical poromechanical model of human skin under physiological conditions, coupling mechanical, micro-circulatory, and biochemical responses, and to validate it against experimental *in vivo* data.

This work combines mathematical modelling with experimental validation. A poromechanical formulation incorporating the solid phase of the skin, the interstitium (including interstitial fluid and mobile cells), and the vascular micro-circulation was implemented using open-source software FEniCSx. *In vivo* tensile tests on human skin provided data to validate the model's ability to reproduce the time-dependent mechanical response. Then an experimental study using skin indentation coupled with laser Doppler perfusion measurements was conducted during the Ph.D. to characterise the micro-circulatory response under external loading. The model was extended to include the vascular network and incorporate biological processes such as oxygen diffusion.

This work thus proposes an approach to studying the interactions between mechanical stress and skin damage mechanisms through coupled modelling of mechanical and biological processes. By providing a tool that accounts for the multiscale complexity of human tissue and inter-individual variability, this research could inform improved strategies for personalised prevention and treatment, particularly in the context of pressure ulcers, wounds, and device-related injuries.

## **Keywords:**

Human skin, Poromechanics, Multi-compartment, Blood flow, FEniCSx

# Table of Contents

Acknowledgments . . . . .	iii
Résumé . . . . .	v
Abstract . . . . .	vii
Table of Contents . . . . .	ix
List of Figures . . . . .	xi
List of Tables . . . . .	xiii

<b>Introduction</b>	<b>1</b>
---------------------	----------

<b>I Literature review</b>	<b>9</b>
1 Introduction . . . . .	11
1.1 Introduction (FR) . . . . .	11
1.2 Introduction (EN) . . . . .	13
2 Clinical description of human skin . . . . .	15
2.1 Structure . . . . .	15
2.2 Functions . . . . .	18
2.3 Pathology . . . . .	19
3 Experimental characterisation of human skin . . . . .	21
3.1 Solid behaviour . . . . .	22
3.2 Fluid behaviour within the skin . . . . .	24
3.3 Vascular evaluation . . . . .	27
4 Mathematical description of human skin . . . . .	33
4.1 Modelling the behaviour of the skin . . . . .	33
4.2 Toward porous media mechanics for the skin . . . . .	38
5 Computational framework . . . . .	43
5.1 Mathematical considerations in a porous medium . . . . .	43
5.2 Computational tools . . . . .	46

*Table of Contents*

6 Conclusion . . . . .	51
<b>II Tutorial implementation of poromechanics in FEniCSx</b>	<b>55</b>
7 FEniCSx tutorial . . . . .	57
7.1 Synopsis (FR) . . . . .	57
7.2 Synopsis (EN) . . . . .	60
7.3 Article . . . . .	62
<b>III <i>In vivo</i> evaluation of a single-compartment model</b>	<b>111</b>
8 <i>In vivo</i> evaluation of a single-compartment model . . . . .	113
8.1 Synopsis (FR) . . . . .	113
8.2 Synopsis (EN) . . . . .	115
8.3 Article . . . . .	117
<b>IV <i>In vivo</i> evaluation of a two-compartment model</b>	<b>143</b>
9 <i>In vivo</i> evaluation of a two-compartment model . . . . .	145
9.1 Synopsis (FR) . . . . .	145
9.2 Synopsis (EN) . . . . .	148
9.3 Article . . . . .	151
<b>V Numerical phantoms and <i>in silico</i> evaluation</b>	<b>207</b>
10 Numerical phantoms and <i>in silico</i> evaluation . . . . .	209
10.1 Synopsis (FR) . . . . .	209
10.2 Synopsis (EN) . . . . .	211
10.3 Article . . . . .	213
<b>VI General conclusion and perspectives</b>	<b>239</b>
<b>Scientific contributions</b>	<b>253</b>
<b>Bibliography</b>	<b>259</b>

# List of Figures

Figure 1:	Graphical abstract . . . . .	6
Figure 2:	Schematic representation of human skin . . . . .	16
Figure 3:	Multiscale structures of the skin . . . . .	24
Figure 4:	Closed and open mechanical systems . . . . .	44
Figure 5:	1D-consolidation column boundary conditions . . . . .	66
Figure 6:	Numerical results vs Terzaghi analytical solution . . . . .	80
Figure 7:	Convergence analysis for the hyper-elastic case . . . . .	81
Figure 8:	Hyper-elastic poromechanical benchmark results . . . . .	84
Figure 9:	Two-compartment benchmark results . . . . .	93
Figure 10:	GMSH and FEniCSx local refinement . . . . .	104
Figure 11:	Elastic displacement and pressure fields . . . . .	108
Figure 12:	Hyper-elastic displacement and pressure fields . . . . .	109
Figure 13:	Convergence analysis of the benchmarks . . . . .	110
Figure 14:	Portable extensometer description . . . . .	122
Figure 15:	Experimentally measured displacement and reaction force . . . . .	123
Figure 16:	Mesh, boundary and initial conditions of the problem . . . . .	128
Figure 17:	Calibration and validation regions in the reaction force curve . . . . .	129
Figure 18:	Numerical response superposed with the experimental data . . . . .	133
Figure 19:	Model response at different times: $u$ , $p^l$ and fluid flow . . . . .	134
Figure 20:	LDF Experimental set-up . . . . .	157
Figure 21:	LDF experimental loading conditions . . . . .	158
Figure 22:	Description of the representative elementary volume . . . . .	159
Figure 23:	2-compartment consolidation test boundary conditions . . . . .	169
Figure 24:	Phalanx model and boundary conditions . . . . .	172
Figure 25:	Median LDF and temperature experimental results . . . . .	177
Figure 26:	Median normalised LDF experimental results . . . . .	179
Figure 27:	2-compartment 1D consolidation test results . . . . .	182

## List of Figures

Figure 28: Speed-up for the computation as the CPU count increases . . . . .	183
Figure 29: 2-compartment models versus experimental corridors . . . . .	185
Figure 30: 3D model response: $u$ , blood flux, $\varepsilon^b$ . . . . .	187
Figure 31: First order sensitivity analysis of the 2-compartment model . . . . .	203
Figure 32: Automatic porous scaffold generation . . . . .	218
Figure 33: Sample microstructure $N = 3000$ . . . . .	228
Figure 34: From STL to voxel spaces . . . . .	230
Figure 35: Example of EDAC output fields R.O.I. . . . .	232
Figure 36: Example of EDAC output: histograms . . . . .	232
Figure 37: Distribution of creeping regime parameters . . . . .	233
Figure 38: Volume fraction distributions for sample characteristic lengths . . .	234
Figure 39: Example of experimental setup for permeability evaluation . . . . .	235
Figure 40: Evolution of the principal direction permeability $\bar{K}_{33}$ . . . . .	236
Figure 41: Experimental considerations for evaluation of the <i>in silico</i> campaign	246

# List of Tables

Table 1:	Review of the elastic properties of the skin . . . . .	35
Table 2:	Review of usual porous parameters . . . . .	40
Table 3:	Elastic mechanical parameters to compare with the Terzaghi solution	69
Table 4:	Hyper-elastic mechanical parameters of the benchmark . . . . .	69
Table 5:	Initial conditions for the single compartment model . . . . .	75
Table 6:	Mechanical parameters for the bi-compartment model . . . . .	85
Table 7:	Initial conditions for the bi-compartment model . . . . .	88
Table 8:	NRMSE computed for each studied variable . . . . .	94
Table 9:	Description of the phases for a 1-compartment model . . . . .	116
Table 10:	Initial mechanical parameters for the bi-compartment model . . . .	131
Table 11:	Calibrated parameters for each layer and optimal cost function value	132
Table 12:	Sobol indices of the model's parameters . . . . .	139
Table 13:	2-compartment biphasic phases (synopsys) . . . . .	149
Table 14:	2-compartment biphasic phases . . . . .	159
Table 15:	Mechanical parameters for 2-compartment biphasic model . . . . .	170
Table 16:	Material parameters for the sensitivity analysis . . . . .	175
Table 17:	First-order sobol indices . . . . .	184
Table 18:	Second-order sobol indices . . . . .	184
Table 19:	Geometrical and computational information of synthetic samples .	229



# Introduction

## Context and Motivation of the thesis

An international consortium (composed of the National Pressure Injury Advisory Panel, the European Pressure Ulcer Advisory Panel, and the Pan Pacific Pressure Injury Alliance) redefined the definition of a pressure injury in 2016 as "*A pressure injury [which] is localised damage to the skin and underlying soft tissue [...]. The injury occurs as a result of intense and/or prolonged pressure or pressure in combination with shear*". Pressure ulcers are generally categorised into two types: superficial pressure ulcers, which develop on the skin due to prolonged contact with an external device, and deep pressure ulcers, which form internally at the interface between soft tissues and bones. Notably, superficial pressure ulcers account for approximately 70% of all pressure ulcer cases Kim et al. 2020; Moore et al. 2019.

The prevalence of pressure ulcers varies considerably among at-risk populations (for example, elderly, diabetic patients, amputees, etc.). It is estimated that 34 % of amputees have experienced a skin lesion (Lyon et al. 2000), leading to a prosthesis abandonment rate of 25 %-57 % (Meulenbelt et al. 2009). Furthermore, between 9 % and 20 % of hospitalised patients in Europe have been reported to have a pressure ulcer (Vanderwee et al. 2007). On a wider scale, pressure ulcers are experienced by more than half of hospitalised patients worldwide (Ayello 2008; Parvizi et al. 2023), making it the third most costly disorder (Bennett et al. 2004; Parvizi et al. 2023). For example, the estimated annual cost of PU care in the United States has increased from 11.6 to 26.8 billion dollars between 2000 and 2016 (Padula and Delarmente 2019). The prevalence of PUs is not only an economical, but also a social concern. PUs can result in long-term hospitalisation, increasing the risk of loneliness and isolation of the patient, further leading to depression. The National Pressure Ulcer Advisory Panel (NPUAP) reports a healing time of approximately 9

## *Introduction*

to 12 months with permanent scars from a full-thickness pressure injury. In addition, PUs are a factor that increases the morbidity and mortality of patients. Infection is often related to these sores and can lead to drastic measures such as amputation.

To prevent the onset of PU, various qualitative strategies have been developed that leverage clinical scales such as the Braden (Bergstrom et al. 1987) and Norton (Pancorbo-Hidalgo et al. 2006) scales. These scale evaluates the condition of the skin (moisture, loading history), the patient level of activity, state of mind, mobility, nutrition, and exposure to friction and shear. Based on these items, a score is developed and is believed to indicate the risk of the onset of PU in a patient. Then it will lead to the development of a preventive intervention plan that includes repositioning, adapted support surfaces to reduce local pressure in the tissue, regular cleaning and drying of the skin, and monitoring of the person's nutrition (NPUAP). These strategies emphasise the importance of the medical team, particularly nurses, maintaining a vigilant and proactive approach. The process involves a wide range of actions, such as regularly mobilising and repositioning patients, which are critical to reducing the risk of PU development. Nurses and healthcare professionals play an essential role in consistently monitoring and implementing these preventive measures to ensure patient safety and comfort.

However, the large number of identified cases of PU suggests that this qualitative method of risk assessment is not fully satisfying and their reliability can be questioned (Anthony et al. 2008). Therefore, efforts have been made to find quantitative markers that may be more closely related to the onset of PU.

Preclinical studies on cellular cultures and animals first helped assess multiscale and multiphysics processes at the onset of PUs. As highlighted in Figure 9 of Oomens et al. 2014, two primary mechanisms are involved in the development of pressure ulcers, operating in competition during their onset. On the macroscopic scale, excessive load as well as a sustained moderate load can cause the onset of PU (Ceelen et al. 2008; Loerakker et al. 2011; Loerakker et al. 2010; Nierop et al. 2010; Stekelenburg et al. 2006; Traa et al. 2019; Tsuji et al. 2005). On the microscopic scale, the absence of oxygen diffusion, followed by a sudden supply of oxygen initiated by moderate and sustained local deformations, promotes cell damage (referred to as ischaemia-reperfusion) and is believed to be responsible for PU (Loerakker et al. 2011; Stekelenburg et al. 2006; Tsuji et al. 2005). The current status of the skin has been further shown by Reswick and Rogers 1976; Swisher et al. 2015; Tsuji et al.

2005 to play a key role in the risk assessment. For example, using magnetic methods, Swisher et al. 2015 demonstrated that the duration of sustained compression is a critical factor in determining tissue damage. Specifically, tissue damage remains reversible up to a certain threshold duration; beyond this critical time, the damage becomes irreversible.

However, these observations cannot be directly transferred to human beings and clinics. Clinical studies have been carried out and it has been found that a relation can be established between similar biomechanical factors and current knowledge on a "patient scale" - provided by the clinical scales - as proposed by (Coleman et al. 2014). These biomechanical factors can be subdivided into intrinsic parameters (skin morphology, oxygen level) and extrinsic factors (external loading). However, there is no single factor that can explain the risk of pressure ulcers, but rather a complex interplay of factors (Coleman et al. 2013). It follows that the investigation of the biomechanical behaviour dependent on time of vascularised soft tissues is crucial to improve our understanding of the onset of PU, allowing better prevention.

To investigate the interplay between mechanical loading and micro-circulation, current methodologies typically employ multiscale 3D-1D approaches. These methods include an explicit representation of the vascular system (Bauer et al. 2005; Mithraratne et al. 2012; Sree et al. 2019a). However, such models necessitate an explicit description of the vascular tree, leading to computationally intensive simulations, and often exhibit weak coupling between the mechanical and vascular responses. In contrast, porous models offer an efficient alternative by incorporating biochemical and diffusion processes through a more robust coupling, as demonstrated in Sciumè et al. 2014a. Indeed, a mechanical approach based on porous media mechanics allows the coupling of a solid phase with fluid compartments, where biochemical exchanges occur. Such models, initially developed for soil engineering (Terzaghi 1943), are transferable to soft tissues given their multiphasic and multiphysics nature. For example, these models have been applied to various soft biological tissues, including the brain (Budday et al. 2019; Carrasco-Mantis et al. 2023; Greiner et al. 2021; Hervas-Raluy et al. 2023; Hosseini-Farid et al. 2020; Urcun et al. 2023; Urcun et al. 2022), the liver (Ricken and Lambers 2019), the meniscus (Bulle 2022; Kazemi et al. 2013; Uzuner et al. 2022; Uzuner et al. 2020), and muscle tissue (Lavigne et al. 2022b). Although poromechanics theory has been extensively applied in other soft biological tissues, only a few studies have been published for

## Introduction

the skin, and these were limited to *in silico* and *ex vivo* studies.

Pressure ulcers are often associated with tissue damage which has been extensively studied in the literature (Fromy et al. 1998; Gefen et al. 2022; Loerakker et al. 2010; Oomens et al. 2014; Sree et al. 2019b; Stekelenburg et al. 2006). Differently, the primary focus of this project is the development of a hierarchical poromechanical model that explicitly incorporates the vascular system to explicitly model the onset of damage due to hypoxia and mechanics. Hence, in this study, **only physiological ranges** are considered; no explicit modelling of damage mechanisms is undertaken. The central research hypothesis is that **a hierarchical poromechanical framework enables the integrated modelling of both mechanical behaviour and microvascular response of skin tissue, under physiological conditions and mechanical loading**. This thesis aims to contribute computational tools that bridge the existing gap between preclinical findings and clinical observations. Situated at the intersection of multiple disciplines, including physics, biology, mathematics, computational mechanics, and clinical science, this work aspires to advance understanding and application across these fields by addressing the following key research questions:

- ☞ Can a poromechanical model reproduce the skin's time-dependent behaviour?
- ☞ How to include the vascular system in a poromechanical model?
- ☞ How to evaluate the reliability of numerical predictions?

Many studies rely on commercial finite element software (such as ABAQUS), but these tools often limit customisation and require expensive licences. Using FEniCSx for finite element modelling offers significant advantages in addressing these questions. FEniCSx is an open source computing platform for solving partial differential equations (PDE) that provides robust tools for developing and implementing complex biomechanical models. It allows for high flexibility in defining custom equations and boundary conditions, which is crucial for accurately modelling the coupled mechanical and biochemical behaviour of skin tissues. The ease of integration with other scientific libraries and its support for parallel computing make FEniCSx particularly suitable for the large-scale simulations required in this study (Logg et al. 2012). The use of open-source software like FEniCSx not only facilitates reproducibility and transparency in research, but also democratises access to advanced computational tools. This openness allows researchers worldwide to collaborate,

verify, and build on each other's work, accelerating scientific progress. Furthermore, community-driven development of open source software ensures continuous improvement and adaptation of tools to the latest scientific needs, thus enhancing the reliability and applicability of research results (Hasselbring et al. 2020).

## Presentation of the manuscript

This manuscript is a cumulative thesis, with Parts II, III, IV, and V comprising published or under review works (except Part V which is currently in preprint). The Introduction, Part I (*"Literature review"*), and Part VI (*"Perspectives and general conclusion"*) are integral components of the thesis itself. The material related to the articles is available on Github (links are included in the articles). Figure 1 summarises the proposed approach to answer the research question. It reflects the organisation of this dissertation.

Part I, *"Literature review"*, is divided into 4 sections, starting from the clinics to the computational frameworks. Through this structured approach, the chapter aims to bridge the gap between clinical observations, experimental findings, mathematical modelling, and computational simulations. It provides a robust foundation for the application of porous media mechanics to the study of human skin, paving the way for advances in predictive modelling and therapeutic applications.

Part II, *"Tutorial implementation of poromechanics in FEniCSx"*, provides a foundational analysis, offering an in-depth exploration of the theoretical framework that underpins the Ph.D. models. This theory was then applied through a tutorial-based approach using the open-source software FEniCSx, where it was optimised for parallel computation. Single- and two-compartment poromechanical models were introduced, rigorously evaluated against benchmark cases. These models serve as the foundation for the subsequent chapters. The corresponding article was accepted for publication in 2023 in the *Journal of the Mechanical Behavior of Biomedical Materials* as a Tutorial article.

Part III, *"In vivo evaluation of a single-compartment porous model"*, aims to address the research question: "Can a poromechanical model reproduce the skin's time-dependent behaviour?". Unpublished experimental data of *in vivo* human skin during extension test were used in the study. The objective was to assess the relevance

## Introduction

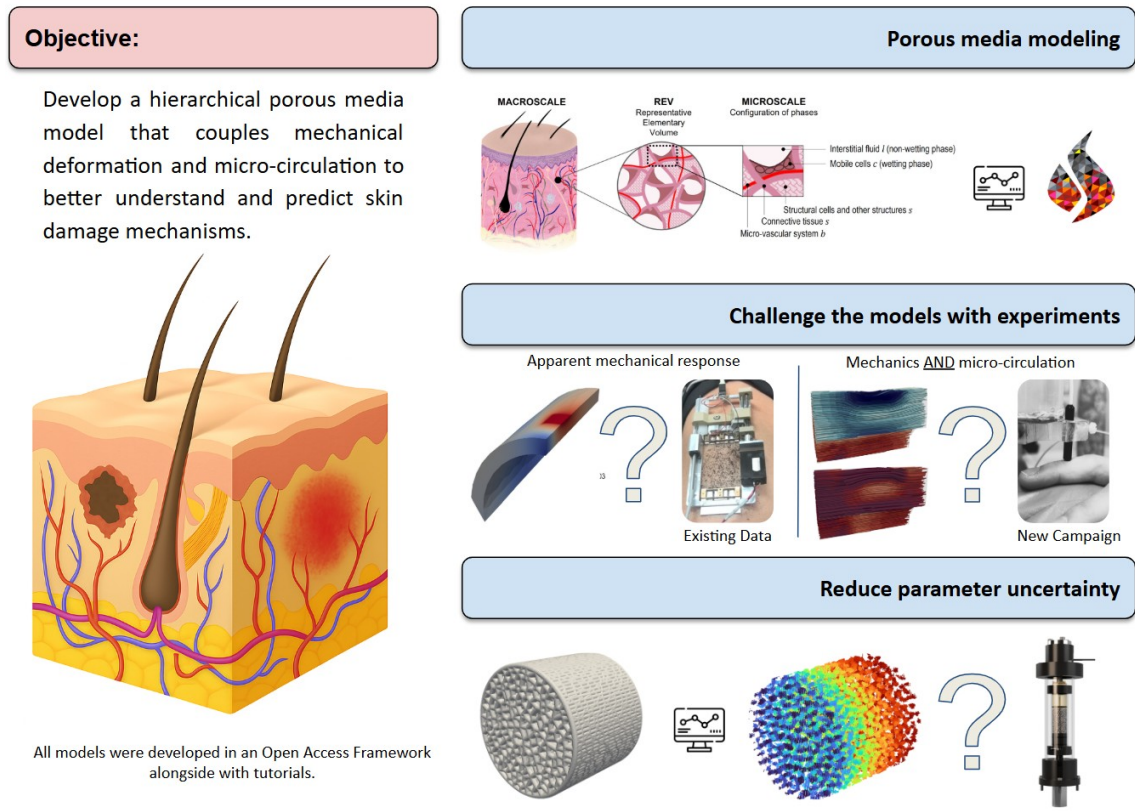


**Figure 1:** This study focused on the development and evaluation of porous models to represent skin mechanics and related biological responses. Initially, a one-compartment model was assessed to test its ability to replicate the apparent mechanical behavior observed during extension testing. Subsequently, a two-compartment model was designed and evaluated in conjunction with an experimental campaign to integrate both mechanical response and microcirculatory dynamics. Additionally, a computational pipeline was proposed to reduce uncertainty in material parameter estimation using numerical phantoms.

of employing a poromechanical approach to capture aspects of the time-dependent response of the skin. In this proof of concept, a simplified bi-layered geometry was developed to model the upper arm skin of a 22-year-old female, incorporating the cutis and subcutis layers. A single-compartment poro-hyper-elastic model was introduced. Calibration was performed using half of the dataset, while the remaining half was utilised for validation. Material parameters in the range of values reported in the literature were identified, achieving a low root mean square error between the model response and the experimental data. However, a single experiment on a single patient was available, highlighting the need for a more comprehensive experimental campaign, with particular attention to boundary conditions (to respect the specific

needs of multi-phase simulation). The corresponding article is under peer review.

Part IV, "*In vivo evaluation of a two-compartment porous model*", aims to integrate both experimental and modelling approaches. Specifically, a two-compartment poro-elastic model was developed to incorporate microvasculature. The experimental campaign, performed during this thesis, involved the use of a Laser Doppler Flowmetry (LDF) probe to apply an indentation load on the second phalanx of the middle finger skin. Four cycles of loading, sustaining, unloading, and sustaining steps were performed, during which both ischaemia and hyperaemia were observed. The sensitivity analysis of the model identified three dominant parameters of the material that influence blood flow. The model successfully accounted for both ischaemia and hyperaemia using literature-based material parameter values. However, a one-to-one calibration was not conducted because of the absence of displacement field data, as calibration using only the flux could potentially result in multiple local minima. Once again, control of the boundary conditions remains a challenge. The corresponding article is under peer review.

Part V, "*Towards a better control of boundary conditions: method for phantom generation and in silico evaluation*" introduces a numerical methodology for evaluating permeability in non-periodic porous structures. This approach leverages automated geometry generation, high-fidelity simulations, and statistical estimation techniques to provide a comprehensive assessment of permeability. Previous sections have highlighted the significant influence of critical parameters such as the Young's modulus and the permeability of the porous network on the mechanical and micro-circulatory responses. However, despite their importance, these parameters continue to be subject to considerable variability and uncertainty in their identification, underscoring the need for more precise and reliable methods to accurately quantify them. 3D porous structures are created with Neper and Pymesh, involving tessellation, sphere placement, and Constructive Solid Geometry (CSG) processing for voxelised simulations. Fluid dynamics are modelled using the Entropically Damped Artificial Compressibility method, with permeability assessed under creeping flow conditions (Reynolds number  $Re \ll 1$ , normalised vorticity  $\Delta\omega^* \ll 1$ ) and estimated via the Moore-Penrose pseudo-inverse method with Monte Carlo sampling. This methodology enables *in silico* permeability identification and validation via 3D printing, with applications in tissue engineering and biomedical implants. Similarly to the other sections, this work is made available as open-access, providing the codes on GitHub.

## *Introduction*

This study corresponds to work in progress and is currently in preprint.

Part VI: "*General conclusion and perspectives*" outlines the key findings of this thesis as a foundational step toward the integration of multi-compartment porous media mechanics in the clinical description of human skin. These findings mark a significant advancement in our modelling and understanding of the complex biomechanical behaviour of the skin, offering new avenues for improved diagnostics, treatments, and therapeutic interventions in dermatology. The section further explores potential developments in both experimental methodologies and computational modelling techniques. Future experiments could delve deeper into the characterisation of the skin's porous structure at both macroscopic and microscopic levels, considering additional biological factors such as cellular interactions, and response to biochemical environmental stimuli. The inclusion of multi-compartment modelling could be expanded to account for more granular variations in skin properties across different regions of the body, incorporating anatomical and physiological variability. In terms of computational frameworks, there are opportunities to improve the precision and efficiency of numerical simulations. Incorporating more advanced algorithms, such as those based on machine learning or artificial intelligence, could allow for real-time predictive modelling of skin behaviour under various conditions. Furthermore, advances in computational power could support the development of more complex, high-resolution models that simulate mechanical interactions between skin layers, embedded structures, and external forces with greater accuracy.

# **Part I**

## **Literature review**



# 1 Introduction

## Table of Contents

---

1.1	Introduction (FR) . . . . .	11
1.2	Introduction (EN) . . . . .	13

---

### 1.1 Introduction (FR)

L'objectif principal de ce travail de recherche est d'évaluer l'efficacité d'une modélisation basée sur la mécanique des milieux poreux pour simuler le comportement de la peau humaine en fonction du temps, y compris son réseau vasculaire, et donc de permettre l'intégration potentielle de la réponse biologique. Une compréhension globale des propriétés et du comportement du tissu cutané, en condition physiologique et sous chargement mécanique, est essentielle pour répondre à la questions de recherche susmentionnée. En conséquence, ce chapitre établit les connaissances fondamentales nécessaires à l'application de la mécanique des milieux poreux à la peau humaine. Le contenu est systématiquement organisé en quatre sections interdépendantes, formant une progression logique allant des observations cliniques à la modélisation numérique prédictive :

- Description clinique de la peau humaine,
- Caractérisation expérimentale de la peau humaine,
- Description mathématique de la peau humaine,
- Framework numérique.

## *1 Introduction*

La première section, axée sur la description clinique de la peau humaine, fournit un examen détaillé de la structure anatomique et des composants de la peau, élucidant ses fonctions physiologiques à multiples facettes et les pathologies courantes qui peuvent affecter son intégrité. Cette perspective clinique constitue une base essentielle pour les sections suivantes.

S'appuyant sur ces connaissances cliniques, la deuxième section se penche sur la caractérisation expérimentale de la peau humaine. La discussion porte sur les techniques expérimentales utilisées pour étudier les propriétés mécaniques des tissus cutanés. L'accent est mis sur ses caractéristiques solides et fluides, ce qui permet de mieux comprendre l'interaction complexe de ces composants dans diverses conditions.

La troisième section passe à un cadre mathématique, synthétisant les connaissances acquises à partir des observations expérimentales. Cette partie présente les principaux modèles et analyses mathématiques conçus pour améliorer la compréhension de la mécanique de la peau. Elle présente également une compilation des paramètres de modèles couramment utilisés et de leurs valeurs associées, servant de ressource pour les études futures dans ce domaine.

La dernière partie met l'accent sur les aspects informatiques, en présentant le cadre poromécanique et les perspectives mathématiques. Une attention particulière est accordée à l'application d'outils logiciels libres, soulignant leur accessibilité et leur potentiel pour faire avancer la recherche dans ce domaine. Cette section décrit également les défis de la mise en œuvre et les possibilités d'affiner les capacités prédictives.

Grâce à cette approche structurée, le chapitre vise à dresser, pour la peau, l'état de l'art des observations cliniques, des résultats expérimentaux, de la modélisation mathématique et de la simulation numérique. Il fournit une base solide pour l'application de la mécanique des milieux poreux à l'étude de la peau humaine, ouvrant la voie à des avancées en matière de modélisation prédictive et d'applications thérapeutiques.

## 1.2 Introduction (EN)

The primary objective of this PhD research is to evaluate the effectiveness of a modelling approach based on porous media mechanics in simulating the time-dependent mechanical behaviour of human skin, including its vascular network, and therefore, allowing for the potential integration of the biological response. A comprehensive understanding of the properties and behaviour of skin tissue, under physiological conditions and under loaded conditions, is crucial to addressing the aforementioned research question. Accordingly, this chapter establishes the foundational knowledge required for the application of porous media mechanics to human skin. The content is systematically organised into four interrelated sections, forming a logical progression from clinical observations to computational analysis and predictive modelling:

- Clinical description of human skin,
- Experimental characterisation of human skin,
- Mathematical modelling of human skin,
- Computational framework and implementation.

The first section, focused on the clinical description of human skin, provides a detailed examination of the anatomical structure and constituent components of the skin, elucidating its multifaceted physiological functions and common pathologies that may affect its integrity. This clinical perspective is necessary for the subsequent sections.

Building on this clinical knowledge, the second section delves into the experimental characterisation of human skin. Here, the discussion encompasses a review of state-of-the-art experimental techniques used to investigate the mechanical properties of the skin tissue. The focus extends to its solid and fluid constituents, offering insights into their complex interplay under various conditions.

The third section transitions into a mathematical framework, synthesising the insights gained from experimental observations. This segment introduces key mathematical models and analyses designed to improve our understanding of skin mechanics. It also presents a curated compilation of commonly used model parameters and their associated values, serving as a resource for future studies in this domain.

## *1 Introduction*

The final section emphasises computational aspects and presents the poromechanical framework. Particular attention is paid to the application of open source software tools, highlighting their accessibility and potential to deepen research in this field. This section also outlines the implementation challenges and opportunities for refining predictive capabilities.

Through this structured presentation of the skin mechanics, the chapter aims to provide a state-of-the-art overview of clinical observations, experimental results, mathematical modelling, and computer simulation. It provides a robust foundation for the application of porous media mechanics to the study of human skin, paving the way for advances in predictive modelling and therapeutic applications.

# 2 Clinical description of human skin

## Table of Contents

---

2.1	Structure	15
2.2	Functions	18
2.3	Pathology	19

---

### 2.1 Structure

The skin, a component of the integumentary system, exhibits significant variability both between individuals (*e.g.*, pigmentation) and within a single individual, influenced by factors such as age and anatomical location. Age-related changes include the development of wrinkles and a decrease in skin integrity. Furthermore, skin thickness varies between different regions of the body, as evidenced by thinner skin on the lips compared to thicker skin on the soles of the plantar foot (Gaboriau and Murakami 2001). It is the largest organ of the human body, accounting for approximately 7 % of total body weight. Anatomically, the skin comprises **three main layers**: the epidermis, the dermis, and the hypodermis (see Figure 2). In particular, there is a correlation between the thickness of the epidermis and the dermis, with a thicker epidermis often accompanied by a thicker dermis to enhance the effect of the dermis on overall skin thickness. Furthermore, a thicker epidermis tends to

## 2 Clinical description of human skin

be associated with a more vascularised upper dermis, ensuring adequate nutrient supply to the outermost layers (Diegel et al. 2018).

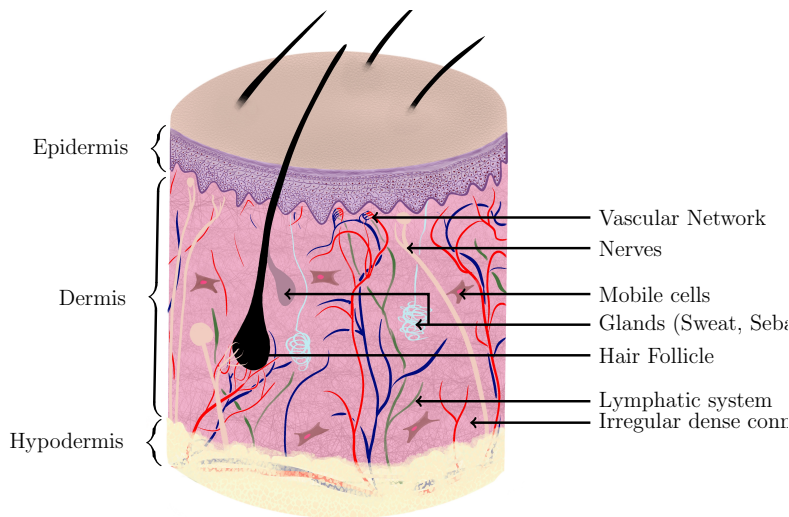


**Figure 2:** Schematic representation of human skin. The skin is a stratified soft tissue subdivided into the epidermis (isotropic), the dermis (fibrous) and subcutis (isotropic). [Original Image inspired from Pfisterer et al. 2021]

The **epidermis**, the outermost layer, usually reaches 50 to 150 µm in thickness (Abdo et al. 2020; Burns et al. 2010; Joodaki and Panzer 2018; Wong et al. 2015; Yazdi and Baqersad 2022) and is primarily composed of keratinocytes. It is subdivided into four layers: the stratum corneum, the stratum granulosum, the stratum spinosum, and the stratum basale, depending on the cellular position and microscopic characteristics. The epidermis undergoes continuous renewal, with cells progressing from the stratum basale to the stratum corneum over approximately 5 to 30 days (Burns et al. 2010). This process, known as cornification, varies according to the anatomical site and the health of the skin (Diegel et al. 2018). The epidermis also contains melanocytes, Langerhans cells, and Merkel cells, which contribute to skin colour, immune response, and sensory function, respectively.

The **dermis** lies beneath the epidermis, connected by an irregularly shaped basement membrane. Together, these layers are often referred to as the cutis. The dermis is significantly thicker than the epidermis, ranging from 0.5 to 5 mm (Burns et al. 2010; Yazdi and Baqersad 2022). It consists of the papillary and reticular dermis and serves as a supportive matrix composed of macromolecules that retain water (about **60 % of the total weight of the dermis is bound or free water**) (Burns et al. 2010; Dwivedi et al. 2022). The main components of the dermal extra-

cellular matrix include collagen (80-85 % of the dry weight), which provides tensile strength; elastin (2-4 % of the matrix), which allows stretch and movement; and reticulin, which supports organs and glands (Abdo et al. 2020; Burns et al. 2010; Diegel et al. 2018; Joodaki and Panzer 2018). The orientation of collagen fibbers in the dermis generally follows the underlying muscle fibers, a pattern mapped as Langer lines (Abyaneh et al. 2014). This dense and irregular layer of connective tissue imparts mechanical strength and influences the time-dependent mechanical behaviour of the skin (Dwivedi et al. 2022). Unlike the avascular epidermis, the dermis is **highly vascularised** and contains sweat glands, hair follicles (approximately 11 per cm<sup>2</sup>), nerves, and lymphatics (see Figure 2). Braverman 1989; Liao et al. 2013 describe the dermal vasculature as consisting of two interconnected systems: the superficial vascular plexus in the papillary dermis and the deep vascular plexus at the dermal-subcutaneous interface. The superficial plexus comprises paired arterioles and venules, with capillaries arising from these arterioles, extending upward into the papillary dermis, and looping back to the venules. The deep vascular plexus includes arterioles and venules of larger diameter originating from the underlying muscles and subcutaneous fat. Terminal arterioles are typically 17-26 µm in diameter. Sensory nerves in both types of skin release vasoactive agents in response to thermal, chemical, and mechanical stimuli, influencing the vascular tone of the skin and providing feedback to the central nervous system for the regulation of local blood flow. Capillaries, typically 5-10 µm in diameter, are endothelial tubes surrounded by a basement membrane that allows the exchange of chemical substances between blood and surrounding tissues. Although capillaries cannot actively dilate or contract, the exchange surface area can be regulated to some extent by precapillary sphincters, rings of smooth muscle. The capillary bed is an interwoven network comprising true capillaries, which facilitate the exchange of oxygen, carbon dioxide, and nutrients, and vascular shunts, which are short vessels that directly connect arterioles and venules within the bed (Braverman 1989; Liao et al. 2013).

The deepest layer, the **hypodermis**, or subcutaneous tissue or subcutis, lies between the dermis and the underlying organs. This layer is rich in adipose tissue and loose aerolar tissue (Kim and Dao 2023). In non-obese individuals, approximately 80 % of body fat is located in this subcutaneous layer (Burns et al. 2010). Imaging 67 subjects, Querleux et al. 2002 further described the composition of the subcutaneous adipose tissue which contains 7.4 % of water, 7.3 % of unsaturated lipids and 85.3 % of saturated lipids.

## 2.2 Functions

The skin contributes to maintaining **homeostasis**, the body's tendency to maintain a stable internal environment. This involves regulating temperature, blood pressure, hydration, and other physiological variables through feedback mechanisms (Caon 2020). In fact, the skin is the first line of defence against numerous environmental hazards, including physical trauma, temperature fluctuations, infectious agents, and harmful chemicals (Burns et al. 2010; Proksch et al. 2008). The skin also orchestrates the wound healing process through homeostasis, inflammation, proliferation, and remodelling. This involves coagulation, immune cell infiltration, tissue formation, and extracellular matrix remodelling (Kim and Dao 2023).

The epidermis is the main protective barrier function against pathogens and regulates water loss (Kanitakis 2002). Restricts water loss while providing immune responses to external threats such as bacteria, viruses, and fungi. The physical barrier of the skin prevents the direct entry of pathogens. Junction proteins and keratin filaments reinforce cell connections, while antimicrobial peptides (AMPs) and lipids disrupt bacterial membranes (Kim and Dao 2023). Melanocytes within the epidermis produce melanin, which protects against the genotoxic effects of UV radiation and binds potentially harmful compounds such as cations and metals (Diegel et al. 2018). Merkel cells act as mechanoreceptors, aiding in tactile sensation and **signalling** changes in blood flow (Diegel et al. 2018).

The dermis provides the skin with **tensile strength** through collagen and elasticity through elastic fibers. The extensive network of blood vessels on the skin contributes to thermoregulation through vasoconstriction and vasodilation, working in conjunction with the sweat glands during physical activity (Burns et al. 2010). In addition, it plays vital roles in nutrient delivery, oxygen supply, protection, and maintenance of **homeostasis** (Jo and Kwon 2012; Klee et al. 2007; Lademann et al. 2022; Petrofsky and Berk 2012; Strömberg et al. 2014). This layer also contains various immune cells, including Langerhans cells and dermal dendritic cells, which are vital for adaptive and innate immune defence (Diegel et al. 2018). Furthermore, the dermis contains sensory receptors that respond to touch, temperature, and pain, thus playing a critical role in sensory perception (Kanitakis 2002).

The subcutis is the frontier between the cutis and the internal structures of the body. This **soft honeycomb** structure provides support to cushioning trauma and

load-bearing (Burns et al. 2010; Diegel et al. 2018). Furthermore, this adipose tissue represents counter-acting actors in energy metabolism (Avram et al. 2005; Ibrahim 2009). Indeed, it allows the storage of excess energy as lipids and can use the accumulated lipids as a source for chemical energy that is released as heat, providing insulation to internal organs for thermoregulation.

## 2.3 Pathology

This section aims to provide an overview of common skin pathologies that can generally be related to one of the following categories: aesthetic pathologies, infectious diseases, cancers, and environmental-related damage.

Aesthetic pathologies such as acne vulgaris and atopic dermatitis (also known as eczema) are the result of inflammatory conditions Gawkroger and Ardern-Jones 2020. Acne vulgaris is characterised by keratin overproduction, increased sebum, and inflammation mediated by *Cutibacterium acnes*. Atopic dermatitis, a chronic disease, involves genetic factors, epidermal junction defects, and reduced immunity. Another common pathology is psoriasis, an autoimmune disorder that accelerates the turnover of skin cells, resulting in thick and scaly patches Nickoloff et al. 2007. The pathophysiology of psoriasis involves hyperproliferation of keratinocytes and immune system dysfunction.

Infectious skin diseases include bacterial, viral, and fungal infections. Common bacterial infections include cellulitis and impetigo, caused by *Staphylococcus aureus* and *Streptococcus pyogenes*, respectively (Gawkroger and Ardern-Jones 2020). Viral infections, such as those caused by the herpes simplex virus or human papillomavirus, affect the skin and mucous membranes. Fungal infections, such as athlete's foot and ringworm, present with symptoms like itching, scaling, and redness.

The skin cancer category encompasses three primary cancer types: basal cell carcinoma (BCC), squamous cell carcinoma (SCC), and melanoma, each with distinct characteristics and risk factors. BCC, the most prevalent, originates from the basal cells of the epidermis and is strongly associated with ultraviolet (UV) radiation, leading to mutations in tumour suppressor genes and proto-oncogenes (Pellegrini et al. 2017). Clinically, it manifests as a pink and pearly papule with telangiectasia, and a biopsy is necessary for confirmation (Pellegrini et al. 2017). SCC, arising from

## *2 Clinical description of human skin*

epidermal keratinocytes, has the potential to metastasise if left untreated. It usually presents as erythematous papules, plaques, or nodules that can ulcerate or become hyperkeratotic, particularly in areas exposed to sunlight, with diagnosis confirmed by biopsy (Waldman and Schmults 2019). Melanoma, the most lethal form of skin cancer due to its high metastatic potential, originates from melanocytes and is classified into four sub-types: superficial spreading, nodular, lentigo maligna, and acral lentiginous. Early detection using the ABCDE criteria (asymmetry, border irregularity, colour variation, diameter, and evolution) is crucial for effective management and prognosis (Abbasi et al. 2004; Armstrong and Kricker 1995).

Other dermatologic conditions, such as burns and **pressure ulcers**, involve direct tissue damage from external interactions. Burns caused by excessive heat, radiation, or chemical exposure are classified by depth and area of skin involvement. Severe burns can result in dehydration, and sepsis, necessitating immediate and specialised medical intervention. The severity of burns ranges from superficial, affecting only the epidermis, to fourth degree, which extends beyond the skin to the underlying tissues. Pressure ulcers, also known as bed sores, are localised areas of tissue necrosis resulting from prolonged pressure on the skin. These ulcers can occur from the interaction of the skin with external devices or from pressure over bony prominences, leading to superficial or deep tissue damage (Gefen et al. 2022).

Although the clinical understanding of skin pathologies is well-established through biological and medical research, their physical underpinnings, particularly in terms of mechanical behaviour, have historically received less attention. Most studies have focused on **cellular mechanisms**, **immunological pathways**, or **genetic predispositions**, often overlooking the **mechanical environment** in which these pathologies develop and evolve. However, recent findings suggest that physical factors such as stress and tissue deformation may play a critical role in the onset and progression of various skin disorders. This has led to a growing interest in the biomechanical and physics-based characterisation of human skin, which offers complementary insights to traditional biological approaches.

## **3 Experimental characterisation of human skin**

### **Table of Contents**

---

3.1 Solid behaviour . . . . .	22
3.2 Fluid behaviour within the skin . . . . .	24
3.3 Vascular evaluation . . . . .	27

---

Since the 1970s, the study of skin has gained interest in the biomechanical field to better understand its mechanical behaviour, leading to a potential prevention of skin integrity loss. Consequently, skin has been tested under a wide variety of experimental conditions, and several reviews have been proposed in recent years to identify trends in its response (Connesson et al. 2023; Joodaki and Panzer 2018; Jor et al. 2013; Kalra and Lowe 2016; Oomens et al. 2017; Yazdi and Baqersad 2022). Similarly to its structure (Section 2.1), the mechanical properties of the skin are influenced by intra- and inter-individual factors. For example, its apparent stiffness is sensitive to ageing processes (Agache et al. 1980; Bader and Bowker 1983; Escoffier et al. 1989; Sanders 1973; Tonge et al. 2013; Zahouani et al. 2011). Gaboriau and Murakami 2001 explained this trend by the rearrangement of the skin into thick, coarse bundles of straight fibbers in the dermis.

### 3 Experimental characterisation of human skin

#### 3.1 Solid behaviour

Depending on the mechanical properties and anatomical structure studied, different experimental tests have been conducted under *in vivo* and *ex vivo* conditions. Until the 1970s, experiments on human skin were limited mainly to cadaver samples (Sanders 1973). The advantage of *ex vivo* experiments lies in the precise control of the boundary conditions; however, the conclusions drawn do not necessarily hold for the skin under physiological conditions. Therefore, various testing methods were introduced to characterise the physiological response of the skin to external loads, including uniaxial tests (Annaidh et al. 2012; Gallagher et al. 2012; Gibson et al. 1969; Jacquet et al. 2017a; Khatyr et al. 2004; Ottenio et al. 2015), suction tests (Connesson et al. 2023; Diridollou et al. 2000; Elouneg et al. 2023; Grahame and Holt 1969; Hendriks et al. 2003; Lakhani et al. 2021), torsion tests (Agache et al. 1980; Escoffier et al. 1989; Finlay 1970), and indentation tests (Bader and Bowker 1983; Boyer et al. 2007; Cornillon et al. 2024; Elleuch et al. 2006; Khaothong 2010; Pailler-Mattei et al. 2008; Raveh Tilleman et al. 2004; Segain et al. 2024; Zahouani et al. 2011). Although only a few examples are listed here, most studies refer to one of these testing conditions, with some variations, to assess the mechanical behaviour of the skin.

From these studies, trends in the mechanical response of the skin have been observed. Firstly, the stress-strain curves of the skin follow a **non-linear "J-shaped"** path, with three distinct regions identified (Gibson et al. 1969; Joodaki and Panzer 2018; Yazdi and Baqersad 2022). Initially, the collagen fibbers align with each other in the toe region of the curve, resulting in a linear region and large deformations of the skin under a small amount of force. As the fibbers align, the second region is characterised by a rapid increase in stiffness due to fibber elongation. Finally, all the fibbers are in a stretched state, leading to a second linear phase (third region) with the highest stiffness.

The dermis is a fibrous layer (section 2.1), which explains the **anisotropic** response of human skin (Annaidh et al. 2012; Ayadh et al. 2023; Gibson et al. 1969; Joodaki and Panzer 2018; Kalra and Lowe 2016; Khatyr et al. 2004; Yazdi and Baqersad 2022) and is related to Langer lines (Abyaneh et al. 2014). The skin is **pre-stressed** in a tensile state to maintain the body's geometry, and these lines indicate the direction of maximum skin tension, parallel to the collagen fibbers. This behaviour

was studied by Jacquet et al. 2017a who have shown that during an *in vivo* extension test, the orientation of the loading device on the skin led to significantly different stress-strain responses, (*i.e.*, apparent elastic properties). More recently, Ayadh et al. 2023 identified the main directions of natural skin tension in the forearm and thigh based on tests performed on 42 female volunteers representing two age groups (20–30 and 45–55 years). The directions were 40°–60° for the forearm and 0°–20° for the thigh, with the longitudinal axis of the body at 90° and the transverse axis at 0° (see Figure 1, 10 and Table 3 in Ayadh et al. 2023).

The skin response also exhibits **time dependence**. Tests carried out at different speeds or under creep conditions (Bader and Bowker 1983; Eshel and Lanir 2001; Gallagher et al. 2012; Humbert et al. 2017; Sanders 1973; Shergold et al. 2006) highlighted the apparent viscoelastic behaviour of the skin. This behaviour is due in part to the fluid present in the interstitium and cells, with bound and free water accounting for  $71.8 \pm 2.4\%$  of the weight of the dermis (Téllez-Soto et al. 2021), and in part due to the viscous properties of the extracellular matrix (Chaudhuri et al. 2020). Despite these studies, the interaction between the contribution of fluid movement and the viscous property of the extracellular matrix to the time-dependent response of the skin remains undetermined.

Most of the aforementioned studies disregard the multilayered structure of the tissue due to experimental limitations. Indeed, the large thickness variations between the layers requires heavy experimental resolutions (for imagery techniques for instance) and heavy numerical simulations. Often, only the boundary stress-strain is accessible, limiting the ability to study multilayered behaviour without introducing mathematical modelling and simulations (Hendriks et al. 2003; Pailler-Mattei et al. 2008). Recently, Connesson et al. 2023 proposed a novel method to determine the stiffness of soft tissues using a suction device. By applying suction to tissue samples and inducing deformation, they measured the mechanical response and identified the stiffness properties of the tissues, considering their bilayer structure. The main results highlight the effectiveness of this suction-based approach in accurately assessing the mechanical properties of soft tissues. Preliminary tests on *in vivo* abdominal tissue provided Young's Moduli for skin and underlying adipose tissue at 54 kPa and 4.8 kPa, respectively. This method offers valuable information for medical diagnostic and biomechanical studies.

## 3.2 Fluid behaviour within the skin

Skin is inherently a **multiphase tissue**, as described in 2.1. It comprises a solid phase of the extracellular matrix, skin appendices (glands, hair follicles), and stroma cells interspersed with immiscible fluid phases: circulating cells (such as immune cells), interstitial fluid, vascular system, and lymphatic system (Figure 3). Understanding the fluids' behaviour within the skin and the tissue's permeability is crucial for enhancing biomedical technologies such as intradermal injection and grafting. Furthermore, studying permeation is of primary interest for drug delivery (Bartek et al. 1972; Lucio et al. 2023; Lucio et al. 2024; Mitragotri et al. 2011; Touitou 2002).

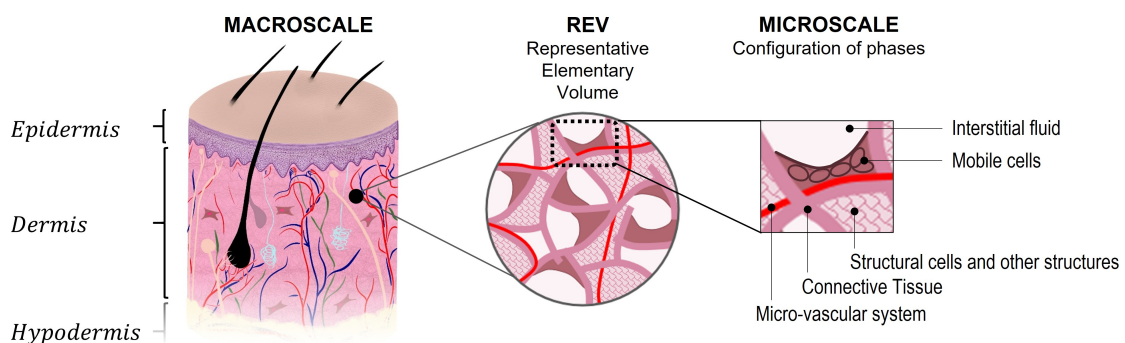


**Figure 3:** Mind representation of the structures present at the micro-scale of the skin, namely: the solid scaffold comprising the connective tissue, appendices and stroma cells (pink), the circulating cells (brown), the interstitial fluid (white), and the micro-vascular system (red). Nutrient and oxygen exchanges occur between the fluid phases. [Original image]

The **interstitial fluid**, also known as extracellular fluid, is a fluid that surrounds cells and tissues and represents 15 % – 25 % of the total weight of the skin. It is most abundant in the lower viable epidermis and the upper dermis (up to 70 %) (Iwanowska-Chomiak and Walicka 2019; Jiang et al. 2024). This quantity is dynamic and can change in volume and chemical composition during immune responses and in conditions such as cancer and specifically within the interstitium of tumours (Iwanowska-Chomiak and Walicka 2019). In addition, it has been found that interstitial fluid collected from the skin (i.e., dermal interstitial fluid) contains many of the same biomolecules, including metabolites, proteins, and nucleic acids, as blood. For example, glucose has been detected in dermal interstitial fluid, and its concen-

### 3 Experimental characterisation of human skin

tration was shown to be highly correlated with concentrations in blood and plasma (Jiang et al. 2024).

More precisely, several experimental protocols allowed to measure the volume fraction (**porosity**) occupied by the interstitial fluid. Wang et al. 2015 proposed a three-dimensional histological analysis of the human dermis based on micro-computed tomography (micro-CT) images. The porosity, pore size, and wall thickness of the human acellular dermal matrix (ADM) were assessed. Three-dimensional reconstructions of collagen and elastic fibres were created. The average proportions of collagen and elastic fibres across the entire dermis were  $28.9 \pm 14.6\%$  and  $8.1 \pm 3.8\%$ , respectively. The porosity of ADM, determined by microCT, was  $68.3 \pm 5.8\%$ . Using *in vivo* confocal Raman spectroscopy on 73 female participants, including 40 healthy young adults (19 – 37 years), 17 non-diabetic elderly individuals (50 – 80 years), and 16 diabetic elderly individuals (54 – 91 years), Téllez-Soto et al. 2021 quantified the total water content of the dermis:  $74.4 \pm 3.7\%$  for diabetic elderly,  $71.8 \pm 2.4\%$  for healthy young adults and  $73.7 \pm 3.7\%$  for healthy elderly women. This technique also identified the bounded water in the collagen binders: 31.8% in healthy young adults, 34.7% in healthy older women, and 33.5% in diabetic elderly women. Similarly, Liu et al. 2024 used panoramic images of skin sections captured using a microscope to reconstruct in 3D skin samples. A dermal porosity of  $18.9 \pm 4.4\%$  was identified with an average pore diameter of  $219.3 \pm 34.3\text{ }\mu\text{m}$ . Furthermore, Samant and Prausnitz 2018 reported a fluid proportion in the skin of approximately 70%, based on the work of Aukland and Nicolaysen 1981. They also identified a loss of 24% for pig skin that we associate with the percentage of free water.

The fluid can be characterised by material parameters such as its **dynamic viscosity**. Dynamic viscosity is defined as the force needed to overcome internal friction in a fluid. The interstitial fluid is clear to light yellowish in colour and is generally more viscous than sweat. Sowinski et al. 2021 provided expected viscosity ranges for various human fluids: cerebrospinal fluid (0.7 – 1.0 mPa s), blood (3.0 – 67.7 mPa s), and ascitic fluid (0.5 – 1.5 mPa s). Fu et al. 2019 reported synovial viscosities in the range of 3 – 20 mPa s. Furthermore, Swartz and Fleury 2007 detailed viscosity values for plasma (12 mPa s), lymphatic (15 – 22 mPa s), and synovial fluids ( $10^2$ - $10^5$  mPa s) and Li et al. 2024 collected viscosities used for the simulation of the viscous micro-environment of the extra-cellular fluid ranging  $1 - 10^3$  mPa s. The

### 3 Experimental characterisation of human skin

viscosity of the interstitial fluid has been shown to influence cell behaviour Li et al. 2024. Elevated viscosity can affect critical cellular processes, including cell migration, spreading, and mechanotransduction Gonzalez-Molina et al. 2018; Pittman et al. 2022. Specifically, Gonzalez-Molina et al. 2018 demonstrated that polymer solutions that enhance viscosity promote mesenchymal migration in liver cancer cell lines. Similarly, Pittman et al. 2022 used biocompatible polymers to increase the viscosity of the culture medium, revealing unexpected but consistent responses in various types of adherent cells to elevated viscosity.

Another parameter used to characterise a fluid flow is the **permeability** which describes the ability of a medium to conduct fluids. The permeability of the skin medium has been reported with values ranging from  $1 \times 10^{-16} \text{ m}^2$  to  $1 \times 10^{-11} \text{ m}^2$  (Levick 1987; Lucio et al. 2023; Oftadeh et al. 2018; Swartz and Fleury 2007; Wahlsten et al. 2019; Zakaria et al. 1997). Recent studies applied pressure-driven fluid flow across the epidermal and dermal layers of skin tissue in a one-dimensional configuration, measuring the resulting flow rate, and capturing cross-sectional optical coherence tomography (OCT) images of tissue deformation (Weir Weiss et al. 2023; Weir Weiss et al. 2024). The skin tissue exhibited a non-linear relationship between pressure and fluid flow, with the increase in flow decreasing as the pressure increased. Compressive strain was observed near the supported base, which increased with driving pressure, while the tissue near the free surface experienced relatively little strain. Permeability followed an exponential permeability-volumetric strain relationship with material constants: initial uniform permeability ( $k_0$ ) of  $9.6 \times 10^{-15} \text{ m}^2$  and degree of nonlinearity ( $\beta$ ) of 2.45. Darcy's law and the permeability-strain relationship were used to analyse the results, showing a good similarity between the observed and calculated flow rates (Weir Weiss et al. 2023; Weir Weiss et al. 2024). Oftadeh et al. 2023, based on poroelastic considerations (poro-viscoelastic finite element modelling identification), identified the hydraulic permeability of water for 3 layers of skin (stratum corneum, epidermis, dermis). Analysing 14 *ex vivo* human skin samples tested both macroscopic and nano-indentation methodologies, a hydraulic permeability of  $5 - 15 \times 10^{-14} \text{ m}^2 \text{ Pa}^{-1} \text{ s}^{-1}$  was found on the nanoscopic scale and  $0.5 - 2 \times 10^{-14} \text{ m}^2 \text{ Pa}^{-1} \text{ s}^{-1}$  on the mesoscopic scale, with a higher value for the dermis at both scales.

The skin is inherently a pre-stressed tissue, playing a crucial role in maintaining the body's shape. Consequently, the fluids within the skin are also subjected to

pre-stress. The experimental literature provides a wide range of values for the **initial physiological pressure** of the interstitial fluid. For the subcutis of the leg, Hargens et al. 1981 reported 2144 Pa, averaged from 19 healthy patients. In the palm subcutis, Wiig and Noddeland 1983 measured values ranging from  $-670$  to  $+536$  Pa using micro-puncture and needle winking techniques in 7 healthy patients. Repetitive measurements on pig skin in Samant and Prausnitz 2018 indicated a mean physiological pressure of 725 Pa.

### 3.3 Vascular evaluation

Understanding micro-circulation haemodynamics is crucial for preventing skin pathologies. It serves as a control in various fields such as **oncology** (Fukumura and Jain 2007; Russell et al. 2015; Tesselaar et al. 2017), **dermatology** (Baran et al. 2015; Braverman 1989; Kelly et al. 1995), **hypertension risk assessment** (Farkas et al. 2004; Rossi et al. 2006b), and **pressure ulcer prevention** (Liao et al. 2013; Nguyen-Tu et al. 2013; Sree et al. 2019a; Tsuji et al. 2005). For instance, hypoxia associated to the ischaemic response of the skin has been identified as a biological factor at the onset of PU. Blood supplies tissues with essential chemical species; for example, the physiological partial oxygen pressure is 65 mmHg, but it can drop to a hypoxic level of 31 mmHg with reduced vascular response (Sree et al. 2019a).

Various methodologies have been developed to evaluate skin blood flow, including **laser Doppler imaging** (Kubli et al. 2000; Millet et al. 2011; Svedman et al. 1998) and **laser speckle techniques** (Millet et al. 2011), which assess the spatial distribution of micro-vessel reactivity. Laser Doppler flowmetry (LDF) non-invasively measures dynamic changes in blood flow in small areas (Durand et al. 2002; Folgosí-Correa and Nogueira 2012; Fromy et al. 1998; Fromy et al. 2000; Kelly et al. 1995; Lenasi 2011; Poffo et al. 2014; Varghese et al. 2009). These techniques rely on the Doppler effect, observing a frequency shift when there is relative movement between the target and the source (Fang et al. 2024; Pedanekar et al. 2018). Given the size and speed of red blood cells, the LDF probe uses a fixed wavelength of 780 nm. The shift in wavelength after hitting red blood cells is proportional to their number and speed, regardless of the direction of movement (Fang et al. 2024; Pedanekar et al. 2018). However, LDF is sensitive to positioning and external factors and has a limited penetration depth of 0.5-1 mm (Fredriksson et al. 2009; Humeau-Heurtier et al.

### *3 Experimental characterisation of human skin*

2013; Poffo et al. 2014). In addition, calibration procedures and reproducibility are essential for ensuring the reliability of LDF measurements. Factors such as contact force between the probe and the skin, temperature, and tobacco use can affect accuracy and need to be controlled (Ajan et al. 2024; Kouadio et al. 2018; Nogami et al. 2019; Petrofsky and Berk 2012).

Advanced imaging modalities and analytical techniques have significantly improved the accuracy and resolution of vascular density measurements. **High-resolution magnetic resonance imaging** and **micro-CT** are recent methods used to quantify vascular networks in tissue samples, offering detailed visualisation and quantification of microvascular structures, providing insight into tissue perfusion and angiogenesis (Hansen and Carlsen 2021; Settecasi and Rayz 2021). **Optical Coherence Tomography** (OCT) provides detailed imaging of capillary blood flow within the skin, which is useful for diagnosing and managing skin diseases (An et al. 2010). Furthermore, dermatological optical devices, based on line-field confocal optical coherence tomography (LC-OCT, Dubois et al. 2018; Ogien et al. 2020), offers real-time 3D images with near-micrometre resolution, comparable to histology (Dubois et al. 2018). However, like LDF, this tool has a limited penetration depth, balancing depth, and resolution that arises primarily from the physical properties of light, specifically the wavelength and coherence length of the light source used in the imaging system, and the absorption properties of the tissues. Using shorter wavelengths improves resolution but limits penetration depth, while longer wavelengths enhance penetration depth but may reduce resolution.

Similarly to the characterisation of the interstitial fluid above, fluidic characteristics of the blood have been identified in the literature, based on the experimental techniques mentioned above. Regarding the volume fraction of the skin's vascular system, Kelly et al. 1995 used morphometry (based on fluorescein angiographic and native capillaroscopic fields) to evaluate the volume fraction of blood in 25 subjects (12 young, mean age 23.2 years, and 13 elderly, mean age 74.9 years) on the forehead and forearm. For young subjects, the volume fractions were respectively  $0.0791 \pm 0.0067$  and  $0.0481 \pm 0.0036$  for the dermal papillary loops and  $0.0571 \pm 0.0123$  and  $0.0223 \pm 0.0043$  for the horizontal vessels. In older subjects, these values were lower for the capillary loops but higher for horizontal vessels, respectively:  $0.0494 \pm 0.0037$  and  $0.0266 \pm 0.0029$  for the dermal papillary loops, and  $0.1121 \pm 0.0124$  and  $0.1013 \pm 0.0069$  for horizontal vessels. Tsuji et al. 2005 high-

lighted the importance of functional vessel density in animals, showing that repeated **ischaemia-reperfusion** cycles damage micro-circulation more severely than a single prolonged ischaemia event. Although hypoxic damage has been investigated in previous studies Loerakker et al. 2011; Sree et al. 2019a, it remains a long-term research objective and falls outside the scope of the present dissertation.

Various **viscometers**, such as rotational viscometers, falling ball viscometers, and microfluidic devices, have been developed to measure blood viscosity with high precision using minimal sample volumes (Khounou et al. 2019; Kim et al. 2013; Muramoto et al. 2010). These tools underscore the complex fluid dynamics of blood, which exhibits **non-Newtonian** characteristics: its viscosity varies with **shear rate**. This shear-thinning behaviour is essential for efficient blood flow, particularly under micro-circulatory conditions (Antonova 2012; Nader et al. 2019; Samanta et al. 2024; Tran-Minh and Karlsen 2018). In healthy individuals, blood viscosity typically ranges from 3.6 to 6.1 mPa s, with variations depending on age and sex (Filatova et al. 2015; Salazar-Vázquez 2011). More broadly, viscosity in biological fluids, including blood, is generally observed within the range of 3 to 32 mPa s (Nader et al. 2019). Under low shear rates ( $0.8$  to  $1.5\text{ s}^{-1}$ ), the viscosity of the blood can vary widely, ranging from 1.0 to 22.2 mPa s (Hermann et al. 2019). In contrast, at high shear rates ( $230\text{ s}^{-1}$ ), the viscosity of whole blood in older women has been reported to be approximately 13.5 mPa s (Ge et al. 2013).

The non-Newtonian nature of blood arises from the dynamics and deformability of red blood cells (RBCs). Under increasing shear stress, red blood cells can tumble, roll, and deform into various shapes, directly influencing the viscosity of the blood (Lanotte et al. 2016). At low shear rates, red blood cells tend to aggregate into cylindrical structures, increasing the viscosity. As shear rates increase, these aggregates disperse, leading to a reduced viscosity (Javadi et al. 2023; Nader et al. 2019). Furthermore, the deformability of the RBC is affected by factors such as haematocrit levels and plasma viscosity, with changes in these parameters significantly impacting blood viscosity and flow behaviour (Nader et al. 2019; Urevc et al. 2017). External forces, such as compressive loads, also influence the formation of the cell-free layer (CFL) in micro-vessels. Higher compressive loads improve RBC deformability, modify CFL, and alter blood rheology (Yalcin et al. 2015; Zhang 2011).

The **hydrostatic pressure** in the skin capillaries varies significantly between segments. The mean hydrostatic pressure ranges from 32-38 mmHg in the arterial

### *3 Experimental characterisation of human skin*

part, decreases to 17-20 mmHg in the transitional part, and further reduces to 12-18 mmHg in the venous part. Given that the physiological pressure of the whole blood remains approximately constant at 25 mmHg, the effective filtration and re-absorption pressure difference between the arterial and venous parts of the capillaries are approximately 7-13 mmHg (933-1733 Pa), respectively Fedorovich et al. 2018. The average capillary blood flow velocity (CBV) in the capillaries of human skin under thermoneutral conditions ranges from 400 to 900  $\mu\text{m s}^{-1}$ , showing an oscillatory nature (Fedorovich et al. 2018; Rossi et al. 2006a). Fagrell et al. 1977 reported a mean resting CBV of  $0.65 \pm 0.3 \text{ mm s}^{-1}$  at an average skin temperature of  $30.4 \pm 2.3$  degrees Celsius. Another study with 64 healthy subjects found a mean resting CBV of  $0.60 \pm 0.51 \text{ mm s}^{-1}$  at a skin temperature of  $30.9 \pm 3.2$  degrees Celsius, noting that the skin temperature, but not the resting CBV, was significantly higher in men. A weak positive correlation between CBV and skin temperature was observed, particularly above 31 degrees Celsius. During post-occlusive reactive hyperaemia (PORH), CBV reached a maximum of  $1.17 \pm 0.66 \text{ mm s}^{-1}$  at  $7.8 \pm 2.4$  seconds after cuff release (Ostergren and Fagrell 1986). Reactive hyperaemia (RH) is a physiological response that leads to an increase in microvascular blood flow to the skin. Optical coherence tomography (OCT) has been used to visualise and quantify the microvascular changes of the skin in response to RH in humans, demonstrating an increase in microvascular diameter, flow rate, speed and density after a stimulus (Argarini et al. 2020; Wang-Evers et al. 2021).

The CBV is regulated by a multifaceted process involving neural, mechanical, and chemical factors that collectively ensure proper thermoregulation and tissue perfusion. A key player in this regulation is the sympathetic nervous system, which controls vasoconstriction and vasodilation. However, ageing impairs this system, leading to diminished thermoregulatory capacity and heightened vulnerability to extreme temperatures (Francisco and Minson 2018; Holowatz and Kenney 2010). In addition, vasomotion, characterised by oscillations in arteriolar diameter, distributes blood flow within the microvascular bed of the skin. This process is influenced by endothelial, sympathetic, and myogenic factors, highlighting its dependence on multiple regulatory pathways (Cracowski et al. 2006; Folgosi-Correia and Nogueira 2012; Johnson and Kellogg Jr. 2010; Rossi et al. 2006a). In addition to local and systemic factors that modulate skin blood flow (skin temperature, moisture content, nitric oxide production (Basiladze et al. 2015; Choi et al. 2014; Golay et al. 2004; Horn et al. 2022; Johnson et al. 2016; Leo et al. 2020; Petrofsky and Berk 2012; Rosen-

berry and Nelson 2020; Tang et al. 2023; Wong et al. 2006)), mechanical forces such as pressure and shear stress in blood vessels have a huge impact along with tissue osmolarity, and free radicals (Balasubramanian et al. 2021; Fuchs et al. 2017; Petrofsky 2012; Treml et al. 2018). Together, these mechanisms underscore the complexity of skin blood flow regulation and its essential role in adapting to physiological and environmental challenges.

Experimental characterisation of the skin - through assessments of its solid mechanics, interstitial fluid behaviour, and vascular responses - provides valuable information on the complex, **multiscale** nature of skin physiology and the existing **interplay between the phases**. Although microcirculation and mechanical factors have been shown to interact in the onset of tissue damage, the present work focuses on the development of an alternative methodology, restricted to the physiological range. To accurately capture and predict the coupled behaviours observed experimentally, **mathematical modelling** emerges as an essential tool. Early models often treated the skin as a homogeneous elastic layer but advances in experimental techniques have highlighted the need for more sophisticated frameworks that can integrate mechanical, fluidic, and vascular interactions. In this context, modelling approaches based on porous media mechanics have emerged as promising tools that offer a unified theoretical framework to describe the skin as a multiphasic and hierarchically structured continuum.



# 4 Mathematical description of human skin

## Table of Contents

---

4.1	Modelling the behaviour of the skin . . . . .	33
4.2	Toward porous media mechanics for the skin . . . . .	38

---

### 4.1 Modelling the behaviour of the skin

Based on experimental observations, which reveal non-linear, anisotropic, and time-dependent behaviours, several mathematical models have been developed to describe and identify the mechanical properties of the skin under physiological loading.

Skin geometry is generally modelled as a single homogenised layer which partially explains the **large variability** in estimated **elastic modulus** values due to the differing thickness of skin layers across various body regions. To address this, recent studies have explored multilayered representations, which are expected to yield more accurate values and reduce intra-variability if the thickness of each layer is known. However, experiments capable of isolating each skin layer to estimate their mechanical parameters are challenging because of the large difference in thickness of the layers. Currently, primarily *in silico* formulations have been proposed to investigate potential multilayer skin model candidates (Pailler-Mattei et al. 2008; Sree et al. 2019a; Yazdi and Baqersad 2022), but limited data are available. Anatomical and functional knowledge suggests a stiffer epidermis (due to the stratum corneum)

#### 4 Mathematical description of human skin

than the dermis, despite the assumption that the dermis dominates the load-bearing process.

Furthermore, despite the non-linear nature of the stress-strain curve, the mechanical properties of the skin are often described with a single elastic modulus. For example, Oomens et al. 2017 noted that around 30 % of the papers in their review used an isotropic linear elastic Hookean model with a wide range of elastic moduli (5 kPa to 196 MPa). Kalra and Lowe 2016 reported Young's modulus values ranging from 4 to 15 MPa under quasi-static tensile conditions and from 14 to 100 MPa for dynamic tensile loading. Indentation, torsion, and suction tests yielded Young's modulus values from 10 kPa to 2.4 MPa, 20 kPa to 1.12 MPa, and 25 to 260 kPa, respectively, highlighting the strong dependence on the measurement technique and modelling hypotheses (see Table 1).

Given the characteristic "**J-shaped" stress-strain**" relationship of the skin, the linear elastic approximation may not be suitable, as the elastic modulus should increase with strain. An approach to address this is to use **piecewise elasticity** models, such as bilinear models (Jacquet et al. 2017a; Lakhani et al. 2021), which incorporate skin stiffening in larger stretches. Alternatively, **hyper-elastic** phenomenological models are often used (Benítez and Montáns 2017; Oomens et al. 2017; Yazdi and Baqersad 2022), which account for non-linear deformations, are often used. Models such as reduced polynomial, Ogden, Mooney-Rivlin, exponential, Yeoh, and Neo-Hookean have been employed, yet significant variability in material properties remains, without a clear trend in infinitesimal shear modulus values.

The reported elastic modulus values exhibit a wide range, influenced by factors such as ageing, loading conditions, model choice, and geometry considerations. An often overlooked factor is tissue compressibility, related to the Poisson ratio in models. The community has not found a consensus on the Poisson ratio value, with models assuming values from 0.3 to 0.5 (Kalra and Lowe 2016; Lakhani et al. 2021; Mukhina et al. 2020; Pailler-Mattei et al. 2008; Raveh Tilleman et al. 2004; Sanders 1973), which can further affect the estimated elastic modulus.

Given the fibrous and anisotropic nature of skin, various models have been developed to accurately represent the complex directional variations in its mechanical properties. Meijer et al. 1999 applied a 2D incompressible fibrous tissue model, originally developed by Lanir 1983, to *in vivo* stretch tests. They identified that the

## 4 Mathematical description of human skin

Uni-axial test	Population (age)	In vivo Ex vivo	Skin source	Thickness (Layer)	Elastic Modulus [Pa]	Poisson Ratio [-]
Khatyr et al. 2004	63 (N-S)	<i>In vivo</i>	Forearm	N-S	$(6.57 \pm 2.19) \times 10^5$ ( $\parallel$ arm) $(1.3 \pm 0.62) \times 10^5$ ( $\perp$ arm)	N-S
Annaidh et al. 2012	7 (81-97) 56 samples	<i>Ex vivo</i>	Back	$2.56 \pm 0.39$ mm (Dermis)	$(83.3 \pm 34.9) \times 10^6$	N-S
Gallagher et al. 2012	3 (77-85)	<i>Ex vivo</i>	Back	N-S	$(98.97 \pm 97) \times 10^6$	0.1-1.1
Ottenio et al. 2015	1 (90) 33 samples	<i>Ex vivo</i>	Back	$2.37 \pm 0.4$ mm (Dermis)	$(76.7 \pm 40.3) \times 10^6$ ( $0.06\text{s}^{-1}$ ) $(104.4 \pm 44.7) \times 10^6$ ( $53\text{s}^{-1}$ ) $(169.1 \pm 70.5) \times 10^6$ ( $167\text{s}^{-1}$ )	N-S
Jacquet et al. 2017a	20 (18-57)	<i>In vivo</i>	Forearm	$1.39 \pm 0.3$ mm	$(56.58 \pm 13.27) \times 10^3$ (Initial) $(2.24 \pm 0.48) \times 10^6$ (Final)	N-S
			Abdomen	$1.96 \pm 0.26$ mm	$(18.358 \pm 7.8) \times 10^3$ (Initial) $(0.74 \pm 0.59) \times 10^6$ (Final)	N-S
			Calf	$1.28 \pm 0.14$ mm	$35.6 \times 10^3$ (Initial) $4.59 \times 10^6$ (Final)	N-S
Torsion test	Population (age)	In vivo Ex vivo	Skin source	Thickness (Layer)	Elastic Modulus [Pa]	Poisson Ratio [-]
Sanders 1973	19 (6-61)	<i>In vivo</i>	Forearm	1mm	$2 \times 10^4$ to $1 \times 10^5$	0.5
Agache et al. 1980	138 (3-89)	<i>In vivo</i>	Forearm	1 mm	$4.2 \times 10^5$ (Young) $8.5 \times 10^5$ (Elderly)	N-S
Escoffier et al. 1989	123 (8-90)	<i>In vivo</i>	Forearm	0.5-0.9mm	$1.12 \times 10^6$	N-S
Suction test	Population (age)	In vivo Ex vivo	Skin source	Thickness (Layer)	Elastic Modulus [Pa]	Poisson Ratio [-]
Diridollou et al. 2000	10 (20-30)	<i>In vivo</i>	Forearm	$0.92 \pm 0.12$ mm (Cutis)	$(129 \pm 88) \times 10^3$	0.5
Hendriks et al. 2003	10 (19-24)	<i>In vivo</i>	Forearm	$1.35 \pm 0.10$ mm (Dermis) 0.81mm (Fat)	$(56.3 \pm 20.4) \times 10^3$ N-S	N-S
Lakhani et al. 2021	12 (26-31)	<i>In vivo</i>	Forearm	$1.17 \pm 0.06$ mm	$(0.52 \pm 0.09) \times 10^6$ (Initial) $(3.09 \pm 0.47) \times 10^6$ (Final)	0.5
Connesson et al. 2023	1 (38)	<i>In vivo</i>	Abdomen	$2.21 \pm 0.033$ mm (Cutis) N-S (Subcutis)	$(53.5 \pm 1.05) \times 10^3$ $(4.8 \pm 0.1) \times 10^3$	0.45-0.5
Elouneg et al. 2023	1 (28)	<i>In vivo</i>	Forearm	1.47mm	$(1.35 \pm 0.65) \times 10^6$ ( $\parallel$ arm) $(0.43 \pm 0.07) \times 10^6$ ( $\perp$ arm)	$0.43 \pm 0.09$
Indentation test	Population (age)	In vivo Ex vivo	Skin source	Thickness (Layer)	Elastic Modulus [Pa]	Poisson Ratio [-]
Ravesh Tilleman et al. 2004	23 samples (N-S)	<i>Ex vivo</i>	cancerous tissue	N-S	$52 \pm 45 \times 10^3$	$0.43 \pm 0.12$
Elleuch et al. 2006	3 (24-26)	<i>In vivo</i>	Forearm	N-S	$14 \times 10^3$	0.3
Boyer et al. 2007	4 (23-28)	<i>In vivo</i>	Forearm	N-S	$13.2 \times 10^3$ to $33.4 \times 10^3$	N-S
Paillet-Mattei et al. 2008	10 (30)	<i>In vivo</i>	Forearm	$\leq 80\mu\text{m}$ (Epidermis) 1.2-1.5mm (Dermis) 0.8mm (Subcutis)	N-S $35 \times 10^3$ $2 \times 10^3$	N-S N-S N-S
Khaothong 2010	12 (19-21)	<i>In vivo</i>	Forearm	N-S	$(0.17 \pm 0.07) \times 10^6$	N-S

**Table 1:** Evaluation of the elastic properties of the skin. The human skin has been tested under a wide variety of experimental conditions. Elastic properties is sensitive to ageing, strain rates, and the experimental boundary conditions. The Poisson ratio is not always referred to and a single elastic value is often provided. Both single or multi- layer evaluations have been performed.

stiffness of the collagen fibber in the dermis is between 50-90 MPa. Later, Koys and Nguyen 2012 assessed skin behaviour by comparing a fully integrated distributed fibber model with a 2D fibber structure, the pre-integrated Gasser-Ogden-Holzapfel model with a 3D fibber structure, and with a 2D fibber structure. Their comparison, based on *ex vivo* dorsal skin tested according to the thin shell theory requirements, demonstrated that the fully integrated distributed fibber model accurately repro-

#### 4 Mathematical description of human skin

duced the skin response, unlike the Gasser-Ogden-Holzapfel models. Additionally, modified models based on fibre orientations have been proposed. Groves et al. 2013 utilised an anisotropic, hyper-elastic constitutive model, evaluating it with 8 human and 14 Murine *ex vivo* skin samples. This model relies on the constitutive developments of Weiss et al. 1996, incorporating an isotropic matrix that describes the fibres (Veronda and Westmann 1970). They confirmed that the straightening of dermal fibres is accompanied by exponential stiffening of the tissue as a whole. Other research teams have chosen to apply transversely isotropic or orthotropic models to skin due to its fibrous nature (Elouneg et al. 2023; Khatyr et al. 2004). These studies identified several material characteristics along the principal axes. Khatyr et al. 2004's orthotropic model was able to correlate the results for 50 out of 63 subjects in their tests. In other cases, discrepancies could be attributed to experimental errors or the material not being perfectly orthotropic, since perfect perpendicularity between axes is rarely found in biological systems.

To capture the **time-dependent** response of the skin, previous studies have applied **viscoelastic** models such as Kelvin-Voigt, generalised Maxwell (Prony series) and quasilinear viscoelasticity (Benítez and Montáns 2017; Joodaki and Panzer 2018; Yazdi and Baqersad 2022). These models provide parameters for the instantaneous elastic response and characteristic times, allowing the investigation of time-dependence, hysteresis, and preconditioning effects observed in experiments, predicting non-linearity and tension-compression asymmetry. In particular, the skin exhibits two characteristic times that influence its response (Crichton et al. 2013; Flynn and McCormack 2008; Flynn et al. 2010; Giavazzi et al. 2010; Khatyr et al. 2004; Yazdi et al. 2018), with the second time being at least ten times higher than the first. Despite capturing the time-dependent response, the material properties obtained from these models are limited by sample size, geometry, and test conditions, which hinders a comprehensive description of the underlying physics of the skin.

An alternative to these viscoelastic models — which characterise the time-dependent response as independent of fluid flow — is offered by **poromechanical approaches**, which instead attribute the time-dependent behaviour to fluid–structure interactions (Lucio et al. 2023; Lucio et al. 2024; Oftadeh et al. 2023; Oomens et al. 1987b; Wahlsten et al. 2019). Based on Budday et al. 2019, Urcun et al. 2022 proposed a poromechanical model for the cerebral tissue, interpreting the two viscosity times as

representing the viscous response of the cells and the movement of the interstitial fluid, further discussed in Section 4.2. Hendriks et al. 2004 also identified that hydration influences the mechanical properties of human skin with a different effect for different subjects. Introducing porous-media mechanics would therefore extend the possibilities in understanding the impact of the fluid in the overall time-dependent mechanical response.

Porous models also present an alternative to current practice in including **biochemistry and diffusion processes** through a strong coupling as developed in Sciumè et al. 2014b, Urcun et al. 2021 for tumour growth and as proposed by Lucio et al. 2023, Lucio et al. 2024 for drug delivery. Indeed, current practices generally require multiscale modelling, with, for instance, explicit modelling of the vascular system. The study by Sree et al. 2019a investigates the diffusion of oxygen in human skin using a multilayered model comprising the stratum corneum, the viable epidermis, and the dermis. The model considers a volume  $1 \text{ mm}^3$  that required 1,208,437 elements, which is considerably heavy. The model applies an isotropic Neo-Hookean description and considers a fractal branching of vessels with blood pressure set at 20 mmHg (Ortiz-Prado et al. 2019) in the inner walls of the vascular inclusion. The study assumes that the total volume of blood in the skin is proportional to the oxygen available on the tissue scale, with the source term proportional to the normalised volume fraction. They found a microvascular collapse that depends on the orientation distribution of the vessel and is driven by compression rather than shear. Ortiz-Prado et al. 2019 further identified that the partial pressure of the oxygen in the external layer of the skin ranges from 3.2 to 8mmHg, in the papillary dermis from 6.4 to 24 mmHg and below the subcutaneous fat, from 8 to 38 mmHg.

Similar **3D-1D** coupled models were introduced by Bauer et al. 2005 to gain a deeper understanding of the underlying physiological mechanisms of the initial micro-circulatory response to mechanical skin irritation. Furthermore, Mithraratne et al. 2012 proposed a coupled 3D-1D computational model of the foot, in which hydrostatic pressure acts on the external surface of blood vessels, leading to a reduction in the flow cross-sectional area and, consequently, to a decrease in blood supply.

## 4.2 Toward porous media mechanics for the skin

Initially developed for soil mechanics, porous media mechanics is more recently commonly used in biomechanics.

The core concept of these porous models is to integrate classical solid mechanical equations with fluid evolution within the solid scaffold. This mixed approach often employs **Biot's theory** and **Darcy's law**, introducing an effective stress tensor that accounts for fluid pressure in the medium. Further details are provided in part II. Consequently, these models typically use the solid mechanics parameters (elastic, hyper-elastic, visco-elastic), combined with the medium's permeability and fluid viscosity.

According to the theory presented by Terzaghi 1943, the time characteristics of porous models depend on the sample size and are not solely related to material parameters. Thus, these models can help derive material parameters that are transferable between experimental environments.

Given the multiphase anatomy of human soft tissues, such as skin (detailed in section 2.1), these models show promise in replicating the time-dependent behaviour of human porous soft tissues. Taking into account the blood and lymphatic systems, tissue comprises three other phases: the extracellular matrix, cells, and interstitial fluid, which consists of interstitial water and its solutes (Wiig and Swartz 2012). Previous studies applied porous formulations to various soft tissues, including the brain (Budday et al. 2019; Carrasco-Mantis et al. 2023; Greiner et al. 2021; Hervas-Raluy et al. 2023; Hosseini-Farid et al. 2020; Urcun et al. 2023; Urcun et al. 2022), liver (Ricken and Lambers 2019), meniscus (Bulle 2022; Kazemi et al. 2013; Uzuner et al. 2022; Uzuner et al. 2020), and muscle tissue (Lavigne et al. 2022b).

Similarly, porous-media mechanics has been considered for skin mechanics for various applications such as drug testing, disease modelling, and wound healing. Oomens et al. 1987b first introduced a mixture approach to mimic the quasi-static skin response. More recent studies followed this path. Wahlsten et al. 2019 studied animal skin (Murine) and *ex vivo* (abdominal and breast region) and *in vivo* (forearm) human skin samples under tensile conditions. They reported that porous media mechanics allowed for the inclusion of volume loss due to the expulsion of interstitial fluid. Using a single-layer model, they identified elastic tensile moduli of  $89 \pm 27$  kPa

for human skin and  $288 \pm 178$  kPa for Murine skin, considering an *ex vivo* hydraulic conductivity of  $5 \times 10^{-13}$  m<sup>2</sup> Pa<sup>-1</sup> s<sup>-1</sup> and a reference solid volume fraction of 0.30 (Nakagawa et al. 2010). The biphasic model reproduced the large and rapid stress relaxation observed in human skin (75% in the first 2 minutes of the experiment).

Other research teams combined viscous and porous modelling (Ehlers and Markert 2001; Oftadeh et al. 2023; Oftadeh et al. 2018; Wang et al. 2020). Wang et al. 2020 identified two time scales for porcine tissue: a shorter scale due to the viscosity of the extracellular matrix and a longer scale due to the porous description. The same trend is identified for the behaviour of brain tissue in Budday et al. 2019; Urcun et al. 2022. The skin was assumed to be compressible with a Poisson ratio of  $\nu = 0.39 \pm 0.026$ . Oftadeh et al. 2018 investigated the role of ECM viscosity and fluid in the mechanical response of the mouse dermis. Poroelasticity was predominant at high indentation rates, whereas viscoelasticity dominated at lower loading rates, indicating that at high rates, the interstitial fluid bears the load and at lower rates, the fluid moves, and the mechanical response is governed by the viscous ECM (and cell movements). Here, the skin was also considered compressible with a Poisson ratio of  $\nu = 0.1$ , and the hydraulic conductivity was set to  $7 \times 10^{-13}$  m<sup>2</sup> Pa<sup>-1</sup> s<sup>-1</sup>.

Applying a porous model, whether poromechanical or poro-visco-mechanical, requires specific assumptions about geometry and **initial/boundary conditions**. The first consideration is the **continuum description**: how many different phases for how many different compartments? Current techniques do not fully allow for a precise idea of the proportion of each phase in the representative elementary volume. Depending on the fluid or equivalent fluid, the identified porous parameters (porosity: volume fraction occupied by the fluid, permeability: ability of the medium to conduct fluids, viscosity: force needed to overcome internal friction in a fluid) may differ. Table 2 summaries values found in the literature for some parameters of the porous medium. Additionally, the intrinsic permeability is closely related to the fluid dynamic viscosity as their ratio, also called hydraulic permeability/-conductivity, is used in the Darcy's law. Sowinski et al. 2021 supported this idea and collected the expected viscosity ranges for different human fluids (Section 3.2. Consequently, tissues with similar intrinsic permeabilities can have vastly different hydraulic conductivities and time-dependent responses). The proportion of fluid within the volume also affects the time-dependent behaviour.

Another challenge in applying porous media mechanics to the skin is accounting for

## 4 Mathematical description of human skin

Reference	Porosity (-)	Viscosity (cPa s)	Intrinsic Permeability (m <sup>2</sup> )	Hydraulic permeability (m <sup>2</sup> Pa <sup>-1</sup> s <sup>-1</sup> )
Wiig and Swartz 2012	0.2 – 0.5	1	$1 \times 10^{-9}; 1 \times 10^{-7}$	$1 \times 10^{-7}; 1 \times 10^{-5}$
Humphrey and O'Rourke 2015	N-S	1.2; 3.5	N-S	N-S
Hoskins et al. 2017	N-S	0.28; 1.5	N-S	N-S
Oftadeh et al. 2018	N-S	1	$(1.47 \pm 0.23) \times 10^{-15}$	$(1.47 \pm 0.23) \times 10^{-13}$
Samant and Prausnitz 2018	$0.24 \pm 0.06$	N-S	N-S	N-S
Wahlsten et al. 2019	0.7	1	$5 \times 10^{-15}$	$5 \times 10^{-13}$
Sowinski et al. 2021	N-S	0.07-6.77	N-S	N-S
Leng et al. 2021	0.1	1	$9.8 \times 10^{-14}; 9.8 \times 10^{-12}$	$9.8 \times 10^{-12}; 9.8 \times 10^{-10}$
Han et al. 2023	0.01	1	$1 \times 10^{-15}; 1 \times 10^{-13}$	$1 \times 10^{-13}; 1 \times 10^{-11}$
Torres-Terán et al. 2023	N-S	0.1; 0.15	N-S	N-S
Oftadeh et al. 2023	N-S	1	$0.5-2 \times 10^{-16}$	$0.5-2 \times 10^{-14}$

**Table 2:** This table summarise porous parameters values, either measured experimentally or used in the models. *Italic values* correspond to computed ones by the author from the studies. In absence of values for the viscosity, it was arbitrarily set to 1 cPa s for the computation of deriving parameters.

the **pre-stressed** state of the skin, which includes initial pressures of different fluids (osmotic and colloidal osmotic pressures). Samant and Prausnitz 2018 reported an osmotic pressure of about 0.7 kPa in the dermis, while Torres-Terán et al. 2023 reported colloidal osmotic pressures ranging from 1 to 2.4 kPa. These initial pressures can be included in models to better assess the mechanical behaviour of the tissue, as proposed by Han et al. 2023.

Therefore, regardless of the solid phase's mechanical behaviour (elastic, hyperelastic, viscoelastic), porous media mechanics require additional boundary and initial conditions (e.g., leakage, imposed pressure gradient, initial pressure), which are often difficult to assess experimentally. Depending on the testing conditions, a porous media model might be less efficient than a purely viscoelastic one.

Furthermore, as previously outlined, the theory of porous media provides a robust framework for incorporating **biological exchanges** between distinct fluid phases (which may reside in separate compartments), such as the micro-circulatory system, the interstitial fluid, and the cellular environments. This formalism enables the modelling of mass, momentum, and energy transfer across these compartments. Consequently, porous-media mechanics holds significant promise for coupling mechanical behaviour with biological phenomena within a unified model, particularly through diffusive transport mechanisms. The **oxygen biochemistry** has been described by Xing et al. 2014 and has been adapted to living tissues (Sciumè et al. 2014b) in the context of onco-physics. This approach has further been used to in-

vestigate glioblastoma evolution (Urcun et al. 2023; Urcun et al. 2022; Urcun et al. 2021), which introduces oxygen diffusion and the mechanobiology of tumour cells; or to develop a model for plantar tissue, including the extracellular matrix, living and dead cells, and chemical species for a diabetic foot (Sciumè et al. 2014a). Oxygen transport is also studied for the skin to account for chemical transport under load (Han et al. 2023; Lucio et al. 2023; Lucio et al. 2024) or to study large tissue deformation induced by subcutaneous injection (Leng et al. 2021). Given these developments, porous media mechanics appear to be a promising approach to preventing tissue injuries.

Although mathematical models based on the mechanics of porous media offer a powerful framework for understanding the behaviour of skin (and the interplay between solid mechanics and micro-circulatory variations), their practical application requires **robust computational tools**. The complex geometry and multi-physical interactions of skin—spanning solid mechanics, fluid dynamics, and vascular flow—demand **advanced mathematical developments and numerical techniques for accurate simulations**. Consequently, a range of computational tools have been developed, both commercial and open-source, that facilitate meshing, finite element analysis (FEA), and multiphysics simulations. These tools enable the implementation of mathematical models and provide a platform for exploring intricate interactions within the skin, thus translating theoretical insights into actionable predictions guiding future experimental research.



# 5 Computational framework

## Table of Contents

---

5.1 Mathematical considerations in a porous medium . . . . .	43
5.2 Computational tools . . . . .	46

---

### 5.1 Mathematical considerations in a porous medium

The following developments are based on the work of Detournay and Cheng 1993; Guéguen et al. 2004; Sciumè 2021; Thimus et al. 2020. A mechanical description first requires defining the studied system. Only the general aspects are given below. A precise development of the equations considered within this PhD work is provided in the next part.

According to Holzapfel 2002, a system is a quantity of mass whose complement, that is, the mass or region outside the system, is referred to as the surroundings. Three categories of systems are defined (Figure 4).

A **closed system** (or control mass) "consists of a fixed amount of mass in a properly selected region  $\Omega$  in space with boundary surface  $\partial\Omega$  which depends on time  $t$ . No mass can cross (enter or leave) its boundary, but energy, in the form of work or heat, can cross the boundary. The volume of a closed system does not have to be fixed. If even energy does not interact between the system and its surroundings, then we say that the boundary is insulated. Such a system is called mechanically

## 5 Computational framework

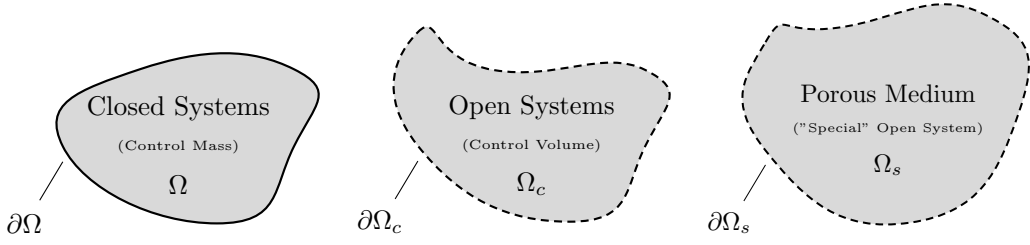


**Figure 4:** There are three different type of mechanical systems: closed systems. [Original image]

and thermally isolated, which is an idealization for a physical system. There always exist electromagnetic and other types of forces which permeate the space. Note that no physical system is truly isolated."

In contrast, an **open system**, also known as a control volume, "consists of a fixed amount of volume of a properly selected region  $\Omega_c$ , which is independent of time  $t$ . The enclosing boundary of a control volume, over which both mass and energy can cross (enter or leave), is called a control surface, which we denote by  $\partial\Omega_c$ ."

The **porous medium** is a **special open system**, with a fluid moving within a solid scaffold. The control volume  $\Omega_s$  is occupied by the solid scaffold. Since the solid is deformable,  $\Omega_s$  and  $\partial\Omega_s$  depend on time. Essentially, the deforming solid scaffold ( $s$ ) serves as the reference space (material description), within which the motion of the fluid phases is described spatially. The material derivative (with regard to the solid) of a function  $f$  is introduced for the description of this system and is defined by:

$$\frac{D^s f}{Dt} = \frac{\partial f}{\partial t} + \nabla f \cdot \mathbf{v}^s \quad (1)$$

For the sake of simplicity and clarity, we refer here to the most simple porous medium model consisting of a solid scaffold saturated by a fluid phase. The primary variables of this porous medium model include solid displacement and fluid pressure. The parameters affecting the mechanical response are:

- Young's modulus ( $E$ ), which provides the drained stiffness of the medium.
- The Poisson ratio of the solid phase ( $\nu$ ).
- The intrinsic permeability of the medium ( $k$ ), which describes the ability of the medium to conduct fluids.

- The porosity ( $\varepsilon$ ), which is the volume fraction occupied by the fluid.
- The dynamic viscosity ( $\mu^f$ ), which corresponds to the force needed to overcome internal friction in a fluid.

By definition, the volume fraction constraint give the following relation:

$$\sum_{\alpha=s,f} \varepsilon^\alpha = 1 \quad (2)$$

where  $\alpha = s, f$  represents the solid phase and the fluid phase.

The behaviour of the system is described using the classical **laws of continuum mechanics**. In the case of biological soft tissues, the system typically experiences **large strains**. Hence, a full and strong coupling between the solid and fluid phases exists. The governing equations are as follows:

- Conservation equations of mass for each considered phase,
- Conservation equations of momentum for each considered phase,
- + Chemical reaction equations.

Fluid transport in the interstitial space is described using **Darcy's law** which is obtained from the conservation equation of momentum of the fluid phase under certain assumptions (see Appendix A, Sciumè et al. 2013, New Journal of Physics) and allows for the introduction of **pore pressure** instead of **fluid velocity** in the fluid's continuity equation.

For **momentum conservation**, a total stress tensor is required. The stress tensor for the solid phase is given by:

$$\mathbf{t}^s = \tau^s - p^s \mathbf{1} \quad (3)$$

where  $\tau^s$  is the effective stress tensor of the solid phase and is  $p^s$  the solid pressure which comes from the effect of the fluid phase (which evolve inside the solid skeleton). The effective stress is a fundamental concept in porous models that represents the stress actually carried by the solid phase, which controls its deformation and strength behaviour.

## 5 Computational framework

For each fluid phase  $f$ , a fluid stress tensor resulting from the pore pressure is described as:

$$\mathbf{t}^f = -p^f \mathbf{1} \quad (4)$$

where  $p^f$  is the fluid phase pressure. Under compression,  $p^f$  is positive.

The total stress tensor is obtained by summing the phase tensors weighted by their respective volume fractions:

$$\mathbf{t}^T = \sum_{\alpha=s,f} \varepsilon^\alpha \mathbf{t}^\alpha = \varepsilon^s (\tau^s - p^s \mathbf{1}) - \sum_f \varepsilon^f p^f \mathbf{1} \quad (5)$$

By incorporating the total stress tensor into the momentum conservation equations and accounting for the coupling of the phases' continuity equations with Darcy's law, we can derive the poromechanical model that describes the physical system. The number of equations and the coupling strongly depend on the modelling assumptions considered and the phases included. In each of the following chapters, the full derivation of the mathematical model is provided and specialised according to the application.

## 5.2 Computational tools

Constitutive laws are generally local laws that can be extended to a macroscopic form through integration. Because identifying the analytical solution of a mechanical problem is often challenging, approximated resolution methods have been proposed. One of the most common methods is the **finite element method**, whose development began in 1941 with the work of Hrennikoff 1941 in the field of structural engineering. This method has since been extended to various fields, including structural/stress analysis (Hartmann and Katz 2013; Rugarli 2010), heat transfer analysis (Gosz 2017; Lewis et al. 1996), fluid flow analysis (Connor and Brebbia 2013; Lewis et al. 2004), electric or magnetic potential distribution analysis (Hwang and Lord 1974; Pao-La-Or et al. 2010), and biomechanical engineering (Cornillon et al. 2023; Segain et al. 2024).

The finite element method is based on the definition of a **weak form** that introduces a test function for a discrete representation of the domain, known as a **mesh**.

Shape functions are used to interpolate the solution from the nodes to the continuous domain. This method allows for the modelling of irregularly shaped models, handling of general load conditions, modelling of multi-material bodies, introduction of various types of boundary conditions, and locally refined meshes, thus enhancing the description of the solution (Mano et al. 2003).

This method has been extensively introduced in biomechanical and biomedical research, leading to the development of tools for both mesh generation and simulations to test hypotheses and propose predictive tools for clinical use. There are two categories of software available: **commercial** and **open source**.

Commercial softwares are pre-programmed and typically provide access to various common tools (*e.g.* meshers, user-friendly graphical interfaces) needed for the finite element process. The main advantage of these software packages is their user-friendly design. In addition, they offer stable versions that are often compatible across different releases. However, most pre-programmed tools are presented to users as "black boxes," making the introduction of custom extensions and subroutines a complex task. For example, implementing a non-linear hyperelastic material model using user subroutines in ABAQUS (*3DS Dassault Softwares n.d.*) is detailed in the tutorial by Fehervary et al. 2020. Although documentation is available, it often lacks derivations, details, and background information, making the implementation complex and error-prone. Furthermore, these software packages require expensive licences, which can limit the straightforward reproducibility of research by other teams. Despite these drawbacks, commercial software is widely used in industry and academia due to its robustness and extensive support.

The second category includes open source softwares, which offer a good alternative with packages available to all users. These tools promote **transparency** and **flexibility**, allowing researchers to modify and extend the code to suit their specific needs. This adaptability makes open-source softwares particularly appealing for academic research and specialised applications (*e.g.* clinical modules in 3D-Slicer). However, some of these tools lack comprehensive documentation, which requires users to have advanced research skills and often necessitating engagement with forums or communities for understanding. The **collaborative** nature of open-source projects means that updates and new features are frequently added, although this can sometimes lead to issues with maintaining updates and compatibility. In

## 5 Computational framework

addition, the support for open source softwares typically relies on community contributions, which can vary in quality and availability.

In the context of finite element computations, commercial and open-source software solutions are complemented by specialised tools for Computer Aided Design (CAD) modelling, mesh generation, forming an integrated ecosystem for engineering simulations and research.

The next four paragraphs outline the commonly used softwares for mesh generation and finite element simulations.

CATIA (*3DS Dassault Softwares* n.d.), Fusion 360 (*Autodesk Fusion 360* n.d.), and FreeCAD (*FreeCAD* n.d.) are prominent CAD software tools, each catering to diverse design and engineering needs. CATIA, developed by Dassault Systèmes, is extensively used in aerospace, automotive, and industrial design for comprehensive 3D modelling, simulation, and product life-cycle management, including solid modelling, surface modelling, and assembly design. Fusion 360, a cloud-based tool from Autodesk, integrates CAD, Computer-Aided Manufacturing (CAM), and Computer-Aided Engineering (CAE) features into a single platform, facilitating 3D modelling, simulation, and manufacturing. Its collaborative features allow multiple users to work on projects in real-time, making it popular among designers, engineers, and manufacturers. FreeCAD, an open-source parametric 3D modeller, supports a broad range of applications from product design to architecture. Its modular architecture allows extensive customisation through plugins, enhancing its versatility and adaptability to various design needs. Together, these tools offer robust solutions for engineering simulations, CAD modelling, and mesh generation, catering to a wide array of applications in academia, research, and industry.

**GMSH** (Geuzaine and Remacle 2009), NETGEN (Schöberl 1997), and TETGEN (Si 2015) are open-source tools designed to generate 3D meshes, each offering unique capabilities while sharing a common purpose. GMSH is a versatile 3D finite element mesh generator with an integrated CAD engine and post-processor, supporting structured, unstructured, and hybrid meshes. This versatility makes it widely used in engineering simulations for creating high-quality meshes. NETGEN is an automatic 3D tetrahedral mesh generator known for producing high-quality meshes from complex geometries, suitable for finite element analysis and computational fluid dynamics, and integrates well with other simulation software. TETGEN focusses on

generating tetrahedral meshes specifically for 3D domains, excelling in efficiency and robustness, and is widely used for finite element and finite-volume methods due to its ability to handle complex geometries and maintain good mesh quality. Together, these tools provide comprehensive solutions for mesh generation needs in various engineering and simulation applications.

For finite element computations, COMSOL Multiphysics (*Comsol* n.d.), ANSYS (*ANSYS* n.d.), ABAQUS (*3DS Dassault Softwares* n.d.), ACEFEM/ACEGEN (*AceFEM/AceGen* n.d.), and RADIOSS (*Altair radioss* n.d.) are powerful engineering simulation software packages, each with unique strengths but sharing core functionalities. COMSOL Multiphysics and ANSYS provide comprehensive multiphysics simulation capabilities, utilising Finite Element Analysis (FEA) to tackle complex engineering problems across structural mechanics, fluid dynamics, electromagnetism, and heat transfer. Their flexible and user-friendly interfaces make them widely adopted in research, engineering, and industrial applications. ABAQUS excels in FEA and computer-aided engineering with advanced capabilities to create geometries and simulate complex structural and thermal behaviours. ACEFEM, paired with ACEGEN, is an extension of Mathematica software, offering specialised finite element analysis solutions, with ACEGEN generating optimised code for custom formulations, enhancing the efficiency and customisation of engineering simulations. RADIOSS, part of the Altair HyperWorks suite, is known for its high performance in solving linear and non-linear problems under dynamic loading conditions, particularly excelling in crash simulations, impact analysis, and structural dynamics. Together, these tools cater to a broad spectrum of simulation needs, from high-fidelity multiphysics analyses to specialised structural and dynamic studies.

DEAL.ii (Arndt et al. 2023; Arndt et al. 2021), **FEniCSx** (Alnæs et al. 2015; Alnæs et al. 2014; Baratta et al. 2023; Scroggs et al. 2022b, NGSOLVE (*NGSolve* n.d.) and CAST3M (*CAST3M* n.d.; Pasquet 1999) are open-source software libraries designed to solve partial differential equations (PDEs) using finite element methods (FEM), each offering unique features while sharing common goals. DEAL.ii provides a highly flexible environment with adaptive mesh refinement, parallel computing, and various finite element types, which makes it valuable for academic research and custom simulation solutions of complex PDEs. FEniCSx, the next generation version of the FEniCS project, offers a high-level programming interface that allows users to define and solve complex PDEs with minimal code, emphasising ease of use, flexibility, and

## *5 Computational framework*

performance for academic research and industrial applications. NGSOLVE, another open source finite element library, supports a wide range of finite elements and is known for its flexibility, enabling users to define custom finite element spaces and formulations for academic and industrial needs. CAST3M, developed by the French Atomic Energy and Alternative Energies Commission (CEA), is a comprehensive tool for structural analysis and multiphysics simulations, providing advanced capabilities for meshing, solving, and post-processing PDEs. It is particularly used in engineering and industrial research. Together, these libraries offer robust solutions to PDE problems, promoting flexibility, efficiency, and adaptability in various research and application contexts.

For direct applicability and transferability to the research community, in this Ph.D. work **GMSH** and **FEniCSx** are chosen as the primary computational tools to solve systems of partial differential equations governing the poromechanical behaviour of the skin. GMSH offers a versatile platform for mesh generation, ensuring the accurate discretisation of complex geometries, while FEniCSx provides a high-level interface that allows for a seamless translation from the mathematical formulation to the computational model. This direct mapping from theory to simulation is crucial for handling complex coupled systems of solid mechanics and fluid dynamics inherent in porous media. In addition, both tools support parallel computing, significantly improving computational efficiency for large-scale problems. Their open-source nature ensures broad accessibility and promotes collaboration, enabling the community to reproduce, extend, and build upon the work presented here.

# 6 Conclusion

This chapter has established the theoretical and conceptual foundation necessary to develop in this thesis **a hierarchical poromechanical approach enables the modelling of both the mechanical behaviour and the microvascular response of the skin, under physiological conditions and in the presence of mechanical loading.**

The review highlights that human skin, while extensively studied, remains incompletely understood from a mechanical perspective, especially when we want to account for the coupling between the skin deformation and the micro-circulation. Its **multilayered structure** and **multiphase composition** create inherent challenges for both experimental characterisation and mathematical modelling. Traditional models, often based on homogenised or single-phase assumptions, fail to fully capture the coupled behaviour between solid matrix deformation and fluid flow, particularly under sustained mechanical loading. In addition, despite advances in viscoelastic and anisotropic formulations, many models lack physiological relevance because of limited experimental validation and poorly defined boundary conditions.

Furthermore, vascular contribution, particularly **microvascular haemodynamics**, has been sparsely integrated into mechanical models. Although imaging techniques like Laser Doppler Flowmetry and Optical Coherence Tomography provide valuable data, they rarely translate into computational models with predictive power. The literature reveals a gap in **quantitative models** that can simultaneously simulate mechanical stress distribution and vascular perfusion, despite their critical interplay in skin health and pathology, particularly in conditions such as pressure ulcers.

**Poromechanics** emerges as a promising framework, offering the ability to link fluid-solid interactions and capture time-dependent behaviour through parameters such as permeability, porosity, and viscosity. However, the application of this theory to biological tissues remains constrained by a lack of precise material parameter

## 6 Conclusion

values, difficulty in defining and controlling boundary conditions, and the absence of comprehensive validation studies. The poromechanical theory is still evolving in terms of physiological fidelity, particularly in multi-compartment or vascularised extensions that account for biological function and anatomical complexity.

In light of these limitations, this thesis aims to bridge the gap between theoretical modelling and physiological realism by developing and evaluating a **hierarchical (modular) poromechanical framework** for skin. This framework is designed to model the interaction between solid mechanics, interstitial fluid dynamics, and microvascular flow under physiological loading. The objective is not only to advance the state of the art on biomechanical modelling, but also to contribute computational tools that can eventually inform clinical decision in skin-related pathologies.

To systematically address this objective, the dissertation is organised as follows.

Part II, “*Tutorial implementation of poromechanics in FEniCSx*”, establishes the computational framework by implementing single- and two-compartment poromechanical models using the open-source FEM library FEniCSx. The models are verified and validated against benchmark cases, providing a flexible and scalable foundation for the application of poromechanics to soft tissues.

Part III, “*In vivo evaluation of a single-compartment porous model*”, assesses whether a poromechanical model can replicate the mechanical behaviour dependent on the time of human skin. Using unpublished experimental data from an in vivo extension test, this part develops a bi-layered poro-hyper-elastic model and calibrates it against empirical observations, highlighting both the relevance of the model and its limitations due to restricted datasets and experimental variability.

Part IV, “*In vivo evaluation of a two-compartment porous model*”, expands the scope by introducing a two-compartment poroelastic model to account for the microvascular response. The model is tested against a custom experimental protocol using laser Doppler flowmetry to monitor haemodynamic changes during skin indentation. The work identifies critical material parameters that influence vascular perfusion, but also underscores the ongoing challenge of regulating boundary conditions and the need for richer datasets.

Part V, “*Towards a better control of boundary conditions: method for phantom generation and in silico evaluation*”, addresses one of the main gaps identified in the

literature: the difficulty of reliably estimating parameters of porous materials such as permeability. A methodology combining numerical simulation, statistical inference, and 3D printed phantoms is proposed to enable the *in silico* characterisation and experimental validation of these parameters. This work serves as both a complement to previous chapters and as a general contribution to the field of porous biomaterials.

Part VI, “*General conclusion and perspectives*”, synthesises the findings and discusses the implications for the future of poromechanical modelling in dermatology and biomedical engineering. It outlines future directions for refining experimental protocols, improving model fidelity, and incorporating biological processes such as tissue adaptation, inflammation, or drug transport.

Overall, this dissertation contributes to closing the gap between experimental evidence and computational modelling of skin mechanics by advancing poromechanical approaches grounded in physiological realism. Especially, built upon the general theoretical context of TCAT (Thermodynamically Constrained Averaging Theory), the developed model couples mechanical state and vascular responses and proposes modularity. The hierarchical framework proposed here seeks to elevate the predictive capabilities of skin models, setting the stage for future integration into diagnostic and therapeutic strategies.



## **Part II**

# **Tutorial implementation of poromechanics in FEniCSx**



# 7 Implementation and evaluation of the computational framework in FEniCSx

## Table of Contents

---

7.1	Synopsis (FR) . . . . .	57
7.2	Synopsis (EN) . . . . .	60
7.3	Article . . . . .	62

---

### 7.1 Synopsis (FR)

Ce chapitre présente un tutoriel détaillé et reproductible pour la mise en œuvre de modèles poroélastiques à simple et double compartiments appliqués à la modélisation des tissus biologiques, en s'appuyant sur le logiciel open-source FEniCSx. Ce travail répond à un besoin croissant dans la communauté : celui de disposer d'un pipeline modulaire et libre d'accès, permettant la reproductibilité, l'intégration facile de processus biologiques complexes, et la réutilisation des modèles de milieux poreux et poreux vascularisés développés au cours de cette thèse.

L'approche proposée repose sur les développements mathématiques formulés pour la recherche oncologique par Urcun et al. 2023, et sur l'inclusion des effets de la microcirculation dans des tissus biologiques par Sciumè 2021. Ces modèles s'inscrivent

dans le cadre théorique général de TCAT (Thermodynamically Constrained Averaging Theory), qui propose une formulation systématique et rigoureuse des équations de conservation à différentes échelles (pore, REV, etc.) en tenant compte de phénomènes multi-physiques couplés. Cependant, malgré sa richesse conceptuelle, TCAT reste difficile à implémenter directement dans les logiciels d'éléments finis.

Le présent tutoriel répond à cette difficulté en proposant une traduction directe et opérationnelle de la formulation variationnelle vers une implémentation numérique avec FEniCSx, tout en fournissant les clés de compréhension nécessaires à l'utilisation efficace de cet environnement. Il s'adresse ainsi à un public de chercheurs souhaitant explorer ou développer des modèles poroélastiques robustes et personnalisables. Par exemple, la modélisation poroélastique constitue une approche particulièrement précieuse, car elle permet d'intégrer des données multi-échelles et multi-physiques, offrant ainsi la possibilité d'étudier des phénomènes biologiquement pertinents à petite échelle et d'incorporer ces mécanismes dans des modèles à grande échelle (voir Section 4.2). Ces modèles rendent possible l'étude des interactions complexes au sein des tissus biologiques, où les écoulements de fluides et les déformations mécaniques sont intimement liés. Pour illustrer l'application de FEniCSx à la modélisation poroélastique, plusieurs cas de référence sont présentés. Ces cas servent d'outils de validation, mettant en évidence la précision et la fiabilité de l'implémentation tout en fournissant des exemples pratiques aux chercheurs.

Le tutoriel débute par les bases théoriques de la poroélasticité et présente en détail l'approche de formulation mixte. Cette méthode est particulièrement avantageuse pour coupler la mécanique des fluides et des solides, car elle permet de résoudre simultanément les champs de pression des pores et de déformation des solides. Les concepts fondamentaux, tels que les équations gouvernantes, les relations constitutives et les hypothèses associées, sont introduits pour fournir une base solide au processus de mise en œuvre. Le lecteur est ensuite guidé à travers le processus de création de modèles numériques, y compris la génération de domaines géométriques et de maillages pour des cas en 2D et en 3D. Le tutoriel explique également comment spécifier les conditions aux limites et initiales, en garantissant leur cohérence avec le problème physique modélisé.

Le premier cas de référence concerne le problème classique de consolidation de Terzaghi (sous l'hypothèses de petites perturbations), un test fondamental pour les modèles poroélastiques. Ce problème simule le comportement transitoire d'un milieu

poreux saturé soumis à une charge soudaine et fournit une solution analytique permettant de comparer les résultats numériques. Le tutoriel guide le lecteur dans la configuration de la simulation et montre comment évaluer la précision des résultats numériques à l'aide de métriques telles que l'erreur quadratique moyenne normalisée (RMSE). Les résultats confirment la fiabilité de FEniCSx pour simuler les interactions fluide-solide inhérentes aux milieux poroélastiques.

Le second cas teste la capacité du modèle à gérer de grandes déformations et à simuler le comportement mécanique des tissus mous dans des conditions physiologiquement pertinentes. Ce cas se concentre sur les matériaux hyperélastiques, qui présentent des relations contrainte-déformation non linéaires caractéristiques des tissus biologiques. Le tutoriel explique la mise en œuvre des propriétés matérielles non linéaires, en soulignant l'importance de capturer ces comportements pour les applications en biomécanique des tissus.

Le dernier cas de référence aborde le modèle poroélastique bicompartment, un scénario plus avancé qui prend en compte les tissus avec deux compartiments fluides distincts. Ces compartiments représentent les flux de fluide interstitiel et sanguin, permettant de simuler des interactions et des dynamiques plus complexes au sein des tissus perfusés. Ce cas illustre la capacité de FEniCSx à gérer des mécanismes de couplage fluide-solide complexes et valide son aptitude à modéliser la mécanique des systèmes biologiques. Un tel couplage permet notamment d'analyser les interactions entre les mécanismes mécaniques et biologiques impliqués dans les processus d'endommagement des tissus.

Tout au long du chapitre, des exemples pratiques et des extraits de code sont fournis pour faciliter l'apprentissage et la reproductibilité. Les lecteurs sont invités à explorer les ressources supplémentaires du tutoriel disponibles à l'adresse suivante ([https://github.com/Th0masLavigne/Dolfinx\\_Porous\\_Media.git](https://github.com/Th0masLavigne/Dolfinx_Porous_Media.git)) ainsi que le workshop complémentaire ([https://github.com/Th0masLavigne/FEniCSx\\_GMSH\\_tutorials.git](https://github.com/Th0masLavigne/FEniCSx_GMSH_tutorials.git)). Ces ressources comprennent des instructions détaillées sur l'installation du logiciel, des scripts d'exemple et des supports de formation supplémentaires pour résoudre divers problèmes mécaniques.

À la fin de ce tutoriel, les lecteurs auront acquis les connaissances et les compétences nécessaires pour implémenter des modèles poroélastiques monocompartimentaux et

bicompartimentaux dans FEniCSx, leur permettant de contribuer à l'avancement des recherches sur la mécanique des tissus mous biologiques.

## 7.2 Synopsis (EN)

This chapter presents a detailed and reproducible tutorial for implementing single- and dual-compartment poroelastic models applied to the simulation of biological tissues, using the open-source software FEniCSx. This work addresses a growing need in the scientific community for a modular and openly accessible pipeline that supports reproducibility, integration of complex biological processes, and reusability of porous and vascularized porous media models developed during this thesis.

The proposed approach builds upon the mathematical formulations developed for cancer research by Urcun et al. 2023, and the incorporation of micro-circulation effects in biological tissues described by Sciumè 2021. These models are framed within the general theoretical context of TCAT (Thermodynamically Constrained Averaging Theory), which provides a systematic and rigorous formulation of conservation laws at different scales (pore, REV, etc.) while accounting for multiphysics couplings. However, despite its conceptual richness, TCAT remains challenging to implement directly in finite element software.

This tutorial addresses this difficulty by providing a direct and operational translation of the variational formulation into a numerical implementation using FEniCSx, while offering the necessary conceptual tools for effective use of this environment. It is intended for researchers interested in exploring or developing robust and customizable poroelastic models. For instance, poroelastic modelling is particularly valuable because it allows for the integration of multiscale and multiphysics data, enabling the study of biologically relevant phenomena at small scales and their incorporation into large-scale models (see Section 4.2). These models facilitate the study of complex interactions within biological tissues, where fluid flows and mechanical deformations are intimately linked. To illustrate the application of FEniCSx in poroelastic modelling, several benchmark cases are presented. These cases serve as validation tools, showcasing the accuracy and reliability of the implementation while providing practical examples for researchers.

The tutorial begins with the theoretical foundations of poroelasticity and presents the mixed-formulation approach in detail. This approach is particularly advantageous for coupling fluid and solid mechanics, as it allows for the simultaneous solution of pore pressure and solid deformation fields. Fundamental concepts, such as the governing equations, constitutive relationships, and relevant assumptions, are introduced to provide a solid grounding for the implementation process. The reader is then guided through the process of creating computational models, including the generation of geometrical domains and meshes for both 2D and 3D cases. The tutorial also explains how to specify boundary and initial conditions, ensuring consistency with the physical problem being modelled.

The first benchmark case involves the classic Terzaghi consolidation problem, a foundational test for poroelastic models. This problem simulates the transient behaviour of a saturated porous medium subjected to a sudden load, and provides an analytical solution against which numerical results can be compared. The tutorial guides the reader through the simulation setup and demonstrates how to evaluate the accuracy of the numerical results using metrics such as using the normalised Root Mean Square Error (RMSE). The outcomes confirm the reliability of FEniCSx in capturing the fluid-solid interactions inherent in poroelastic media.

The second case evaluates the model's ability to handle large deformations and simulate the mechanical behaviour of soft tissues under physiologically relevant conditions. This case focuses on hyperelastic materials, which exhibit the non-linear stress-strain relationships characteristic of biological tissues. The tutorial explains how to implement these non-linear material properties, emphasizing the importance of capturing such behaviours for applications in tissue biomechanics.

The final benchmark addresses the bi-compartment poroelastic model, a more advanced scenario that accounts for tissues with two distinct fluid compartments. These compartments represent interstitial fluid and blood flow, enabling the simulation of more complex interactions and dynamics within perfused tissues. This benchmark showcases the ability of FEniCSx to handle intricate fluid-solid coupling mechanisms and validates its suitability for modelling the mechanics of biological systems. Such coupling allows for the analysis of interactions between mechanical and biological processes involved in tissue damage mechanisms.

Throughout the chapter, practical examples and code snippets are provided to fa-

cilitate learning and reproducibility. Readers are encouraged to explore the tutorial resources available at the following link ([https://github.com/Th0masLavigne/Dolfinx\\_Porous\\_Media.git](https://github.com/Th0masLavigne/Dolfinx_Porous_Media.git)) as well as a complementary wrokshop available on github ([https://github.com/Th0masLavigne/FEniCSx\\_GMSH\\_tutorials.git](https://github.com/Th0masLavigne/FEniCSx_GMSH_tutorials.git)). These resources include detailed instructions on software installation, sample scripts, and additional training materials for solving various mechanical problems.

By the end of this tutorial, the readers will have gained the knowledge and skills required to implement single- and bi- compartment poroelastic models in FEniCSx, enabling them to contribute to advancing research in the mechanics of biological soft tissues.

## 7.3 Article

This work was accepted for publication in 2023 in the Journal of the Mechanical Behavior of Biomedical Materials. **ERRATUM: Please note that for the hyper-elastic case, the Nanson formula must be used to change PK1 to Cauchy stress.**

### Contribution (CRediT author statement)

Conceptualisation, Methodology, Investigation, Software, Writing – original draft.

# Single and bi-compartment poro-elastic model of perfused biological soft tissues: FEniCSx implementation and tutorial

T. Lavigne<sup>a,b,c</sup>, S. Urcun<sup>a</sup>, P-Y. Rohan<sup>b</sup>, G. Sciumè<sup>c</sup>, D. Baroli<sup>d,\*</sup>, S.P.A. Bordas<sup>a,e,f</sup>,

<sup>a</sup> Institute of Computational Engineering, Department of Engineering, University of Luxembourg, 6, avenue de la Fonte, Esch-sur-Alzette, L-4364, Luxembourg, <sup>b</sup> Arts et Metiers Institute of Technology, IBHGC, 151 bd de l'hôpital, Paris, 75013, France, <sup>c</sup> Arts et Metiers Institute of Technology, Univ. of Bordeaux, CNRS, Bordeaux INP, INRAE, I2M Bordeaux, Avenue d'Aquitaine, Pessac, 33607, France, <sup>d</sup> Università della Svizzera Italiana, Euler Institute, Lugano, Switzerland, <sup>e</sup> Clyde Visiting Fellow, Department of Mechanical Engineering, The University of Utah, Salt Lake City, Utah, United States, <sup>f</sup> Visiting Department of Medical Research, China Medical University Hospital, China Medical University, Taichung, Taiwan

---

**Abstract:** Soft biological tissues demonstrate strong time-dependent and strain-rate mechanical behavior, arising from their intrinsic visco-elasticity and fluid-solid interactions. The time-dependent mechanical properties of soft tissues influence their physiological functions and are related to several pathological processes. Poro-elastic modeling represents a promising approach because it allows the integration of multiscale/multiphysics data to probe biologically relevant phenomena at a smaller scale and embeds the relevant mechanisms at the larger scale. The implementation of multiphase flow poro-elastic models however is a complex undertaking, requiring extensive knowledge. The open-source software FEniCSx Project provides a novel tool for the automated solution of partial differential equations by the finite element method. This paper aims to provide the required tools to model the mixed formulation of poro-elasticity, from the theory to the implementation, within FEniCSx. Several benchmark cases are studied. A column under confined compression conditions is compared to the Terzaghi analytical solution, using the L2-norm. An implementation of poro-hyper-elasticity is proposed. A bi-compartment column is compared to previously published results (Cast3m implementation). For all cases, accurate results are obtained in terms of a normalized Root Mean Square Error (RMSE). Furthermore, the FEniCSx computation is found three times faster than the legacy FEniCS one. The benefits of parallel computation are also highlighted.

**Keywords:** Mixed Space; Poro-elasticity; Bi-compartment; FEniCSx

---

## Introduction

Numerous biomechanical problems aim to reproduce the behavior of a deformable solid matrix that experiences flow-induced strain such as the brain (Budday et al. 2019; Franceschini et al. 2006; Hosseini-Farid et al. 2020; Urcun et al. 2022), muscle tissues (Lavigne et al. 2022b), tumors (Sciumè et al. 2013; Sciumè 2021, Oftadeh et al. 2018), articular cartilages (Ateshian 2009) and lumbar inter-vertebral discs (Argoubi and Shirazi-Adl 1996). The time-dependent mechanical properties of soft tissues influence their physiological functions and are related to several pathological processes. Although a fluid-structure interaction (FSI) problem, the number, and range of fluid flows are generally so vast that the direct approach of a defined boundary between fluid and solid is impossible to apply, as it requires an exponential computational cost at the organ scale with the requirement of extensive data acquisition at the micro-scale. In these cases, homogenization and statistical treatment of the material-fluid system is possibly the only way forward. A prominent technique of this type is that of poro-elasticity.

Extensive studies have shown that poro-elastic models can accurately reproduce the time-dependent behavior of soft tissues under different loading conditions (Argoubi and Shirazi-Adl 1996; Franceschini et al. 2006; Gimnich et al. 2019; Hosseini-Farid et al. 2020; Lavigne et al. 2022b; Peyrounette et al. 2018; Siddique et al. 2017). Compared to a visco-(hyper)-elastic formulation (Simms et al. 2012; Vaidya and Wheatley 2020; Van Loocke et al. 2009; Wheatley et al. 2015), the poro-elastic properties are independent of the sample size (please refer to Appendix A of Urcun et al. 2022 for further justification). Furthermore, a poro-elastic approach can integrate multiscale/multiphysics data to probe biologically relevant phenomena at a smaller scale and embed the relevant mechanisms at the larger scale (in particular, biochemistry of oxygen and inflammatory signaling pathways), allowing the interpretation of the different time characteristics (Gray and Miller 2014; Mascheroni et al. 2016; Sciumè et al. 2013; Sciumè 2021; Urcun et al. 2021).

In most commercially available FE software packages used for research in biomechanics (ABAQUS, ANSYS, RADIOSS, etc), pre-programmed material models for soft biological tissues are available. The disadvantage of these pre-programmed models is that they are presented to the user as a "black box". Therefore, many researchers turn to implement their material formulations through user subroutines

(the reader is referred, for example, to the tutorial of Fehervary et al. 2020 on the implementation of a nonlinear hyper-elastic material model using user subroutines in ABAQUS). This task, however, is complex. When documentation is available, these only provide expressions, without any derivations, lack details and background information, making the implementation complex and error-prone. In addition, in case of a custom formulation or the introduction of biochemical equations for example, specific computational skills are required making the task even more challenging. In the end, the use of commercially available FE software packages may limit the straightforward reproducibility of the research by other teams.

The interest in open-source tools has skyrocketed to increase the impact of the studies within the community (for example FEBio, FreeFem, and Utopia Zulian et al. 2016; Zulian et al. 2021). For Finite Element modeling, the FEniCS project (Alnæs et al. 2015) is an Open-Access software that has proven its efficiency in biomechanics (Mazier et al. 2022). Based on a Python/C++ coding interface and the Unified Form Language, it allows to easily solve a defined variational form. Furthermore, its compatibility with open-source meshers like GMSH makes its use appealing. The project has already shown its capacity to solve large deformation problems (Mazier et al. 2021) and mixed formulations (Bulle 2022; Urcun et al. 2023; Urcun et al. 2022; Urcun et al. 2021). Previous work provided the implementation of poro-mechanics within the FEniCS project (Haagenson et al. 2020; Joodat et al. 2018). However, the FEniCS project is legacy and has been replaced by the FEniCSx project in August 2022 (Alnæs et al. 2014; Scroggs et al. 2022a; Scroggs et al. 2022b).

The aim of this paper is to propose a step-by-step explanation on how to implement several poro-mechanical models in FEniCSx with a special attention to parallel computation. First, an instantaneous uni-axial confined compression of a porous elastic medium is proposed. This example corresponds to an avascular tissue. Then, the same single-compartment model is computed for a hyper-elastic solid scaffold followed by a confined bi-compartment modeling.

## Confined compression of a column: geometrical definition

The time-dependent response of soft tissues are often assessed based on confined compression creep and stress relaxation test data (Budday et al. 2019; Franceschini et al. 2006; Hosseini-Farid et al. 2020; Urcun et al. 2022). All the benchmark examples focus on uni-axial confined compression of a column sample as shown in figure 5. Both 2D and 3D geometries are studied. The column is described by its width ( $0.1*h$ ) and height ( $h$ ) in 2D and its length ( $0.1*h$ ) in 3D.

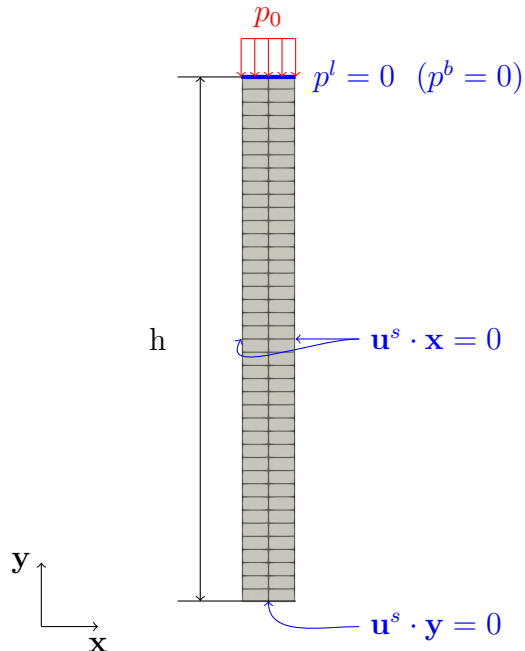


**Figure 5:** Load (red), Boundary conditions (blue) and mesh (gray) of the uni-axial confined compression of a porous 2D column of height  $h$ .

The dolfinx version used in this paper is v0.5.2. FEniCSx is a proficient platform for parallel computation. All described codes here-under are compatible with multi-kernel computation. The corresponding terminal command is:

```
1 mpirun -n <N> python3 <filename>
```

Where  $<N>$  is the number of threads to use and  $<\text{filename}>$  is the python code of the problem.

Within the FEniCSx software, the domain (geometry) is discretized to match with the Finite Element (FE) method. The space is thus divided in  $n_x \times n_y = 2 \times 40$  elements in 2D and  $n_x \times n_y \times n_z = 2 \times 40 \times 2$  elements in 3D. The choice of the number of elements is further discussed section 7.3. In this article, the meshes are directly created within the FEniCSx environment. However, as a strong compatibility exists with the GMSH API (Geuzaine and Remacle 2020), it is recommended to use GMSH for this step. An example of the use of GMSH API for a more complex geometry is given section Appendix B. It is worth noting that we identify all the boundaries of interest at this step for the future declaration of boundary conditions.

## 2D mesh

Conversely to the legacy FEniCS environment, FEniCSx requires to separately import the required libraries. To create the 2D mesh, the first step is to import the following libraries:

```
1 import dolfinx
2 import numpy as np
3 from dolfinx.mesh      import create_rectangle, CellType, locate_entities, meshtags
4 from mpi4py             import MPI
```

Then, the domain of resolution (mesh) is computed with:

```
1 Width, Height = 1e-5, 1e-4 #[m]
2 nx, ny        = 2, 40      #[ ]
3 mesh  = create_rectangle(MPI.COMM_WORLD, np.array([[0,0],[Width, Height]]), [nx,ny],
                           cell_type=CellType.quadrilateral)
```

Once the mesh object has been created, its boundaries are identified using couples of (marker, locator) to tag with a marker value the elements of dimension  $fdim$  fulfilling the locator requirements.

For the 2D mesh, the (marker, locator) couples are given by:

```
1 # identifiers: 1 , 2, 3, 4 = bottom, right, top, left
2 boundaries = [(1, lambda x: np.isclose(x[1], 0)),
3                 (2, lambda x: np.isclose(x[0], Width)),
4                 (3, lambda x: np.isclose(x[1], Height)),
5                 (4, lambda x: np.isclose(x[0], 0))]
```

Finally the entities are marked by:

```

1 facet_indices, facet_markers = [], []
2 # dimension of the elements we are looking for
3 fdim = mesh.topology.dim - 1
4 for (marker, locator) in boundaries:
5     facets = locate_entities(mesh, fdim, locator)
6     facet_indices.append(facets)
7     facet_markers.append(np.full_like(facets, marker))
8 facet_indices = np.hstack(facet_indices).astype(np.int32)
9 facet_markers = np.hstack(facet_markers).astype(np.int32)
10 sorted_facets = np.argsort(facet_indices)
11 # the meshtags() function requires sorted facet_indices
12 facet_tag = meshtags(mesh, fdim, facet_indices[sorted_facets], facet_markers[
    sorted_facets])

```

## 3D mesh

The method for a 3D mesh is similar to the 2D case. First, the libraries are imported and the geometry is created using a 3D function. The (marker, locator) tuples are completed to describe all the boundaries of the domain. The same tagging routine is used.

```

1 ## libraries
2 import dolfinx
3 import numpy
4 from dolfinx.mesh      import create_box, CellType, locate_entities, meshtags
5 from mpi4py             import MPI
6 ## Mesh generation
7 Length, Height, Width = 0.1, 1, 0.1 #[m]
8 nx, ny, nz = 2, 40, 2
9 mesh = create_box(MPI.COMM_WORLD, numpy.array([[0.0,0.0,0.0],[Length, Height, Width]]),
10                  [nx, ny, nz], cell_type=CellType.hexahedron)
10 ## Define the boundaries of the domain:
11 # 1, 2, 3, 4, 5, 6 = bottom, right, top, left, back, front
12 boundaries = [(1, lambda x: numpy.isclose(x[1], 0)),
13                 (2, lambda x: numpy.isclose(x[0], Length)),
14                 (3, lambda x: numpy.isclose(x[1], Height)),
15                 (4, lambda x: numpy.isclose(x[0], 0)),
16                 (5, lambda x: numpy.isclose(x[2], Width)),
17                 (6, lambda x: numpy.isclose(x[2], 0))]
18 facet_indices, facet_markers = [], []
19 fdim = mesh.topology.dim - 1
20 for (marker, locator) in boundaries:
21     facets = locate_entities(mesh, fdim, locator)
22     facet_indices.append(facets)
23     facet_markers.append(numpy.full_like(facets, marker))
24 facet_indices = numpy.hstack(facet_indices).astype(numpy.int32)
25 facet_markers = numpy.hstack(facet_markers).astype(numpy.int32)
26 sorted_facets = numpy.argsort(facet_indices)
27 facet_tag = meshtags(mesh, fdim, facet_indices[sorted_facets], facet_markers[
    sorted_facets])

```

## Single-compartment porous medium

We propose to reproduce the instantaneous uni-axial confined compression at the top surface of a single-compartment porous column of height  $h$ , Figure 5, described by a 2D elastic or a 3D hyper-elastic solid scaffold. Regarding the 2D elastic case, the column has a height of  $h = 100\mu\text{m}$ , the instantaneous load  $p_0$  has a magnitude of 100Pa and is applied during 6 s. Regarding the 3D hyper-elastic case, the column has a height of  $h = 1\text{m}$ , the instantaneous load  $p_0$  has a magnitude of  $p_0 = 0.3\text{MPa}$  and is applied during 100000 s. The mechanical parameters are respectively given Table 3 and Table 4. To assess the reliability of our results, we compare our computed solutions to Terzaghi's analytical solution and the results of Selvadurai and Suvorov 2016, for the elastic and hyper-elastic scaffolds respectively.

Parameter	Symbol	Value	Unit
Young modulus	$E$	5000	Pa
Poisson ratio	$\nu$	0.4	-
Intrinsic permeability	$k^\varepsilon$	$1.8 \times 10^{-15}$	$\text{m}^2$
Biot coefficient	$\beta$	1	-
Density of phase $\alpha$	$\rho^\alpha$	-	$\text{kg m}^{-3}$
IF viscosity	$\mu^l$	$1 \times 10^{-3}$	$\text{Pa s}$
Porosity	$\varepsilon^l$	0.5	-
Solid grain Bulk modulus	$K^s$	$1. \times 10^{10}$	Pa
Fluid Bulk modulus	$K^l$	$2.2 \times 10^9$	Pa

**Table 3:** Elastic mechanical parameters to compare with the Terzaghi solution

Parameter	Symbol	Value	Unit
Young modulus	$E$	600000	Pa
Poisson ratio	$\nu$	0.3	-
Bulk modulus	$K$	500000	Pa
Intrinsic permeability	$k^\varepsilon$	$3 \times 10^{-14}$	$\text{m}^2$
IF viscosity	$\mu^l$	$1 \times 10^{-3}$	$\text{Pas}$
Porosity	$\varepsilon^l$	0.2	-
Solid grain Bulk modulus	$K^s$	$1. \times 10^{10}$	Pa
Fluid Bulk modulus	$K^l$	$2.2 \times 10^9$ or $5 \times 10^5$	Pa
Biot coefficient	$\beta$	$1 - \frac{K}{K^s} \approx 1$	-

**Table 4:** Hyper-elastic mechanical parameters from Selvadurai and Suvorov 2016. In the absence of information on the porosity, solid grain bulk modulus and fluid bulk modulus, the parameter are arbitrarily chosen.

## Terzaghi's Analytical solution

The Terzaghi consolidation problem is a reference in poro-mechanics, that have been comprehensively described by classical authors such as Biot 1941; Detournay and Cheng 1993; Verruijt 2013. Such problem is often used for benchmarking porous media mechanics, as an analytical solution to this problem exists. An implementation of this experiment was proposed by Haagenson et al. 2020, within the legacy FEniCS project. The Terzaghi problem is a uni-directional confined compression experiment of a column (see Figure 5). Assuming small and uni-directional strains, incompressible homogeneous phases, and constant mechanical properties, the analytical expression of the pore pressure is given in terms of series in Equation 6.

$$p^l = \frac{4p_0}{\pi} \sum_{k=1}^{+\infty} \frac{(-1)^{k-1}}{2k-1} \cos \left[ (2k-1) \frac{\pi}{2} \frac{y}{h} \right] \exp \left[ -(2k-1)^2 \frac{\pi^2}{4} \frac{c_v t}{h^2} \right] \quad (6)$$

$$c_v = \frac{k^\varepsilon}{\mu^l (S_\beta + \frac{\beta^2}{M})} \quad (7)$$

$$M = \frac{3K^s(1-\nu)}{(1+\nu)} \quad (8)$$

$$S_\beta = \frac{\beta - \varepsilon_0^l}{K^s} + \frac{\varepsilon_0^l}{K^l} \quad (9)$$

Where  $p_0 = \mathbf{t}^{\text{imposed}} \cdot \mathbf{n}$  is the full applied load,  $y$  is the altitude,  $h$  is the initial height of the sample,  $c_v$  is the consolidation coefficient defined by (Equation 7),  $M$  the longitudinal modulus (Equation 8),  $S_\beta$  the inverse of the Biot Modulus (Equation 9) and  $\varepsilon_0^l$  is the initial porosity.

## Governing equations

Let one consider a bi-phasic structure composed of a solid scaffold filled with interstitial fluid (IF). The medium is assumed saturated. In this section, to set up the governing equations, we make the hypothesis of a Biot coefficient equal to 1. The following convention is assumed: the superscript "s" ( $\bullet^s$ ) denotes the solid phase and the superscript "l" ( $\bullet^l$ ) denotes the fluid phase. For example,  $\rho^s$  and  $\rho^l$  would respectively denote the density of the solid phase and of the fluid phase. The primary variables of the problem are the pressure applied in the pores of the porous

medium, namely  $p^l$ , and the displacement of the solid scaffold, namely  $\mathbf{u}^s$ . (Equation 10) constrains the different volume fractions. The volume fraction of the phase  $\alpha$  is defined by (Equation 11).  $\varepsilon^l$  is called the porosity of the medium.

$$\varepsilon^s + \varepsilon^l = 1 \quad (10)$$

$$\varepsilon^\alpha = \frac{\text{Volume}^\alpha}{\text{Volume}^{total}} \quad (11)$$

Assuming that there is no inter-phase mass transport, the continuity equations (mass conservation) of the liquid and solid phases are respectively given by Equation 12 and Equation 13.

$$\frac{\partial}{\partial t}(\rho^l \varepsilon^l) + \nabla \cdot (\rho^l \varepsilon^l \mathbf{v}^l) = 0 \quad (12)$$

$$\frac{\partial}{\partial t}(\rho^s(1 - \varepsilon^l)) + \nabla \cdot (\rho^s(1 - \varepsilon^l) \mathbf{v}^s) = 0 \quad (13)$$

Regarding the distributivity of the divergence term, with  $a$  scalar and  $\mathbf{V}$  vector,

$$\nabla \cdot (a \mathbf{V}) = a \nabla \cdot (\mathbf{V}) + \nabla a \cdot \mathbf{V} \quad (14)$$

Applied to 12 and Equation 13, and considering the definition of the material derivative,  $\frac{D^s}{Dt} f = \frac{\partial f}{\partial t} + \nabla f \cdot \mathbf{v}^s$ , the continuity equations are given by:

$$\frac{D^s}{Dt}(\rho^s(1 - \varepsilon^l)) + \rho^s(1 - \varepsilon^l) \nabla \cdot \mathbf{v}^s = 0 \quad (15)$$

$$\frac{D^s}{Dt}(\rho^l \varepsilon^l) + \nabla \cdot (\rho^l \varepsilon^l (\mathbf{v}^l - \mathbf{v}^s)) + \rho^l \varepsilon^l \nabla \cdot \mathbf{v}^s = 0 \quad (16)$$

For the fluid phase, the Darcy's law (Equation 17) is used to evaluate the fluid flow in the porous medium.

$$\varepsilon^l (\mathbf{v}^l - \mathbf{v}^s) = -\frac{k^\varepsilon}{\mu^l} (\nabla p^l - \rho^l \mathbf{g}) \quad (17)$$

Where  $k^\varepsilon$  is the intrinsic permeability ( $\text{m}^2$ ),  $\mu^l$  is the dynamic viscosity ( $\text{Pa s}$ ) and  $\mathbf{g}$  the gravity.

Introducing the state law  $\frac{1}{\rho^\alpha} \frac{D^s \rho^\alpha}{Dt} = \frac{1}{K^\alpha} \frac{Dp^\alpha}{Dt}$ ,  $K^\alpha$  being the bulk modulus of the phase alpha, the Darcy's law and summing 15 and Equation 16, we obtain:

$$\left( \frac{\varepsilon^l}{K^l} + \frac{1 - \varepsilon^l}{K^s} \right) \frac{D^s p^l}{Dt} + \nabla \cdot \mathbf{v}^s - \nabla \cdot \left( \frac{k^\varepsilon}{\mu^l} \nabla p^l \right) = 0 \quad (18)$$

Where  $S = \left( \frac{\varepsilon^l}{K^l} + \frac{1 - \varepsilon^l}{K^s} \right)$  is called the storativity coefficient.

Once the continuity equations are settled, one can define the quasi-static momentum balance of the porous medium, Equation 19.

$$\nabla \cdot \mathbf{t}^{\text{tot}} = 0 \quad (19)$$

Where  $\mathbf{t}^{\text{tot}}$  is the total Cauchy stress tensor. We introduce an effective stress tensor denoted  $\mathbf{t}^{\text{eff}}$ , responsible for all deformation of the solid scaffold. Then,  $\mathbf{t}^{\text{tot}}$  can be expressed as:

$$\mathbf{t}^{\text{tot}} = \mathbf{t}^{\text{eff}} - \beta p^l \mathbf{I}_d \quad (20)$$

Where  $\mathbf{I}_d$  is the identity matrix and  $\beta$  is the Biot coefficient.

Finally, the governing equations of this single compartment porous medium are:

$$\left( \frac{\varepsilon^l}{K^l} + \frac{1 - \varepsilon^l}{K^s} \right) \frac{D^s p^l}{Dt} + \nabla \cdot \mathbf{v}^s - \nabla \cdot \left( \frac{k^\varepsilon}{\mu^l} \nabla p^l \right) = 0 \text{ on } \Omega \quad (21)$$

$$\nabla \cdot \mathbf{t}^{\text{tot}} = 0 \text{ on } \Omega \quad (22)$$

Three boundaries are defined: the first one,  $\Gamma_u$  has imposed displacement (Equation 23), the second one  $\Gamma_s$  has imposed external forces (Equation 24) and  $\Gamma_p$  is submitted to an imposed pressure (fluid leakage condition (Equation 25)). We obtain:

$$\mathbf{t}^{\text{eff}} = \mathbf{t}^{\text{imposed}} \text{ on } \Gamma_s \quad (23)$$

$$\mathbf{u}^s = \mathbf{u}^{\text{imposed}} \text{ on } \Gamma_u \quad (24)$$

$$p = 0 \text{ on } \Gamma_p \quad (25)$$

According to Figure 5,  $\Gamma_p = \Gamma_s$  is the top surface and  $\Gamma_u$  covers the lateral and bottom surfaces.

## Effective stress

Two types of solid constitutive laws are considered: an elastic scaffold and a hyper-elastic one.

### Linear elasticity

In case of an elastic scaffold, the effective stress tensor is defined as follows:

$$\epsilon(\mathbf{u}) = \frac{1}{2}(\nabla\mathbf{u} + \nabla\mathbf{u}^T) \quad (26)$$

$$\mathbf{t}^{\text{eff}} = 2\mu\epsilon(\mathbf{u}^s) + \lambda\text{tr}(\epsilon(\mathbf{u}^s))\mathbf{I}_d \quad (27)$$

Where  $\mathbf{I}_d$  is the identity matrix and  $(\lambda, \mu)$  the Lame coefficients.

### Hyper-elasticity

In case of a hyper-elastic scaffold, other quantities are required. Let one introduce the deformation gradient  $\mathbf{F}$ :

$$\mathbf{F} = \mathbf{I}_d + \nabla\mathbf{u}^s \quad (28)$$

Then,  $J$  is the determinant of  $\mathbf{F}$ :

$$J = \det(\mathbf{F}) \quad (29)$$

According to the classic formulation of a finite element procedure, we introduce  $\mathbf{C}$  the right Cauchy-Green stress tensor and its first invariant  $I_1$ . By definition:

$$\mathbf{C} = \mathbf{F}^T \mathbf{F} \quad (30)$$

$$I_1 = \text{Tr}(\mathbf{C}) \quad (31)$$

The theory of hyper-elasticity defines a potential of elastic energy  $W(\mathbf{F})$ . The generalized Neo-Hookean potential (Equation 32) introduced by Treloar 1975, implemented in Abaqus and used by Selvadurai and Suvorov 2016 is evaluated in this

article.

$$W(\mathbf{F}) = \frac{\mu}{2}(J^{-2/3}I_1 - \text{tr}(\mathbf{I}_d)) + \left(\frac{\lambda}{2} + \frac{\mu}{3}\right)(J-1)^2 \quad (32)$$

However, other potential were developed. It was shown that the hyper-elastic potential can be expressed as the combination of a isochoric component and a volumetric component (Horgan and Saccomandi 2004; Marino 2018; Simo 1988). We define the lame coefficients by  $\mu = \frac{E}{2(1-\nu)}$  and  $\lambda = \frac{E\nu}{(1+\nu)(1-2\nu)}$ . For a Neo-Hookean material, we further have:

$$W(\mathbf{F}) = \tilde{W}(I_1, J) + U(J) \quad (33)$$

Where  $\tilde{W}(I_1, J)$  is the isochoric part and  $U(J)$  the volumetric one. The study of Selvadurai and Suvorov 2016 presented a compressible case ( $\nu = 0.3$ ) reaching high deformation. Therefore, a compressible formulation of the Neo-Hookean strain-energy potential from Horgan and Saccomandi 2004; Pence and Gou 2014 is also computed for comparison. Therefore, the implemented isochoric part of the strain energy potential is:

$$\tilde{W}_1(I_1, J) = \frac{\mu}{2}(I_1 - \text{tr}(\mathbf{I}_d) - 2\log[J]) \quad (34)$$

Two different volumetric parts ( $U_1$  and  $U_2$ ) which were proposed in Doll and Schweizerhof 2000 are implemented,

$$U_1(J) = \frac{\lambda}{2}\log[J]^2 \quad (35)$$

$$U_2(J) = \frac{\lambda}{2}(J-1)^2 \quad (36)$$

Finally, from the potential (Equation 33 or 32) derives the first Piola-Kirchhoff stress tensor as the effective stress such that:

$$\mathbf{t}^{\text{eff}} = \frac{\partial W}{\partial \mathbf{F}} \quad (37)$$

## Variational formulation

For the computation of the Finite Element (FE) model, the variational form of Equation 21 and Equation 22 is introduced. Let one consider  $(q, v)$  the test functions

defined in the mixed space  $L_0^2(\Omega) \times [H^1(\Omega)]^2$ .

With a first order approximation in time, Equation 21 gives:

$$\begin{aligned} \frac{S}{dt} \int_{\Omega} (p^l - p_n^l) q d\Omega + \frac{1}{dt} \int_{\Omega} \nabla \cdot (\mathbf{u}^s - \mathbf{u}_n^s) q d\Omega \\ + \frac{k^\varepsilon}{\mu^l} \int_{\Omega} \nabla p^l \nabla q d\Omega = 0, \forall q \in L_0^2(\Omega) \end{aligned} \quad (38)$$

Similarly, by integrating by part Equation 22, and including the Neumann boundary conditions, we get:

$$\begin{aligned} \int_{\Omega} \mathbf{t}^{\text{eff}} : \nabla \mathbf{v} d\Omega - \int_{\Omega} \beta p^l \nabla \cdot \mathbf{v} d\Omega - \int_{\Gamma_s} \mathbf{t}^{\text{imposed}} \cdot \mathbf{n} \cdot \mathbf{v} d\Gamma_s = 0, \\ \forall \mathbf{v} \in [H^1(\Omega)]^2 \end{aligned} \quad (39)$$

The first order approximation in time impose to define the initial conditions which are fixed according to Table 5.

Parameter	Symbol	Value	Unit
Displacement	$\mathbf{u}^s$	0	m
Displacement at previous step	$\mathbf{u}_n^s$	0	m
IF pressure	$p^l$	$\mathbf{t}^{\text{imposed}} \cdot \mathbf{n}$	Pa
IF pressure at previous step	$p_n^l$	0	Pa

**Table 5:** Initial conditions for the single compartment model

Finally, the problem to solve is: Find  $(p^l, \mathbf{u}^s) \in L_0^2(\Omega) \times [H^1(\Omega)]^2$  such that Equation 38 and Equation 39 are verified.

## 2D linear elastic solid scaffold

### FEniCSx implementation

This section aims to provide a possible implementation of a 2D elastic problem and its comparison with the Terzaghi analytical solution. Conversely to the former FEniCS project, Dolfinx is based on a more explicit use of the libraries and requires to import them in the FEniCSx environment separately. Therefore, each function

## 7 FEniCSx tutorial

used in the following implementation of the problem needs to be imported as a first step.

```
1 import numpy as np
2 from dolfinx          import nls
3 from dolfinx.fem.petsc import NonlinearProblem
4 from ufl              import VectorElement, FiniteElement, MixedElement, TestFunctions,
5     TrialFunction
6 from ufl              import Measure, FacetNormal
7 from ufl              import nabla_div, dx, dot, inner, grad, derivative, split
8 from petsc4py.PETSc   import ScalarType
9 from mpi4py            import MPI
10 from dolfinx.fem       import (Constant, dirichletbc, Function, FunctionSpace,
11     locate_dofs_topological)
12 from dolfinx.io        import XDMFFile
```

Then, the time parametrization is introduced, the load value  $T$  such that  $t^{\text{imposed}} = p_0 \cdot \mathbf{n}$  with  $\mathbf{n}$  the outward normal to the mesh, and the material parameters which are defined as ufl constants over the mesh.

```
1 ## Time parametrization
2 t      = 0                      # Start time
3 Tf    = 6.                      # End time
4 num_steps = 1000                 # Number of time steps
5 dt    = (Tf-t)/num_steps # Time step size
6 ## Material parameters
7 E      = Constant(mesh, ScalarType(5000))
8 nu    = Constant(mesh, ScalarType(0.4))
9 lambda_m = Constant(mesh, ScalarType(E.value*nu.value/((1+nu.value)*(1-2*nu.value))))
10 mu   = Constant(mesh, ScalarType(E.value/(2*(1+nu.value))))
11 rhos = Constant(mesh, ScalarType(1))
12 kepsilon = Constant(mesh, ScalarType(1.8e-15))
13 mul  = Constant(mesh, ScalarType(1e-2))
14 rhol = Constant(mesh, ScalarType(1))
15 beta = Constant(mesh, ScalarType(1))
16 epsilonl = Constant(mesh, ScalarType(0.2))
17 Kf   = Constant(mesh, ScalarType(2.2e9))
18 Ks   = Constant(mesh, ScalarType(1e10))
19 S    = (epsilonl/Kf)+(1-epsilonl)/Ks
20 ## Mechanical loading
21 pinit = 100 #[Pa]
22 T     = Constant(mesh,ScalarType(-pinit))
```

The surface element for integration based on the tags and the normals of the mesh are computed.

```
1 # Create the surfacic element
2 ds = Measure("ds", domain=mesh, subdomain_data=facet_tag)
3 # compute the mesh normals to express t^imposed = T.normal
4 normal = FacetNormal(mesh)
```

Two types of elements are defined for displacement and pressure, then combined to obtain the mixed space (MS) of the solution.

```

1 displacement_element = VectorElement("CG", mesh.ufl_cell(), 2)
2 pressure_element     = FiniteElement("CG", mesh.ufl_cell(), 1)
3 MS                  = FunctionSpace(mesh, MixedElement([displacement_element,
    pressure_element]))
```

The space of resolution being defined, we can introduce the Dirichlet boundary conditions according to Equation 24, Equation 25 and Figure 5.

```

1 # 1 = bottom: uy=0, 2 = right: ux=0, 3=top: pl=0 drainage, 4=left: ux=0
2 bcs      = []
3 fdim = mesh.topology.dim - 1
4 # uy=0
5 facets = facet_tag.find(1)
6 dofs    = locate_dofs_topological(MS.sub(0).sub(1), fdim, facets)
7 bcs.append(dirichletbc(ScalarType(0), dofs, MS.sub(0).sub(1)))
8 # ux=0
9 facets = facet_tag.find(2)
10 dofs   = locate_dofs_topological(MS.sub(0).sub(0), fdim, facets)
11 bcs.append(dirichletbc(ScalarType(0), dofs, MS.sub(0).sub(0)))
12 # ux=0
13 facets = facet_tag.find(4)
14 dofs   = locate_dofs_topological(MS.sub(0).sub(0), fdim, facets)
15 bcs.append(dirichletbc(ScalarType(0), dofs, MS.sub(0).sub(0)))
16 # leakage p=0
17 facets = facet_tag.find(3)
18 dofs   = locate_dofs_topological(MS.sub(1), fdim, facets)
19 bcs.append(dirichletbc(ScalarType(0), dofs, MS.sub(1)))
```

The problem depends on the time Equation 38. Initial conditions in displacement and pressure are required. Therefore, we defined  $X_0$  the unknown function and  $X_n$  the solution at the previous step. Giving the `collapse()` function, the initial displacement function  $U_n$  and its mapping within the  $X_n$  solution are identified. Then, its values are set to 0 and reassigned in  $X_n$  using the map. `Xn.x.scatter_forward()` allows to update the values of  $X_n$  in case of parallel computation. The same method is used to set up the initial pressure field. To fit with the studied problems, the load is instantaneously applied. Therefore, the initial pore pressure of the sample is assumed equal to  $p_0$ .

```

1 # X0, Xn: Solution and previous functions of space
2 X0 = Function(MS)
3 Xn = Function(MS)
4 # Initial values
5 # Solid Displacement
6 Un_, Un_to_MS = MS.sub(0).collapse()
7 FUn_ = Function(Un_)
8 with FUn_.vector.localForm() as initial_local:
```

## 7 FEniCSx tutorial

```
9     initial_local.set(ScalarType(0.0))
10 # Assign in Xn and broadcast to all the threads
11 Xn.x.array[Un_to_MS] = FUn_.x.array
12 Xn.x.scatter_forward()
13 # IF Pressure
14 Pn_, Pn_to_MS = MS.sub(1).collapse()
15 FPn_ = Function(Pn_)
16 with FPn_.vector.localForm() as initial_local:
17     initial_local.set(ScalarType(pinit))
18 # Assign in Xn and broadcast to all the threads
19 Xn.x.array[Pn_to_MS] = FPn_.x.array
20 Xn.x.scatter_forward()
```

The deformation and effective stress given Equation 26 and Equation 27 are defined by the following function:

```
1 def teff(u,lambda_m,mu):
2     from ufl import sym, grad, nabla_div, Identity
3     ## Deformation
4     epsilon = sym(grad(u))
5     ## Stress
6     return lambda_m * nabla_div(u) * Identity(u.geometric_dimension()) + 2*mu*epsilon
```

Finally, splitting the two functions X0, Xn, and introducing the test functions, the weak form is implemented as follows.

```
1 u,p      =split(X0)
2 u_n,p_n=split(Xn)
3 # Set up the test functions
4 v,q = TestFunctions(MS)
5 # Equation 33
6 F = (1/dt)*nabla_div(u-u_n)*q*dx + (kepsilon/mu)*dot(grad(p),grad(q))*dx + ( S/dt )*( p-p_n)*q*dx
7 # Equation 34
8 F += inner(grad(v),teff(u))*dx - beta * p * nabla_div(v)*dx - T*inner(v,normal)*ds(3)
```

Introducing the trial function of the mixed space dX0, we define the non-linear problem based on the variational form, the unknown, the boundary conditions and the Jacobian:

```
1 dX0      = TrialFunction(MS)
2 Js       = derivative(F, X0, dX0)
3 Problem = NonlinearProblem(F, X0, bcs = bcs, J = Js)
```

## Solving and results

To solve the non-linear problem defined here-above, a Newton solver is tuned.

```

1 solver = nls.petsc.NewtonSolver(mesh.comm, Problem)
2 # Absolute tolerance
3 solver.atol = 5e-10
4 # relative tolerance
5 solver.rtol = 1e-11
6 solver.convergence_criterion = "incremental"

```

The parameters were set according to Table 3. During the resolution, we computed for each step the error in  $L^2$ -norm in pressure defined Equation 40. These formulations are easily evaluated within the FEniCSx environment by defining the following functions:

$$E(p^l) = \frac{\sqrt{\int_{\Omega}(p^l - p^{ex})^2 dx}}{\sqrt{\int_{\Omega}(p^{ex})^2 dx}} \quad (40)$$

Where  $p^{ex}$  is the exact solution, computed from the Terzaghi's analytical formula.

```

1 def terzaghi_p(x):
2     kmax=1e3
3     p0,L=pinit,Height
4     cv = kepsilon.value/mul.value*(lambda_m.value+2*mu.value)
5     pression=0
6     for k in range(1,int(kmax)):
7         pression+=p0*4/np.pi*(-1)**(k-1)/(2*k-1)*np.cos((2*k-1)*0.5*np.pi*(x[1]/L))*np.
8         exp(-(2*k-1)**2*0.25*np.pi**2*cv*t/L**2)
9     pl=pression
10    return pl
11
12 def L2_error_p(mesh,pressure_element,__p):
13     V2 = FunctionSpace(mesh, pressure_element)
14     pex = Function(V2)
15     pex.interpolate(terzaghi_p)
16     L2_errorp, L2_normp = form(inner(__p - pex, __p - pex) * dx), form(inner(pex, pex) *
17     dx)
18     error_localp = assemble_scalar(L2_errorp)/assemble_scalar(L2_normp)
19     error_L2p = np.sqrt(mesh.comm.allreduce(error_localp, op=MPI.SUM))
20
21    return error_L2p

```

To get a code suitable for parallel computation, the solutions needed to be gathered on a same processor using the MPI.*allreduce()* function. Once the error functions were defined, the problem is solved within the time loop:

```

1 # Create an output xdmf file to store the values
2 xdmf = XDMFFile(mesh.comm, "./terzaghi.xdmf", "w")
3 xdmf.write_mesh(mesh)
4 # Solve the problem and evaluate values of interest
5 t = 0
6 L2_p = np.zeros(num_steps, dtype=PETSc.ScalarType)
7 for n in range(num_steps):
8     t += dt
9     num_its, converged = solver.solve(X0)

```

```

10 X0.x.scatter_forward()
11 # Update Value
12 Xn.x.array[:] = X0.x.array
13 Xn.x.scatter_forward()
14 __u, __p = X0.split()
15 # Export the results
16 __u.name = "Displacement"
17 __p.name = "Pressure"
18 xdmf.write_function(__u,t)
19 xdmf.write_function(__p,t)
20 # Compute L2 norm for pressure
21 error_L2p = L2_error_p(mesh,pressure_element,__p)
22 L2_p[n] = error_L2p
23 # Solve tracking
24 if mesh.comm.rank == 0:
25     print(f"Time step {n}, Number of iterations {num_its}, Load {T.value}, L2-error
26 p {error_L2p:.2e}")
27 xdmf.close()

```

The results obtained for pressure and displacements are provided Figure 6. The code to evaluate the pressure at given points is provided Appendix C.

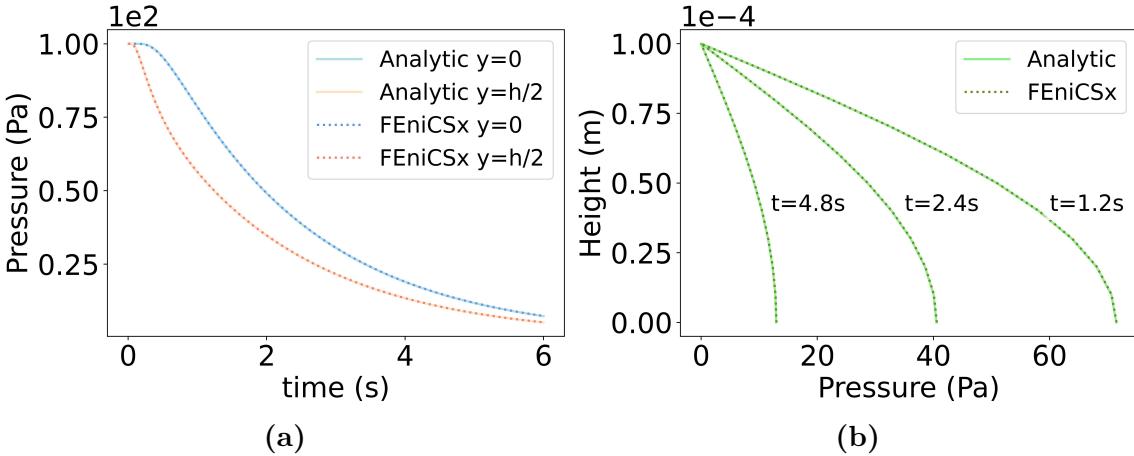


**Figure 6:** Comparison of the computed pore pressure against the analytical solution: in (a) time and (b) space. The pressure was well recovered based on the evaluation of the  $L^2$ -norm error  $(3.57 \pm 2.46) \times 10^{-3}$ . The full vertical displacement and pressure fields are provided at different time steps Appendix D.

The curves show the efficiency of the simulation to reproduce the analytical solution. The accuracy of the simulation was also supported by the estimation of the error based on the  $L^2$ -norm of the pressure equal to  $(3.57 \pm 2.46) \times 10^{-3}$  which is deemed satisfactory. The same problem was solved using the legacy FEniCS version. The proposed FEniCSx implementation was faster. It was computed in 9.48 seconds compared to the previously 31.82 seconds.

To show the efficiency of the parallel computation, the 3D case Appendix A and a refine 2D case ( $10 \times 500$  discretization) are considered. For a given 3D spatio-temporal discretization, a larger computational time of 1 hour 4 minutes 29 seconds is needed using FEniCSx. To reduce the time, the code naturally supports parallel computation. The same code was run for several number of threads. Computed on 2 threads, the code required 53 minutes 27 seconds. For 4 threads, the running time was further reduced to 46 minutes 27 seconds. Finally, using 8 threads, the computation time was reduced up to 28 minutes 9 seconds. For the 2D case, a computation time of 9 minutes was required on a single thread. Computed on 2 threads it reduced to 5 minutes 35 seconds which corresponds to a 48% improvement and further decreased up to 3 minutes 38 seconds on 4 threads corresponding to a 60% improvement. Computed on 8 threads, 2 minutes 43 seconds seconds were required which is an improvement of 70%.

Finally, a convergence analysis on the meshing of the column was carried out. The  $L_2$  error metric was used and its evolution for a  $n_x \times n_y$  discretized mesh is given Figure 7. As we could have expected from the 1D behavior of a confined compression Terzaghi case, the error is almost independent from the  $n_x$  choice. Figure 7(a) shows that a  $n_y \geq 10$  gives better estimations. According to Figure 7(b), a balance between precision and computation time must be considered. The more elements, the higher the computation time. To ensure obtaining a reliable solution, a mesh of  $n_x \times n_y = 2 \times 40$  was used (the convergence curve for the hyper-elastic case is provided Appendix E).

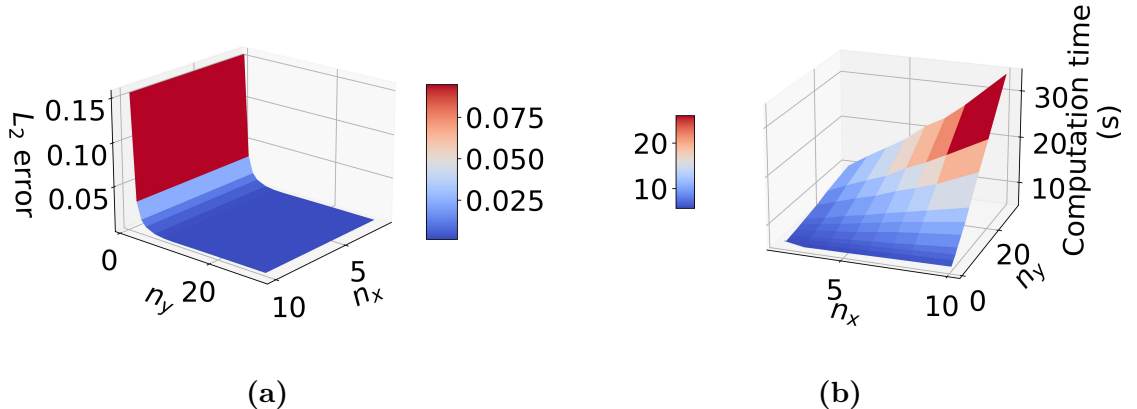


**Figure 7:** Convergence analysis for a  $n_x \times n_y$  discretized mesh: L-2 norm (a) and Computation time (b)

## 3D hyper-elastic scaffold

### FEniCSx implementation

The implementation method of the 3D case is the same. However, special attention must be placed on the boundary. Indeed, moving from 2D to 3D introduces two more boundaries. Therefore, the Dirichlet boundary conditions definition is completed with:

```

1 # uz=0
2 facets = facet_tag.find(5)
3 dofs   = locate_dofs_topological(MS.sub(0).sub(2), fdim, facets)
4 bcs.append(dirichletbc(ScalarType(0), dofs, MS.sub(0).sub(2)))
5 # uz=0
6 facets = facet_tag.find(6)
7 dofs   = locate_dofs_topological(MS.sub(0).sub(2), fdim, facets)
8 bcs.append(dirichletbc(ScalarType(0), dofs, MS.sub(0).sub(2)))

```

The effective stress tensor is also different. As an example, the stress tensor resulting from the potential  $W(\mathbf{F}) = \tilde{W}_1(I_1, J) + U_1(J)$  is defined in FEniCSx by:

```

1 def teff(u,lambda_m,mu):
2     from ufl import variable, Identity, grad, det, tr, ln, diff
3     ## Deformation gradient
4     F = variable(Identity(len(u)) + grad(u))
5     J  = variable(det(F))
6     ## Right Cauchy-Green tensor
7     C = variable(F.T * F)
8     ## Invariants of deformation tensors
9     Ic = variable(tr(C))
10    ## Potential
11    W = (mu / 2) * (Ic - 3) - mu * ln(J) + (lambda_m / 2) * (ln(J))**2
12    return diff(W, F)

```

All other developed potential are available in the supplementary material.

## Results

The same solver options as for the 2D case were used. To limit the computation time, the time step was made variable:  $dt=500$  for  $t \in [0, 20000]$ ,  $dt=1000$  for  $t \in [20000, 60000]$  and  $dt=10000$  for  $t \in [60000, 100000]$ . A total of 84 time steps was then considered.

The parameters were set according to Table 4. The results for the previously defined strain-energy potential are given Figure 8. Each finite element problem was

computed in  $23.6 \pm 4.3$  seconds on 8 threads (instead of  $49.6 \pm 9.9$  seconds on a single thread). Independently from the choice of the potential, the consolidated pressure was retrieved. On the contrary, the resulting displacement depends on the chosen potential but a same order of magnitude is found for all the cases and describe well the observations proposed in Selvadurai and Suvorov 2016.

In the absence of information about the porosity or the fluid bulk modulus in the referent study, two fluid bulk modulus were considered. In case where the fluid bulk modulus is made close to the water one ( $K^f = 2.2 \times 10^9$ ), the hyper-elastic material well recovers the expected values. However, mismatches appear for a linear scaffold. This can result from the use of a elastic law for large deformations. In case of a lower value of the fluid bulk modulus  $K^f = 5 \times 10^5$  (*i.e.*, it can correspond to a non-constant value of the permeability and the porosity), the elastic behavior was recovered but differences on the hyper-elastic formulation were obtained.

We believe that these differences result from a permeability depending on the stress state of the column which has not been developed in the referent paper ('Initial values of the permeability and viscosity are the same for all three materials.' from Selvadurai and Suvorov 2016).

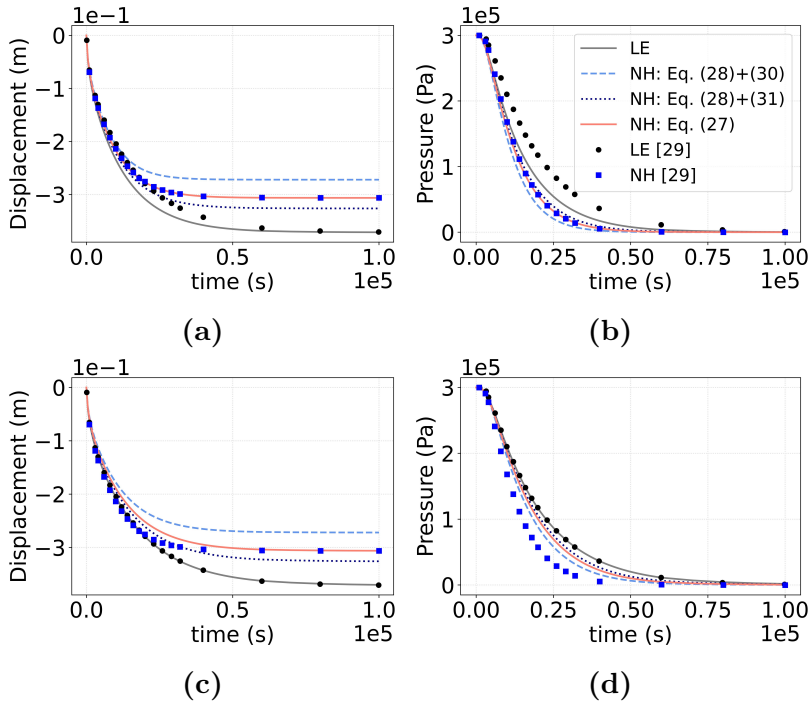


**Figure 8:**  $K^f = 2.2 \times 10^9$ : (a) Displacement of the top surface points and (b) pressure at the bottom of the column.  $K^f = 5 \times 10^5$ : (c) Displacement of the top surface points and (d) pressure at the bottom of the column. The computed Linear Elastic (LE) and Neo-Hookean (NH) for both volumetric functions and the found calibrated parameters are super-imposed with the expected values from Selvadurai and Suvorov 2016. The full vertical displacement and pressure fields (for the Equation (32) constitutive law) are provided at different time steps Appendix C.

## Confined bi-compartment porous-elastic medium

Sections 7.3 proposed a poro-mechanical modeling of a single-compartment porous medium (suitable for an avascularised tissue for instance). In case of *in vivo* modeling, at least one more fluid phase is required: the blood. A 3D confined compression example of a column of height 100  $\mu\text{m}$  is proposed, based on the here-after variational formulation and Sciumè 2021 study. The load is applied as a sinusoidal ramp up to the magnitude of 100 Pa during 5 seconds. Then, the load is sustained for 125 seconds.

For more complex geometries, a gmsh example of a rectangle geometry indented by a cylindrical beam on its top surface and the corresponding local refinement are proposed Appendix B.

Parameter	Symbol	Value	Unit
Young modulus	$E$	5000	Pa
Poisson ratio	$\nu$	0.2	-
IF viscosity	$\mu^l$	1	Pas
Intrinsic permeability	$k^e$	$1. \times 10^{-14}$	$m^2$
Biot coefficient	$\beta$	1	-
Density of phase $\alpha$	$\rho^\alpha$	-	$kg\ m^{-3}$
Porosity	$\varepsilon^l$	0.5	-
Vessel Bulk modulus	$K^v$	$1 \times 10^3$	Pa
vessel Intrinsic permeability	$k_b^e$	$2 \times 10^{-16}$ or $4 \times 10^{-16}$	$m^2$
Blood viscosity	$\mu^b$	$4.0 \times 10^{-3}$	Pas
Initial vascular porosity	$\varepsilon_0^b$	0% or 2% or 4%	-
Vascular porosity	$\varepsilon^b$	Equation 53	-

**Table 6:** Mechanical parameters for the bi-compartment model

## Governing Equations

Let one consider a vascular multi-compartment structure composed of a solid scaffold filled with interstitial fluid (IF) and blood. The medium is assumed saturated. The following convention is assumed: the superscript "s" ( $\bullet^s$ ) denotes the solid phase, the superscript "l" ( $\bullet^l$ ) denotes the interstitial fluid phase and the superscript ( $\bullet^b$ ) denotes the vascular part. The primary variables of the problem are the pressure applied in the pores of the extra-vascular part of the porous medium, namely  $p^l$ , the blood pressure, namely  $p^b$ , and the displacement of the solid scaffold, namely  $\mathbf{u}^s$ . (Equation 41) links the different volume fractions. The volume fraction of the phase  $\alpha$  is defined by (Equation 11).  $\varepsilon^l$  is called the extra-vascular porosity of the medium.

$$\varepsilon^s + \varepsilon^l + \varepsilon^b = 1 \quad (41)$$

Assuming that there is no inter-phase mass transport (*i.e.* the IF and the blood are assumed pure phases), the continuity equations (mass conservation) of the solid, the

IF and the blood phases are respectively given by Equation 42, 43, 44.

$$\frac{\partial}{\partial t}(\rho^s(1 - \varepsilon^l - \varepsilon^b)) + \nabla \cdot (\rho^s(1 - \varepsilon^l - \varepsilon^b)\mathbf{v}^s) = 0 \quad (42)$$

$$\frac{\partial}{\partial t}(\rho^l\varepsilon^l) + \nabla \cdot (\rho^l\varepsilon^l\mathbf{v}^l) = 0 \quad (43)$$

$$\frac{\partial}{\partial t}(\rho^b\varepsilon^b) + \nabla \cdot (\rho^b\varepsilon^b\mathbf{v}^b) = 0 \quad (44)$$

According to section 7.3, and dividing each equation by the corresponding density, the continuity equations can be re-expressed as:

$$\frac{D^s}{Dt}(1 - \varepsilon^l - \varepsilon^b) + (1 - \varepsilon^l - \varepsilon^b)\nabla \cdot \mathbf{v}^s = 0 \quad (45)$$

$$\frac{D^s\varepsilon^l}{Dt} + \nabla \cdot (\varepsilon^l(\mathbf{v}^l - \mathbf{v}^s)) + \varepsilon^l\nabla \cdot \mathbf{v}^s = 0 \quad (46)$$

$$\frac{D^s\varepsilon^b}{Dt} + \nabla \cdot (\varepsilon^b(\mathbf{v}^b - \mathbf{v}^s)) + \varepsilon^b\nabla \cdot \mathbf{v}^s = 0 \quad (47)$$

For the fluid phase, Darcy's law (Equation 48, 49) is used to evaluate the fluid flow in the porous medium.

$$\varepsilon^l(\mathbf{v}^l - \mathbf{v}^s) = -\frac{k^{\varepsilon}}{\mu^l}(\nabla p^l - \rho^l \mathbf{g}) \quad (48)$$

$$\varepsilon^b(\mathbf{v}^b - \mathbf{v}^s) = -\frac{k^b}{\mu^b}(\nabla p^b - \rho^b \mathbf{g}) \quad (49)$$

Where  $k^{\varepsilon}$ ,  $k^b$  are the intrinsic permeabilities ( $\text{m}^2$ ),  $\mu^l$ ,  $\mu^b$  are the dynamic viscosities ( $\text{Pas}$ ),  $p^l$ ,  $p^b$  the pressures and  $\mathbf{g}$  the gravity.

Equation 44 gives the following relationship:

$$\frac{D^s\varepsilon^l}{Dt} = -\frac{D^s\varepsilon^b}{Dt} + (1 - \varepsilon^l - \varepsilon^b)\nabla \cdot \mathbf{v}^s \quad (50)$$

Considering Equations 48, 50, Equation 46 becomes:

$$-\frac{D^s\varepsilon^b}{Dt} - \nabla \cdot \left( \frac{k^{\varepsilon}}{\mu^l} \nabla p^l \right) + (1 - \varepsilon^b)\nabla \cdot \mathbf{v}^s = 0 \quad (51)$$

Then, reading Equation 49, Equation 47 gives:

$$\frac{D^s \varepsilon^b}{Dt} - \nabla \cdot \left( \frac{k^b}{\mu^b} \nabla p^b \right) + \varepsilon^b \nabla \cdot \mathbf{v}^s = 0 \quad (52)$$

Considering a vascular tissue, we assume that the blood vessels are mostly surrounded by IF so they have weak direct interaction with the solid scaffold. Furthermore, the vessels are assumed compressible. Therefore, a state equation for the volume fraction of blood is introduced Equation 53.

$$\varepsilon^b = \varepsilon_0^b \cdot \left( 1 - \frac{p^l - p^b}{K^\nu} \right) \quad (53)$$

Where  $\varepsilon_0^b$  denotes the blood volume fraction when  $p^l = p^b$ ,  $K^\nu$  is the vessel compressibility.

It follows that Equations 51, 52 can be re-written as:

$$-\frac{\varepsilon_0^b}{K^\nu} \left( \frac{D^s p^l}{Dt} - \frac{D^s p^b}{Dt} \right) - \nabla \cdot \left( \frac{k^\varepsilon}{\mu^l} \nabla p^l \right) + (1 - \varepsilon^b) \nabla \cdot \mathbf{v}^s = 0 \quad (54)$$

$$\frac{\varepsilon_0^b}{K^\nu} \left( \frac{D^s p^l}{Dt} - \frac{D^s p^b}{Dt} \right) - \nabla \cdot \left( \frac{k^b}{\mu^b} \nabla p^b \right) + \varepsilon^b \nabla \cdot \mathbf{v}^s = 0 \quad (55)$$

Once the continuity equations are settled, one can define the quasi-static momentum balance of the porous medium, Equation 56.

$$\nabla \cdot \mathbf{t}^{\text{tot}} = 0 \quad (56)$$

Where  $\mathbf{t}^{\text{tot}}$  is the total Cauchy stress tensor. We introduce an effective stress tensor denoted  $\mathbf{t}^{\text{eff}}$ , responsible for all deformation of the solid scaffold. Then,  $\mathbf{t}^{\text{tot}}$  can be expressed as:

$$\mathbf{t}^{\text{tot}} = \mathbf{t}^{\text{eff}} - (1 - \zeta) p^l \mathbf{I}_d - \zeta p^b \mathbf{I}_d \quad (57)$$

$$\boldsymbol{\epsilon}(\mathbf{u}) = \frac{1}{2} (\nabla \mathbf{u} + \nabla \mathbf{u}^T) \quad (58)$$

$$\mathbf{t}^{\text{eff}} = 2\mu \boldsymbol{\epsilon}(\mathbf{u}^s) + \lambda \text{tr}(\boldsymbol{\epsilon}(\mathbf{u}^s)) \mathbf{I}_d \quad (59)$$

$$\zeta = \varepsilon_0^b \left( 1 - 2 \frac{p^l - p^b}{K^\nu} \right) \quad (60)$$

Four boundaries are defined: the first one,  $\Gamma_u$  has imposed displacement (Equation 61), the second one  $\Gamma_s$  has imposed external forces (Equation 62) and  $\Omega_p$  has imposed pressure (fluid leakage condition (Equation 63, 64)). We obtain:

$$\mathbf{t}^{\text{eff}} = \mathbf{t}^{\text{imposed}} \text{ on } \Gamma_s \quad (61)$$

$$\mathbf{u}^s = \mathbf{u}^{\text{imposed}} \text{ on } \Gamma_u \quad (62)$$

$$p^l = 0 \text{ on } \Gamma_p \quad (63)$$

$$p^b = 0 \text{ on } \Gamma_p \quad (64)$$

The initial conditions are given Table 7.

Parameter	Symbol	Value	Unit
Displacement	$\mathbf{u}^s$	0	m
Displacement at previous step	$\mathbf{u}_n^s$	0	m
IF pressure	$p^l$	0	Pa
IF pressure at previous step	$p_n^l$	0	Pa
Blood pressure	$p^b$	0	Pa
Blood pressure at previous time step	$p_n^b$	0	Pa
Vascular porosity	$\varepsilon^b$	$\varepsilon_0^b$	-

**Table 7:** Initial conditions for the bi-compartment model

## Variational Form

For the computation of the FE model, the variational form of Equation 54-56 must be introduced. Let one consider  $(q^l, q^b, v)$  the test functions defined in the mixed space  $L_0^2(\Omega) \times L_0^2(\Omega) \times [H^1(\Omega)]^3$ . With a first order approximation in time, Equation 54, 55 gives:

$$\begin{aligned} -\frac{\varepsilon_0^b}{K^\nu} \frac{1}{dt} \int_{\Omega} (p^b - p_n^b - p^l + p_n^l) q^l d\Omega + \frac{1 - \varepsilon^b}{dt} \int_{\Omega} \nabla \cdot (\mathbf{u}^s - \mathbf{u}_n^s) q^l d\Omega \\ + \frac{k^\varepsilon}{\mu^l} \int_{\Omega} \nabla p^l \nabla q^l d\Omega = 0, \forall q^l \in L_0^2(\Omega) \end{aligned} \quad (65)$$

$$\begin{aligned} \frac{\varepsilon^b}{K^\nu} \frac{1}{dt} \int_{\Omega} (p^b - p_n^b - p^l + p_n^l) q^b d\Omega + \frac{\varepsilon^b}{dt} \int_{\Omega} \nabla \cdot (\mathbf{u}^s - \mathbf{u}_n^s) q^b d\Omega \\ + \frac{k^b}{\mu^b} \int_{\Omega} \nabla p^b \nabla q^b d\Omega = 0, \forall q^b \in L_0^2(\Omega) \end{aligned} \quad (66)$$

Similarly, by integrating by part Equation 56, and including the Neumann boundary conditions, we get:

$$\begin{aligned} & \int_{\Omega} \mathbf{t}^{\text{eff}} : \nabla \mathbf{v} d\Omega - \int_{\Omega} (1 - \zeta) p^l \nabla \cdot \mathbf{v} d\Omega \\ & \quad - \int_{\Omega} \zeta p^b \nabla \cdot \mathbf{v} d\Omega \\ & - \int_{\Gamma_s} \mathbf{t}^{\text{imposed}} \cdot \mathbf{v} d\Gamma_s = 0, \forall \mathbf{v} \in [\mathbf{H}^1(\Omega)]^3 \end{aligned} \quad (67)$$

## FEniCSx Implementation

This section provides the code of a multi-compartment 3D column in confined compression. In order to evaluate the FEniCSx implementation, this case is similar to the Cast3m solution proposed in Sciumè 2021. 3 cases are studied: avascular tissue, vascular porosity of 2% and vascular porosity of 4%. The load is applied as a sine ramp during 5 seconds and then sustained during 125 seconds.

The time discretization is introduced.

```

1 t, t_ramp, t_sust = 0, 5, 125          # Start time
2 Tf           = t_ramp+t_sust            # End time
3 num_steps    = 1301                   # Number of time steps
4 dt           = (Tf-t)/num_steps        # Time step size

```

We then introduce the material parameters according to Table 7. The three cases of vascularization and Equation 60 are defined.

```

1 E           = Constant(mesh, ScalarType(5000))
2 nu          = Constant(mesh, ScalarType(0.2))
3 kepsilon_l = Constant(mesh, ScalarType(1e-14))
4 mu_l        = Constant(mesh, ScalarType(1))
5 lambda_m   = Constant(mesh, ScalarType(E.value*nu.value/((1+nu.value)*(1-2*nu.value))))
6 mu          = Constant(mesh, ScalarType(E.value/(2*(1+nu.value))))
7 Knu         = Constant(mesh, ScalarType(1000))      #compressibility of the vessels
8 mu_b        = Constant(mesh, ScalarType(0.004))    #dynamic mu_l of the blood
9 case=1
10 if case ==0:
11     epsilon_b_0=Constant(mesh, ScalarType(0.00)) #initial vascular porosity
12     k_b=Constant(mesh, ScalarType(2e-16))      #intrinsic permeability of vessels
13     def zeta(pl,pb):
14         return Constant(mesh,ScalarType(0.))
15 elif case ==1:
16     epsilon_b_0=Constant(mesh, ScalarType(0.02)) #initial vascular porosity
17     k_b=Constant(mesh, ScalarType(2e-16))      #intrinsic permeability of vessels
18     def zeta(pl,pb):
19         return epsilon_b_0.value*(1-2*(pl-pb)/Knu.value)

```

## 7 FEniCSx tutorial

```

20 elif case ==2:
21     epsilon_b_0 = Constant(mesh, ScalarType(0.04)) #initial vascular porosity
22     k_b = Constant(mesh, ScalarType(4e-16))    #intrinsic permeability of vessels
23     def zeta(pl,pb):
24         return epsilon_b_0.value*(1-2*(pl-pb)/Knu.value)

```

Then, the integration space, boundary and initial conditions are set up for the displacement, the IF pressure and the blood pressure.

```

1 ## Mechanical loading (Terzaghi)
2 pinit = 200 #[Pa]
3 T      = Constant(mesh,ScalarType(-pinit))
4 ## Define Mixed Space (R2,R, R) -> (u,pl, pb)
5 element      = VectorElement("CG", mesh.ufl_cell(), 2)
6 pressure_element = FiniteElement("CG", mesh.ufl_cell(), 1)
7 MS          = FunctionSpace(mesh, MixedElement([element,pressure_element,
8     pressure_element]))
9 # Create the solution and initial spaces
10 X0 = Function(MS)
11 Xn = Function(MS)
12 # Create the surfacic element
13 ds = Measure("ds", domain=mesh, subdomain_data=facet_tag)
14 # compute the normals
15 normal = FacetNormal(mesh)
16 # Define the Dirichlet conditions
17 bcs   = []
18 # uy=0
19 facets = facet_tag.find(1)
20 dofs   = locate_dofs_topological(MS.sub(0).sub(1), fdim, facets)
21 bcs.append(dirichletbc(ScalarType(0), dofs, MS.sub(0).sub(1)))
22 # ux=0
23 facets = facet_tag.find(2)
24 dofs   = locate_dofs_topological(MS.sub(0).sub(0), fdim, facets)
25 bcs.append(dirichletbc(ScalarType(0), dofs, MS.sub(0).sub(0)))
26 # uz=0
27 facets = facet_tag.find(4)
28 dofs   = locate_dofs_topological(MS.sub(0).sub(0), fdim, facets)
29 bcs.append(dirichletbc(ScalarType(0), dofs, MS.sub(0).sub(0)))
30 # uz=0
31 facets = facet_tag.find(5)
32 dofs   = locate_dofs_topological(MS.sub(0).sub(2), fdim, facets)
33 bcs.append(dirichletbc(ScalarType(0), dofs, MS.sub(0).sub(2)))
34 # uz=0
35 facets = facet_tag.find(6)
36 dofs   = locate_dofs_topological(MS.sub(0).sub(2), fdim, facets)
37 bcs.append(dirichletbc(ScalarType(0), dofs, MS.sub(0).sub(2)))
38 # leakage pl=pb=0
39 facets = facet_tag.find(3)
40 dofs   = locate_dofs_topological(MS.sub(1), fdim, facets)
41 bcs.append(dirichletbc(ScalarType(0), dofs, MS.sub(1)))
42 dofs   = locate_dofs_topological(MS.sub(2), fdim, facets)
43 bcs.append(dirichletbc(ScalarType(0), dofs, MS.sub(2)))
44 # Set Initial values

```

```

44 # Displacement
45 Un_, Un_to_MS = MS.sub(0).collapse()
46 FUn_ = Function(Un_)
47 with FUn_.vector.localForm() as initial_local:
48     initial_local.set(ScalarType(0.0))
49 # Update Xn for all threads
50 Xn.x.array[Un_to_MS] = FUn_.x.array
51 Xn.x.scatter_forward()
52 # IF Pressure
53 Pn_, Pn_to_MS = MS.sub(1).collapse()
54 FPn_ = Function(Pn_)
55 with FPn_.vector.localForm() as initial_local:
56     initial_local.set(ScalarType(0))
57 # Update Xn for all threads
58 Xn.x.array[Pn_to_MS] = FPn_.x.array
59 Xn.x.scatter_forward()
60 # Blood Pressure
61 Pbn_, Pbn_to_MS = MS.sub(2).collapse()
62 FPbn_ = Function(Pbn_)
63 with FPbn_.vector.localForm() as initial_local:
64     initial_local.set(ScalarType(0))
65 # Update Xn for all threads
66 Xn.x.array[Pbn_to_MS] = FPbn_.x.array
67 Xn.x.scatter_forward()

```

Internal variables are required. The vessels are compressible so we include the evolution of the vascular porosity as a function representing Equation 53.

```

1 # Internal variables: vascular porosity
2 Poro_space      = FunctionSpace(mesh,pressure_element)
3 poro_b  = Function(Poro_space) # vascular porosity
4 # Initialize
5 with poro_b.vector.localForm() as initial_local:
6     initial_local.set(ScalarType(epsilon_b_0.value))
7 # Update
8 poro_b.x.scatter_forward()
9 poro_b.name="poro_b"

```

A xdmf file is opened to store the results.

```

1 xdmf = XDMFFile(mesh.comm, "terzaghi.xdmf", "w")
2 xdmf.write_mesh(mesh)

```

The test functions as well as the variational form are introduced according to Equations 65, 66, 67.

```

1 u, pl, pb      = split(X0)
2 u_n, pl_n, pb_n = split(Xn)
3 v, ql, qb = TestFunctions(MS)
4 dx = Measure("dx", metadata={"quadrature_degree": 4})
5 F = (1-poro_b)*(1/dt)*nabla_div(u-u_n)*ql*dx + (kepsilon_l/(mu_l))*dot(grad(pl),grad(
    ql))*dx - (epsilon_b_0/Knu)*( (1/dt)*(pb-pb_n-pl+pl_n) )*ql*dx

```

## 7 FEniCSx tutorial

```
6 F += poro_b*(1/dt)*nabla_div(u-u_n)*qb*dx + ( k_b/(mu_b) )*dot( grad(pb),grad(qb) )*dx +
    (epsilon_b_0/Knu)*( (1/dt)*(pb-pb_n-pl+pl_n) )*qb*dx
7 F += inner(grad(v),teff(u))*dx - (1-zeta(pl,pb))*pl*nabla_div(v)*dx - zeta(pl,pb)*pb*
    nabla_div(v)*dx - T*inner(v,normal)*ds(3)
```

Finally, the problem to be solved is defined and a Newton method is used for each time step, the vascular porosity is updated and the results are stored in the xdmf file.

```
1 dX0      = TrialFunction(MS)
2 J        = derivative(F, X0, dX0)
3 Problem = NonlinearProblem(F, X0, bcs = bcs, J = J)
4 solver  = nls.petsc.NewtonSolver(mesh.comm, Problem)
5 # Set Newton solver options
6 solver.atol = 5e-10
7 solver.rtol = 1e-11
8 solver.convergence_criterion = "incremental"
9 t = 0
10 for n in range(num_steps):
11     t += dt
12     if t < t_ramp:
13         f1 = 0.5 * (1 - np.cos(np.pi*t/t_ramp))
14     else:
15         f1 = 1
16     T.value = -200*f1
17     num_its, converged = solver.solve(X0)
18     X0.x.scatter_forward()
19     # Update Value
20     Xn.x.array[:] = X0.x.array
21     Xn.x.scatter_forward()
22     # Update porosity
23     poro_b.x.array[:] = epsilon_b_0.value*(1-(1/Knu.value)*(X0.x.array[Pn_to_MS]-X0.x.
24         array[Pbn_to_MS]))
25     poro_b.x.scatter_forward()
26     # Save data
27     __u, __pl, __pb = X0.split()
28     __u.name = "Displacement"
29     __pl.name = "Pressure IF"
30     __pb.name = "Pressure blood"
31     xdmf.write_function(__u,t)
32     xdmf.write_function(__pl,t)
33     xdmf.write_function(__pb,t)
34     xdmf.write_function(poro_b,t)
35 xdmf.close()
```

## Results

The evolution of the vascular and interstitial pressures at the bottom points and the vertical displacement at the top points are provided Figure 9. Each solution was

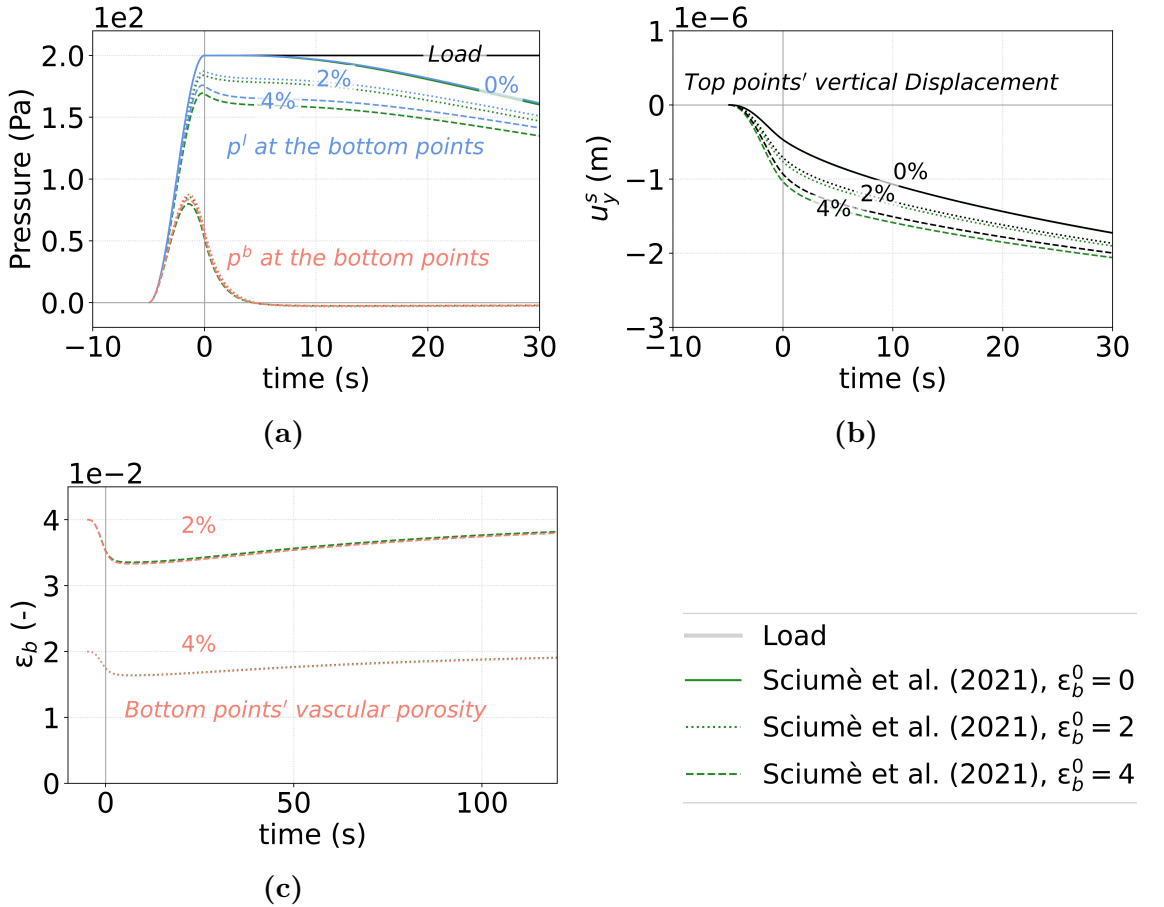


**Figure 9:** Comparison of the results obtained using FEniCSx against Sciumè 2021 results. All results were shifted to obtain similar figures. The solid, dotted and dashed lines respectively represent the 0%, 2% 4% initial vascular porosity. (a) Evolution of the pressure at the bottom points. (b) Displacement of the top points. (c) Vascular porosity at the bottom points. The behavior was well retrieved for all the cases with a NRMSE lower than 10% for all variables according to Table 8.

obtained in  $6 \pm 2$  minutes on 8 threads (instead of  $10.6 \pm 1.7$  minutes on a single thread) and the mesh was kept the same as in the previous section. The convergence curve is provided Appendix E. The overall behavior of the interstitial fluid pressure, the blood pressure and the solid displacement were retrieved. To quantitatively assess the reliability of our implemented model, The normalized root mean square error (NRMSE, Equation 68) was computed for each case with the results obtained with Cast3m in Sciumè 2021, Table 8.

$$\text{NRMSE}(x, x^{\text{ref}}) = \frac{\sqrt{\frac{1}{N} \sum_{i \in [1, N]} (x - x^{\text{ref}})^2}}{\text{mean}(x^{\text{ref}})} \quad (68)$$

Parameter	0%	2%	4%
$p^l$	1.4 %	3.1 %	5.1 %
$u_y$	0.3 %	2.2 %	3.7 %
$p^b$	-	4.7 %	8.8 %
$\varepsilon_0^b$	-	0.4 %	0.6 %

**Table 8:** NRMSE computed for each studied variable.

The NRMSE was found lower than 10% for all unknowns. The differences are assumed to result from the method of resolution which differs between Cast3m and FEniCSx. Indeed, the Cast3m procedure relies on a staggered solver whereas our results were obtained using a monolithic solver. The order of magnitudes of the NRMSE made us however consider our solution as trustworthy.

## Conclusion

The objective of this paper was to propose a step-by-step explanation of how to implement several poro-mechanical models in FEniCSx with special attention to parallel computation. Several benchmark cases for a mixed formulation were evaluated. First, a confined column was simulated under compression. Accurate results according to the L2-norm were found compared to the analytical solution. Furthermore, the code was computed 3 times faster than in the legacy FEniCS environment. Then, a possible implementation of a hyper-elastic formulation was proposed. The model was validated using Selvadurai and Suvorov 2016 values. Finally, a confined bi-compartment sample was simulated. The results were compared to Sciumè 2021 data. Small differences were observed due to the choice of the solver (staggered or monolithic) but remained acceptable. The authors hope that this paper will contribute to facilitate the use of poro-elasticity in the biomechanical engineering community. This article and its supplementary material constitute a starting point to implement their own material models at a preferred level of complexity.

## Supplementary material

The python codes corresponding to the workflows and the docker file of this article are made available for 2D and 3D cases on the following link: <https://github.com/>

[Th0masLavigne/Dolfinx\\_Porous\\_Media.git](#).

## Declaration of Competing Interest

Authors have no conflicts of interest to report.

## Acknowledgment

This research was funded in whole, or in part, by the Luxembourg National Research Fund (FNR), grant reference No. 17013182. For the purpose of open access, the author has applied a Creative Commons Attribution 4.0 International (CC BY 4.0) license to any Author Accepted Manuscript version arising from this submission. The present project is also supported by the National Research Fund, Luxembourg, under grant No. C20/MS/14782078/QuaC.

## Appendix A: 3D Terzaghi example

Here-after is proposed a minimal working code corresponding to the 2D case included within the text.

```

1 import numpy as np
2 import csv
3 from petsc4py import PETSc
4 import dolfinx
5 from dolfinx import nls
6 from dolfinx.io import XDMFFile
7 from dolfinx.mesh import CellType, create_box, locate_entities_boundary,
8     locate_entities, meshtags
9 from dolfinx.fem import (Constant, dirichletbc, Function, FunctionSpace,
10    locate_dofs_topological, form, assemble_scalar)
11 from dolfinx.fem.petsc import NonlinearProblem
12 from dolfinx.geometry import BoundingBoxTree, compute_collisions,
13     compute_colliding_cells
14 from petsc4py.PETSc import ScalarType
15 from mpi4py import MPI
16 from ufl import (FacetNormal, Identity, Measure, TestFunctions,
17     TrialFunction, VectorElement, FiniteElement, dot, dx, inner, grad, nabla_div, div,
18     sym, MixedElement, derivative, split)
19 #

```

## 7 FEniCSx tutorial

```

15 def epsilon(u):
16     return sym(grad(u))
17 #
18 def teff(u):
19     return lambda_m * nabla_div(u) * Identity(u.geometric_dimension()) + 2*mu*epsilon(u)
20 #
21 kmax=1e3
22 def terzaghi_p(x):
23     p0,L=pinit,Height
24     cv = permeability.value/viscosity.value*(lambda_m.value+2*mu.value)
25     pression=0
26     for k in range(1,int(kmax)):
27         pression+=p0*4/np.pi*(-1)**(k-1)/(2*k-1)*np.cos((2*k-1)*0.5*np.pi*(x[1]/L))*np.exp
28             (-2*k-1)**2*0.25*np.pi**2*cv*t/L**2)
29     pl=pression
30     return pl
31 #
32 def L2_error_p(mesh,pressure_element,__p):
33     V2 = FunctionSpace(mesh, pressure_element)
34     pex = Function(V2)
35     pex.interpolate(terzaghi_p)
36     L2_errorp, L2_normp = form(inner(__p - pex, __p - pex) * dx), form(inner(pex, pex) *
37         dx)
38     error_localp = assemble_scalar(L2_errorp)/assemble_scalar(L2_normp)
39     error_L2p = np.sqrt(mesh.comm.allreduce(error_localp, op=MPI.SUM))
40     return error_L2p
41 #
42 ## Create the domain / mesh
43 Height = 1e-4 #[m]
44 Width = 1e-5 #[m]
45 Length = 1e-5 #[m]
46 mesh = create_box(MPI.COMM_WORLD, np.array([[0.0,0.0,0.0],[Length, Width, Height]]),
47 [8, 8, 20], cell_type=CellType.tetrahedron)
48 #
49 ## Define the boundaries:
50 # 1 = bottom, 2 = right, 3=top, 4=left, 5=back, 6=front
51 boundaries = [(1, lambda x: np.isclose(x[2], 0)),
52                 (2, lambda x: np.isclose(x[0], Length)),
53                 (3, lambda x: np.isclose(x[2], Height)),
54                 (4, lambda x: np.isclose(x[0], 0)),
55                 (5, lambda x: np.isclose(x[1], Width)),
56                 (6, lambda x: np.isclose(x[1], 0))]
57 #
58 facet_indices, facet_markers = [], []
59 fdim = mesh.topology.dim - 1
60 for (marker, locator) in boundaries:
61     facets = locate_entities(mesh, fdim, locator)
62     facet_indices.append(facets)
63     facet_markers.append(np.full_like(facets, marker))
64 facet_indices = np.hstack(facet_indices).astype(np.int32)
65 facet_markers = np.hstack(facet_markers).astype(np.int32)
66 sorted_facets = np.argsort(facet_indices)
67 facet_tag = meshtags(mesh, fdim, facet_indices[sorted_facets], facet_markers[
68     sorted_facets])

```

```

65 #
66 ## Time parametrization
67 t      = 0           # Start time
68 Tf     = 6           # End time
69 num_steps = 1000      # Number of time steps
70 dt     = (Tf-t)/num_steps # Time step size
71 #
72 ## Material parameters
73 E      = Constant(mesh, ScalarType(5000))
74 nu    = Constant(mesh, ScalarType(0.4))
75 lambda_m = Constant(mesh, ScalarType(E.value*nu.value/((1+nu.value)*(1-2*nu.value))))
76 mu    = Constant(mesh, ScalarType(E.value/(2*(1+nu.value))))
77 rhos   = Constant(mesh, ScalarType(1))
78 permeability = Constant(mesh, ScalarType(1.8e-15))
79 viscosity   = Constant(mesh, ScalarType(1e-2))
80 rhol   = Constant(mesh, ScalarType(1))
81 beta    = Constant(mesh, ScalarType(1))
82 porosity  = Constant(mesh, ScalarType(0.2))
83 Kf     = Constant(mesh, ScalarType(2.2e9))
84 Ks     = Constant(mesh, ScalarType(1e10))
85 S      = (porosity/Kf)+(1-porosity)/Ks
86 #
87 ## Mechanical loading
88 pinit = 100 #[Pa]
89 T      = Constant(mesh,ScalarType(-pinit))
90 #
91 # Create the surfacic element
92 ds = Measure("ds", domain=mesh, subdomain_data=facet_tag)
93 normal = FacetNormal(mesh)
94 #
95 # Define Mixed Space (R2,R) -> (u,p)
96 displacement_element = VectorElement("CG", mesh.ufl_cell(), 2)
97 pressure_element     = FiniteElement("CG", mesh.ufl_cell(), 1)
98 MS                  = FunctionSpace(mesh, MixedElement([displacement_element,
99                                pressure_element]))
100 #
101 # Define the Dirichlet condition
102 # 1 = bottom: uy=0, 2 = right: ux=0, 3=top: pl=0 drainage, 4=left: ux=0
103 bcs    = []
104 # uz=0
105 facets = facet_tag.find(1)
106 dofs   = locate_dofs_topological(MS.sub(0).sub(2), fdim, facets)
107 bcs.append(dirichletbc(ScalarType(0), dofs, MS.sub(0).sub(2)))
108 # ux=0
109 facets = facet_tag.find(2)
110 dofs   = locate_dofs_topological(MS.sub(0).sub(0), fdim, facets)
111 bcs.append(dirichletbc(ScalarType(0), dofs, MS.sub(0).sub(0)))
112 # uy=0
113 facets = facet_tag.find(4)
114 dofs   = locate_dofs_topological(MS.sub(0).sub(0), fdim, facets)
115 bcs.append(dirichletbc(ScalarType(0), dofs, MS.sub(0).sub(0)))
116 # uy=0
117 facets = facet_tag.find(5)

```

## 7 FEniCSx tutorial

```
117 dofs    = locate_dofs_topological(MS.sub(0).sub(1), fdim, facets)
118 bcs.append(dirichletbc(ScalarType(0), dofs, MS.sub(0).sub(1)))
119 # uy=0
120 facets = facet_tag.find(6)
121 dofs    = locate_dofs_topological(MS.sub(0).sub(1), fdim, facets)
122 bcs.append(dirichletbc(ScalarType(0), dofs, MS.sub(0).sub(1)))
123 # drainage p=0
124 facets = facet_tag.find(3)
125 dofs    = locate_dofs_topological(MS.sub(1), fdim, facets)
126 bcs.append(dirichletbc(ScalarType(0), dofs, MS.sub(1)))
127 #
128 # Create the initial and solution spaces
129 X0 = Function(MS)
130 Xn = Function(MS)
131 #
132 # Initial values
133 #
134 Un_, Un_to_MS = MS.sub(0).collapse()
135 FUn_ = Function(Un_)
136 with FUn_.vector.localForm() as initial_local:
137     initial_local.set(ScalarType(0.0))
138 #
139 # Update Xn
140 Xn.x.array[Un_to_MS] = FUn_.x.array
141 Xn.x.scatter_forward()
142 #
143 Pn_, Pn_to_MS = MS.sub(1).collapse()
144 FPn_ = Function(Pn_)
145 with FPn_.vector.localForm() as initial_local:
146     initial_local.set(ScalarType(pinit))
147 #
148 # Update Xn
149 Xn.x.array[Pn_to_MS] = FPn_.x.array
150 Xn.x.scatter_forward()
151 #
152 # Variational form
153 # Identify the unknowns from the function
154 u,p    =split(X0)
155 u_n,p_n=split(Xn)
156 # Set up the test functions
157 v,q = TestFunctions(MS)
158 # Equation 17
159 F = (1/dt)*nabla_div(u-u_n)*q*dx + (permeability/viscosity)*dot(grad(p),grad(q))*dx +
160     ( S/dt )*(p-p_n)*q*dx
161 # Equation 18
162 F += inner(grad(v),teff(u))*dx - beta * p * nabla_div(v)*dx - T*inner(v,normal)*ds(3)
163 # Non linear problem definition
164 dX0    = TrialFunction(MS)
165 J      = derivative(F, X0, dX0)
166 Problem = NonlinearProblem(F, X0, bcs = bcs, J = J)
167 # set up the non-linear solver
168 solver = nls.petsc.NewtonSolver(mesh.comm, Problem)
169 # Absolute tolerance
170 solver.atol = 5e-10
```

```

170 # relative tolerance
171 solver.rtol = 1e-11
172 solver.convergence_criterion = "incremental"
173 #
174 t = 0
175 L2_p = np.zeros(num_steps, dtype=PETSc.ScalarType)
176 for n in range(num_steps):
177     t += dt
178     num_its, converged = solver.solve(X0)
179     X0.x.scatter_forward()
180     # Update Value
181     Xn.x.array[:] = X0.x.array
182     Xn.x.scatter_forward()
183     __u, __p = X0.split()
184     # Compute L2 norm for pressure
185     error_L2p = L2_error_p(mesh, pressure_element, __p)
186     L2_p[n] = error_L2p
187     # Solve tracking
188     if mesh.comm.rank == 0:
189         print(f"Time step {n}, Number of iterations {num_its}, Load {T.value}, L2-error p {error_L2p:.2e}")
190 if mesh.comm.rank == 0:
191     print(f'L2 error p, min {np.min(L2_p):.2e}, mean {np.mean(L2_p):.2e}, max {np.max(L2_p):.2e}, std {np.std(L2_p):.2e}')

```

## Appendix B: Local refinement

A 3D geometry can be meshed using the GMSH API of python (Geuzaine and Remacle 2020). This allows to represent complex geometries including circle arcs. An optimized and locally refined mesh can be therefore obtained. This example uses the method proposed in the FEniCS project tutorial<sup>1</sup> provided by J. Dokken and G. Wells. An alternative procedure in the FEniCSx environment with local refinement is then proposed in Appendix B.

### Meshing using GMSH API

First, the environment is initialized and the physical variables required for the box/-cylinder creation are defined.

```

1 import gmsh
2 import numpy as np
3 #

```

---

<sup>1</sup>see [https://docs.fenicsproject.org/dolfinx/main/python/demos/demo\\_gmsh.html](https://docs.fenicsproject.org/dolfinx/main/python/demos/demo_gmsh.html)

## 7 FEniCSx tutorial

```
4 gmsh.initialize()
5 #
6 # box parameters
7 [Length, Width, Height] = [6e-4, 2.5e-4, 4e-5]
8 # cylinder parameters
9 xc,yc,zc,dx,dy,dz, r = 6e-4/2, 0, 0, 0, 0, 4e-5, 1.5e-4
10 # expected dimension of the mesh
11 gdim = 3
```

The geometries are created using built-in functions of GMSH; potential duplicates are removed.

```
1 # create the geometry
2 box      = gmsh.model.occ.addBox(0, 0, 0, Length, Width, Height)
3 cylinder = gmsh.model.occ.addCylinder(xc,yc,zc,dx,dy,dz, r,tag=1000,angle=np.pi)
4 gmsh.model.occ.synchronize()
5 # Remove duplicate entities and synchronize
6 gmsh.model.occ.removeAllDuplicates()
7 gmsh.model.occ.synchronize()
```

Physical groups are defined: the volumes for the 3D meshing and the surfaces for tagging. Surface groups were identified based on the coordinates of the center of mass of each surface.

```
1 surfaces, volumes = [gmsh.model.getEntities(d) for d in [ gdim-1, gdim]]
2 print(volumes)
3 # Volumes
4 gmsh.model.addPhysicalGroup(volumes[0][0], [volumes[0][1]], -1)
5 gmsh.model.setPhysicalName(volumes[0][0], -1, 'Half_Cylinder')
6 gmsh.model.addPhysicalGroup(volumes[1][0], [volumes[1][1]], -1)
7 gmsh.model.setPhysicalName(volumes[1][0], -1, 'Box')
8 # 1 = loading, 2 = top minus loading, 3 = bottom, 4 = left, 5 = right, 6 = Front, 7 =
     back
9 bottom_marker, front_marker, back_marker, left_marker, right_marker, top_marker,
    indenter_marker = 3, 6, 7, 4, 5, 2, 1
10 bottom, front, back, left, right, top, indenter = [],[],[],[],[],[],[]
11 boundaries = gmsh.model.getBoundary(volumes, oriented=False)
12 for boundary in boundaries:
13     center_of_mass = gmsh.model.occ.getCenterOfMass(boundary[0], boundary[1])
14     if np.isclose(center_of_mass[1], Width):
15         back.append(boundary[1])
16     elif np.isclose(center_of_mass[1], 0):
17         front.append(boundary[1])
18     elif np.isclose(center_of_mass[0], 0):
19         left.append(boundary[1])
20     elif np.isclose(center_of_mass[0], Length):
21         right.append(boundary[1])
22     elif np.isclose(center_of_mass[2], 0):
23         bottom.append(boundary[1])
24     elif np.isclose(center_of_mass[2], Height) and center_of_mass[1]>Width/3:
25         top.append(boundary[1])
26 else:
```

```

27     indenter.append(boundary[1])
28 # mark the surfaces
29 gmsh.model.addPhysicalGroup(boundaries[0][0], bottom, bottom_marker)
30 gmsh.model.setPhysicalName(boundaries[0][0], bottom_marker, 'bottom')
31 gmsh.model.addPhysicalGroup(boundaries[0][0], front, front_marker)
32 gmsh.model.setPhysicalName(boundaries[0][0], front_marker, 'front')
33 gmsh.model.addPhysicalGroup(boundaries[0][0], back, back_marker)
34 gmsh.model.setPhysicalName(boundaries[0][0], back_marker, 'back')
35 gmsh.model.addPhysicalGroup(boundaries[0][0], left, left_marker)
36 gmsh.model.setPhysicalName(boundaries[0][0], left_marker, 'left')
37 gmsh.model.addPhysicalGroup(boundaries[0][0], right, right_marker)
38 gmsh.model.setPhysicalName(boundaries[0][0], right_marker, 'right')
39 gmsh.model.addPhysicalGroup(boundaries[0][0], top, top_marker)
40 gmsh.model.setPhysicalName(boundaries[0][0], top_marker, 'top')
41 gmsh.model.addPhysicalGroup(boundaries[0][0], indenter, indenter_marker)
42 gmsh.model.setPhysicalName(boundaries[0][0], indenter_marker, 'indenter')
43 gmsh.model.occ.synchronize()
44 # Write a geo file for verification in the GMSH GUI
45 gmsh.write('Geom_2reelle_8EP.geo_unrolled')
```

Then, a threshold function is defined over a distance field to mesh the circular area. This allows for creating an adaptive mesh: coarse far from the circular area, refine close to it.

```

1 indenter_interface = surfaces[0][1]
2 distance = gmsh.model.mesh.field.add("Distance")
3 gmsh.model.mesh.field.setNumbers(distance, "FacesList", [indenter_interface])
4 # A threshold function is defined:
5 resolution = r/10
6 threshold = gmsh.model.mesh.field.add("Threshold")
7 gmsh.model.mesh.field.setNumber(threshold, "IField", distance)
8 gmsh.model.mesh.field.setNumber(threshold, "LcMin", resolution)
9 gmsh.model.mesh.field.setNumber(threshold, "LcMax", 5*resolution)
10 gmsh.model.mesh.field.setNumber(threshold, "DistMin", 0.6*r)
11 gmsh.model.mesh.field.setNumber(threshold, "DistMax", r)
12 # If several fields are defined:
13 minimum = gmsh.model.mesh.field.add("Min")
14 gmsh.model.mesh.field.setNumbers(minimum, "FieldsList", [threshold]) # add other fields
   in the list if needed
15 gmsh.model.mesh.field.setAsBackgroundMesh(minimum)
```

Finally, the options of the mesher are defined and the mesh is created.

```

1 gmsh.model.occ.synchronize()
2 gmsh.option.setNumber("General.Terminal",1)
3 gmsh.option.setNumber("Mesh.Optimize", True)
4 gmsh.option.setNumber("Mesh.OptimizeNetgen", True)
5 gmsh.model.occ.synchronize()
6 # gmsh.option.setNumber("Mesh.MshFileVersion", 2.0)
7 gmsh.option.setNumber("Mesh.MeshSizeExtendFromBoundary", 0)
8 gmsh.option.setNumber("Mesh.MeshSizeFromPoints", 0)
9 gmsh.option.setNumber("Mesh.MeshSizeFromCurvature", 0)
```

```

10 #
11 gmsh.model.mesh.generate(gdim)
12 gmsh.write("Mesh.msh")
13 gmsh.finalize()

```

## Local refinement within FEniCSx

Using GMSH API, an exact circular interface is generated. However, a similar mesh could have been obtained within FEniCSx through the approximation of the circular interface around the indenter by local refining. Here-after is proposed a minimal code for local refinement inside the circular area.

First, the required libraries are imported and a box mesh is created.

```

1 ## Librairies
2 import dolfinx
3 import numpy as np
4 from dolfinx.mesh import create_box, CellType, refine, locate_entities, meshtags
5 from dolfinx.io import XDMFFFile
6 from mpi4py import MPI
7 #
8 ## Box
9 # Dimensions of the sample
10 [Length, Width, Height] = [6e-4, 2.5e-4, 4e-5]
11 # Discretization
12 [nx,ny,nz] = [30,15,8]
13 mesh = create_box(MPI.COMM_WORLD,np.array([[0.0,0.0,0.0],[Length, Width, Height]]), [nx,
    ny,nz], cell_type=CellType.tetrahedron)

```

Then a locator is introduced to identify all the edges ( $\text{fdim} = 1$ ) which are part of the region we aim to refine.

```

1 def test_on_boundary(x):
2     return (np.sqrt(np.power(x[0]-3e-4,2)+np.power(x[1],2))<=1.5e-4)
3 #
4 refine_boudaries = [(11, lambda x: test_on_boundary(x))]

```

Finally, a loop is performed to compute several times the refinement ( $np.arange(N)$ ), using the existing `refine()` function.

```

1 for _ in np.arange(2):
2     # Refinement
3     refine_indices, refine_markers = [], []
4     fdim = mesh.topology.dim-2
5     for (marker, locator) in refine_boudaries:
6         facets = locate_entities(mesh, fdim, locator)
7         refine_indices.append(facets)

```

```

8     refine_markers.append(np.full_like(facets, marker))
9 refine_indices = np.hstack(refine_indices).astype(np.int32)
10 refine_markers = np.hstack(refine_markers).astype(np.int32)
11 # indices in meshtag must be sorted
12 sorted_facets_refine = np.argsort(refine_indices)
13 refine_tag = meshtags(mesh, fdim, refine_indices[sorted_facets_refine], refine_markers
14     [sorted_facets_refine])
15 mesh.topology.create_entities(fdim)
16 mesh = refine(mesh, refine_indices[sorted_facets_refine])

```

The facets are tagged to apply boundary conditions and the mesh is written as a .xdmf file.

```

1 def Omega_top(x):
2     return np.logical_and((x[2] == Height), (np.sqrt(np.power(x[0]-3e-4,2)+np.power(x
3         [1],2))<=1.5e-4))
4 #
5 def Omega_loading(x):
6     return np.logical_and((x[2] == Height), (np.sqrt(np.power(x[0]-3e-4,2)+np.power(x
7         [1],2))>=1.2e-4))
8 #
9 # Create the facet tags (identify the boundaries)
10 # 1 = loading, 2 = top minus loading, 3 = bottom, 4 = left, 5 = right, 6 = Front, 7 =
11     back
12 boundaries = [(1, lambda x: Omega_loading(x)),
13                 (2, lambda x: Omega_top(x)),
14                 (3, lambda x: np.isclose(x[2], 0.0)),
15                 (4, lambda x: np.isclose(x[0], 0.0)),
16                 (5, lambda x: np.isclose(x[0], Length)),
17                 (6, lambda x: np.isclose(x[1], 0.0)),
18                 (7, lambda x: np.isclose(x[1], Width))]
19 # Mark them
20 facet_indices, facet_markers = [], []
21 fdim = mesh.topology.dim - 1
22 for (marker, locator) in boundaries:
23     facets = locate_entities(mesh, fdim, locator)
24     facet_indices.append(facets)
25     facet_markers.append(np.full_like(facets, marker))
26 facet_indices = np.hstack(facet_indices).astype(np.int32)
27 facet_markers = np.hstack(facet_markers).astype(np.int32)
28 sorted_facets = np.argsort(facet_indices)
29 facet_tag = meshtags(mesh, fdim, facet_indices[sorted_facets], facet_markers[
30     sorted_facets])
31 facet_tag.name = "facets"
32 #
33 # Write XDMF
34 mesh.topology.create_connectivity(mesh.topology.dim-1, mesh.topology.dim)
35 with XDMFFile(mesh.comm, "facet_tags.xdmf", "w") as xdmftag:
36     xdmftag.write_mesh(mesh)
37     xdmftag.write_meshtags(facet_tag)
38 xdmftag.close()

```

Figure 10 gives the comparison of the mesh obtained using GMSH and the one using

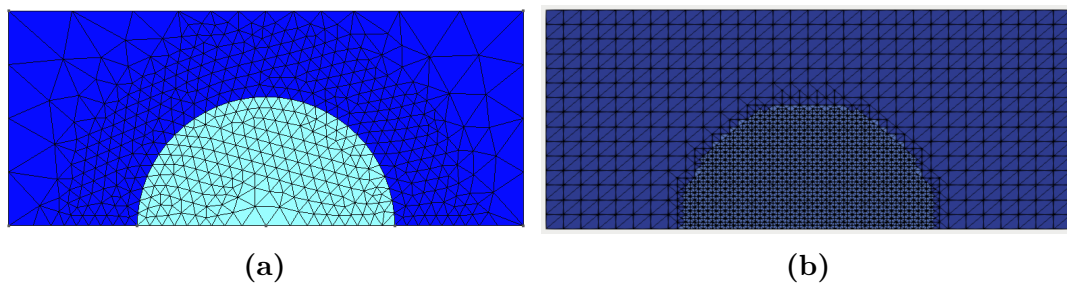


**Figure 10:** GMSH (a) and FEniCSx (b) generated meshes.

local refinement.

## Import an external mesh (XDMF or MSH)

Once the mesh is generated as a tagged .msh or .xdmf file, one can consider directly read them to compile the domain and read the markers using:

```

1 from dolfinx.io.gmshio import read_from_msh
2 from dolfinx.io          import XDMFFile
3 # set value to 0 if .xdmf, set it to 1 if .msh
4 mesher = 1
5 #
6 if mesher == 0:
7     #####
8     ## Read XDMF mesh      ##
9     #####
10    filename = "filename.xdmf"
11    with XDMFFile(MPI.COMM_WORLD, filename, "r") as file:
12        mesh = file.read_mesh()
13        mesh.topology.create_connectivity(mesh.topology.dim-1, mesh.topology.dim)
14        facet_tag = file.read_meshtags(mesh, "tag.name")
15    #
16 elif mesher == 1:
17     #####
18     ## Read gmsh  mesh    ##
19     #####
20     mesh, cell_tag, facet_tag = read_from_msh("filename.msh", MPI.COMM_WORLD, 0, gdim=3)
21    #
22 else:
23     print('The mesh type is wrongly defined. mesher should equal 0 for xdmf and 1 for msh
24         files.')
25     exit()
```

## Appendix C: Evaluate the function at a physical point

One strength of using FEniCSx is its ability to evaluate the solution at given points, summing the contribution of the neighbor cells of the mesh <sup>2</sup>. The following code allowed to compute the figures presented for the results of the sections 7.3 and ref 7.3. First, one need to define the points where to evaluate the solution.

```

1 import numpy as np
2 num_points = 11
3 y_check = np.linspace(0,Height,num_points)
4 points_for_time = np.array([[Width/2, 0., 0.], [Width/2, Height/2, 0.]])
5 points_for_space = np.zeros((num_points,3))
6 for ii in range(num_points):
7     points_for_space[ii,0]=Width/2
8     points_for_space[ii,1]=y_check[ii]
9 points = np.concatenate((points_for_time,points_for_space))

```

The following step is to identify the cells contributing to the points.

```

1 from dolfinx.geometry import BoundingBoxTree, compute_collisions,
    compute_colliding_cells
2 tree = BoundingBoxTree(mesh, mesh.geometry.dim)
3 cell_candidates = compute_collisions(tree, points)
4 colliding_cells = compute_colliding_cells(mesh, cell_candidates, points)
5 # Here is an example to select cells contributing to the first and second points.
6 cells_y_0 = colliding_cells.links(0)
7 cells_y_H_over_2 = colliding_cells.links(1)

```

Knowing the shape of the functions to evaluate, lists are created and will be updated during the resolution procedure. Regarding parallel computation, these lists are only created on the first kernel.

```

1 from mpi4py           import MPI
2 if MPI.COMM_WORLD.rank == 0:
3     pressure_y_0 = np.zeros(num_steps, dtype=PETSc.ScalarType)
4     pressure_y_Height_over_2 = np.zeros(num_steps, dtype=PETSc.ScalarType)
5     pressure_space0 = np.zeros(num_points, dtype=PETSc.ScalarType)
6     pressure_space1 = np.zeros(num_points, dtype=PETSc.ScalarType)
7     pressure_space2 = np.zeros(num_points, dtype=PETSc.ScalarType)

```

A function is created to evaluate a function given the mesh, the function, the contributing cells to the point and the list with its index to store the evaluated value in.

---

<sup>2</sup>see [https://jorgensd.github.io/dolfinx-tutorial/chapter2/ns\\_code2.html?highlight=eval](https://jorgensd.github.io/dolfinx-tutorial/chapter2/ns_code2.html?highlight=eval)

## 7 FEniCSx tutorial

```
1 def evaluate_point(mesh, function, contributing_cells, point, output_list, index):
2     from mpi4py import MPI
3     function_eval = None
4     if len(contributing_cells) > 0:
5         function_eval = function.eval(point, contributing_cells[:1])
6     function_eval = mesh.comm.gather(function_eval, root=0)
7     # Choose first pressure that is found from the different processors
8     if MPI.COMM_WORLD.rank == 0:
9         for element in function_eval:
10            if element is not None:
11                output_list[index]=element[0]
12                break
13    pass
```

Finally, the problem is solved for each time steps. The functions are evaluated for all kernels and gathered on the first one where the first pressure found by the different processors will be uploaded in the here-above lists.

```
1 # time steps to evaluate the pressure in space:
2 n0, n1, n2 = 200,400,800
3 #
4 t = 0
5 L2_p = np.zeros(num_steps, dtype=PETSc.ScalarType)
6 for n in range(num_steps):
7     t += dt
8     try:
9         num_its, converged = solver.solve(X0)
10    except:
11        if MPI.COMM_WORLD.rank == 0:
12            print("*****")
13            print("Solver failed")
14            print("*****")
15        pass
16    X0.x.scatter_forward()
17    # Update Value
18    Xn.x.array[:] = X0.x.array
19    Xn.x.scatter_forward()
20    __u, __p = X0.split()
21    #
22    # Export the results
23    __u.name = "Displacement"
24    __p.name = "Pressure"
25    xdmf.write_function(__u,t)
26    xdmf.write_function(__p,t)
27    #
28    # Compute L2 norm for pressure
29    error_L2p      = L2_error_p(mesh,pressure_element,__p)
30    L2_p[n] = error_L2p
31    #
32    # Solve tracking
33    if MPI.COMM_WORLD.rank == 0:
34        print(f"Time step {n}/{num_steps}, Load {T.value}, L2-error p {error_L2p:.2e}")
35    # Evaluate the functions
```

```
36 # in time
37 if n == n0:
38     for ii in range(num_points):
39         evaluate_point(mesh, __p, colliding_cells.links(ii+2), points[ii+2],
40                     pressure_space0, ii)
41         t0 = t
42     elif n==n1:
43         evaluate_point(mesh, __p, colliding_cells.links(ii+2), points[ii+2],
44                     pressure_space1, ii)
45         t1 = t
46     elif n==n2:
47         evaluate_point(mesh, __p, colliding_cells.links(ii+2), points[ii+2],
48                     pressure_space2, ii)
49         t2 = t
50     #
51 xdmf.close()
```

## Appendix D: Full field FE solutions

### Single compartment column with an elastic scaffold

The vertical displacement and pressure fields for a single compartment model column with an elastic scaffold are given at different time steps Figure 11.

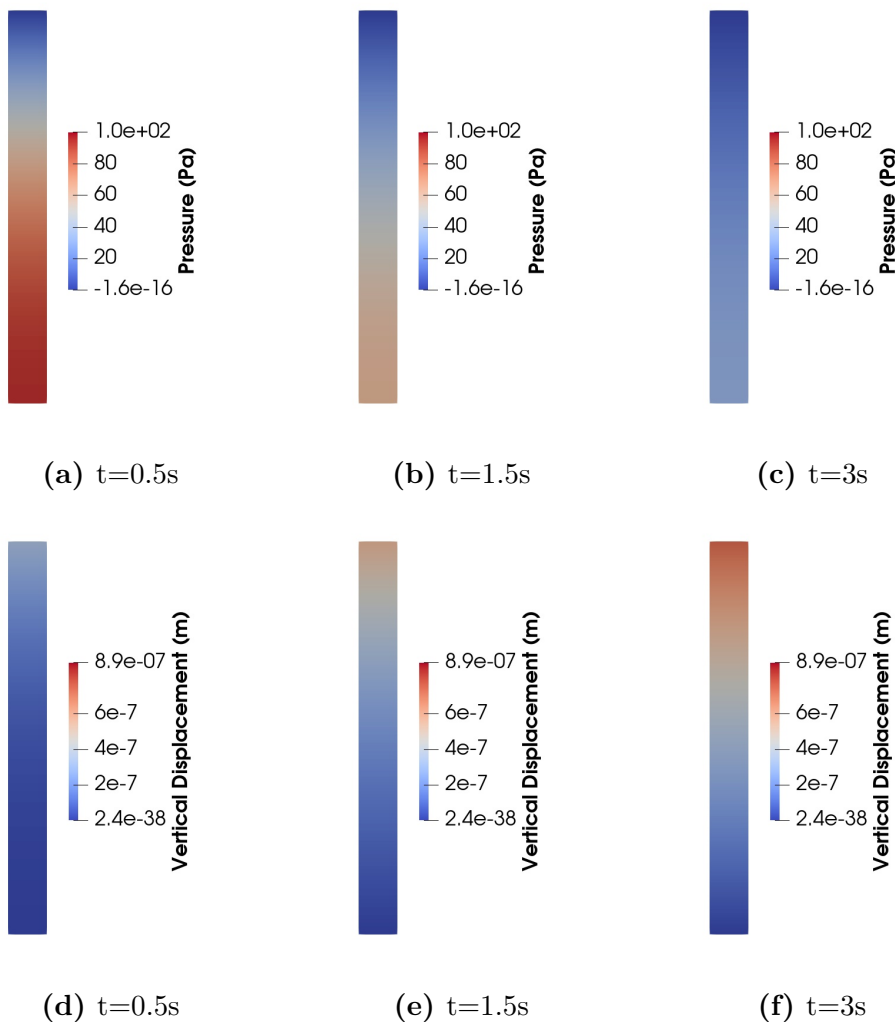


**Figure 11:** Full vertical displacement field and pressure field at given time points.

## Single compartment column with a hyper-elastic scaffold

The vertical displacement and pressure fields for a single compartment model column with a hyper-elastic scaffold Equation (32) are given at different time steps Figure 12.

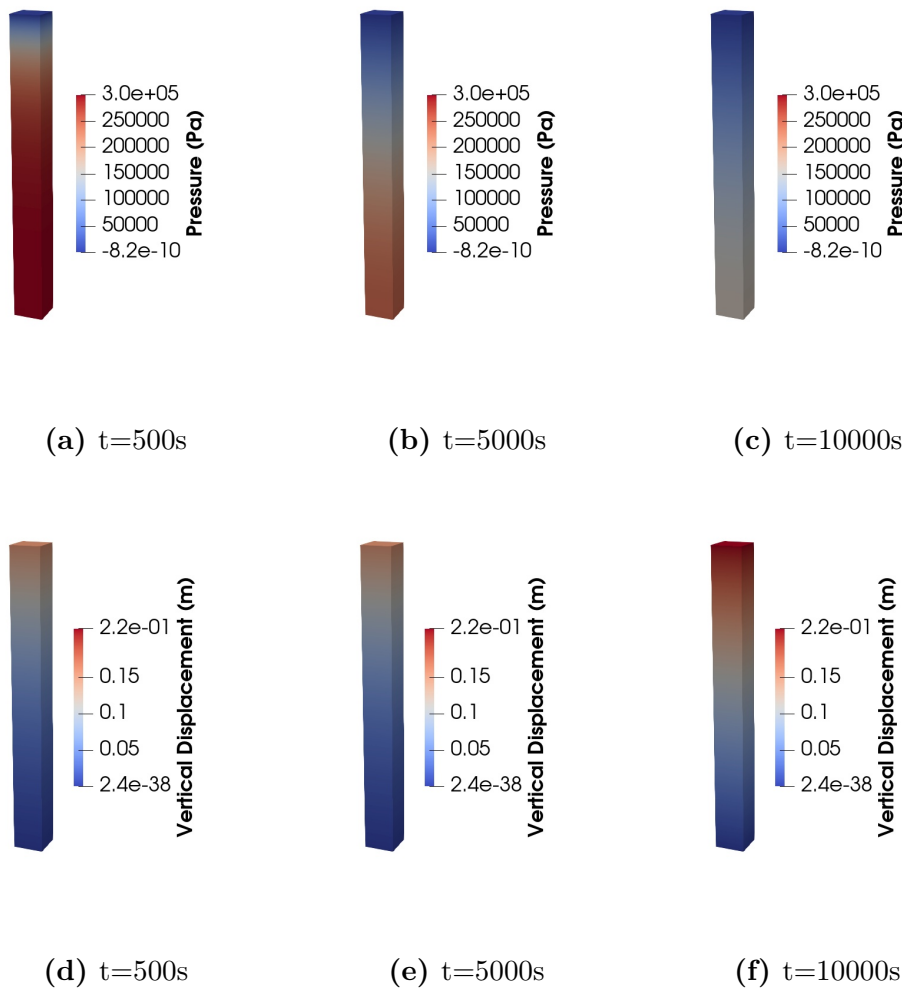


**Figure 12:** Full vertical displacement field and pressure field at given time points.

## Appendix E: Convergence curves

The normalized root mean square error (NRMSE) was computed between the solution obtained given a vertical discretization ( $n_z$ ) and one obtained with a refined discretization ( $n_z = 300$ ) which was deemed to approximate the exact solution. In the case of the hyper-elastic scaffold, the Equation (32) was considered. For the bi-compartment model, the 2% vacularization case was computed. In every cases, the error to the refined solution reached a plateau with  $n_z = 40$ . This results support the choice of a vertical discretization of 40 which has been considered in the article.

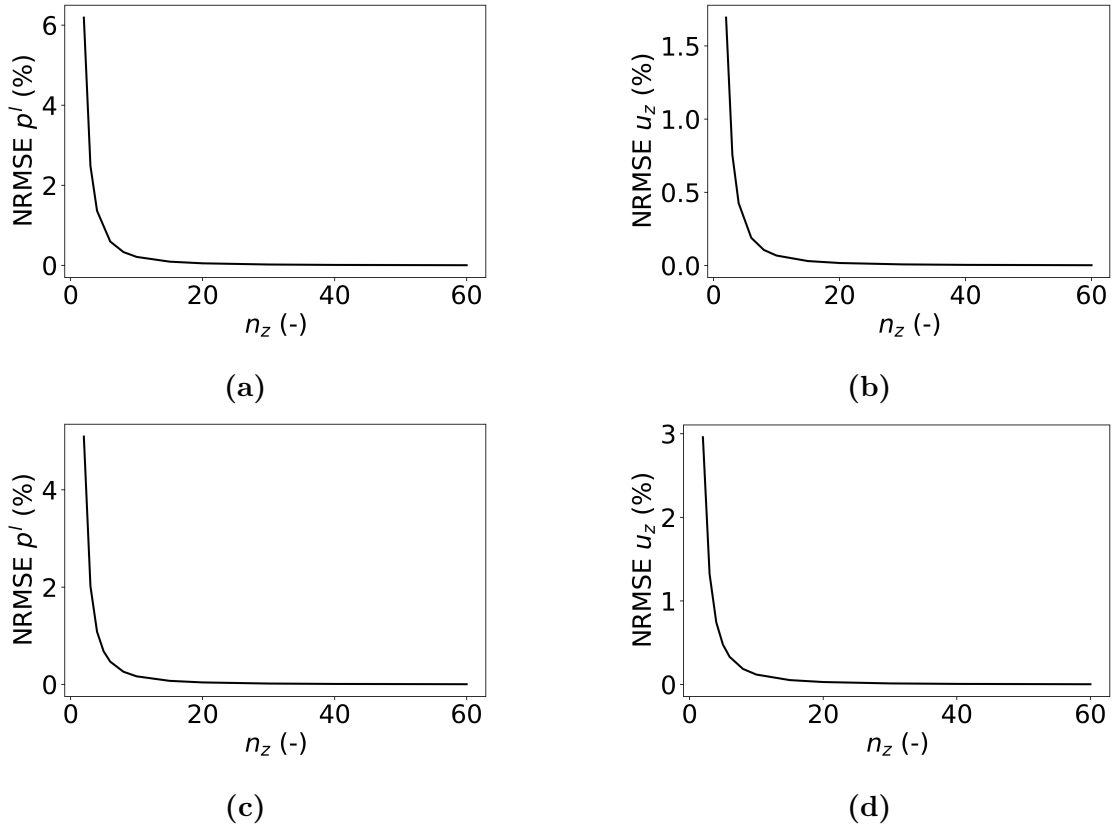


**Figure 13:** Convergence curves for (a,b) a single compartment column with a hyper-elastic scaffold; (c,d) a bi-compartment column.  $u_z$  stands for the vertical displacement at the top points,  $p^l$  denotes the fluid pressure at the bottom points and  $n_z$  is the number of elements in the vertical direction.

## **Part III**

### ***In vivo* evaluation of a single-compartment porous model**



# 8 *In vivo* evaluation of a single-compartment model

## Table of Contents

---

8.1 Synopsis (FR) . . . . .	113
8.2 Synopsis (EN) . . . . .	115
8.3 Article . . . . .	117

---

### 8.1 Synopsis (FR)

L’objectif principal de cette étude est de répondre à la question de recherche suivante : « *Un modèle poromécanique peut-il reproduire l’évolution temporelle de la réponse mécanique de la peau ?* ». Bien que l’utilisation de l’approche poromécanique se soit démocratisée pour modéliser les tissus vivants, peu d’étude ont évalué ces modèles par rapport à des données expérimentales acquises *in vivo*. Afin de contribuer à l’étude de la faisabilité sur l’utilisation de la poromécanique pour reproduire la réponse mécanique de la peau et sa caractéristiques, cette recherche propose un modèle constitutif biphasique qui prend en compte l’interaction entre ses composantes solides et fluides (Tableau 9). Cette approche offre une alternative aux principales limites des approches viscoélastiques traditionnelles, qui ne reflètent souvent pas la complexité structurelle et compositionnelle des tissus biologiques.

## 8 *In vivo* evaluation of a single-compartment model

Des données expérimentales issues de tests *in vivo* réalisés sur le bras supérieur d'une femme de 22 ans ont servi de base à cette étude. Ces expériences ont utilisé un extensomètre conçu sur mesure, appliquant une charge uniaxiale cyclique contrôlée à vitesse constante (dans le plan de la peau) et mesurant la réponse mécanique sur quatre cycles de chargement, de maintien et de déchargement. Les données collectées ont permis de capturer la réponse en contrainte ainsi que le comportement de relaxation de la peau sous charge maintenue. Le modèle a été implémenté dans FEniCSx, un environnement numérique adapté à la résolution d'équations différentielles partielles couplées. Cette plateforme a permis de réaliser des simulations numériques et une calibration des paramètres, incluant l'optimisation des modules d'Young et de la perméabilité tissulaire.

La peau a été décrite comme une structure à deux couches : le cutis, composée de l'épiderme et du derme, et le subcutis, représentant l'hypoderme. Chaque couche a été modélisée comme un matériau biphasique constitué d'une matrice solide et d'un fluide interstitiel. La cutis, plus rigide, absorbe principalement les charges mécaniques externes, tandis que la subcutis, dotée d'une perméabilité plus élevée, facilite la redistribution des fluides. La nature biphasique du modèle a permis de simuler à la fois la déformation du solide et l'écoulement du fluide, reproduisant ainsi les comportements mécaniques critiques dépendants du temps de la peau.

L'évaluation du modèle avec les données expérimentales a montré sa capacité à reproduire les forces de réaction dépendantes du temps observées lors des tests de chargement cyclique, avec une erreur quadratique moyenne (RMSE) de  $8,84 \times 10^{-3}$  N. Ce résultat souligne la capacité du modèle à reproduire la réponse mécanique de la peau, y compris la relaxation des contraintes et la dynamique des fluides interstitiels. Une analyse plus approfondie a mis en évidence le rôle significatif des fluides interstitiels dans la dissipation des charges mécaniques et la restauration des tissus à l'équilibre après déformation. Pendant le chargement, le modèle a reproduit la dilatation des pores et l'afflux de fluides, tandis que les phases de maintien et de déchargement ont révélé des schémas distincts de redistribution des fluides. Ces résultats mettent en avant l'importance d'intégrer la mécanique des solides et des fluides pour comprendre pleinement le comportement mécanique de la peau.

Bien que l'étude démontre le potentiel d'une approche poromécanique pour rendre compte du caractère temporel de la réponse mécanique de la peau, elle présente des

limitations. La dépendance à des données provenant d'un seul sujet limite la généralisation des résultats. De plus, l'hypothèse d'isotropie des propriétés mécaniques de la peau ne tient pas compte de son anisotropie transverse, liée à l'alignement des fibres de collagène. Regrouper l'épiderme et le derme en une seule couche peut également simplifier excessivement les contributions distinctes de ces couches au comportement mécanique. Il est essentiel de remédier à ces limitations dans les travaux futurs pour améliorer la précision du modèle. L'augmentation de la taille de l'échantillon à plusieurs sujets, le raffinement de la représentation des couches de la peau et l'intégration des propriétés anisotropes amélioreraient considérablement l'applicabilité du modèle. Plus de données expérimentale permettrait de réduire l'incertitude sur les paramètres matériau identifiés.

Cette recherche jette les bases d'une modélisation avancée de la mécanique de la peau, offrant des perspectives précieuses pour des applications cliniques et biomécaniques. En intégrant la poromécanique, le modèle fournit un outil pour analyser l'interaction entre les facteurs biochimiques et mécaniques dans la santé et les maladies des tissus. Les applications potentielles incluent l'étude de conditions telles que la formation de chéloïdes et les escarres, où le stress mécanique et la dynamique des fluides jouent un rôle central. Les résultats de cette étude démontrent l'utilité des modèles poromécaniques pour combler le fossé entre les prédictions théoriques et les observations expérimentales, faisant progresser la compréhension des mécanismes complexes de la peau humaine.

## 8.2 Synopsis (EN)

The primary objective of this study is to address the following research question: "*Can a poromechanical model reproduce the skin's time-dependent behaviour?*". While the use of poromechanical approaches has become increasingly used for modelling living tissues, few studies have validated such models against *in vivo* experimental data. To contribute to the assessment of the feasibility of using poromechanics to reproduce the mechanical response and characteristics of skin, this research proposes a biphasic constitutive model that accounts for the interaction between its solid and fluid components (Table 9). This approach provides an alternative to the main limitations of traditional viscoelastic models, which often fail to capture the structural and compositional complexity of biological tissues.

## 8 In vivo evaluation of a single-compartment model

Species Phase \	Species Phase	ECM	Other structures (glands, hair, etc.)	Cells in the interstitium	Water	Oxygen	Other Species
Solid (s)	✓	✓	✓	✓	✓		
Liquid (l)				✓	✓	✓	✓

**Table 9:** Description of the phases. ECM stands for Extra-Cellular Matrix.

Unpublished experimental data from *in vivo* tests in the upper arm of a 22-year-old subject provided the basis for this study. These experiments used a custom-built extensometer, which applied controlled cyclic uniaxial loading at a constant speed (in the skin plane) and measured the mechanical response in four loading, sustaining and unloading cycles. The data captured both the stress response and the relaxation behaviour of the skin under sustained loading. The model was implemented in FEniCSx, a computational environment ideal for solving coupled partial differential equations. This platform enabled numerical simulations and parameter calibration, including optimisation of Young’s moduli and tissue permeability.

The skin was described by a two-layered structure: the cutis, consisting of the epidermis and dermis, and the subcutis, representing the hypodermis. Each layer was treated as a biphasic material composed of a solid matrix and interstitial fluid. The cutis, being stiffer, primarily absorbs external mechanical loads, while the subcutis, with its higher permeability, facilitates fluid redistribution. The biphasic nature of the model enabled simulation of both solid deformation and fluid flow, capturing the critical time-dependent mechanical behaviours of the skin.

Evaluation of the model against experimental data demonstrated its capacity in reproducing the time-dependent reaction forces observed during cyclic loading tests, with a Root Mean Square Error (RMSE) of  $8.84 \times 10^{-3}$  N. This result highlights the ability of the model to replicate the mechanical response of the skin, including stress relaxation and interstitial fluid dynamics. Further analysis showed the significant role of interstitial fluid in dissipating mechanical loads and restoring tissue to equilibrium after deformation. During loading, the model simulated pore dilation and fluid influx, while sustained loading and unloading phases revealed distinct patterns of fluid redistribution. These insights emphasise the importance of incorporating both solid and fluid mechanics to fully understand skin mechanical behaviour.

Although the study demonstrates the promise of a poromechanical approach to reproduce the time characteristics of skin mechanical response, it has limitations.

Reliance on data from a single test subject restricts the generalisability of the findings. Furthermore, the assumption of isotropy in skin mechanical properties does not account for its known transverse anisotropy caused by collagen fibre alignment. Combining the epidermis and dermis into a single layer can also oversimplify the distinct contributions of these layers to mechanical behaviour. Addressing these issues in future work is essential for improving the accuracy of the model. Expanding the data set to include multiple subjects, refining the representation of skin layers, and incorporating anisotropic properties would significantly enhance the applicability of the model. This would allow to evaluate the uncertainties related to parameters identification.

This research lays the foundation for advanced skin mechanics modelling, offering valuable insight for clinical and biomechanical applications. By integrating poromechanics, the model provides a tool to analyse the interplay of biochemical and mechanical factors in tissue health and disease. Potential applications include studying conditions such as keloid formation and pressure ulcers, where mechanical stress and fluid dynamics play a pivotal role. The results of this study demonstrate the utility of poromechanical models in bridging the gap between theoretical predictions and experimental observations, advancing understanding of the complex mechanics of human skin.

### 8.3 Article

This work was submitted for peer review in 2024 (International Journal of Numerical Methods in Biomedical Engineering). It is already available in Arxiv <https://arxiv.org/pdf/2412.07374>.

#### Contribution (CRediT author statement)

Conceptualisation, Methodology, Investigation, Software, Writing – original draft.

## Poromechanical modelling of the time-dependent response of *in vivo* human skin during extension

Thomas Lavigne<sup>a,b,c</sup>, Stéphane Urcun<sup>a</sup>, Emmanuelle Jacquet<sup>e</sup>, Jérôme Chambert<sup>e</sup>,

Aflah Elouneg<sup>e</sup>, Camilo A. Suarez-Afanador<sup>a</sup>, Stéphane P.A. Bordas<sup>a</sup>, Giuseppe Sciumè<sup>c,d</sup>, Pierre-Yves Rohan<sup>b,\*</sup>

<sup>a</sup> Institute of Computational Engineering, Department of Engineering, University of Luxembourg,  
2 place de l'université, Esch-sur-Alzette, L-4365, Luxembourg, <sup>b</sup> Arts et Metiers Institute of  
Technology, IBHGC, 151 bd de l'hôpital, Paris, 75013, France, <sup>c</sup> Arts et Metiers Institute of  
Technology, Univ. of Bordeaux, CNRS, Bordeaux INP, INRAE, I2M Bordeaux, Avenue  
d'Aquitaine, Pessac, 33607, France, <sup>d</sup> Institut Universitaire de France (IUF) <sup>e</sup> Université Marie  
et Louis Pasteur, CNRS, institut FEMTO-ST, Besançon, F-25000, France

**Abstract:** This paper proposes a proof of concept application of a biphasic constitutive model to identify the mechanical properties of *in vivo* human skin under extension. Although poromechanics theory has been extensively used to model other soft biological tissues, only a few studies have been published for skin, and most have been limited to *ex vivo* or *in silico* conditions. However, *in vivo* procedures are crucial to determine the subject-specific properties at different body sites. This study focuses on cyclic uni-axial extension of the upper arm skin, using unpublished data collected by Chambert et al. Our analysis shows that a two-layer finite element model allows representing all relevant features of the observed mechanical response to the imposed external loading, which was composed, in this contribution, of four loading-sustaining-unloading cycles. The Root Mean Square Error (RMSE) between the calibrated model and the measured Force-time response was  $8.84 \times 10^{-3}$  N. Our biphasic model represents a preliminary step toward investigating the mechanical conditions responsible for the onset of injury. It allows for the analysis of changes in Interstitial Fluid (IF) pressure, flow, and osmotic pressure, in addition to the mechanical fields. Future work will focus on the interaction of multiple biochemical factors and the complex network of regulatory signals.

**Keywords:** Human skin; Poro-elasticity; Time-dependent; FEniCSx

## Introduction

The skin is a multi-layered structure, the largest organ in the human body. It is vital for protecting the tissues from pollutants, bacterial infections, and sunlight. Knowledge of the ways the skin behaves under mechanical load is crucial for various applications such as skin surgery (Ogawa et al. 2012), diagnostic tools for skin pathology (Jasaitiene et al. 2011), design of medical devices or devices for personal care or trans-epidermal drug delivery with micro-needles or micro-jets (Waghule et al. 2019), and treatment monitoring of skin diseases (Dubois et al. 2018). Several *in vivo* measurement tests have been specifically designed to accurately determine the behaviour of skin tissues, such as the suction test (Alexander and Cook 1977; Humbert et al. 2017), torsion test (Agache et al. 1980; Humbert et al. 2017), compressive test (Bosboom et al. 2001; Oomens et al. 1985; Oomens et al. 1987b; Pailler-Mattéi and Zahouani 2004; Tran 2007; Zhang et al. 1994), indentation test (Pailler-Mattéi and Zahouani 2004), and longitudinal extension test (Humbert et al. 2017; Khatyr et al. 2004).

In particular, these studies considered a broad spectrum of models and have shown the strain rate dependency of skin mechanical properties (Eshel and Lanir 2001; Humbert et al. 2017; Shergold et al. 2006). Yet, attempts to characterise the time-dependence of the mechanical response of skin tissue to external loading generally assume a viscoelastic formulation (Flynn et al. 2010; Gerhardt et al. 2012). These models ignore the structural bi-phasic nature of the tissue.

Poroelastic constitutive models have been proposed as an alternative to viscoelastic models to capture the time-dependent response of soft tissues. Initially introduced for soil mechanics, these models are largely used in biomechanics. They allow the coupling of the solid behaviour of a scaffold with the fluid mechanics of one or more fluids saturating the solid medium and have been adapted to the biomechanical field (Argoubi and Shirazi-Adl 1996; Franceschini et al. 2006; Gimlich et al. 2019; Hosseini-Farid et al. 2020; Peyrounette et al. 2018; Sciumè et al. 2014a; Siddique et al. 2017). Porous media models represent a promising approach for integrating multiscale/multiphysics data to probe biologically relevant phenomena at smaller scales and embed relevant mechanisms at larger scales. This is particularly the case with the interaction of multiple biochemical factors (enzymes, growth factors, hormones, proteins) and the complex network of regulatory signals, which determine

## 8 *In vivo* evaluation of a single-compartment model

tissue characteristics and their evolution in processes such as growth and remodelling (Eskandari and Kuhl 2015), ageing, and the onset of injuries such as pressure ulcers (Gefen et al. 2022; Sree et al. 2019a).

A number of research teams have proposed utilising this approach to characterise and model the mechanical response of various tissues, including the brain (Budday et al. 2019; Carrasco-Mantis et al. 2023; Greiner et al. 2021; Hervas-Raluy et al. 2023; Hosseini-Farid et al. 2020; Urcun et al. 2023; Urcun et al. 2022), the liver (Ricken and Lambers 2019), the meniscus (Bulle 2022; Kazemi et al. 2013; Uzuner et al. 2022; Uzuner et al. 2020), and muscle tissue (Lavigne et al. 2022b). In these studies, the biological tissues were modelled as biphasic systems with the behaviour governed by the properties of the porous solid and the fluid occupying the pores. This was based on the balance of mass and momentum conservation equations.

Although the theory of poromechanics has been extensively applied in other soft biological tissues, only a few studies have been published for skin, and these were limited to *in silico* and *ex vivo* studies.

One of the first contributions was made by (Oomens et al. 1987a). The authors developed a poroelastic model of the skin based on the large strain theory, using a hyper-elastic (Tong and Fung 1976) constitutive model for the solid phase and a nonlinear strain-dependent permeability. The model was implemented in a Finite Element model to simulate the quasi-static indentation response of *ex vivo* porcine skin (Oomens et al. 1987b). More recently, Weir Weiss et al. 2023 developed a custom setup to apply a pressure-driven fluid flow across skin tissues. The resulting flow rate and cross-sectional image acquisition by optical coherence tomography (OCT) combined with digital image correlation (DIC) were used to calculate the internal strains within the tissue and to characterise *ex vivo* local strain and permeability of porcine skin tissue under compression loading. Likewise, Wahlsten et al. 2023 analysed the mechanical behaviour of skin from the cellular to the tissue length scale through dedicated experiments to resolve these discrepancies. Of particular interest, the same team also conducted uni-axial monotonic, cyclic, and relaxation experiments on a total of 37 human and 33 Murine skin samples (Wahlsten et al. 2019). They showed that skin volume is significantly reduced due to tensile elongation. However, the loading was not controlled and applied by a human operator. To the best of the authors' knowledge, little application of biphasic constitutive modelling of the skin *in vivo* has been proposed. Yet, the development of *in vivo*

procedures is crucial to determine subject-specific properties at different body sites given different loading conditions.

In this study, we focus on the cyclic uni-axial extension of the upper arm skin from unpublished data previously collected by Chambert et al. under conditions similar to those described in Chambert et al. 2019. The relaxation phenomenon observed in this experiment is of great interest to the poromechanical approach. Indeed, poromechanics takes into account the pressurisation of interstitial fluid in the different layers of the skin, which makes an important contribution to this relaxation during sustained tensile loading.

The experimental data are presented followed by the poromechanical model. The values of the parameters are then discussed based on the physiological and modelling literature. The process of identifying the physical parameters is explained and the numerical response of the model over time is shown. This study is an encouraging step towards the use of poromechanics for *in vivo* skin modelling. The authors hope that it will encourage experimentalists to improve their experimental protocols and measure other quantities (e.g. fluid pressures, fluid flows) further to test the reliability of porous media modelling approaches.

## Materials and methods

### Portable extensometer description

A portable in-house extensometer (Figure 14) has been used to perform an uniaxial *in vivo* tensile test while limiting disturbances from the skin surrounding the region of interest (Chambert et al. 2019; Jacquet et al. 2017a; Jacquet et al. 2017b). The portable extensometer consists essentially of an electric motor, two guiding pillars and two double pads and a rectangular frame. The two double pads, one fixed to the frame and the other one is actuated by an electrical motor, allow for the application of imposed displacement to the skin. Each double pad, made up of a central pad (also called measuring pad) surrounded by a 'U-shaped' guarding pad, is assumed to be rigidly attached to the skin surface by means of an adhesive used in dermatological surgery. The pads are initially separated by a length of  $L_0 = 36$  mm. The LVDT displacement sensor provides the position of the mobile pad. The force sensor is a

## 8 In vivo evaluation of a single-compartment model

bronze-beryllium cantilever beam equipped with strain gauges stuck on the sensor. The measured reaction force corresponds to the force applied to the central pad. A detailed description of the experimental device can be found in Jacquet et al. 2017b.

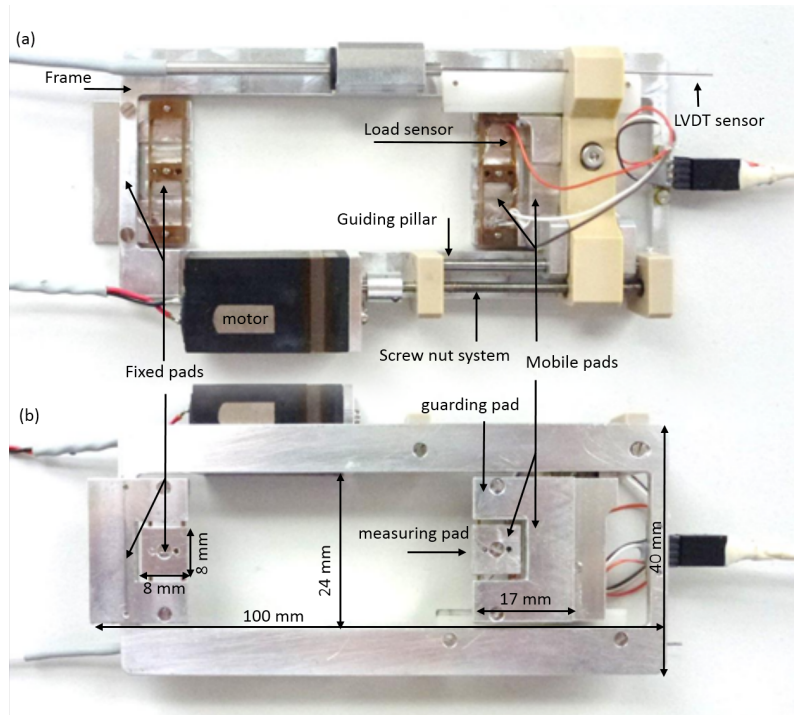


**Figure 14:** Portable extensometer: (a) top view; (b) bottom view (from Jacquet et al. 2017b with permission).

## Data Acquisition

Using an ultra-light, in-house portable extensometer described in Jacquet et al. 2017b, Chambert et al. have carried out uni-axial extension measurements on the left upper arm (dorsal aspect) of a 22-year-old female. The extensometer is a prototype consisting of two sets of square pads: one static and one mobile. Each set includes a central pad, where measurements are taken, and a surrounding 'U-shaped' guarding pad. The guarding pad is designed to minimize disturbances from the surrounding skin in the region of interest by applying the same extension to the neighbouring skin, thereby ensuring uni-axial extension. Further details about the device, along with images of the extensometer, can be found in Jacquet et al. 2017a; Jacquet et al. 2017b and Chambert et al. 2019.

During this experimental campaign, four loading-sustaining-unloading repetitions (relaxation tests) were performed at a controlled speed of  $1 \text{ mm s}^{-1}$  to exhibit the time-dependent properties (Figure 15). The unloading-loading step between the third and fourth cycles was made slightly different, and the real displacement was recorded all along the experiment using a LVDT sensor, providing the exact loading.

The reaction force was monitored every 0.01 s, and the maximum applied displacement was set to 9.45 mm (Figure 15). This reaction force corresponds to the difference between the current stress state and the pre-stressed state of the skin. The initial negative reaction force (and the resulting force after unloading) is believed to arise from the installation of the extensometer on the skin. This can be likened to a pre-stress state, which is discussed in the section 9.3. All measurements have been made in temperature and hygrometry-regulated rooms ( $20\text{--}22^\circ\text{C}$ , 40–60% relative humidity) after a rest time of 20 min. The experimental data is accessible in the github as supplementary material.

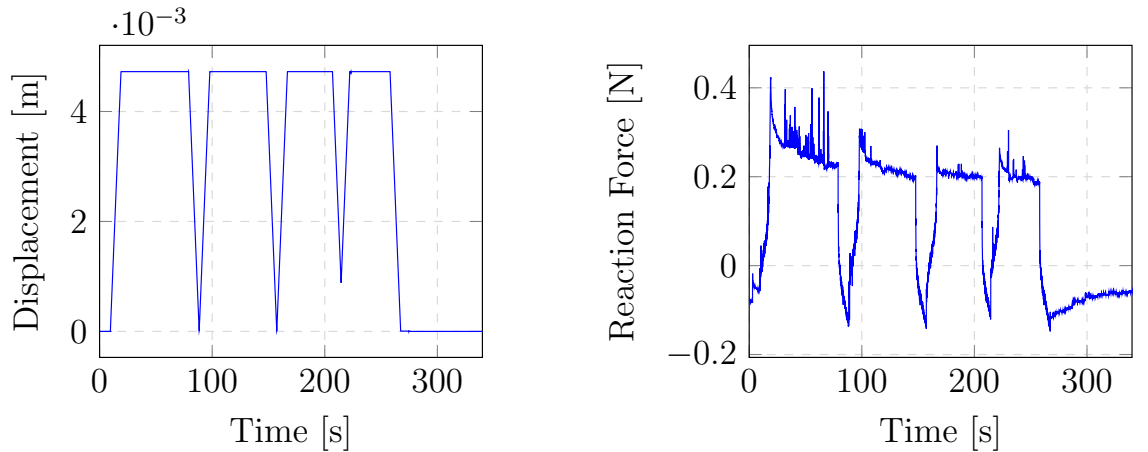


**Figure 15:** Imposed displacement (half of the displacement extracted from the LVDT sensor for symmetry purpose in the model) and resulting reaction force.

## Geometrical modelling

Two curved layers were considered, namely the cutis (composed of the epidermis and the dermis) and the subcutis (defined as the hypodermis) (Figure 16). The model is a low fidelity bilayered model assuming only different material properties without relative displacement between the layers. Therefore we assume that the cutis and

## 8 In vivo evaluation of a single-compartment model

the subcutis are strongly related and displace together at the interface, including stress continuity.

Before the experiment, an echography was performed on the dorsal upper arm using a commercial device (Aixplorer, SuperSonic Imagine, France) with a linear ultrasound probe of 8 MHz central frequency (SuperLinear SL 15-4). The echography parameters used in this study did not permit the identification of the subcutis boundaries, so the image was utilised solely to measure the thickness of the cutis. A thickness of approximately 2 mm was identified for the cutis, based on the image scale. The subcutis thickness was defined based on prior studies (Birkebaek et al. 1998; Mellor et al. 2004). Therefore, a curved bi-layer geometry was considered with a thickness of 2 mm for the cutis and 8 mm for the subcutis. The radius was fixed to 48 mm according to the previous work of Elouneg 2023, and based on the measured perimeter of the arm.

Considering the geometry and the boundary conditions (especially of the in-house extensometer geometry and the uni-axial aspect of the experiment), two axes of symmetry were introduced. The symmetries are represented by the harsh surfaces in Figure 16. A mesh of 11,310 tetrahedral elements was generated using the gmsh software (Geuzaine and Remacle 2020) and a local refinement close to the in-house device was performed. Given the strong compatibility between the gmsh and FEniCSx environments, the facets, as well as the elements, were tagged at this stage to apply the boundary conditions. The distances on the x- and y- directions were artificially increased to limit the risks of edge effects in the region of interest, *i.e.* the region covered by the in-house device.

Another refined mesh of 43,767 elements was also created to assess the trustworthiness of the computed fields. A root mean square error of  $8.01 \times 10^{-3}$  N was found between the resulting reaction forces obtained by the two meshes. This difference was deemed acceptable given the required increase in computation time which changed from 1h45min to 22h06min with the same configuration of the computer. Hence, the mesh of 11,310 elements was considered for this study.

## Material modelling

During the experiment, the skin was stretched up to 25 %. This level of stretching goes beyond the hypothesis of small strains. Furthermore, previous studies highlighted the non-linear behaviour of the skin with its “J-shaped” stress-strain curve (Joodaki and Panzer 2018; Yazdi and Baqersad 2022).

A poro-hyper-elastic model was therefore assumed to model the mechanical behaviour of skin tissue. Since the replicated experiment was uni-axial (and supposed to be aligned with the fibre direction of the dermis), for sake of simplicity, the material was assumed to be isotropic, whereas the skin response is known to be transversely isotropic (Annaidh et al. 2012; Elouneg et al. 2023; Joodaki and Panzer 2018; Kalra and Lowe 2016; Khatyr et al. 2004; Yazdi and Baqersad 2022).

The model is based on the equations of mass and momentum conservation of the fluid and solid phases (Equations (69) and (70)) as described in Lavigne et al. 2023b. The two phases considered in the model are: the solid phase (collagen-elastin matrix, structural cells), the fluid phase (interstitial fluid). The primary variables in the problem are the pressure in the interstitial space and the solid displacement (assuming the skin is saturated with a single fluid). Considering  $\Omega_c$  for the cutis and  $\Omega_s$  for the subcutis:

$$\left( \frac{\varepsilon_i^l}{K_i^l} + \frac{1 - \varepsilon_i^l}{K_i^s} \right) \frac{D^s p^l}{Dt} + \nabla \cdot \mathbf{v} - \nabla \cdot \left( \frac{k_i^\varepsilon}{\mu^l} \nabla p^l \right) = 0 \text{ on } \Omega_i, \quad i \in [c, s], \quad (69)$$

$$\nabla \cdot \mathbf{t}^{\text{tot}} = 0 \text{ on } \Omega_i, \quad i \in [c, s], \quad (70)$$

where  $\frac{D^s f}{Dt} = \frac{\partial f}{\partial t} + \nabla f \cdot \mathbf{v}^s$  is the material derivative,  $\varepsilon_i^l = \frac{\text{Liquid Volume}}{\text{Total Volume}}$  is the porosity of the medium,  $K_i^l$  and  $K_i^s$  respectively denotes the liquid and solid bulk moduli,  $p^l$  is the interstitial pressure,  $\mathbf{v}$  is the solid velocity,  $k_i^\varepsilon$  corresponds to the intrinsic permeability,  $\mu^l$  is the fluid viscosity, and  $\mathbf{t}^{\text{tot}}$  is the total stress tensor.

The total stress tensor is expressed as  $\mathbf{t}^{\text{tot}} = \mathbf{t}^{\text{eff}} - \beta p^l \mathbf{I}_d$ ,  $\mathbf{t}^{\text{eff}}$  being the effective stress in the sense of porous media mechanics, and assuming that the Biot coefficient ( $\beta$ ) is close to one as typically done in biomechanics (Lavigne et al. 2023b). This assumption results from a bulk modulus of the solid phase  $K_i^s$  largely higher than the overall bulk modulus of the porous scaffold (Sciumè 2021). To describe the solid behaviour, a Neo-Hookean hyper-elastic potential has been considered because of the

## 8 In vivo evaluation of a single-compartment model

straightforward relationship of its parameters (the Lamé coefficients by  $\mu_i = \frac{E_i}{2(1-\nu_i)}$  and  $\lambda_i = \frac{E_i\nu_i}{(1+\nu_i)(1-2\nu_i)}$  in  $\Omega_i$ ) with the Young's modulus ( $E_i$ ) and Poisson's ratio ( $\nu_i$ ). This choice was further supported by the ease of interpretation as such energy formulation allows for a direct evaluation of usual elastic parameters. Other strain-energy density functions (a comparison between strain-energy functions for the brain has been proposed in Budday et al. 2019 can be easily introduced in FEniCSx such as performed for the volumetric part in Lavigne et al. 2023b).

Let  $\mathbf{F}$  denote the deformation gradient (Equation (71)),  $J$ , its determinant and  $\mathbf{I}_d$  the identity matrix. The deformation gradient  $\mathbf{F}$  reads

$$\mathbf{F} = \mathbf{I}_d + \nabla \mathbf{u}, \quad (71)$$

where  $\mathbf{u}$  is the displacement of the solid phase.

From the deformation gradient  $\mathbf{F}$ , one can further introduce the right Cauchy-Green stress tensor  $\mathbf{C}$  and its first invariant  $I_1$  (Equations (72) and (73)).

$$\mathbf{C} = \mathbf{F}^T \mathbf{F}, \quad (72)$$

$$I_1 = \text{tr}(\mathbf{C}), \quad (73)$$

The theory of hyper-elasticity defines a potential of elastic energy  $W(\mathbf{F})$  which can be expressed as the combination of an isochoric component and a volumetric component (Horgan and Sacco 2004; Marino 2018; Simo 1988).

$$W(\mathbf{F}) = \tilde{W}(I_1, J) + U(J), \quad (74)$$

where  $\tilde{W}(I_1, J)$  is the isochoric part and  $U(J)$  the volumetric one. A compressible formulation of the Neo-Hookean strain-energy potential from (Horgan and Sacco 2004; Pence and Gou 2014) has been introduced as:

$$\tilde{W}(I_1, J) = \frac{\mu_i}{2}(I_1 - \text{tr}(\mathbf{I}_d) - 2 \ln J), \quad (75)$$

The volumetric part proposed in Doll and Schweizerhof 2000 has been adopted:

$$U(J) = \frac{K_i^s}{2}(\ln J)^2, \quad (76)$$

Finally, from the potential (Equation (74)) derives the first Piola-Kirchhoff stress tensor. Using Nanson's formula we obtain the effective Cauchy stress such that:

$$\mathbf{t}^{\text{eff}} = J^{-1} \frac{\partial W}{\partial \mathbf{F}} \mathbf{F}^T, \quad (77)$$

A same constitutive law is introduced for the cutis ( $\Omega_c$ ) and the subcutis ( $\Omega_s$ ). To introduce the heterogeneity of the material parameters, they are mapped in the space within the considered finite element software FEniCSx. For the numerical introduction, please refer to the GitHub repository where the codes are made openly accessible and consult the tutorial by Lavigne et al. 2023b for additional insights on implementing poromechanics in FEniCSx.

## Boundary and Initial conditions

The poro-hyper-elastic problem is solved using a mixed space (Lavigne et al. 2023b) allowing for the simultaneous solving of displacement (which typically represents the solid deformation) and pressure (which represents the fluid flow or pore pressure) within the same computational framework. Therefore, boundary conditions must be introduced for all the primary unknowns, namely the solid displacement of the scaffold and the interstitial pressure (Figure 16). The mesh not only covers the region of interest but has also been greatly increased to avoid side effects, therefore accounting for a no-flow condition at the boundaries (absence of leakage). No external forces were applied. The amplitude of the displacement applied to the model corresponds to the half of the effective displacement of the experiment recorded by the LVDT sensor. According to Elouneg et al. 2023, the longitudinal displacement is linearly distributed along the central axis, with the displacement at the centre being half of that imposed on the moving pad. The displacement was applied to the patch and its guide pad (limiting rotational effects resulting from the orientation of the Langer lines in the skin). It is assumed that the mechanical problem can be addressed using two planes of symmetry ( $x, z$ ) and ( $y, z$ ) (Figure 16), although this approach does not fully capture the actual geometry and loading conditions. Dirichlet boundary conditions were also introduced on the symmetry planes and the vertical displacement of the bottom surface (Figure 16). The two other lateral surfaces were left free to deform to simulate semi-infinite boundary conditions, thereby reducing the risk of edge effects on the computed reaction force. Unlike the symmetry planes, adding

## 8 In vivo evaluation of a single-compartment model

Dirichlet boundary conditions was not considered appropriate, as no displacement measurements were taken outside of the extensometer. Imposing such conditions could have interfered with the "skin reorganisation" effect.

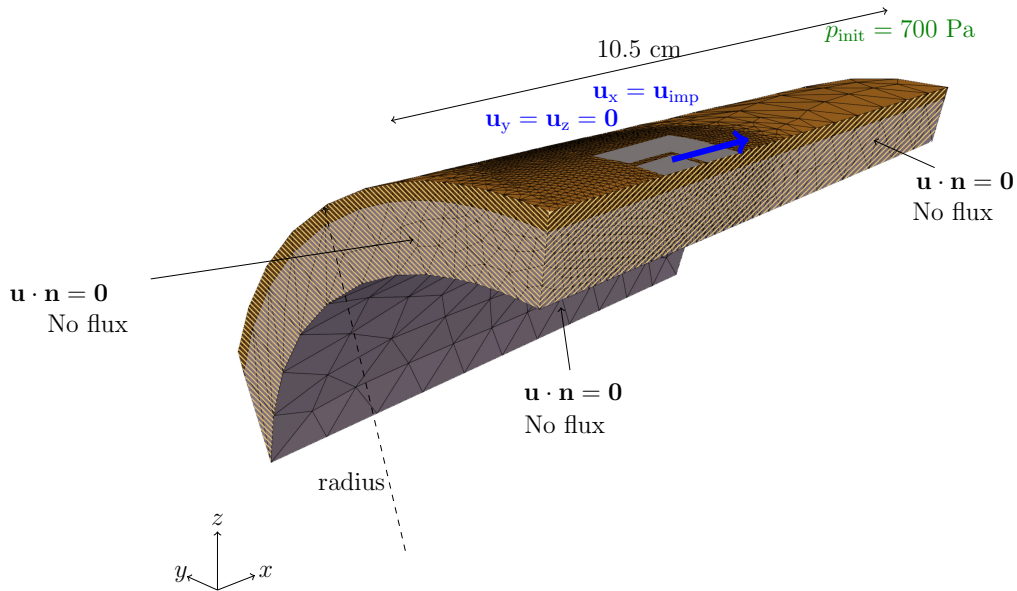


**Figure 16:** Mesh, boundary and initial conditions of the problem. The skin is assumed saturated by a single fluid. The initial pressure is set to 700 Pa to account for the homeostatic pressure. No flux is allowed on the external surfaces. Furthermore, two planes of symmetry are introduced ( $(x, z)$  and  $(y, z)$ ) leading to a normal displacement imposed to zero ( $\mathbf{u} \cdot \mathbf{n} = \mathbf{0}$ ). These are the hashed plans. The vertical displacement is blocked on the bottom surface. The other external surfaces are set free to move. The “u-shaped” patch and the patch itself (in gray) have an imposed displacement along the  $x$ -direction.

In the absence of experimental data regarding the *in vivo* pre-strain, no pre-stress nor pre-strain was introduced in the model. Regarding initial pressure of the interstitial fluid, experimental literature provides a wide range of physiological values: 2144 Pa for leg's subcutis, averaged from 19 healthy patients, in Hargens et al. 1981; from  $-670$  to  $+536$  Pa for palm hand's subcutis of 7 healthy patients, measured by two techniques, micro-puncture and wick-in-needle, in Wiig and Noddeland 1983. Additionally, repetitive measurements on pig's skin in Samant and Prausnitz 2018, give the mean osmotic pressure of 725 Pa (this value is deduced from the increase of initial ionic strength of 4.03448 fold which provokes an increase of 2200 Pa of the homeostatic pressure). An initial guess of 700 Pa has been chosen, and the parameter has been included in the sensitivity analysis.

## Calibration procedure

The poro-hyper-elastic model was implemented in the open-source environment FEniCSx. The implementation process is the same as the one developed in Lavigne et al. 2023b. The corresponding codes are available on github (link here). To limit the effect of local minima during the calibration procedure, only the Young moduli and permeabilities were calibrated for each layer. The other parameters used were fixed according to the literature (see section 8.3). To support this choice, the Sobol' indices have been computed and results are reported in Appendix A.

A cost function based on the root mean square error (RMSE) of the reaction force ( $RF$ ) was introduced (Equation (78)). The calibration was only performed in the first 145 seconds to assess the predictive potential of the model. Then, the identified parameters are used to model the full experiment. The cost function was only computed during the time steps of sustained load.

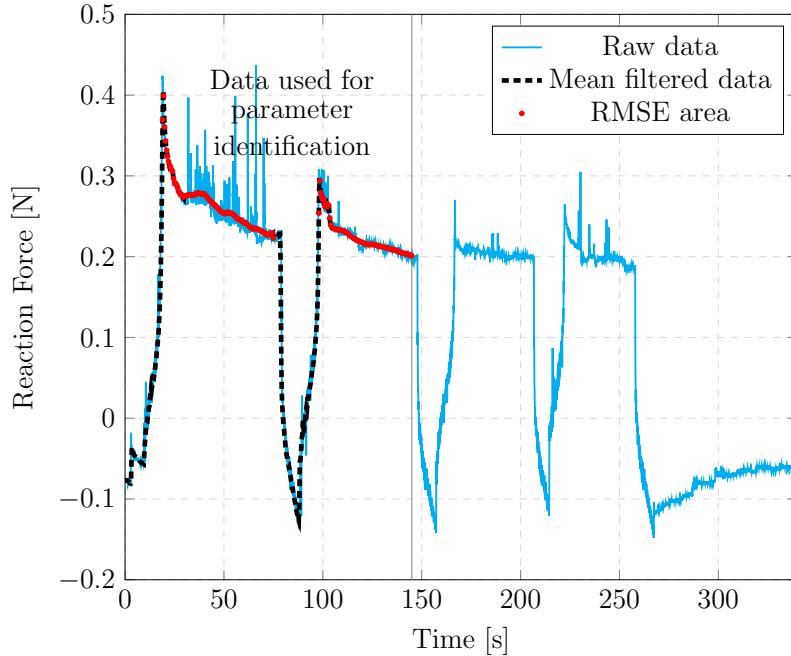


**Figure 17:** Experimental and filtered curves of reaction force versus time. Due to the presence of noise in the raw data (blue), the calibration area was first filtered (black dashed curve) and the cost function was only evaluated during the sustained displacement (red dots).

$$\text{RMSE} = \sqrt{\frac{\sum_{t \in [20, 75]} (RF - RF_{\text{theo}})^2 + \sum_{t \in [98, 140]} (RF - RF_{\text{theo}})^2}{\text{Number of steps}}} \quad (78)$$

A controlled random search (CRS) with local mutation (Kaelo and Ali 2006) from the NLOPT library was chosen. More specifically, the lower and upper bounds for  $[E_c, E_s, k_c, k_s]$  were respectively set to  $[10 \text{ kPa}, 10 \text{ kPa}, 1 \times 10^{-16} \text{ m}^2, 1 \times 10^{-16} \text{ m}^2]$  and  $[500 \text{ MPa}, 500 \text{ MPa}, 1 \times 10^{-10} \text{ m}^2, 1 \times 10^{-10} \text{ m}^2]$ . Since the parameters' ranges differ from several orders, each parameter was prior normalised with regard to the initial guess to have same order of magnitudes between the optimised unknowns. The initial population size was set to  $3 \times (NN + 1)$ , where  $NN$  is the number of parameters ( $NN = 4$  in the present case). This initial population corresponds to random initial points in the search space differing from the input initial guess (15 in the present case). A stopping criterion of 250 evaluations was added, and the optimal solution was kept. Once the calibration was performed, the set of parameters was applied to reproduce the experiment for its complete duration. The algorithm was executed several times, and the result with the lowest RMSE was selected. To ensure convergence, we verified that the material parameters obtained from all calibrations remained within the same order of magnitude, confirming the stability and robustness of the optimization process.

## Initial parameters values

Experimental observations and *in silico* calibration techniques (Annaidh et al. 2012; Gallagher et al. 2012; Jacquet et al. 2017a; Khatyr et al. 2004; Ottenio et al. 2015) have reported a wide range of values for the Young Modulus ranging from 5 kPa to 196 MPa (Oomens et al. 2017). The models proposing multi-layer analysis, such as the one proposed by Han et al. 2023, assume that the cutis is stiffer than the subcutis. This has further been confirmed by the experimental campaigns performed by Connesson et al. 2023 and Pailler-Mattei et al. 2008. As a first guess, the Young's moduli were therefore set to  $E_c = 1.5 \times 10^6 \text{ Pa}$  and  $E_s = 5 \times 10^5 \text{ Pa}$ .

Similarly, a wide domain of values has been reported for the permeability of the medium with values ranging from  $1 \times 10^{-16} \text{ m}^2$  to  $1 \times 10^{-11} \text{ m}^2$  (Levick 1987; Lucio et al. 2023; Oftadeh et al. 2018; Swartz and Fleury 2007; Wahlsten et al. 2019;

Zakaria et al. 1997). The initial permeabilities were hence set to  $k_c = 1 \times 10^{-14} \text{ m}^2$  and  $k_s = 1 \times 10^{-13} \text{ m}^2$ .

Concerning the other material parameters, namely the interstitial fluid viscosity, the Poisson ratio, and the porosity, their value was fixed according to the literature. Sowinski et al. 2021 gathered expected viscosity ranges for different human fluids: the cerebrospinal fluid has a viscosity ranging between 0.7-1.0 mPa s, blood between 3.0-67.7 mPa s, ascitic fluid between 0.5-1.5 mPa s. Bera et al. 2022 further reported an interstitial fluid dynamic viscosity up to 3.5 mPa s. Swartz and Fleury 2007 respectively reported viscosity values for the plasma, lymph, and synovial fluids of 12 mPa s, 15-22 mPa s and  $10^2\text{-}10^5$  mPa s. The authors fixed the interstitial fluid viscosity at  $\mu^l = 5 \text{ mPa s}$ . The literature still lacks a clear value of the Poisson ratio, especially for multi-layer models. Therefore, the authors tried to be consistent with values commonly used (Levy et al. 2015; Oomens et al. 1987b; Pailler-Mattei et al. 2008; Raveh Tilleman et al. 2004) and assumed a solid scaffold with a compressible behaviour for both phases with a higher Poisson ratio value of the cutis of 0.48 and a more compressible subcutis of 0.3. Finally, Samant and Prausnitz 2018 found that the dermis contains approximately 24% of free moving fluid. The hypodermis is thought to be more porous. The values of the porosities for the cutis and subcutis were respectively fixed at 20% and 40%. The initial guess for the parameters is reported in Table 10.

<b>Cutis Parameters</b>	Initial Value	Unit
Young's modulus ( $E_c$ )	$1.5 \times 10^5$	Pa
Poisson's ratio ( $\nu_c$ )	0.48	-
Intrinsic permeability ( $k_c$ )	$4 \times 10^{-14}$	$\text{m}^2$
<i>Initial Porosity (<math>\varepsilon_c^l</math>)</i>	0.2	-
<b>Subcutis Parameters</b>	Value	Unit
Young's modulus $E_s$	$1 \times 10^5$	Pa
Poisson's ratio ( $\nu_s$ )	0.3	-
Intrinsic permeability ( $k_s$ )	$3 \times 10^{-13}$	$\text{m}^2$
<i>Initial Porosity (<math>\varepsilon_s^l</math>)</i>	0.4	-
<b>Fluid phase</b>	Value	Unit
<i>IF viscosity (<math>\mu^l</math>)</i>	$5 \times 10^{-3}$	Pa s

**Table 10:** Initial mechanical parameters for the bi-compartment model. Italic values refer to the fixed parameters during the calibration procedure.

## Results

Table 11 provides the calibrated set of parameters. The minimal cost function value was  $8.84 \times 10^{-3}$  N (which corresponds to approximately 2% of the peak reaction force).

Cutis Parameter	Value	Unit
Young modulus ( $E_c$ )	$684 \times 10^3$	Pa
Intrinsic permeability ( $k_c$ )	$9.43 \times 10^{-15}$	m <sup>2</sup>
Subcutis Parameter	Value	Unit
Young modulus ( $E_s$ )	$47.8 \times 10^3$	Pa
Intrinsic permeability ( $k_s$ )	$5.03 \times 10^{-13}$	m <sup>2</sup>
Cost Function	Value	Unit
RMSE	$8.84 \times 10^{-3}$	Pa

**Table 11:** Calibrated parameters for each layer and optimal cost function value.

The fluid velocity is computed all along the simulation from Darcy's law (Equations (79)) to evaluate the fluid displacement within the tissue during the experiment.

$$v^l = -\frac{k}{\mu\varepsilon} \nabla p + v^s \quad (79)$$

Figure 18 shows the evaluated response on the complete experiment. As reflected by the optimal RMSE value, even if a difference in reaction force for negative values is observed and is constant over time (discussed in the next section), the model response allows reproducing the overall behaviour of the reaction force. Especially, it is worth noting that the model was able to recreate the final reflux even though it was not part of the calibration domain. It should be noted that the model provides better predictions for the relaxation phases than the loading and unloading phases.

To obtain insight about the physics, Figure 19 shows the displacement map, the pressure map, and the interstitial fluid flux at different time steps. The authors propose the following interpretation, supporting the time-dependent behaviour of the reaction force from the porous structure. When stretching the skin, it is assumed that the pores get dilated and, therefore, the fluid tends to be drawn in. This was observable on the pressure map through negative values of the interstitial fluid pressure. Conversely, the pores tend to close near the edge of the u-pad and the fluid is expelled which results in a positive interstitial pressure.

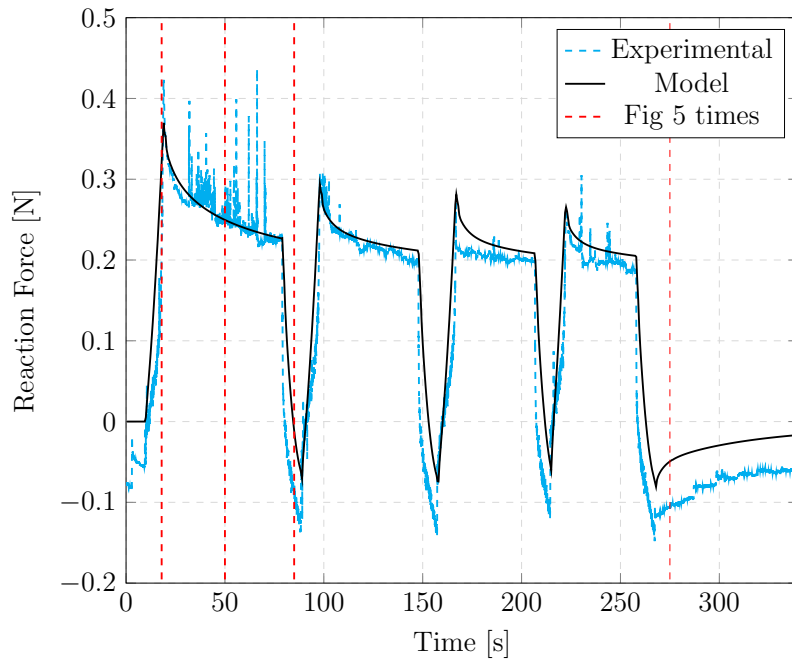


**Figure 18:** Evaluated response of the model (plain) superimposed with the experimental reaction force (dashed) for all the cycles. The model was able to reproduce the reaction force for the four cycles of the experiment. The vertical dashed lines represent the time steps shown in Figure 19.

During a sustained phase, the tissue tends to slowly recover its homeostatic state. When releasing the tissue, a strong reflux occurs with high positive pressure values: the fluid retrieves its initial place. Finally, the last reflux slowly comes back to a homogenised pressure state within the tissue.

It is furthermore worth noting that, due to a lower value of the permeability in the cutis phase, most of the fluid flow is concentrated in the subcutis for all the phases.

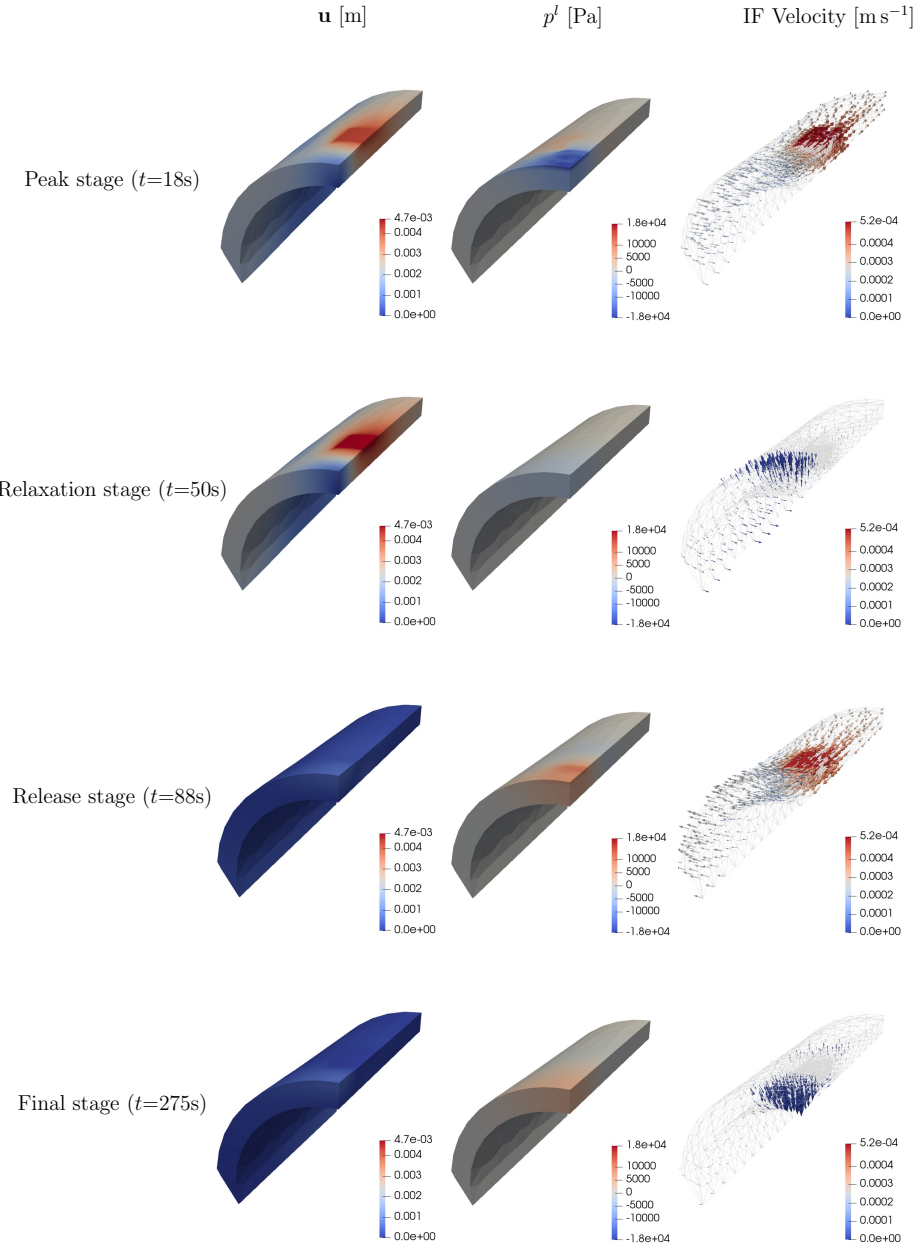


**Figure 19:** From left to right: displacement magnitude, interstitial fluid pressure, interstitial fluid velocity maps. The results represent the maximum load time ( $t = 18\text{ s}$ ), a sustained phase ( $t = 50\text{ s}$ ), a relaxed phase ( $t = 88\text{ s}$ ) and the final reflux ( $t = 275\text{ s}$ ). When stretching the skin, the fluid tends to be drawn in, resulting in negative values of the interstitial fluid pressure. Conversely, the pores tend to close near to the edge of the u-pad and the fluid is expelled which results in a positive interstitial pressure. During a sustained phase, stabilises towards its homeostatic state. When releasing the tissue, a reflux occurs. The fluid flow images are further included in Appendix B for the ease of the reading. A description of the fluid movement is further introduced.

## Discussion

Motivated by the limited *in vivo* application of biphasic constitutive modelling for parameter identification, a poro-hyper-elastic model has been implemented in the FEniCSx environment and calibrated to reproduce the time-dependent mechanical response of upper-arm skin under cyclic uni-axial extension including the final reflux phase. The Root Mean Square Error between the calibrated model and the measured Force-time response was  $8.84 \times 10^{-3}$  N. The calibrated parameters align with previously reported values, confirming that the subcutis is softer than the cutis (section 8.3). The Young's modulus of the cutis ( $E_c = 684$  kPa) maintains the body geometry, being almost 10 times stiffer than the subcutis. Specifically, the Young's modulus of the cutis ( $E_c = 684$ kPa) functions to absorb external mechanical loads. Interstitial fluid presence contributes to load cushioning and sustains the time-dependent mechanical response. A single fluid compartment was considered for each layer, and permeability was calibrated to reflect interstitial fluid movement. The cutis' intrinsic permeability is  $9.43 \times 10^{-15}$  m<sup>2</sup>, while the subcutis permeability is 50 times higher at  $5.03 \times 10^{-13}$  m<sup>2</sup>. As a result, the pressure distribution observed in Figure 19, especially at the corners differs between the cutis and the subcutis. The pressure magnitude is higher in the cutis, and this is due to the heterogeneity in permeability across layers: a smaller permeability results in a higher pressure value.

However, this study has limitations. The first one is related to the noise from the sensors which were firstly designed for keloids (Chambert et al. 2019), which are stiffer than healthy skin. Furthermore, the authors recognise that the current study is based on a single mechanical trial conducted on one subject, serving as an initial investigation to validate the proposed approach. To strengthen the robustness of the findings, future research will involve an expanded sample size and additional trials. Specifically, this patient presented a keloid on her right upper arm and this experimental data was acquired on the other arm to compare the mechanical properties between the keloid-affected area and the healthy skin. This experimental data had not been utilised further and thus provided an opportunity for evaluating the model. Despite this, the study demonstrates the poro-hyper-elastic model's *in vivo* performance in loading-sustaining-unloading tests, providing valuable insights into the dissipative effect of human skin. It is however difficult to distinguish between viscoelastic and poroelastic dissipation when only limited boundary condition infor-

## 8 In vivo evaluation of a single-compartment model

mation is known. Future experimental campaigns should consider testing different strain rates to evaluate the viscoelastic contribution in the mechanical response. Likewise, the permeability values obtained in this article should be understood with a high uncertainty, as their sensitivities are low (see Appendix) and the range of values reported in the literature is wide.

Furthermore, a difference is observed for negative values of the reaction force. We believe that the negative forces are likely due to prestress introduced when the experimental device is glued to the skin. This prestress could arise from the initial tension or deformation caused by the adhesive bond between the device and the skin. However, no pre-stress was introduced and the gap in force is constant for all the minimal values. Overlooking the pre-stress - which may impact the results of a hyper-elastic formulation, the authors however chose not to set to zero the first values to limit misinterpretation of the results. This might impact the Young modulus value, but the global conclusions are not expected to change.

Only two layers were considered in the model: the cutis and the subcutis, similar to the approach taken by Connesson et al. 2023. The cutis, however, can be further subdivided into the epidermis and dermis, with the epidermis primarily composed of cells and the dermis consisting of cells embedded in an extracellular matrix. Given the thickness of each layer and the scale of the geometry under consideration, modelling them as separate layers would significantly increase the number of elements in the mesh, thereby raising the computational cost. This supports the decision to combine them into a single layer. Future studies could explore the subdivision of this layer and investigate its impact on the mechanical response. Integrating ANN-based techniques with our model could help improve computational efficiency and allow for this more detailed multiscale description (Dehghani and Zilian 2023). Furthermore, the interaction between cutis and subcutis is handled through differing material properties rather than explicit displacement/stress boundary conditions. We acknowledge that this creates a lower-fidelity bilayered model but avoids introducing a new unknown in the problem (*e.g.* friction coefficient). Future study could focus on measuring the relative displacement between the layers during extension tests.

Additionally, the skin was stretched up to 25 %. As shown in Figure 19, while the subcutis layer follows the cutis, the deformation is not uniform throughout its depth; the extension test causes deformation that extends into the subcutis layer. Due to a

lack of experimental data, no adherence was modelled at the bottom of the subcutis, but this effect might be more pronounced if adherence were considered, potentially increasing shear within the tissue.

The model assumes isotropy due to the limited data available along other directions, as the experiment only provided measurements of axial force and displacement. However, the skin's fibrous nature suggests at least transversely isotropic behaviour, as supported by previous studies Annaidh et al. 2012; Elouneg et al. 2023; Joodaki and Panzer 2018; Kalra and Lowe 2016; Khatyr et al. 2004; Yazdi and Baqersad 2022. This assumption has implications for the results, as the model may not accurately capture the skin's behaviour in directions where significant anisotropy is expected—such as along the skin's fibres or in response to differential fluid flow.

Future work should focus on extending the model to account for anisotropy by incorporating directional dependencies in the material parameters. Specifically, material properties should vary based on the direction of preferred fluid flow and the orientation of the collagen-elastin fibres in the skin. Additionally, imaging techniques should be integrated to enhance parameter identification and improve the accuracy of the model.

Moreover, the selection of a more suitable hyper-elastic potential should be explored to better capture the mechanical response non-linearity during both the loading and unloading phases. Further developments could also include the introduction of a viscous transverse hyper-elastic phase, which would better accommodate the fast time constants observed in the system.

The model, tested against the *in vivo* data, shows promise, particularly in understanding tissue necrosis, pressure ulcer onsets, and prevention. Indeed, the aetiology of Pressure Ulcers (PUs) showed that multiple factors lead to the onset of such complications. Especially, a (PU) is assumed to result both from excessive loading and ischaemic damage, which occur at different time and length scales (Loerakker et al. 2011). Coupling with a second compartment, representative of microvasculature, could offer insights into biochemical and mechanical reactions during mechanical load application (Kremheller et al. 2019; Sciumè et al. 2013; Urcun et al. 2023; Urcun et al. 2021).

The encouraging results obtained in this preliminary work allow for the analysis of changes in IF pressure and flow and osmotic pressure, in addition to the mechani-

## *8 In vivo evaluation of a single-compartment model*

cal fields. It represents a first step towards investigating the mechanical conditions responsible for tissue characteristics and their evolution in processes such as growth and remodelling, ageing, and the onset of injuries such as pressure ulcers, this preliminary study focused on applying poromechanical models. More specifically, the proposed modelling approach potentially can pave the way for a better understanding of fibrosis phenomena such as keloid disorders by taking into account the time-dependent mechanical behaviour, which is not the case in recent literature (Elouneg 2023; Elouneg et al. 2021; Sutula et al. 2020).

## **Conclusion**

This paper aimed to evaluate a poromechanical model to reproduce unpublished data collected on *in vivo* human skin during extension tests. A complete framework to identify the time-dependent properties of the skin was introduced within the Open-Source environment FEniCSx. The calibration was performed on the first cycles of the experiment. The complete experiment was computed afterwards to evaluate the predictability capacity of the model. A good agreement has been found between the numerical and experimental responses. Furthermore, the identified mechanical parameters are relevant with the literature. This study therefore supports the use of a poro-mechanical model for the skin under extension testing. More experiments are however required with, for the IF phase, a better control on the boundary conditions and a better monitoring during the experiment. This would allow to distinguish between viscoelastic and poroelastic dissipation.

## **Acknowledgments**

This research was funded in whole, or in part, by the Luxembourg National Research Fund (FNR), grant reference No. 17013182. For the purpose of open access, the author has applied a Creative Commons Attribution 4.0 International (CC BY 4.0) license to any Author Accepted Manuscript version arising from this submission. The present project is also supported by the National Research Fund, Luxembourg, under grant No. C20/MS/14782078/QuaC and the French National Research Fund (ANR) under grant No. ANR-21-CE45-0025 for the project S-KELOID. The experimental

part of this work has been achieved in the frame of the EIPHI Graduate school (contract "ANR-17-EURE-0002")

## Declarations

**Competing interests:** The authors declare that they have no known competing financial interests or personal relationships that could have appeared to influence the work reported in this paper.

**Supplementary material:** The python codes corresponding to the FEniCSx models and the experimental data of this article are made available on the following link: [https://github.com/ThomasLavigne/Skin\\_porous\\_modelling.git](https://github.com/ThomasLavigne/Skin_porous_modelling.git).

## Appendix A: Sobol' indices

Sobol' indices were computed for the poromechanical material parameters and the initial IF pressure. More precisely, a 'reference' evaluation was computed and the reaction force was recorded. Each parameter was then moved by 10% forward and backward, and the resulting reaction force was saved.

The error metric defined to evaluate the impact of the parameter is the mean of the relative difference of the reaction force between 18 s and 50 s. The slope of the curve between the error metrics ( $\theta_i$ ) is then computed for each parameter, and the Sobol' indices are estimated as  $S_i = \frac{\theta_i^2}{\sum \theta_i^2}$ . The parameters accounting for 90% of the variance are considered for the calibration.

	$\theta_i$	$S_i$
$E_c$	28.7	$5.27 \times 10^{-1}$
$E_s$	25.4	$4.12 \times 10^{-1}$
$\varepsilon_c$	$-2.44 \times 10^{-5}$	$3.80 \times 10^{-13}$
$\varepsilon_s$	$-2.06 \times 10^{-4}$	$2.71 \times 10^{-11}$
$k_c$	$-1.6 \times 10^{-1}$	$1.64 \times 10^{-5}$
$k_s$	-9.71	$6.02 \times 10^{-2}$
$p_{init}$	$-1.09 \times 10^{-4}$	$7.63 \times 10^{-12}$

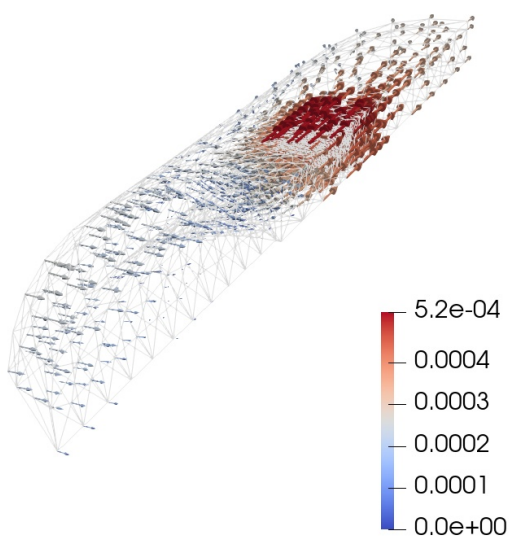
**Table 12:** Sobol indices of the model's parameters.

## 8 *In vivo* evaluation of a single-compartment model

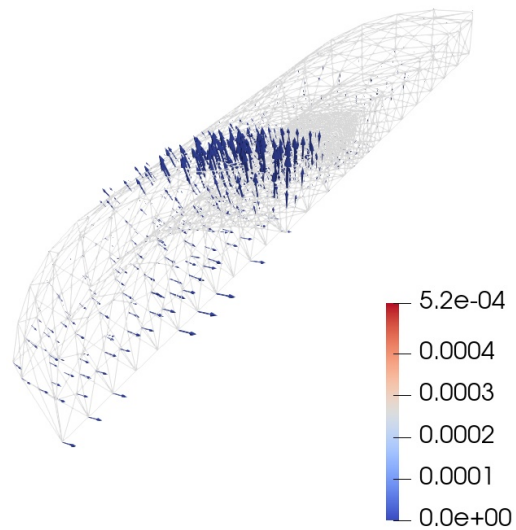
According to Table 12, the governing parameters are the Young moduli and the permeability of the subcutis. The permeability of the cutis was added to the calibrated parameters to complete the set of guesses.

## Appendix B: Interstitial Fluid flow

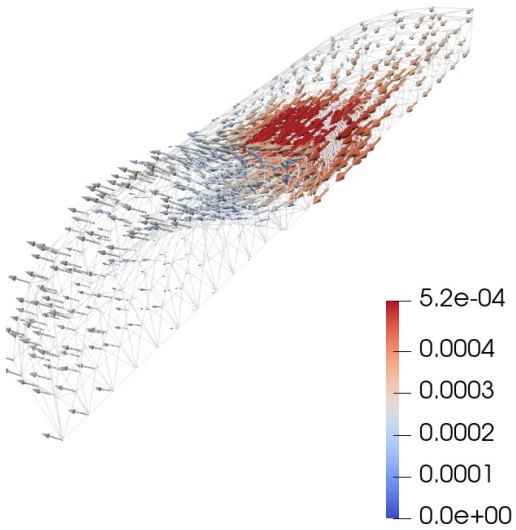
$t = 18\text{ s}$



$t = 50\text{ s}$

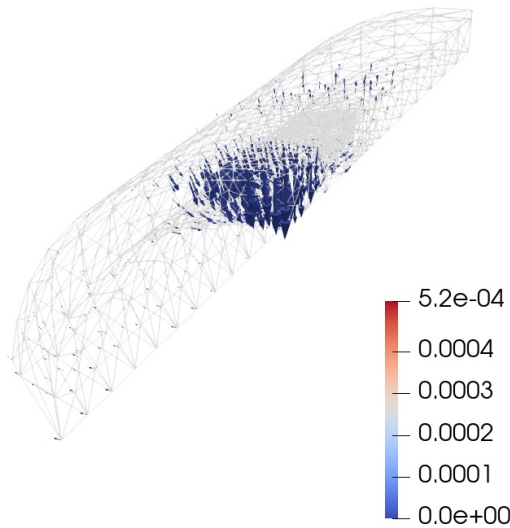


$t = 88\text{ s}$



## 8 In vivo evaluation of a single-compartment model

$t = 275\text{ s}$



When stretching the skin, the fluid underneath the patch slowly follows the patch movements and the neighbouring fluid is drawn in the pores which get dilated (peak at  $t=18\text{s}$ ). During a sustained phase ( $t=50\text{s}$ ), an equilibrium phase is reached and the fluid moves from the subcutis to the cutis. Then, during a release phase ( $t=88\text{s}$ ), the fluid is expelled from the deformed region to be replaced by the one underneath the patch. Finally, during the last stage ( $t=275\text{s}$ ), the initial state is reached again and a movement of fluid from the cutis to the subcutis is expected.

## **Part IV**

### ***In vivo* evaluation of a two-compartment porous model**



# 9 *In vivo evaluation of a two-compartment model*

## Table of Contents

---

9.1	Synopsis (FR) . . . . .	145
9.2	Synopsis (EN) . . . . .	148
9.3	Article . . . . .	151

---

### 9.1 Synopsis (FR)

Afin d'étudier l'interaction entre les chargements mécaniques et la microcirculation, les méthodologies actuelles reposent généralement sur des approches multi-échelles de type 3D-1D. Ces méthodes intègrent une représentation explicite du système vasculaire (Bauer et al. 2005; Mithraratne et al. 2012; Sree et al. 2019a). Toutefois, ces modèles nécessitent une description détaillée du réseau vasculaire, ce qui conduit à des simulations particulièrement coûteuses en ressources de calcul, tout en présentant souvent un couplage faible entre les réponses mécaniques et vasculaires. À l'inverse, les modèles poreux constituent une alternative efficace, en intégrant les processus biochimiques et de diffusion à travers un couplage plus robuste, comme démontré dans Sciumè et al. 2014a.

L'objectif principal de cette étude est d'examiner et de répondre aux questions de recherche suivantes : *"Comment le système vasculaire peut-il être intégré dans*

## 9 *In vivo* evaluation of a two-compartment model

un modèle poromécanique ? Comment le modèle poromécanique avec le système vasculaire peut-il être efficacement évalué ?"

Pour atteindre ces objectifs, un cadre poromécanique à deux compartiments a été développé afin d'explorer le comportement mécanique de la peau humaine et sa micro-circulation lors d'une indentation *in vivo*. Parallèlement, une campagne expérimentale a été réalisée pour mesurer la réponse de la micro-circulation locale à l'indentation. Cette recherche introduit un modèle constitutif innovant à deux compartiments, intégrant un interstitium biphasique qui prend en compte les interactions entre les composants solides et fluides de la peau (Table 13).

Une étude expérimentale a été menée impliquant 11 participants (6 hommes et 5 femmes), après validation par un comité éthique. La technique de mesure de flux par laser Doppler (LDF) repose sur le principe de l'effet Doppler, qui observe un décalage de fréquence résultant du mouvement relatif entre la cible et la source. Le décalage de longueur d'onde survenant lors de l'interaction avec les globules rouges est directement proportionnel à leur concentration et à leur vitesse, indépendamment de la direction du mouvement. La charge appliquée a été introduite au niveau du milieu de la phalange par contact direct avec la sonde LDF, facilité par un pivotmètre. Le chargement a été contrôlé en remplissant un réservoir adjacent à la sonde avec de l'eau, garantissant des conditions de charge précises et constantes.

Étant donné les variabilités connues sur la réponse du LDF, les mesures se sont étalées sur deux jours consécutifs, chaque jour comportant deux sessions séparées par un intervalle de repos de 15 minutes. Chaque session comprenait une séquence de quatre cycles incluant les phases de chargement, de maintien, de déchargement et de maintien. Pour les deux premiers cycles, un volume d'eau de 20mL a été utilisé, tandis que pour les deux cycles suivants, un volume de 40mL a été appliqué, maintenant un débit constant de  $1\text{mL s}^{-1}$ .

Lors de la phase de chargement, une diminution du signal LDF a été observée, indiquant une occlusion vasculaire. Après la libération de la charge, un pic réactif prononcé est apparu, signalant une hyperémie réactive post-occlusive. L'amplitude du plateau ischémique et l'intensité de la réponse de pointe se sont avérées directement corrélées à la charge appliquée.

La modélisation poroélastique offre une méthodologie prometteuse en intégrant des données mécaniques et hémodynamiques, permettant d'explorer des phénomènes bi-

ologiquement pertinents à diverses échelles. Cette approche de modélisation répond efficacement aux limitations inhérentes aux modèles viscoélastiques traditionnels, qui peinent souvent à capturer les caractéristiques structurelles et compositionnelles complexes des tissus biologiques. De plus, les modèles poroélastiques constituent une alternative viable aux modèles computationnels 3D-1D classiques pour relier les réponses vasculaires aux conditions de chargement mécanique.

Dans cette étude, un modèle hiérarchique à deux compartiments a été développé afin de prendre en compte la distribution des fluides au sein de l'espace interstitiel et du système microcirculatoire. Le cadre théorique comprend un interstitium biphasique composé de fluide interstitiel et de cellules, analysé par le biais d'un essai de consolidation unidimensionnel d'une colonne de 100 $\mu\text{m}$ . L'inclusion d'un interstitium biphasique dans le modèle permet une représentation distincte des cellules et du fluide interstitiel, en tenant compte de leurs échelles de temps caractéristiques différentes. Des extensions supplémentaires du modèle, intégrant des mécanismes d'échange biologique tels que le transport de l'oxygène, sont détaillées en annexe. Les analyses préliminaires suggèrent que la viscosité des cellules introduit une échelle de temps caractéristique supplémentaire, en plus de celle associée au mouvement du fluide interstitiel. Cependant, dans des conditions de viscosité cellulaire élevée et de courtes échelles de temps, les cellules présentent un comportement similaire à celui des matériaux solides.

Le modèle a alors été affiné pour simuler la campagne expérimentale réalisée sur de courtes échelles de temps. Lors de cette campagne, une indentation de la deuxième phalange du majeur a été effectuée à l'aide d'une sonde LDF, tout en surveillant simultanément le signal LDF et la température. Les paramètres matériau issus de la littérature existante ont été utilisés pour réaliser une analyse approfondie de sensibilité, identifiant trois paramètres clés et interdépendants : le module de Young, l'exposant régissant la perméabilité et la compressibilité supposée des vaisseaux. En raison de l'indisponibilité des données de déplacement, une calibration directe n'était pas envisageable, soulignant la nécessité d'efforts expérimentaux supplémentaires pour permettre une évaluation directe des propriétés mécaniques individuelles. Malgré cette limitation, le modèle a démontré sa capacité qualitative à capturer à la fois l'ischémie et l'hyperémie réactive post-occlusive, s'alignant étroitement avec les observations expérimentales.

Cette recherche fournit un modèle modulaire permettant de rendre compte de la

## 9 In vivo evaluation of a two-compartment model

réponse micro-circulatoire à un chargement externe. En intégrant la poromécanique, le modèle proposé constitue un outil complet permettant d'analyser l'interaction des facteurs biochimiques et mécaniques dans la santé et la pathologie des tissus. Par exemple une proposition d'intégration de la biochimie de l'oxygène en annexe de l'article.

Toutes les simulations numériques ont été réalisées en utilisant le logiciel open-source FEniCSx v0.9.0. Afin de promouvoir la transparence et la reproductibilité, les données expérimentales anonymisées ainsi que les codes éléments finis correspondants ont été rendus accessibles publiquement sur GitHub.

### 9.2 Synopsis (EN)

To investigate the interplay between mechanical loading and micro-circulation, current methodologies typically employ multiscale 3D-1D approaches. These methods include an explicit representation of the vascular system (Bauer et al. 2005; Mithraratne et al. 2012; Sree et al. 2019a). However, such models necessitate an explicit description of the vascular tree, leading to computationally intensive simulations, and often exhibit weak coupling between the mechanical and vascular responses. In contrast, porous models offer an efficient alternative by incorporating biochemical and diffusion processes through a more robust coupling, as demonstrated in Sciumè et al. 2014a.

The principal aim of this study is to investigate and address the research questions: *"How can the vascular system be incorporated into a poromechanical model? How can the poromechanical model with the vascular system be effectively evaluated?"* To achieve these objectives, a two-compartment poromechanical framework has been developed to explore the mechanical behaviour of human skin and its micro-circulation during *in vivo* indentation. Alongside, an experimental campaign has been carried out to measure the local micro-circulation response to indentation. This research introduces an innovative two-compartment constitutive model that incorporates a biphasic interstitium that considers the interactions between the solid and fluid components of the skin (Table 13).

An experimental study was conducted involving 11 participants (6 males and 5 females), respecting the ethical requirements. The laser Doppler flowmetry (LDF)

Species Phase \	Connective Tissue	Other structures (glands, hair, etc.)	Cells in the interstitium	Water	Oxygen	Other Species
Solid (s)	✓	✓		✓		
Liquid (l)				✓	✓	✓
Cell (c)				✓	✓	✓
Vascular (blood) (b)				✓	✓	✓

**Table 13:** Description of the model phases: the 2-compartment model is assumed to be composed of a solid phase, an interstitium composed of an interstitial fluid phase and a cell phase, and a vascular phase.

technique operates on the principle of the Doppler effect, which observes a frequency shift resulting from relative motion between the target and the source. The wavelength shift occurring upon interaction with red blood cells is directly proportional to their concentration and velocity, irrespective of the direction of movement. The applied load was introduced at the midpoint of the phalanx through direct contact with the LDF probe, facilitated by a pivotmeter. The loading was controlled by filling a reservoir adjacent to the probe with water, ensuring precise and consistent loading conditions.

Given the known variability of LDF techniques, the measurements spanned two consecutive days, with each day comprising two sessions separated by a 15-minute rest interval. Each session involved a sequence of four cycles that included the loading, sustaining, unloading, and sustaining phases. In the first two cycles, a volume of water of 20mL was used, while the second two cycles used a volume of 40mL, maintaining a uniform flow rate of  $1\text{mL s}^{-1}$ .

During the loading phase, a decrease in LDF signal was observed, indicative of vascular occlusion. Upon load release, a pronounced reactive peak emerged, signifying post-occlusive reactive hyperaemia. The magnitude of the ischaemic plateau and the intensity of the peak response were found to be directly correlated with the applied load.

Poroelastic modelling offers a promising methodology by integrating mechanics and haemodynamics, enabling the exploration of biologically relevant phenomena across various scales. This modelling approach effectively addresses the inherent limitations of traditional viscoelastic models, which often struggle to capture the intricate structural and compositional characteristics of biological tissues. In addition, poroelastic models provide a viable alternative to conventional 3D-1D computational models to link vascular responses to mechanical loading conditions.

## *9 In vivo evaluation of a two-compartment model*

In this study, a hierarchical two-compartment model was developed to account for fluid distribution within the interstitial space and the micro-circulatory system. The theoretical framework includes a biphasic interstitium composed of interstitial fluid and cells, which was analysed through a one-dimensional consolidation test of a 100 $\mu\text{m}$  column. The inclusion of a biphasic interstitium within the model enables a distinct representation of cells and interstitial fluid, considering their different characteristic timescales. Further model extensions incorporating biological exchange mechanisms, such as oxygen transport, are detailed in the appendix. Preliminary analyses suggest that cell viscosity introduces an additional characteristic time beyond that associated with interstitial fluid movement. However, under conditions of high cell viscosity and short timescales, cells exhibit behaviour akin to that of solid materials.

Expanding on these findings, the model was refined to simulate the experimental campaign conducted on short timescales. In this campaign, indentation of the second phalanx of the middle finger was performed using the LDF probe, with simultaneous monitoring of both the LDF signal and temperature. Material parameters sourced from existing literature were employed to conduct an in-depth sensitivity analysis, identifying three key and interdependent parameters: Young's modulus, the exponent governing permeability, and the assumed vessel compressibility. Due to the unavailability of displacement data, direct calibration was not feasible, underscoring the need for further experimental efforts to facilitate direct evaluation of one-to-one mechanical properties. Despite this limitation, the model demonstrated its qualitative capability to capture both ischaemia and post-occlusive reactive hyperaemia, aligning closely with experimental observations.

This research develops a modular framework aimed at representing the micro-circulatory response under external mechanical loading. By incorporating poromechanics, the proposed model serves as a comprehensive tool to analyse the interplay of biochemical and mechanical factors in tissue health and pathology. For example, a proposal for the integration of oxygen biochemistry is in the Appendix to the article.

All numerical simulations were performed using the open-source software FEniCSx v0.9.0. To promote transparency and reproducibility, the anonymised experimental data and the corresponding finite element codes have been made publicly available on GitHub.

### **9.3 Article**

This work was accepted in 2025 (International Journal of Numerical Method in Biomedical Engineering) (Lavigne et al. 2025b).

#### **Contribution (CRediT author statement)**

Conceptualisation, Methodology, Investigation, Software, Experiment, Writing – original draft.

# Hierarchical poromechanical approach to investigate the impact of mechanical loading on human skin micro-circulation.

Thomas Lavigne<sup>a,b,c</sup>, Stéphane Urcun<sup>a</sup>, Bérengère Fromy<sup>e,f</sup>, Audrey Josset-Lamaugarny<sup>e,f</sup>, Alexandre Lagache<sup>b,c</sup>, Camilo A. Suarez-Afanador<sup>a</sup>, Stéphane P. A. Bordas<sup>a</sup>, Pierre-Yves Rohan<sup>b</sup>, Giuseppe Sciumè<sup>c,d,\*</sup>

<sup>a</sup> Institute of Computational Engineering, Department of Engineering, University of Luxembourg,  
2 place de l'université, Esch-sur-Alzette, L-4365, Luxembourg, <sup>b</sup> Arts et Metiers Institute of  
Technology, IBHGC, 151 bd de l'hôpital, Paris, 75013, France, <sup>c</sup> Arts et Metiers Institute of  
Technology, Univ. of Bordeaux, CNRS, Bordeaux INP, INRAE, I2M Bordeaux, Avenue  
d'Aquitaine, Pessac, 33607, France, <sup>d</sup> Institut Universitaire de France (IUF), <sup>e</sup> CNRS UMR  
5305, Tissue Biology and Therapeutic Engineering Laboratory (LBTI), Lyon, F-69007, France, <sup>f</sup>  
Claude Bernard University Lyon, Villeurbanne, F-69100, France

---

**Abstract:** Extensive research on human skin anatomy has revealed that the skin functions as a complex multi-scale and multi-phase system, containing up to 70% of bounded and free circulating water. The presence of moving fluids significantly influences the mechanical and biological responses of the skin, affecting its time-dependent behaviour and the transport of essential nutrients and oxygen to cells.

Poroelastic modelling emerges as a promising approach to investigate biologically relevant phenomena at finer scales while embedding crucial mechanisms at larger scales as it facilitates the integration of multi-scale and multi-physics processes. Despite extensive use of poromechanics in other tissues, no hierarchical multi-compartment porous model that incorporates blood supply has yet been experimentally evaluated to simulate the *in vivo* mechanical and micro-circulatory response of human skin.

This paper introduces a hierarchical two-compartment model that accounts for fluid distribution within the interstitium and the micro-circulation of blood. A general theoretical framework, which includes a biphasic interstitium (comprising interstitial fluid and non-structural cells), is formulated and studied through a one-dimensional consolidation test of a 100  $\mu\text{m}$  column. The inclusion of a biphasic interstitium allows the model to account separately for the motion of cells and interstitial fluid, recognising their differing characteristic times. An extension of the model to include biological exchanges such as oxygen transport is discussed in the appendix.

The preliminary evaluation demonstrated that cell viscosity introduces a second characteristic time beyond that of interstitial fluid movement. However, at high cell viscosity values and short time scales, cells exhibit behaviour akin to that of solid materials.

Based on these observations, a simplified version of the model was used to replicate an experimental campaign carried out on short time scales. Local pressure (up to 31 kPa) was applied to the skin of the dorsal face of the middle finger through a laser Doppler probe PF801 (Perimed Sweden) attached to an apparatus as previously described (Fromy Brain Res 1998).

The model demonstrated its qualitative ability to represent both ischaemia and post-occlusive reactive hyperaemia, aligning with experimental observations.

All numerical simulations were performed using the open source software FEniCSx v0.9.0. To promote transparency and reproducibility, the anonymised experimental data and the corresponding finite element codes are publicly available on GitHub.

**Keywords:** Human skin ; Poro-elasticity ; Haemodynamics ; FEniCSx

---

## Introduction

The role of the skin as the primary protective barrier to the external environment makes the skin highly susceptible to pathologies such as pressure ulcers (PU). The National Pressure Injury Advisory Panel redefined the definition of a pressure injury in 2016 as "*A pressure injury [which] is localised damage to the skin and underlying soft tissue, usually over a bony prominence or related to a medical or other device. [...] The injury occurs as a result of intense and/or prolonged pressure or pressure in combination with shear. The tolerance of soft tissue for pressure and shear may also be affected by microclimate, nutrition, perfusion, co-morbidities, and condition of the soft tissue.*". The prevalence of pressure ulcers varies widely among at-risk populations, such as the elderly, diabetic patients, and amputees. For example, between 9 % and 20 % of hospitalised patients in Europe are reported to have pressure ulcers (Vanderwee et al. 2007). In particular, superficial pressure ulcers account for 70 % of all cases (Kim et al. 2020; Moore et al. 2019). Despite extensive research, current qualitative risk assessment methods for PUs lack reliability and

## *9 In vivo evaluation of a two-compartment model*

remain insufficiently accurate (Anthony et al. 2008). Preventing and managing skin injuries requires a deeper understanding of the skin structural composition and mechanical behaviour.

Anatomically, the skin comprises three primary layers: the epidermis, dermis, and hypodermis (Hsu and Fuchs 2021). The epidermis, the outermost layer, usually measures 50 to 150  $\mu\text{m}$  in thickness and consists predominantly of keratinocytes (Abdo et al. 2020; Burns et al. 2010; Joodaki and Panzer 2018; Wong et al. 2015; Yazdi and Baqersad 2022). Beneath the epidermis lies the dermis, connected via a basement membrane. Together, these layers are often referred to as the cutis. The dermis, significantly thicker than the epidermis (0.5 to 5 mm), is composed of the papillary and reticular layers and serves as a structural matrix. This matrix retains water (about 60 % of the total weight of the dermis) and is predominantly made of collagen (80 – 85 % dry weight), elastin (2 – 4 %) and reticulin (Burns et al. 2010; Dwivedi et al. 2022). In contrast to the avascular epidermis, the dermis is highly vascularised (via blood and lymphatic vessels), containing sweat glands, hair follicles (approximately 11 per  $\text{cm}^2$ ), nerves (Braverman 1989; Liao et al. 2013). The innermost layer, the hypodermis (subcutaneous tissue), primarily comprises adipose tissue and loose areolar tissue, which stores approximately 80 % of body fat in non-obese individuals (Querleux et al. 2002). The composition of this layer significantly influences the biomechanical properties of the skin, as detailed by Querleux et al. 2002, who characterised it as 7.4 % water, 7.3 % unsaturated lipids, and 85.3 % saturated lipids.

Understanding the skin's behaviour and the risk to develop a PU during sustained loads thus necessitates multiscale and multiphysics approaches. Injury risk factors are classified into intrinsic parameters (e.g., skin morphology, oxygen levels) and extrinsic factors (e.g., external loading). At the macroscopic level, both excessive and sustained moderate loads can initiate PU formation (Ceelen et al. 2008; Loerakker et al. 2011; Loerakker et al. 2010; Nierop et al. 2010; Stekelenburg et al. 2006; Traa et al. 2019; Tsuji et al. 2005). At the microscopic level, ischaemia-reperfusion injury - characterised by oxygen deprivation followed by sudden re-oxygenation - causes cell damage (Loerakker et al. 2011; Stekelenburg et al. 2006; Tsuji et al. 2005). Temporal factors, including duration of sustained compression, are critical determinants of tissue damage, highlighting the need for a holistic understanding of risk factors for PU formation (Coleman et al. 2013). Consequently, investigating

the time-dependent mechanical behaviour of the soft tissues accounting for their time-dependent response is essential to improve the prevention of PU.

Another crucial aspect is the incorporation of micro-circulation dynamics (Liao et al. 2013; Nguyen-Tu et al. 2013; Sree et al. 2019a; Tsuji et al. 2005). This supports various applications beyond PU prevention, including oncology (Fukumura and Jain 2007; Russell et al. 2015; Tesselaar et al. 2017), dermatology (Baran et al. 2015; Braverman 1989; Kelly et al. 1995), and hypertension risk assessment (Farkas et al. 2004; Rossi et al. 2006b). Blood flow, a key determinant of tissue health, is evaluated in clinical routine using advanced methodologies such as laser Doppler imaging (Kubli et al. 2000; Millet et al. 2011; Svedman et al. 1998) and optical coherence tomography (OCT) (An et al. 2010). Laser Doppler flowmetry is a well-established, non-invasive, real-time technique for measuring micro-circulatory blood flow of the skin (Folgosi-Correa and Nogueira 2012; Poffo et al. 2014; Varghese et al. 2009). The laser Doppler flowmetry method further presents the advantage of a precise temporal evaluation, but includes an averaged spatial response. In this context, computational models, including porous media approaches, offer a robust framework for coupling mechanical and biochemical processes in soft tissues.

3D-1D coupled models were introduced by Bauer et al. 2005 to gain a deeper understanding of the underlying physiological mechanisms of the initial micro-circulatory response to mechanical skin irritation. Mithraratne et al. 2012 proposed a coupled 3D-1D computational model of the foot, in which hydrostatic pressure acts on the external surface of blood vessels, leading to a reduction in the flow cross-sectional area and, consequently, to a decrease in blood supply. Similarly, the study by Sree et al. 2019a investigated oxygen diffusion in human skin using a multilayered model that includes the stratum corneum, the viable epidermis, and the dermis. The model considers a volume  $1 \text{ mm}^3$  that required 1,208,437 elements, which is considerably heavy and limits the scale of the sample studied. Computational homogenisation schemes (in particular, the FE<sup>2</sup> method) have been proposed to bridge the scales between cells and tissue using the strain-time cell death threshold (Breuls et al. 2003; Breuls et al. 2002; Lustig et al. 2021).

Alternatively, mechanical approaches based on porous media mechanics allow the coupling of the behaviour of the solid phase with that of the fluid in the pores, where biochemical exchanges occur. Such models, originally developed for soil mechanics

## 9 *In vivo* evaluation of a two-compartment model

(Terzaghi 1943) are now quite extensively applied in biomechanics in different contexts. Given the multiphasic and multiphysics nature of soft tissues, such models can be transferred to study their behaviour with two important differences: a large strain regime can be reached and there is a strong coupling during the loading between the solid and the fluid phases. These models have been applied to various tissues, including the brain (Budday et al. 2019; Carrasco-Mantis et al. 2023; Greiner et al. 2021; Hervas-Raluy et al. 2023; Hosseini-Farid et al. 2020; Lucio et al. 2024; Urcun et al. 2023; Urcun et al. 2022), the liver (Ricken and Lambers 2019), the meniscus (Bulle 2022; Bulle et al. 2021; Kazemi et al. 2013; Uzuner et al. 2022; Uzuner et al. 2020), and muscle tissue (Lavigne et al. 2022b). Porous models also present an opportunity to current practice in including biochemistry and diffusion processes through a strong coupling as developed in Sciumè 2021; Urcun et al. 2021 for tumour growth and as proposed by Lucio et al. 2023; Lucio et al. 2024 for drug delivery. Although poromechanics theory has been extensively applied in other soft biological tissues, only a few studies have been published for the skin, and these were mainly limited to *in silico* and *ex vivo* studies. Furthermore, to the best of the authors' knowledge, no hierarchical multi-compartment porous model including blood supply has been evaluated with regard to experiments yet.

This paper investigates the feasibility of using a two-compartment porous model to simulate the *in vivo* mechanical and micro-circulatory response of human skin. The proposed theory incorporates a biphasic interstitium and a vascular network. All simulations have been performed using open-source software FEniCSx, which supports parallel computation. Sensitivity analysis of material parameters and qualitative comparisons with experimental data, including laser Doppler flowmetry, are presented to evaluate the model's potential for advancing our understanding of skin mechanics and pathology.

## Materials and methods

### Data Acquisition

The cutaneous perfusion state of the middle finger's mid-phalanx under indentation has been assessed using a Laser Doppler Flowmeter (PERIMED PERIFLUX 5000). Smoking volunteers were excluded from this study. The LDF technique is based

on the Doppler effect, observing a frequency shift when there is relative movement between the target and the source (Fang et al. 2024; Pedanekar et al. 2018). Given the size and speed of red blood cells, the LDF probe uses a fixed wavelength of 780 nm. The shift in wavelength after hitting red blood cells is proportional to their number and speed, regardless of the direction of movement (Fang et al. 2024; Pedanekar et al. 2018).

A total of 11 healthy volunteers (6 men and 5 women), aged  $25 \pm 2$  years, were recruited for the study after informed consent was provided. This study received ethical approval (national registration number RCB: 2023-A00418-37). Volunteers who smoked were excluded from this study. They were seated comfortably and the room temperature was meticulously regulated at  $20.9 \pm 0.6^\circ\text{C}$ . The probe was calibrated prior to measurements using the PERIMED PF1001 calibration tool. In addition, the skin temperature on the dorsum of the hand was continuously monitored to ensure stable thermal conditions. A 10-minute acclimatisation period was observed to allow stabilisation of both skin temperature and LDF readings prior to data collection. The temperature and LDF signals were recorded at 2 Hz intervals.

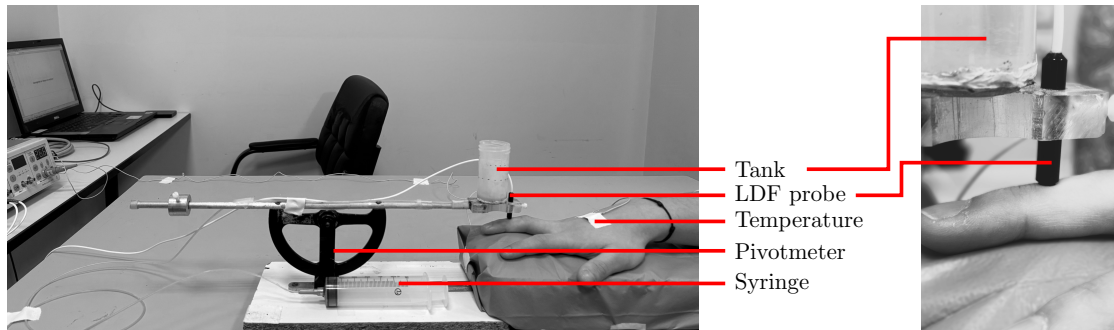


**Figure 20:** Experimental set-up. The load is directly applied to the skin using the LDF probe. The probe is placed at the extremity of the pivotmeter which is initially set at its equilibrium point. A controlled volume of water is then added/removed in the tank aside the probe to increase/decrease the load magnitude.

The load was applied to the midpoint of the phalanx directly via the LDF probe using a pivotmeter. The pivotmeter, depicted in Figure 20, is an in-house loading device developed by Fromy et al. 1998; Fromy et al. 2000. Initially, the device was set to its equilibrium state, with the probe gently contacting the skin under the influence of an equilibrium mass. The loading application was achieved by filling the

## 9 In vivo evaluation of a two-compartment model

tank adjacent to the probe with water, allowing for precise and controlled loading conditions.

Measurements were carried out over two consecutive days, with two sessions per day, each separated by at least a 15-minute rest period. Each session consisted of a sequence of four loading-sustaining-unloading-sustaining cycles. The initial two cycles involved a water volume of 20 mL corresponding to a load of 15 kPa, while the subsequent two cycles used a volume of 40 mL corresponding to a load of 31 kPa (Figure 21).

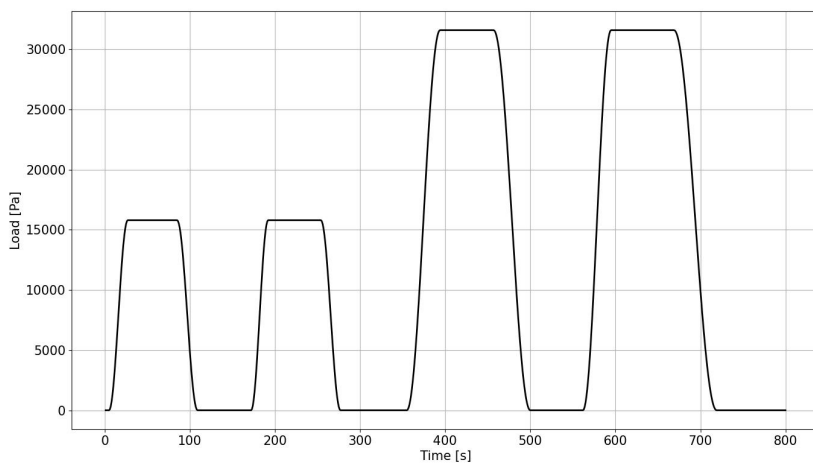


**Figure 21:** Four cycles of loading-sustaining-unloading-sustaining were performed. The first two cycles respectively corresponded to a 15 kPa load and the two last ones to a 31 kPa load.

The water was added and removed from the tank using a syringe and capillary, ensuring precise control of the process at a consistent rate of  $1 \text{ mL s}^{-1}$ . This controlled loading and unloading protocol facilitated an accurate and reproducible assessment of perfusion changes during each cycle and computational modelling.

## The mathematical model

A 2-compartment model has been developed to incorporate a biphasic interstitium. The following developments are based on the previous work of Lavigne et al. 2023b;

Sciumè 2021. As detailed in the anatomy of the skin aforementioned in the introduction, the model considers several distinct phases, which are detailed in Table 14. The Representative Elementary Volume (REV) is provided in Figure 22.

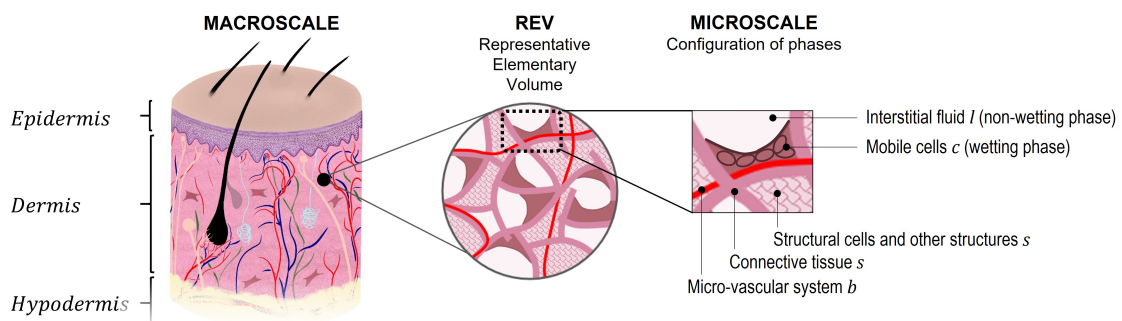


**Figure 22:** Description of the Representative Elementary Volume: the solid scaffold comprising the connective tissue, appendices and stroma cells (pink), the circulating cells (brown), the interstitial fluid (white), and the micro-vascular system (red). Nutrient and oxygen exchanges occur between the fluid phases.

Species Phase	Connective Tissue	Other structures (glands, hair, etc.)	Cells in the interstitium	Water	Oxygen	Other Species
Solid (s)	✓	✓		✓		✓
Liquid (l)				✓	✓	✓
Cell (c)			✓	✓	✓	✓
Vascular (blood) (b)				✓	✓	✓

**Table 14:** Description of the model phases: the 2-compartment model is assumed to be composed of a solid phase, an interstitium composed of an interstitial fluid phase and a cell phase, and a vascular phase.

The water absorbed by the connective tissue constituents is assumed to be locally in equilibrium with the pressure of the interstitial fluid. This equilibrium ensures that vessels within connective tissue are subjected to compression (or dilation) according to the average pressure,  $p^s$ , of the fluids in the interstitium of the solid scaffold. The solid scaffold of tissue can be conceptualised as comprising four key components: connective tissue itself, resident cells, skin appendices, and absorbed fluid, which together define the biomechanical and physiological properties of the structure. The solid scaffold has two other independent compartments: the interstitium and the vascular compartment.

The liquid phase of the interstitium is modelled as a water-like medium that is responsible for transporting oxygen and other nutrients. The cellular phase encompasses non-structural cells within the skin, as well as embedded water, oxygen, and

## 9 *In vivo* evaluation of a two-compartment model

nutrient elements. Lastly, blood in the vascular compartment is characterised as Newtonian and contains red blood cells, which facilitate the delivery of oxygen and nutrients to the interstitial compartment, ensuring sustained metabolic function.

These elements collectively form the foundation of a hierarchical 3D poroelastic model that accounts for haemodynamic processes.

Similar to the classical theory of multiphasic porous media, the proposed model is developed based on the concept of a wetting phase, a non-wetting phase, and their associated capillary pressure within the biphasic interstitium (Sciumè 2021). Within a pore, the interstitial fluid and cells coexist, but typically one phase adheres more closely to the solid scaffold, whereas the other occupies the central region of the pore. These are termed the wetting phase and the non-wetting phase, respectively. In the present case, we consider the interstitial fluid as the non-wetting phase and the cells as the wetting phase. The capillary pressure,  $p^{lc}$ , is defined in Equation 80 as the difference between the pressures of the non-wetting ( $p^l$ ) and wetting phases ( $p^c$ ). This pressure difference is intrinsically related to the saturation levels of each phase, which provides a framework for describing the fluid dynamics within the biphasic interstitium.

$$p^{lc} = p^l - p^c \quad (80)$$

where  $p^c = p^l - p^{lc}$  is the wetting phase pressure, *e.g.* the cell pressure in the present case.

The primary variables of the mathematical model are the displacement field of the solid scaffold  $\mathbf{u}^s$ , the capillary pressure  $p^{lc}$ , the pressure of the interstitial fluid (non-wetting phase)  $p^l$  and the blood pressure  $p^b$ .

### Governing equations

Each phase occupies part of the volume of a Representative Elementary Volume. Within the REV, the volume fractions are defined according to Equation 81 and

respect the constraint Equation 82.

$$\varepsilon^\alpha = \frac{\text{Volume}^\alpha}{\sum_{\text{phases}} \text{Volume}^{\text{phases}}} \quad (81)$$

$$\varepsilon^s + \underbrace{\varepsilon^c + \varepsilon^l}_{\text{extra-vascular porosity}} + \underbrace{\varepsilon^b}_{\text{vascular porosity}} = 1 \quad (82)$$

Specifically, the vascular porosity  $\varepsilon^b$  is introduced along with the extra-vascular porosity  $\varepsilon$ :

$$\varepsilon = \varepsilon^c + \varepsilon^l \quad (83)$$

We further introduce the saturation  $S^\alpha = \frac{\varepsilon^\alpha}{\varepsilon}$  of the wetting and non-wetting non-miscible phases in the interstitium and their constraint Equation 84.

$$S^c + S^l = 1 \quad (84)$$

The porous medium reads the classical conservation laws of mechanics. The momentum conservation of the multiphase continuum gives:

$$\nabla \cdot \mathbf{t}^{\text{tot}} + \mathbf{b} = \mathbf{0} \quad (85)$$

where  $\mathbf{t}^{\text{tot}}$  is the total Cauchy stress tensor.

For the fluid phases, the momentum conservation reads:

$$-\frac{\mathbf{K}^f}{\mu^f} \nabla p^f = \varepsilon^f (\mathbf{v}^f - \mathbf{v}^s), \quad (f = l, c, b) \quad (86)$$

where  $\frac{\mathbf{K}^f}{\mu^f}$  is referred to as hydraulic conductivity, which is influenced by the characteristics of both the moving fluid and the porous solid material. Specifically, it is determined by the dynamic viscosity of the fluid  $\mu^f$  and the intrinsic permeability  $\mathbf{K}^f$  of the solid matrix. In the case of blood, the momentum Equation 86 holds true under the assumptions of slow laminar flow with negligible inertial effects.

The mass conservation Equations are introduced for each phase of the medium using the material derivative operator  $\frac{D^s}{Dt}$  to describe the movement of the fluids

## 9 In vivo evaluation of a two-compartment model

with respect to the solid scaffold (Sciumè 2021):

$$\frac{D^s}{Dt}(\rho^s \varepsilon^s) + \rho^s \varepsilon^s \nabla \cdot \mathbf{v}^s = 0 \text{ solid phase,} \quad (87)$$

$$\underbrace{\frac{D^s}{Dt}(\varepsilon^f)}_{\text{Accumulation rate}} + \underbrace{\nabla \cdot (\varepsilon^f (\mathbf{v}^f - \mathbf{v}^s))}_{\text{Infiltration}} + \underbrace{\varepsilon^f \nabla \cdot \mathbf{v}^s}_{\text{ECM deformation}} = 0 \quad (f = l, c, b), \quad (88)$$

## Constitutive equations

To simplify the mathematical model, the following assumptions were established:

1. Blood vessels mainly interact with fluid constituents, and so they have no relevant mechanical interaction with the "structural" connective tissue fibbers.
2. The solid pressure,  $p^s$ , is assumed to be related to the pressure of the fluids in the extravascular space only and respects Equation 96.
3. Consistently with hypothesis 1, we suppose that  $\varepsilon^b$  depends on  $(p^b - p^s)$ .

As a result, the solid scaffold interacts with the blood vessels through extravascular fluids. This is a reasonable assumption for the system considered and significantly simplifies the mathematical formulation.

Based on Hypothesis 3, we can introduce a state Equation for the vascular volume fraction (which will drive ischaemia and reperfusion):

$$\varepsilon^b = \varepsilon_0^b \cdot \left( 1 - \frac{2}{\pi} \arctan \left( \frac{p^s - p^b}{K} \right) \right) \quad (89)$$

where  $\varepsilon_0^b$  stands for the initial blood volume fraction and  $K$  is the compressibility of the vessels. Increasing the compressibility value of the vessel requires a larger pressure gap to reduce the porosity value. The arc-tangent formulation allows us to prevent negative values.

To account for the non-newtonian behaviour of the blood, the following constitutive Equation based on the porosity evolution for the vascular permeability is proposed to introduce non-linearity:

$$k^b = k_0^b \left( \frac{\varepsilon^b}{\varepsilon_0^b} \right)^{\alpha_b}, \quad \alpha_b \geq 2 \quad (90)$$

where  $k_0^b$  and  $\varepsilon_0^b$ , respectively, denote the initial vascular permeability and the initial vascular porosity. The vascular permeability can further be anisotropic and a ratio has been introduced such that the permeability matrix reads:

$$\mathbf{K}_0^b = \begin{bmatrix} \frac{k_0^b}{ratio_x} & 0 & 0 \\ 0 & \frac{k_0^b}{ratio_y} & 0 \\ 0 & 0 & \frac{k_0^b}{ratio_z} \end{bmatrix} \quad (91)$$

The state law for the saturation-capillary pressure relationship (according to the wetting / non-wetting description) is defined by Equations 92.

$$S^c = 1 - \left[ \frac{2}{\pi} \arctan \left( \frac{p^{lc}}{a} \right) \right] \quad (92)$$

where  $a$  is a constant parameter depending on the microstructure of the connective tissue. The initial saturation in cells is obtained by appropriately selecting of the initial value of  $p^{lc}$ .

The total Cauchy stress tensor can be defined as:

$$\mathbf{t}^{\text{tot}} = \sum_{\alpha=s,c,l,b} \varepsilon^\alpha \mathbf{t}^\alpha = \underbrace{\varepsilon^s \tau^s}_{\mathbf{t}^{\text{eff}}(\mathbf{u}^s)} - \varepsilon^s p^s \mathbf{1} - \varepsilon(S^c p^c + S^l p^l) \mathbf{1} - \varepsilon^b p^b \mathbf{1} \quad (93)$$

$$= \underbrace{\varepsilon^s \tau^s}_{\mathbf{t}^{\text{eff}}(\mathbf{u}^s)} - \varepsilon^s p^s \mathbf{1} - \varepsilon(p^l - S^c p^{lc}) \mathbf{1} - \varepsilon^b p^b \mathbf{1} \quad (94)$$

where  $\varepsilon^s \tau^s$  is the effective stress tensor,  $p^s$  is the empirically defined solid pressure Equation 96.

$$p^s = S^c p^c + S^l p^l \quad (95)$$

$$\xrightarrow{(80)+(84)} p^s = p^l - S^c p^{lc} \quad (96)$$

As a result, introducing Equations 82 and 96 in Equation 94:

$$\mathbf{t}^{\text{tot}} = \mathbf{t}^{\text{eff}} - \underbrace{(1 - \varepsilon^b)}_{=\varepsilon^s + \varepsilon} (p^l - S^c p^{lc}) \mathbf{1} - \varepsilon^b p^b \mathbf{1} \quad (97)$$

In the experiment conducted in this study, the solid scaffold remains in the small strain regime. For the sake of simplicity of the analysis, a linear elastic behaviour

## 9 In vivo evaluation of a two-compartment model

is therefore considered such that:

$$\mathbf{t}^{\text{eff}} = 2\mu \left( \frac{1}{2}(\nabla \mathbf{u} + \nabla \mathbf{u}^T) \right) + \lambda \text{tr} \left( \frac{1}{2}(\nabla \mathbf{u} + \nabla \mathbf{u}^T) \right) \mathbf{1} \quad (98)$$

where  $\lambda, \mu$  are the Lamé coefficients depending on the Young modulus and the Poisson ratio.

### Derivation of the final formulation of the system of partial differential equations

This section outlines the systematic process of integrating the governing and constitutive Equations to derive the final system of Equations for solution.

Starting with the solid phase mass Equation, we have:

$$\frac{D^s}{Dt}(\rho^s \varepsilon^s) + \rho^s \varepsilon^s \nabla \cdot \mathbf{v}^s = 0 \quad (99)$$

$$\xrightarrow{(82)+(99)*\frac{1}{\rho^s}} -\frac{D^s}{Dt}(\varepsilon + \varepsilon^b) + (1 - \varepsilon - \varepsilon^b) \nabla \cdot \mathbf{v}^s = 0 \quad (100)$$

$$\xrightarrow{} \frac{D^s}{Dt}(\varepsilon) = -\frac{D^s}{Dt}(\varepsilon^b) + (1 - \varepsilon - \varepsilon^b) \nabla \cdot \mathbf{v}^s \quad (101)$$

This Equation is used to update the extravascular porosity, which is an internal variable of the problem. A first order approximation in time allows to assess the porosity at the new time-step such that (with  $d\mathbf{u}^s(t) = (\mathbf{u}^s(t) - \mathbf{u}^s(t - dt))$ ):

$$\varepsilon(t) = \frac{\varepsilon(t - dt) + \varepsilon^b(t - dt) - \varepsilon^b(t)(1 + \nabla \cdot d\mathbf{u}^s(t)) + \nabla \cdot d\mathbf{u}^s(t)}{1 + \nabla \cdot d\mathbf{u}^s(t)} \quad (102)$$

Introducing Equation 86 into Equation 88, we can eliminate the fluid velocity and introduce the fluid pressures. As a result, the blood mass conservation gives:

$$\frac{D^s}{Dt}(\varepsilon^b) - \nabla \cdot \left( \frac{k^b}{\mu^b} \nabla p^b \right) + \varepsilon^b \nabla \cdot \mathbf{v}^s = 0 \quad (103)$$

According to the state law defined for the vascular porosity Equation 89, its

derivative can also be expressed as:

$$\frac{D^s \varepsilon^b}{Dt} = \frac{D^s \varepsilon^b}{Dp^s} \frac{D^s p^s}{Dt} + \frac{D^s \varepsilon^b}{Dp^b} \frac{D^s p^b}{Dt} \quad (104)$$

Furthermore, using Equations 96, we get:

$$\frac{D^s p^s}{Dt} = \frac{D^s p^l}{Dt} - \frac{D^s S^c p^{lc}}{Dt} \quad (105)$$

$$= \frac{D^s p^l}{Dt} - S^c \frac{D^s p^{lc}}{Dt} - p^{lc} \frac{D^s S^c}{Dp^{lc}} \frac{D^s p^{lc}}{Dt} \quad (106)$$

$$= \frac{D^s p^l}{Dt} - \underbrace{\left( S^c + p^{lc} \frac{D^s S^c}{Dp^{lc}} \right)}_{=C_{state}} \frac{D^s p^{lc}}{Dt} \quad (107)$$

where  $C_{state}$  is a function defined for ease of reading depending on  $\frac{D^s S^c}{Dp^{lc}} = -\frac{2}{a\pi} \frac{1}{1+\left(\frac{p^{lc}}{a}\right)^2}$ .

Furthermore, we can compute  $C_{e,p} = \frac{D^s \varepsilon^b}{Dp^s}$  such that:

$$C_{e,p} = \frac{D^s \varepsilon^b}{Dp^s} = -\frac{2\varepsilon_0^b}{\pi K} \frac{1}{1+\left(\frac{p^l-S^c p^{lc}-p^b}{K}\right)^2} \quad (108)$$

Immediately, we also have:

$$\frac{D^s \varepsilon^b}{Dp^b} = -C_{e,p} \quad (109)$$

Finally, the derivative of the state function reads:

$$\frac{D^s \varepsilon^b}{Dt} = C_{e,p} \left( \frac{D^s p^l}{Dt} - C_{state} \frac{D^s p^{lc}}{Dt} - \frac{D^s p^b}{Dt} \right) \quad (110)$$

Introducing Equation 110, Equation 103 becomes:

$$C_{e,p} \left( \frac{D^s p^l}{Dt} - C_{state} \frac{D^s p^{lc}}{Dt} - \frac{D^s p^b}{Dt} \right) - \nabla \cdot \left( \frac{k^b}{\mu^b} \nabla p^b \right) + \varepsilon^b \nabla \cdot \mathbf{v}^s = 0 \quad (111)$$

Performing similar operations for the cells' mass conservation Equation, with  $k^c$  and  $\mu^c$  respectively denoting the cell phase permeability and viscosity and introducing

## 9 In vivo evaluation of a two-compartment model

the function  $C_{m,c} = \varepsilon \frac{D^s S^c}{D p^{lc}}$ :

$$\frac{D^s}{Dt}(S^c \varepsilon) - \nabla \cdot \left( \frac{k^c}{\mu^c} \nabla p^c \right) + S^c \varepsilon \nabla \cdot \mathbf{v}^s = 0 \quad (112)$$

$$\implies \left( S^c \frac{D^s}{Dt}(\varepsilon) + \varepsilon \frac{D^s}{Dt}(S^c) \right) - \nabla \cdot \left( \frac{k^c}{\mu^c} \nabla (p^l - p^{lc}) \right) + S^c \varepsilon \nabla \cdot \mathbf{v}^s = 0 \quad (113)$$

$$\stackrel{(101)}{\implies} \left( S^c \left[ -\frac{D^s}{Dt}(\varepsilon^b) + (1 - \varepsilon - \varepsilon^b) \nabla \cdot \mathbf{v}^s \right] + \varepsilon \frac{D^s}{Dt}(S^c) \right) \quad (114)$$

$$- \nabla \cdot \left( \frac{k^c}{\mu^c} \nabla p^l \right) + \nabla \cdot \left( \frac{k^c}{\mu^c} \nabla p^{lc} \right) + S^c \varepsilon \nabla \cdot \mathbf{v}^s = 0$$

$$\implies -S^c \frac{D^s \varepsilon^b}{Dt} + C_{m,c} \frac{D^s p^{lc}}{Dt} - \nabla \cdot \left( \frac{k^c}{\mu^c} \nabla p^l \right) + \nabla \cdot \left( \frac{k^c}{\mu^c} \nabla p^{lc} \right) \quad (115)$$

$$+ S^c (1 - \varepsilon^b) \nabla \cdot \mathbf{v}^s = 0$$

Introducing Equation 103 in Equation 115, we get:

$$\begin{aligned} & S^c \left( -\nabla \cdot \left( \frac{k^b}{\mu^b} \nabla p^b \right) + \varepsilon^b \nabla \cdot \mathbf{v}^s \right) + C_{m,c} \frac{D^s p^{lc}}{Dt} \\ & - \nabla \cdot \left( \frac{k^c}{\mu^c} \nabla p^l \right) + \nabla \cdot \left( \frac{k^c}{\mu^c} \nabla p^{lc} \right) + S^c (1 - \varepsilon^b) \nabla \cdot \mathbf{v}^s = 0 \end{aligned} \quad (116)$$

Finally the mass conservation of the cell phase reads:

$$\begin{aligned} & C_{m,c} \frac{D^s p^{lc}}{Dt} - S^c \nabla \cdot \left( \frac{k^b}{\mu^b} \nabla p^b \right) - \nabla \cdot \left( \frac{k^c}{\mu^c} \nabla p^l \right) \\ & + \nabla \cdot \left( \frac{k^c}{\mu^c} \nabla p^{lc} \right) + S^c \nabla \cdot \mathbf{v}^s = 0 \end{aligned} \quad (117)$$

Finally, the fluid phase in the interstitium mass conservation becomes, with  $k^l$  and

$\mu^l$  respectively denoting the interstitial fluid phase permeability and viscosity:

$$\frac{D^s}{Dt}(S^l \varepsilon) - \nabla \cdot \left( \frac{k^l}{\mu^l} \nabla p^l \right) + S^l \varepsilon \nabla \cdot \mathbf{v}^s = 0 \quad (118)$$

$$\xrightarrow{(80)+(84)} \frac{D^s}{Dt}(\varepsilon) - \frac{D^s}{Dt}(S^c \varepsilon) - \nabla \cdot \left( \frac{k^l}{\mu^l} \nabla p^l \right) + (1 - S^c) \varepsilon \nabla \cdot \mathbf{v}^s = 0 \quad (119)$$

$$\begin{aligned} &\xrightarrow{(101)+(103)+(112)} -\nabla \cdot \left( \frac{k^b}{\mu^b} \nabla p^b \right) + (1 - \varepsilon) \nabla \cdot \mathbf{v}^s - \nabla \cdot \left( \frac{k^c}{\mu^c} \nabla \underbrace{(p^l - p^{lc})}_{=p^c} \right) \\ &+ S^c \varepsilon \nabla \cdot \mathbf{v}^s - \nabla \cdot \left( \frac{k^l}{\mu^l} \nabla p^l \right) + (1 - S^c) \varepsilon \nabla \cdot \mathbf{v}^s = 0 \end{aligned} \quad (120)$$

Finally, we obtain for the mass conservation of the IF phase:

$$-\nabla \cdot \left( \frac{k^b}{\mu^b} \nabla p^b \right) - \nabla \cdot \left( \left[ \frac{k^c}{\mu^c} + \frac{k^l}{\mu^l} \right] \nabla p^l \right) + \nabla \cdot \left( \frac{k^c}{\mu^c} \nabla p^{lc} \right) + \nabla \cdot \mathbf{v}^s = 0 \quad (121)$$

**Remark:** The extension of this model to include biological exchanges is straightforward. An example of mathematical developments for oxygen biochemistry is provided in Appendix B.

### Weak form of the final system of partial differential equations

Mathematical developments have been introduced in the FEniCSx v0.9.0 (Alnæs et al. 2015; Baratta et al. 2023) environment to numerically solve a consolidation test in a 1D column. The finite element framework consists of solving a variational form defined as follows. Consider  $(q^c, q^l, q^b, \mathbf{w})$  the test functions defined in the mixed space  $L_0^2(\Omega) \times L_0^2(\Omega) \times [H^1(\Omega)]^3$ . The solutions of the problem are the capillary pressure, the cell pressure, the blood pressure, and the displacement of the solid:  $(p^l, p^{lc}, p^b, \mathbf{u}^s)$ .

Using Equations 85, 111, 117, 121, the problem to be solved reads:

$$\mathbf{u}^s = \mathbf{u}_{\text{imposed}} \text{ on } \partial\Omega_u \quad (122)$$

$$p^\alpha = p_{\text{imposed}} \text{ on } \partial\Omega_p^\alpha \quad (123)$$

## 9 In vivo evaluation of a two-compartment model

$$\begin{aligned} & \int_{\Omega} C_{m,c} \frac{\mathrm{D}^s p^{lc}}{\mathrm{D}t} q^c \mathrm{d}\Omega + \int_{\Omega} S^c \frac{k^b}{\mu^b} \nabla p^b \nabla q^c \mathrm{d}\Omega + \int_{\Omega} \frac{k^c}{\mu^c} \nabla p^l \nabla q^c \mathrm{d}\Omega \\ & - \int_{\Omega} \frac{k^c}{\mu^c} \nabla p^{lc} \nabla q^c \mathrm{d}\Omega + \int_{\Omega} S^c \nabla \cdot \left( \frac{\mathrm{D}^s \mathbf{u}^s}{\mathrm{D}t} \right) q^c \mathrm{d}\Omega = 0, \forall q^c \in L_0^2(\Omega) \end{aligned} \quad (124)$$

$$\begin{aligned} & \int_{\Omega} \frac{k^b}{\mu^b} \nabla p^b \nabla q^l \mathrm{d}\Omega + \int_{\Omega} \left[ \frac{k^c}{\mu^c} + \frac{k^l}{\mu^l} \right] \nabla p^l \nabla q^l \mathrm{d}\Omega \\ & - \int_{\Omega} \frac{k^c}{\mu^c} \nabla p^{lc} \nabla q^l \mathrm{d}\Omega + \int_{\Omega} \nabla \cdot \left( \frac{\mathrm{D}^s \mathbf{u}^s}{\mathrm{D}t} \right) q^l \mathrm{d}\Omega = 0, \forall q^l \in L_0^2(\Omega) \end{aligned} \quad (125)$$

$$\begin{aligned} & \int_{\Omega} C_{e,p} \frac{\mathrm{D}^s p^l}{\mathrm{D}t} q^b \mathrm{d}\Omega - \int_{\Omega} C_{e,p} C_{state} \frac{\mathrm{D}^s p^{lc}}{\mathrm{D}t} q^b \mathrm{d}\Omega - \int_{\Omega} C_{e,p} \frac{\mathrm{D}^s p^b}{\mathrm{D}t} q^b \mathrm{d}\Omega \\ & + \int_{\Omega} \frac{k^b}{\mu^b} \nabla p^b \nabla q^b \mathrm{d}\Omega + \int_{\Omega} \varepsilon^b \nabla \cdot \left( \frac{\mathrm{D}^s \mathbf{u}^s}{\mathrm{D}t} \right) q^b \mathrm{d}\Omega = 0, \forall q^b \in L_0^2(\Omega) \end{aligned} \quad (126)$$

$$\begin{aligned} & \int_{\Omega} \mathbf{t}^{\text{eff}}(\mathbf{u}^s) : \nabla \mathbf{w} \mathrm{d}\Omega - \int_{\Omega} (1 - \varepsilon^b) (p^l - S^c p^{lc}) \nabla \cdot \mathbf{w} \mathrm{d}\Omega \\ & - \int_{\Omega} \varepsilon^b p^b \nabla \cdot \mathbf{w} \mathrm{d}\Omega - \int_{\Gamma_s} \mathbf{t}^{\text{imposed}} \cdot \mathbf{w} \mathrm{d}\Gamma_s = 0, \forall \mathbf{w} \in [H^1(\Omega)]^3 \end{aligned} \quad (127)$$

## Evaluation of the model and application to the LDF experiment

### 1D column

A one-dimensional consolidation in a column is computed in a manner similar to the approach presented by Lavigne et al. 2023b, which examined a 1D consolidation test for a two-compartment model where the extra-vascular porosity is occupied by a single fluid. The present example aims to show the 2-compartment behaviour, including biphasic interstitium.

The column was 100  $\mu\text{m}$  in height and 20  $\mu\text{m}$  in width. The boundary conditions corresponding to a consolidation test are provided in Figure 23.

The tissue is supposed to have an extra-vascular porosity of 60 %, 50 % interstitial fluid and 10 % non-structural cells, and a vascular porosity of 4 %. The material parameters are provided in Table 15. To appreciate the influence of the cell phase,

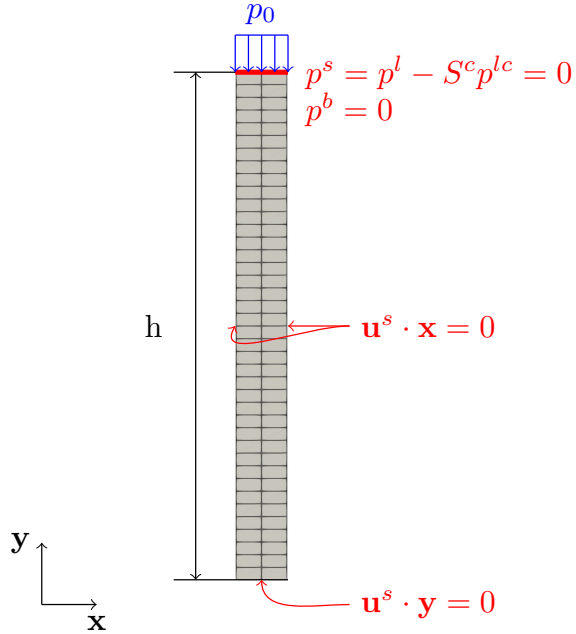


**Figure 23:** Load (blue), Boundary conditions (red) and mesh (gray) of the uniaxial confined compression of a porous 2D column of height  $h$ . For the mono-phasic interstitium model,  $p^s = p^l = 0$  Pa on the boundary (Lavigne et al. 2023b). A null pressure allows the leakage.

a tissue of mono-phasic extravascular porosity of 50 % of interstitial fluid (the remaining 10 % cells being transferred to the solid phase) and a vascular porosity of 4 % were also considered and compared. Given the significant difference in viscosities between the interstitial fluid and the cells, the objective is to analyse how the movement of the cells influences the characteristic times of the observed mechanical response.

An initial time of 10 s is initially set for the system to stabilise. In fact, a capillary pressure  $p_0^{lc}$  is initially set to obtain the desired saturation in cell  $S_0^c$  that provides the expected porosity 10 %. The initial pressure of the interstitial fluid  $p_0^l$  is then calculated to ensure an initial state where  $p_0^s = p_0^l - S_0^c p_0^{lc} = 0$  Pa. For the mono-phasic interstitium model, this step is not required, as we directly consider  $p_0^s =$

## 9 In vivo evaluation of a two-compartment model

$p_0^l = 0$  Pa on the boundary.

$$S_0^c = 1 - \frac{\varepsilon^l}{\varepsilon} \approx 0.17 \quad (128)$$

$$p_0^{lc} = a \cdot \tan\left(\frac{\pi}{2} \cdot (1 - S_0^c)\right) \approx 2240 \text{ Pa} \quad (129)$$

$$p_0^l = S_0^c \cdot p_0^{lc} \approx 380 \text{ Pa} \quad (130)$$

Following initialisation, a 5-second ramp is applied at the top of the sample to reach a  $p_0 = 200$  Pa load. The load is then sustained for 120 seconds. reach a  $p_0 = 200$  Pa load. The load is then sustained for 120 seconds.

Parameter	Symbol	Value	Value (Lavigne et al. 2023b)	Unit
Young modulus	E	5000	5000	Pa
Poisson ratio	$\nu$	0.2	0.2	-
IF viscosity	$\mu^l$	1	1	Pa s
IF intrinsic permeability	$k^l$	$1 \times 10^{-14}$	$1 \times 10^{-14}$	$\text{m}^2$
Cell viscosity	$\mu^c$	1, 5, 20	-	Pa s
Cell intrinsic permeability	$k^c$	$1 \times 10^{-14}$	-	$\text{m}^2$
Initial IF porosity	$\varepsilon^l$	0.5	0.5	-
Initial Cell porosity	$\varepsilon^c$	0.1	-	-
Coefficient pressure-saturation	a	600	-	Pa
Vessel Bulk modulus	K	$1 \times 10^3$	$1 \times 10^3$	Pa
Initial vessel Intrinsic permeability	$k_b^e$	$4 \times 10^{-12}$	$4 \times 10^{-12}$	$\text{m}^2$
Blood viscosity	$\mu^b$	$4.0 \times 10^{-3}$	$4.0 \times 10^{-3}$	Pa s
Initial vascular porosity	$\varepsilon_0^b$	4%	4%	-

**Table 15:** Mechanical parameters for the bi-compartment model including a biphasic interstitium.

### LDF Experiment: simplified interstitium

Supported by the results of the 1D-Column consolidation test and the characteristic times of the experiment (about one minute), the cells are expected to stay close to their initial location because they can be assimilated to highly viscous fluids. As a result, the application to the LDF experiment considers a simplified case with a mono-phasic interstitium to assess the feasibility of using the 2-compartment model to include the haemodynamic response. The model therefore simplifies and  $S^c = 0$ ,  $\varepsilon = \varepsilon^l$  and capillary pressure is no longer considered ( $p^s = p^l$ ). Hence, the

conservation Equations become:

- Solid phase:

$$\frac{D^s}{Dt}(\varepsilon) = -\frac{D^s}{Dt}(\varepsilon^b) + (1 - \varepsilon - \varepsilon^b)\nabla \cdot \mathbf{v}^s \quad (131)$$

- Vascular phase:

$$\tilde{C}_{e,p} \left( \frac{D^s p^l}{Dt} - \frac{D^s p^b}{Dt} \right) - \nabla \cdot \left( \frac{k^b}{\mu^b} \nabla p^b \right) + \varepsilon^b \nabla \cdot \mathbf{v}^s = 0 \quad (132)$$

where  $\frac{D^s \varepsilon^b}{Dt} = \tilde{C}_{e,p} \left( \frac{D^s p^l}{Dt} - \frac{D^s p^b}{Dt} \right)$  and  $\tilde{C}_{e,p} = \frac{D^s \varepsilon^b}{D p^s} = -\frac{2\varepsilon_0^b}{\pi K} \frac{1}{1 + \left( \frac{p^l - p^b}{K} \right)^2}$ .

- IF phase:

$$-\nabla \cdot \left( \frac{k^b}{\mu^b} \nabla p^b \right) - \nabla \cdot \left( \frac{k^l}{\mu^l} \nabla p^l \right) + \nabla \cdot \mathbf{v}^s = 0 \quad (133)$$

The corresponding variational forms are provided in Appendix A.

As depicted in Figure 24, a generic model consisting of a quarter section of the second phalanx of the middle finger is considered. The simplified geometry representing the soft tissue of the finger was created using GMSH, consisting of a quarter cylinder minus bone (Geuzaine and Remacle 2009). Measurements derived from echography—validated against literature values from Kallepalli et al. 2022—determined that the diameter of the simplified phalanx was 2.8 cm and the thickness of the skin 4 mm. An external force was applied over a cylindrical surface region at the top of the phalanx, corresponding to the area contacted by the LDF probe, which has a radius of 2 mm. To avoid boundary effects, the mesh was sufficiently extruded along the z-direction.

LDF is sensitive to positioning and external factors and has a limited penetration depth of 0.5–1 mm (Fredriksson et al. 2009; Humeau-Heurtier et al. 2013; Poffo et al. 2014). The relative LDF value has been computed as the product between the blood cells concentration (represented by the vascular porosity) and the blood velocity in a domain represented by a cylinder of 1 mm depth below the load application surface:

$$LDF [\%] = \frac{\int_{\Omega_{LDF}} \sqrt{\varepsilon^b(v^b - v^s) \cdot \varepsilon^b(v^b - v^s)} d\Omega}{LDF_0} \quad (134)$$

## 9 In vivo evaluation of a two-compartment model

where  $LDF_0$  stands for the established value of the LDF, also known as basal skin blood flow.

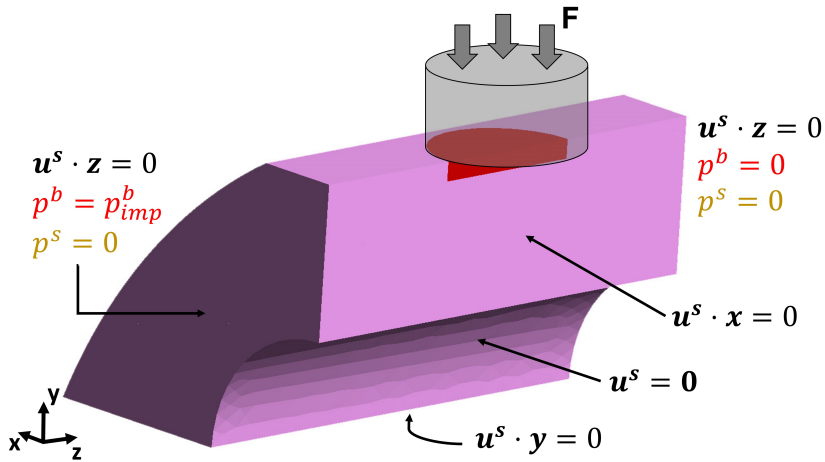


**Figure 24:** A quarter of a phalanx is modelled. Displacements are blocked on the symmetry planes and no flux are allowed. A blood pressure gradient is introduced on the z-axis to create the basal skin blood flow. The interstitial fluid is allowed to get in/out the sample by imposing  $p^s = 0$  Pa. The LDF signal is computed in the red domain directly below the load application surface.

The hydrostatic pressure in the skin capillaries varies significantly between segments. The mean hydrostatic pressure ranges from 32 – 38 mmHg in the arterial part, decreases to 17 – 20 mmHg in the transitional part, and reduces to 12 – 18 mmHg in the venous part. Given that the physiological pressure of the whole blood remains approximately constant at 25 mmHg, the effective filtration and re-absorption pressure gradients in the arterial and venous parts of the capillaries are approximately 7 – 13 mmHg (933 – 1733 Pa), respectively (Fedorovich et al. 2018). As a result, the average Capillary Blood flow Velocity (CBV) in the capillaries of human skin under thermoneutral conditions ranges from 400 to 900  $\mu\text{m s}^{-1}$ , showing an oscillatory nature (Fedorovich et al. 2018; Rossi et al. 2006a). Fagrell et al. 1977 reported a mean resting CBV of  $0.7 \pm 0.3 \text{ mm s}^{-1}$  at an average skin temperature of  $30.4 \pm 2.3^\circ\text{C}$ . Another study with 64 healthy subjects found a mean resting CBV of  $0.6 \pm 0.5 \text{ mm s}^{-1}$  at a skin temperature of  $30.9 \pm 3.2^\circ\text{C}$ .

As a result, boundary conditions ensured that normal displacements were constrained along the symmetric sides, while the interstitial fluid was allowed to flow freely along the z-direction. A blood pressure of 4000 Pa was applied to the left side to reach its maximum value in a span of five seconds, achieving a basal skin blood

flow flow rate of approximately  $400 \text{ } \mu\text{m s}^{-1}$ . All pressures were initialised to zero and a five-second stabilisation period preceded the application of loading to allow the model to reach a homeostatic state.

## Mesh Convergence

Before performing the sensitivity analysis, a comprehensive mesh convergence analysis was performed to ensure numerical accuracy and stability. The same set of parameters was evaluated for four different mesh configurations: 25k elements, 44k elements with local refinement, 125k elements, and 250k elements. The solution obtained with the 250k element mesh was considered the reference mesh for comparison. To quantify the deviation of other meshes from this reference, the root mean square error (RMSE) was calculated using the formula:

$$\text{RMSE} = \frac{1}{N} \sqrt{\sum (LDF - LDF_{250k})^2} \quad (135)$$

where  $N$  represents the number of time points.

## Sensitivity Study

The two-compartment model that includes a mono-phasic interstitium is driven by nine material parameters. Considering the interaction between some of these parameters, the sensitivity analysis is reduced to five parameters provided in Table 16.

For the solid phase, the mechanical behaviour for the elastic law considered is controlled by two parameters: the Young's modulus  $E$  and the Poisson ratio  $\nu$ . These parameters influence the computation of the effective solid stress and are related through the Lamé coefficients. The literature still lacks a clear value for the Poisson ratio, with models assuming values ranging from 0.3 to 0.5 (Kalra and Lowe 2016; Lakhani et al. 2021; Mukhina et al. 2020; Pailler-Mattei et al. 2008; Raveh Tilleman et al. 2004; Sanders 1973). Therefore, the authors aimed to remain consistent with the values commonly used in previous studies and fixed its value at 0.42, as proposed by Lucio et al. 2024.

## 9 *In vivo* evaluation of a two-compartment model

Furthermore, the reported elastic modulus values exhibit a wide range (5 kPa to 196 MPa, according to Oomens et al. 2017), influenced by factors such as ageing, loading conditions, model choice, and geometry considerations. Kalra and Lowe 2016 reported Young's modulus values ranging from 4 to 15 MPa under quasi-static tensile conditions and from 14 to 100 MPa for dynamic tensile loading. Indentation, torsion, and suction tests yielded Young's modulus values of 10 kPa to 2.4 MPa, 20 kPa to 1.12 MPa, and 25 kPa to 260 kPa, respectively. Hence, this study considered values ranging from 50 kPa to 1 MPa.

The mono-phasic interstitium is described as a single fluid whose behaviour is governed by Darcy's law. The corresponding material parameters are the intrinsic permeability  $k^l$  and the viscosity  $\mu^l$ . These two parameters describe the ability of the fluid to flow within the domain, and their ratio can be referred to as the hydraulic permeability  $L^l = \frac{k^l}{\mu^l}$ . The sensitivity analysis focusses on using the ratio of these quantities directly. Wahlsten et al. 2019 studied animal skin (Murine) and *ex vivo* (abdominal and breast region) and *in vivo* (forearm) human skin samples under tensile conditions. They reported that the mechanics of porous media allowed the inclusion of volume loss as a result of the expulsion of interstitial fluid. Using a single layer model, they identified elastic tensile moduli of  $89 \pm 27$  kPa for human skin and  $288 \pm 178$  kPa for murine skin, considering an *ex vivo* hydraulic conductivity of  $5 \times 10^{-13} \text{ m}^2 \text{ Pa}^{-1} \text{ s}^{-1}$  and a reference solid volume fraction of 0.30 (Nakagawa et al. 2010). Oftadeh et al. 2018 investigated the role of ECM viscosity and fluid in the mechanical response of the mouse dermis. The hydraulic conductivity of the skin was set to  $(1.47 \pm 0.23) \times 10^{-13} \text{ m}^2 \text{ Pa}^{-1} \text{ s}^{-1}$ . Oftadeh et al. 2023, based on poroelastic considerations (poro-viscoelastic finite element modelling identification), identified the hydraulic permeability of water for three layers of skin (stratum corneum, epidermis, dermis). Analysing 14 *ex vivo* human skin samples tested with macroscopic and nano-indentation methodologies, a hydraulic permeability of  $5-15 \times 10^{-14} \text{ m}^2 \text{ Pa}^{-1} \text{ s}^{-1}$  was found on the nanoscopic scale and  $0.5-2 \times 10^{-14} \text{ m}^2 \text{ Pa}^{-1} \text{ s}^{-1}$  on the mesoscopic scale. Han et al. 2023; Leng et al. 2021 also considered hydraulic permeabilities in the range  $[0.5 \times 10^{-14}, 9.8 \times 10^{-10}] \text{ m}^2 \text{ Pa}^{-1} \text{ s}^{-1}$ . Therefore, this study considered values ranging from  $0.5 \times 10^{-14} \text{ m}^2 \text{ Pa}^{-1} \text{ s}^{-1}$  to  $1 \times 10^{-13} \text{ m}^2 \text{ Pa}^{-1} \text{ s}^{-1}$ .

Similarly, for the vascular phase, the intrinsic permeability  $k_0^b$  and the blood viscosity  $\mu^b$  are not treated separately, but considered through the hydraulic permeability of

the blood  $L_0^b$ . To ensure the same initial blood flow, the blood pressure on the sample side was modified accordingly. The blood permeability was assumed to be higher than the permeability of the interstitial fluid (Lucio et al. 2024). In the study, values were introduced that ranged from  $1 \times 10^{-10} \text{ m}^2 \text{ Pa}^{-1} \text{ s}^{-1}$  to  $1 \times 10^{-8} \text{ m}^2 \text{ Pa}^{-1} \text{ s}^{-1}$  were introduced.

The blood volume fraction was fixed to maintain the same geometry throughout the study. Regarding the volume fraction of the skin's vascular system, Kelly et al. 1995 used morphometry (based on fluorescein angiographic and native capillaroscopic fields) to evaluate the volume fraction of blood in 25 subjects (12 young, mean age 23.2 years, and 13 elderly, mean age 74.9 years) on the forehead and forearm. For young subjects, the volume fractions were  $0.0791 \pm 0.0067$  and  $0.0481 \pm 0.0036$  for the dermal papillary loops, and  $0.0571 \pm 0.0123$  and  $0.0223 \pm 0.0043$  for the horizontal vessels. In older subjects, these values were lower for the capillary loops but higher for horizontal vessels, respectively:  $0.0494 \pm 0.0037$  and  $0.0266 \pm 0.0029$  for the dermal papillary loops, and  $0.1121 \pm 0.0124$  and  $0.1013 \pm 0.0069$  for horizontal vessels. As the cohort age is  $25 \pm 1$  year, the authors fixed the initial vascular porosity at 8%.

The two remaining parameters used in this sensitivity analysis are the exponent  $\alpha$  and the compressibility of the vessel  $K$ . The exponent in the law of evolution of the permeability and compressibility of blood vessels arbitrarily varied between 2 to 6 and 500 Pa to 5000 Pa, respectively.

Parameter	Initial	Minimal	Maximal
Young Modulus (E)	$2.00 \times 10^5 \text{ Pa}$	$5.00 \times 10^4 \text{ Pa}$	$1.00 \times 10^6 \text{ Pa}$
Hydraulic permeability ISF ( $L^I$ )	$1 \times 10^{-14} \text{ m}^2 \text{ Pa}^{-1} \text{ s}^{-1}$	$1 \times 10^{-15} \text{ m}^2 \text{ Pa}^{-1} \text{ s}^{-1}$	$1 \times 10^{-13} \text{ m}^2 \text{ Pa}^{-1} \text{ s}^{-1}$
Hydraulic permeability Blood ( $L^b$ )	$1 \times 10^{-9} \text{ m}^2 \text{ Pa}^{-1} \text{ s}^{-1}$	$1 \times 10^{-10} \text{ m}^2 \text{ Pa}^{-1} \text{ s}^{-1}$	$1 \times 10^{-8} \text{ m}^2 \text{ Pa}^{-1} \text{ s}^{-1}$
$\alpha$ (Eq. 90)	3	2	6
Vessel Compressibility ( $K$ )	1000	500	5000

**Table 16:** Material parameters for the sensitivity analysis: initial, minimal and maximal values.

We propose using variance-based sensitivity analysis through the Sobol index to evaluate the influence of model parameters on the predicted micro-circulatory response under compression. An initial simulation was conducted using the parameter values specified in Table 16, which yielded the reference skin blood flow response  $R_0$  generated by the model. Subsequently, each of the five parameters was individually perturbed by a random value  $\delta_i$  within the random range  $[-95\%, 900\%]$ . This perturbation produced a modified response  $R_{i,\delta_i\%}$  for the parameter  $i^{\text{th}}$ . The relative

## 9 In vivo evaluation of a two-compartment model

variations in the model's response were then computed as follows:

$$\text{Var}_{i\delta_i\%} = \frac{1}{N} \sum_{i=1}^n \frac{R_{i\delta_i\%}}{R_0} \quad (136)$$

In order to quantify the impact of each parameter, the following linear model was fit:

$$\text{Var}_i = 1 + \sum_i \theta_i x_i \quad (137)$$

where  $x_i$  is the  $i^{th}$  parameter variation  $\in [-95; 900]\%$  and  $\theta_i$  the slope of the variation. Then, the 15 parameter couples were perturbed similarly by random values  $\delta_i, \delta_j$ . The variances  $\text{Var}_{i,j,\delta_i,\delta_j\%,i>j}$  were interpolated by a second-order polynomial model.

$$\text{Var}_{i,j,\delta_i,\delta_j\%,i>j} = 1 + \sum_i \theta_i \alpha_i + \sum_{ij,i>j} \theta_{ij} \alpha_i \alpha_j \quad (138)$$

The first-order analysis give the Sobol indices:

$$S_i = \frac{\theta_i^2}{\sum_i \theta_i^2} \quad (139)$$

The second-order analysis give the Sobol indices:

$$S_i = \frac{\theta_i^2}{\sum_i \theta_i^2 + \sum_{ij,i>j} \theta_{ij}^2} \quad \text{and} \quad S_{ij} = \frac{\theta_{ij}^2}{\sum_i \theta_i^2 + \sum_{ij,i>j} \theta_{ij}^2} \quad (140)$$

## Results

### Experimental Laser Doppler Flowmetry: indentation test

Normality tests were conducted to assess the distribution of the data. As the variables were not normally distributed, nonparametric tests were used. A Wilcoxon rank-sum test was performed. Individual median  $\pm$  interquartile range (IQR) experimental curves are provided in Appendix C. The following aims to analyse the tendency in the ischaemic and hyperaemic responses of the median response ( $\pm$  IQR). Figure 25 presents the raw experimental LDF results together with the measured skin temperature.

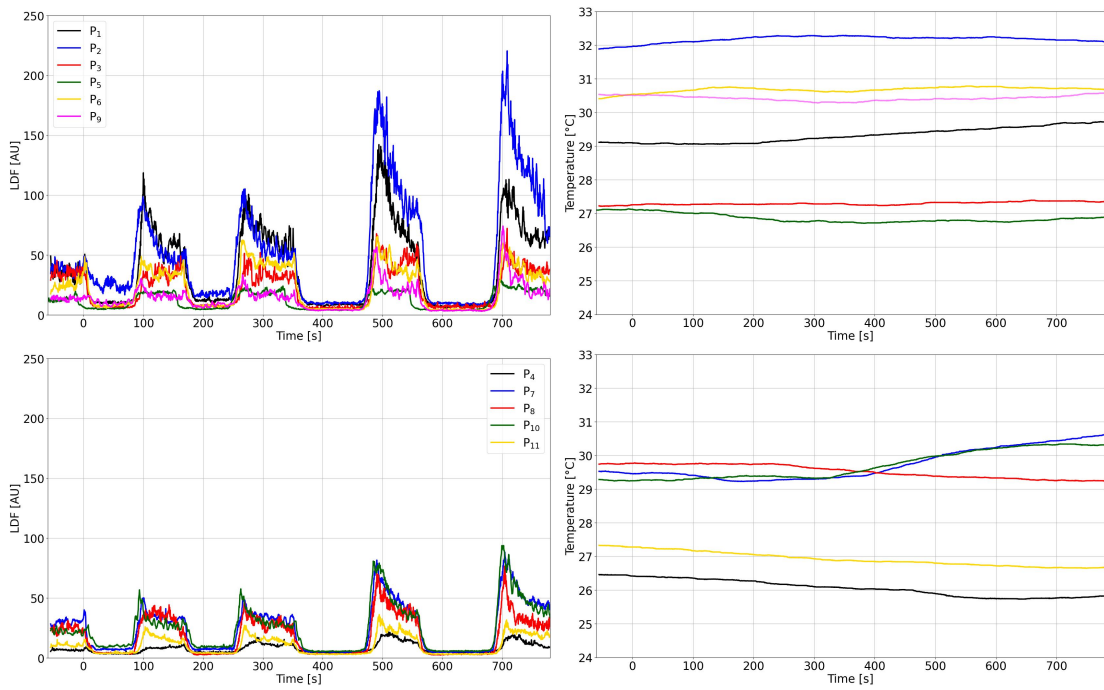


**Figure 25:** Median LDF signals (median $\pm$ IQR are provided in Appendix C) for each of the N=6 male (top) and N=5 female (bottom) patients (left). Dorsal hand temperature recorded during the experiment for each of the patient (right).

### N=6 men

For each cycle, measurements were repeated four times, resulting in a total of  $6 \times 4 = 24$  samples. Since each load was tested over two cycles, the 48 samples were analysed. Before the first load cycle, the skin temperature was  $29.5 \pm 2.8^\circ\text{C}$ . The basal blood flow of the skin, measured during the 60 s preceding the first application of local pressure, was  $24.7 \pm 19.9$  arbitrary units (AU).

Upon application of the compressive load, the laser Doppler flowmetry (LDF) signal decreased, indicating a reduction in blood flow. This ischaemic response was dependent on the intensity of the load. During the first cycle, the LDF values dropped to  $8.0 \pm 5.5$  AU ( $t$ -statistic = 36.3,  $p$ -value =  $1.3 \times 10^{-8}$ ), representing a significant reduction to  $38.47 \pm 25.8\%$  of the basal skin blood flow ( $t$ -statistic = 25.9,  $p$ -value =  $2.3 \times 10^{-6}$ ). In the last two cycles, blood flow further declined to  $5.6 \pm 3.2$  AU ( $t$ -statistic = 5.1,  $p$ -value = 0.06), corresponding to  $22.8 \pm 9.4\%$  of the basal blood flow ( $t$ -statistic = 57.3,  $p$ -value =  $3.5 \times 10^{-13}$ ), indicating a progressive intensification of ischaemia in repeated cycles. The higher the load, the closer the signals became.

## 9 *In vivo* evaluation of a two-compartment model

Following the release of the compressive load, post-occlusive reactive hyperaemia (PORH) was observed (Figure 25). Similarly to the ischaemic response, the hyperaemic peak depended on the applied load intensity. The first load led to an increase in LDF values up to  $66.7 \pm 76.1$  AU ( $t$ -statistic = 26.0,  $p$ -value =  $2.2 \times 10^{-6}$ ), corresponding to approximately 750 % of the basal blood flow ( $251.8 \pm 129.5$  %;  $t$ -statistic = 23.5,  $p$ -value =  $7.9 \times 10^{-6}$ ), demonstrating a strong hyperaemic response. With the second load intensity, LDF values peaked at  $94.1 \pm 89.3$  AU ( $t$ -statistic = 5.8,  $p$ -value = 0.06), reaching approximately 1100 % of the basal blood flow ( $353.0 \pm 270.5$  %;  $t$ -statistic = 14.9,  $p$ -value =  $5.7 \times 10^{-4}$ ). After reaching the PORH peak, the LDF signal gradually returned toward a value slightly above the initial basal level.

### N=5 women

For each cycle, the measurements were repeated four times, resulting in a total of  $5 \times 4 = 20$  samples. Since each load was tested over two cycles, the 40 samples were analysed. Before the first load cycle, the skin temperature was  $27.8 \pm 2.6^\circ\text{C}$ . The basal blood flow of the skin, measured during the 60 s preceding the first application of local pressure, was  $16.6 \pm 17.3$  arbitrary units (AU).

Upon application of the compressive load, the laser Doppler flowmetry (LDF) signal decreased, indicating a reduction in blood flow. This ischaemic response was dependent on the load intensity. During the first cycle, the LDF values dropped to  $4.9 \pm 3.8$  AU ( $t$ -statistic = 10.9,  $p$ -value = 0.004), representing a significant reduction to  $32.8 \pm 24.2$  % of the basal skin blood flow ( $t$ -statistic = 17.6,  $p$ -value =  $1.5 \times 10^{-4}$ ), confirming a substantial decrease. In the last two cycles, blood flow further declined to  $4.3 \pm 1.9$  AU ( $t$ -statistic = 0.9,  $p$ -value = 0.6), corresponding to  $24.3 \pm 17.9$  % of the basal blood flow ( $t$ -statistic = 15.8,  $p$ -value =  $3.7 \times 10^{-4}$ ), indicating a progressive intensification of ischaemia over repeated cycles.

Following the release of the compressive load, post-occlusive reactive hyperaemia (PORH) was observed (Figure 25). Similarly to the ischaemic response, the hyperaemic peak depended on the applied load intensity. The first load led to an increase in LDF values up to  $45.9 \pm 26.1$  AU ( $t$ -statistic = 5.3,  $p$ -value = 0.07), approximately corresponding to 475 % of the basal blood flow ( $255.6 \pm 113.2$  %;  $t$ -statistic = 2.4,  $p$ -value = 0.3), suggesting a moderate but statistically non-significant hyperaemic response. With the second load intensity, LDF values peaked at  $60.3 \pm 58.5$  AU

( $t$ -statistic = 7.3,  $p$ -value = 0.03), reaching approximately 626% of the basal blood flow ( $336.4 \pm 144.6\%$ ;  $t$ -statistic = 2.6,  $p$ -value = 0.3). After reaching the PORH peak, the LDF signal gradually returned toward a value slightly above the initial basal level.

## Differences Between Men and Women

The lowest LDF values were observed in individuals with the lowest skin temperatures. However, as shown in Figure 26, the difference in magnitude and behaviour is reduced when LDF values are expressed relative to basal blood flow of the skin. This normalisation accounts for inter-individual variability in absolute blood flow measurements.

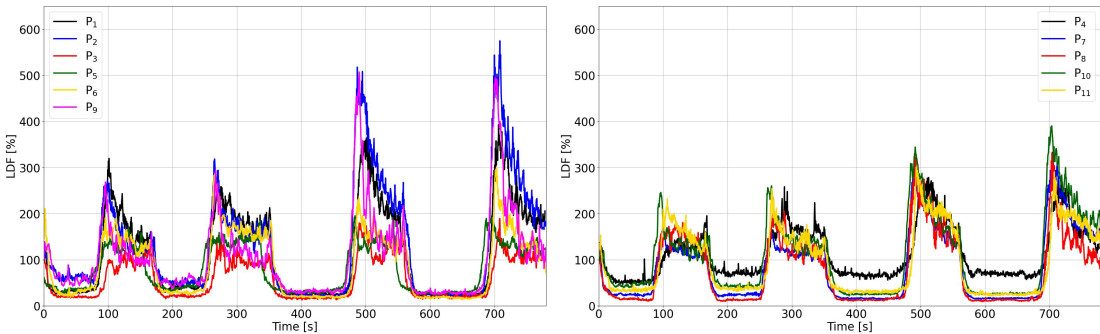


**Figure 26:** Median LDF signals normalised to the basal skin blood flow for each of the  $N = 6$  male (left) and  $N = 5$  female (right) participants. When expressed relative to baseline values, the difference in magnitude and behaviour between groups is reduced. Temperature primarily affects basal skin blood flow rather than the microvascular response to compressive loading.

Statistical analysis using independent Wilcoxon rank tests was performed to compare ischaemic and hyperaemic responses between male and female participants. The null hypothesis that two sets of measurements are drawn from the same distribution. The alternative hypothesis is that the values in one sample are more likely to be larger than the values in the other sample. The results showed significant differences in terms of raw AU signals but did not show significant differences between the groups for any of the conditions tested when looking to the relative evolution to the basal blood flow.

For the raw LDF signal (AU):

## 9 In vivo evaluation of a two-compartment model

- 20 mL ischemia:  $t = 4.13, p = 3.6 \times 10^{-5}$
- 20 mL hyperemia:  $t = 3.41, p = 6.5 \times 10^{-4}$
- 40 mL ischemia:  $t = 3.76, p = 1.7 \times 10^{-4}$
- 40 mL hyperemia:  $t = 3.05, p = 2.3 \times 10^{-3}$

For the relative LDF variation compared to the basal blood flow (in %):

- 20 mL ischemia:  $t = 0.96, p = 0.34$
- 20 mL hyperemia:  $t = 0.69, p = 0.49$
- 40 mL ischemia:  $t = 0.41, p = 0.69$
- 40 mL hyperemia:  $t = 0.46, p = 0.64$

Since all  $p$ -values for the relative LDF variations are well above the standard significance threshold ( $\alpha = 0.05$ ), we do not observe statistically significant differences between men and women in their microvascular responses to compressive loading. These findings indicate that, while absolute LDF values may vary between individuals, relative responses to ischaemia and subsequent hyperaemia are comparable between sexes.

These results further suggest that temperature primarily affects basal skin blood flow rather than the microvascular response to load-induced ischaemia and subsequent hyperaemia. Consequently, expressing the LDF signal as a percentage of the individual's basal blood flow provides a more consistent and reliable measure, reducing the variability associated with baseline differences in skin perfusion.

## Numerical 2-compartment biphasic 1D column

Figure 27 illustrates the model response for the 1D consolidation examples described in Lavigne et al. 2023b; Sciumè 2021, with an initial blood volume fraction of 0.04. The model exhibits behaviour consistent with the findings in Lavigne et al. 2023b; Sciumè 2021, but highlights the influence of cell viscosity  $\mu^c$  on pressure responses. When the cell viscosity matches that of the interstitial fluid  $\mu^l$ , the medium behaves as a mono-phasic system dominated by a fluid-filled interstitium (with increased porosity). In this case, both interstitial fluid pressure and cell pressure relax over

a relatively short timescale. However, as the viscosity of the cells increases, the relaxation time of the cells lengthens. Consequently, the solid pressure and porosities reveal a time-dependent response characterised by two distinct timescales: a shorter timescale associated with interstitial fluid flow and a longer timescale linked to cell phase flow. When cell viscosity is further elevated to a highly viscous regime, the system's short-term behaviour resembles that of a mono-phasic interstitium, as the cell phase effectively behaves like a solid phase.

## 9 In vivo evaluation of a two-compartment model

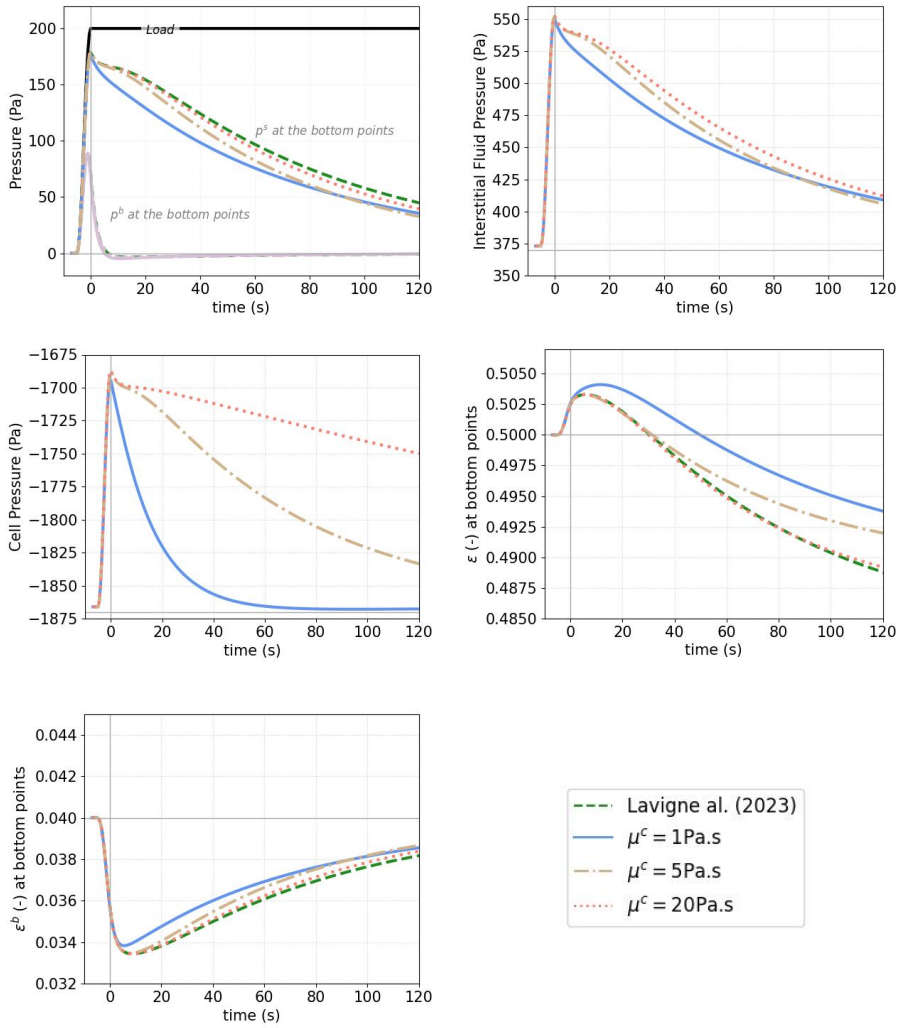


**Figure 27:** Results of the consolidation test on a 1D 2-compartment column including a biphasic interstitium. The interstitial fluid is the non wetting phase occupying 85 % of the interstitium and the cells represent the wetting phase accounting for 15 % of the interstitium. Different cell viscosities are tested ( $\mu^c = 1, 5, 20$ ). The results include the phase as well as the vascular and extra-vascular porosities evaluated at the bottom points of the column. The mono-phasic computation corresponds to the test presented in Lavigne et al. 2023b.

## Mesh Convergence

The analysis, carried out over the first 150 seconds of the experiment, revealed RMSE values of 5.5 %, 2.2 %, and 0.5 % for the 25k, 44k, and 125k element meshes, respectively. Based on these findings, the 44k element mesh, demonstrating a reasonable balance between computational efficiency and accuracy, was selected for

subsequent simulations. Furthermore, the computational codes were validated for parallel execution using the FEniCSX framework. A substantial performance enhancement was achieved, demonstrating a five-fold speed-up when utilising 4 CPUs for the 125k element mesh and 8 CPUs for the 250k element mesh. Figure 28 illustrates the speed-up for the 250k element mesh as the CPU count increases. Due to the limited degrees of freedom, performance gains plateau beyond 8 CPUs. To ensure accurate speed-up analysis, all writing and post-processing were disabled. For details on HPC installation procedures, the reader is referred to Appendix E.

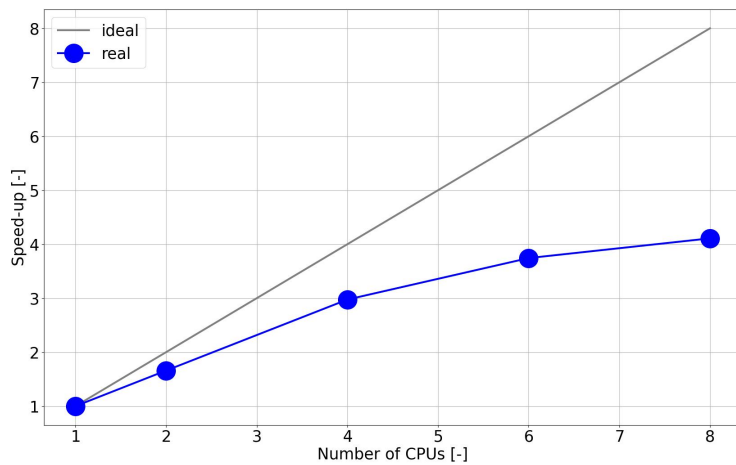


**Figure 28:** Speed-up for the 250k element mesh as the CPU count increases.

## Sensitivity analysis

Appendix D presents the first-order sensitivity curves, and Table 17 provides the first-order Sobol indices. The Sobol indices suggest two dominant parameters, the Young modulus and the exponent  $\alpha$  that account for 92.7 % of the variance. The analysis of the curves reveals that an increase in Young's modulus leads to a reduction in displacement, thereby decreasing the ischaemic response. In contrast, increasing the hydraulic permeability of the interstitial fluid and the compressibility of the vessel tends to alleviate ischaemia and enhance the hyperaemic response. An increase in blood hydraulic permeability results in a decreased hyperaemic response. Both ischaemic and hyperaemic responses are further amplified by an increase in the exponent  $\alpha$ . Interestingly, the Young modulus mainly impacts the displacement magnitude, whereas the other parametric factor played an important role in the hysteresis response of the model in the flux-displacement curves.

## 9 In vivo evaluation of a two-compartment model

Parameter	$\theta_i$ or $\theta_{ij}$ [IU]	$S_i$ or $S_{ij}$ [%]
Young Modulus (E)	$2.00 \times 10^{-1}$	52.78
$\alpha$ (Eq. 90)	$-1.74 \times 10^{-1}$	39.87
Vessel Compressibility ( $K$ )	$5.83 \times 10^{-2}$	4.46
Hydraulic permeability ISF ( $L^l$ )	$4.68 \times 10^{-2}$	2.88
Hydraulic permeability Blood ( $L_0^b$ )	$-2.07 \times 10^{-3}$	$5.64 \times 10^{-3}$

**Table 17:** First-order sobol indices sorted from the largest to the lowest impact on the solution.

The results of the second-order sensitivity analysis, including  $\theta_i$ ,  $\theta_{ij}$ ,  $S_i$ ,  $S_{ij}$ , are provided in Table 18 and are sorted in increasing order of  $S_i$  and  $S_{ij}$ .

Parameter	$\theta_i$ or $\theta_{ij}$ [IU]	$S_i$ or $S_{ij}$ [%]
( $E, \alpha$ )	$-7.90 \times 10^{-1}$	50.9
( $\alpha, K$ )	$-6.90 \times 10^{-1}$	38.9
Young Modulus (E)	$2.00 \times 10^{-1}$	3.28
( $E, K$ )	$1.86 \times 10^{-1}$	2.81
$\alpha$ (Eq. 90)	$-1.74 \times 10^{-1}$	2.48
( $E, L^l$ )	$1.08 \times 10^{-1}$	0.94
Vessel Compressibility ( $K$ )	$5.83 \times 10^{-2}$	0.27
( $L_0^b, \alpha$ )	$-4.76 \times 10^{-2}$	0.19
Hydraulic permeability ISF ( $L^l$ )	$4.68 \times 10^{-2}$	0.17
( $L_0^b, K$ )	$-8.94 \times 10^{-3}$	$6.53 \times 10^{-3}$
( $L^l, L_0^b$ )	$-5.80 \times 10^{-3}$	$2.75 \times 10^{-3}$
( $L^l, K$ )	$3.83 \times 10^{-3}$	$1.19 \times 10^{-3}$
( $L^l, \alpha$ )	$2.22 \times 10^{-3}$	$4.03 \times 10^{-4}$
Hydraulic permeability Blood ( $L_0^b$ )	$-2.07 \times 10^{-3}$	$3.50 \times 10^{-4}$
( $E, L_0^b$ )	$-1.19 \times 10^{-3}$	$1.16 \times 10^{-4}$

**Table 18:** Second-order sobol indices sorted from the largest to the lowest impact on the solution.

Sensitivity analysis reveals that the interaction between parameters influences the variance of the solution, accounting for almost 94 % of this variance. However, three main parameters ( $E$ ,  $\alpha$ ,  $K$ ) now predominantly impact the variance of the solution, both independently and through their interactions, accounting for 98.7 % of this variance. Therefore, blood flow is mainly influenced by the choice of the Young modulus, the exponent  $\alpha$  describing the non-linearity of the permeability, but also  $K$  the compressibility of the vessel.

## Model capacity to reproduce the flow

This section aims at analysing the 3D blood flow obtained in the generic FE model considering the experimental procedure described in Section 9.3. For the sake of comparison, the LDF signal has been post-processed to show the relative variation to the basal skin blood flow at each time point. Three parameter sets have been considered (considering the international standard units):

- Set<sub>1</sub>:  $[E, L^l, L^b, \alpha, K] = [2 \times 10^5, 10^{-14}, 10^{-9}, 3, 10^3]$
- Set<sub>2</sub>:  $[E, L^l, L^b, \alpha, K] = [2 \times 10^5, 10^{-13}, 10^{-9}, 5, 10^3]$
- Set<sub>3</sub>:  $[E, L^l, L^b, \alpha, K] = [8 \times 10^4, 10^{-13}, 10^{-9}, 6, 10^3]$

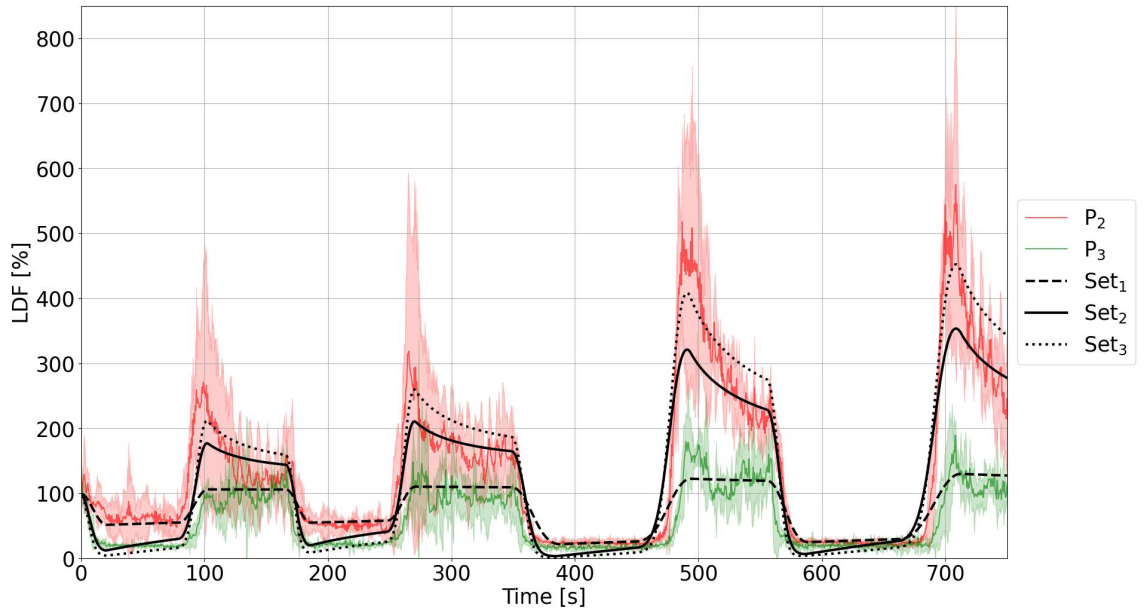


**Figure 29:** Three different sets of parameters were computed to cover different possible outputs of the model. The results are superimposed on the IQR experimental corridor of the maximal and minimal observed responses, highlighting the capacity of the model to qualitatively reproduce both the ischaemic and hyperaemic responses.

The resulting micro-circulatory response (computed LDF signal) is superimposed on the experimental corridor Figure 29. We observe that two of the three models provide post-occlusive reactive hyperaemia. These are the two sets with the highest values of  $\alpha$ . The other one, Set<sub>1</sub> allows for a more accurate reproduction of the

## 9 *In vivo* evaluation of a two-compartment model

ischaemic plateau, but no hyperaemia is observed. A deeper analysis of the  $\text{Set}_2$  is provided in Figure 30.

Initially, the boundary condition allows for a blood flux of approximately  $400 \mu\text{m s}^{-1}$ . During the establishment of this flux, in the initial five time steps, vascular porosity increases slightly to 9 % in the region of interest. During the first two cycles, the application of the load induces a compressive displacement, reducing the flux directly beneath the load. The overall flux adapts by circumventing this region. A concurrent reduction in vascular porosity is observed, indicating the onset of occlusion processes with increased vascular porosity before the loaded region (vasodilation).

Upon releasing the load, strong reflux is observed beneath the probe, characterised by increased blood velocity and an accompanying increase in vascular porosity. This is followed by a gradual relaxation of the flow, returning it to the initial homeostatic state. When a higher load is applied, the maximum displacement reaches 0.6mm, resulting in an increase in intensity and depth of ischaemia, as well as a more pronounced post-occlusive reactive hyperaemia effect. ischaemia, as well as a more pronounced post-occlusive reactive hyperaemia effect.

## Discussion

The primary objective of this study was to evaluate the feasibility of employing a two-compartment porous media mechanical model in conjunction with experimental measurements of skin micro-circulatory haemodynamics. This helps in the reproduction of the mechanical response of the skin under indentation loading *in vivo* in the perspective of injury prevention. Laser Doppler flowmetry (LDF) was used as the experimental method to assess the micro-circulatory response of the skin under load conditions. The load was applied using the LDF probe itself.

LDF is a well-established, non-invasive, real-time technique for measuring micro-circulatory blood flow of the skin (Folgsom-Correa and Nogueira 2012; Poffo et al. 2014; Varghese et al. 2009). However, the method has known limitations. For example, the LDF technique provides measurements from a limited penetration depth of 0.5-1 mm (Fredriksson et al. 2009; Humeau-Heurtier et al. 2013; Poffo et al. 2014), which may not fully capture deeper vascular responses. Furthermore, the precision of LDF is sensitive to various external factors, such as probe position,

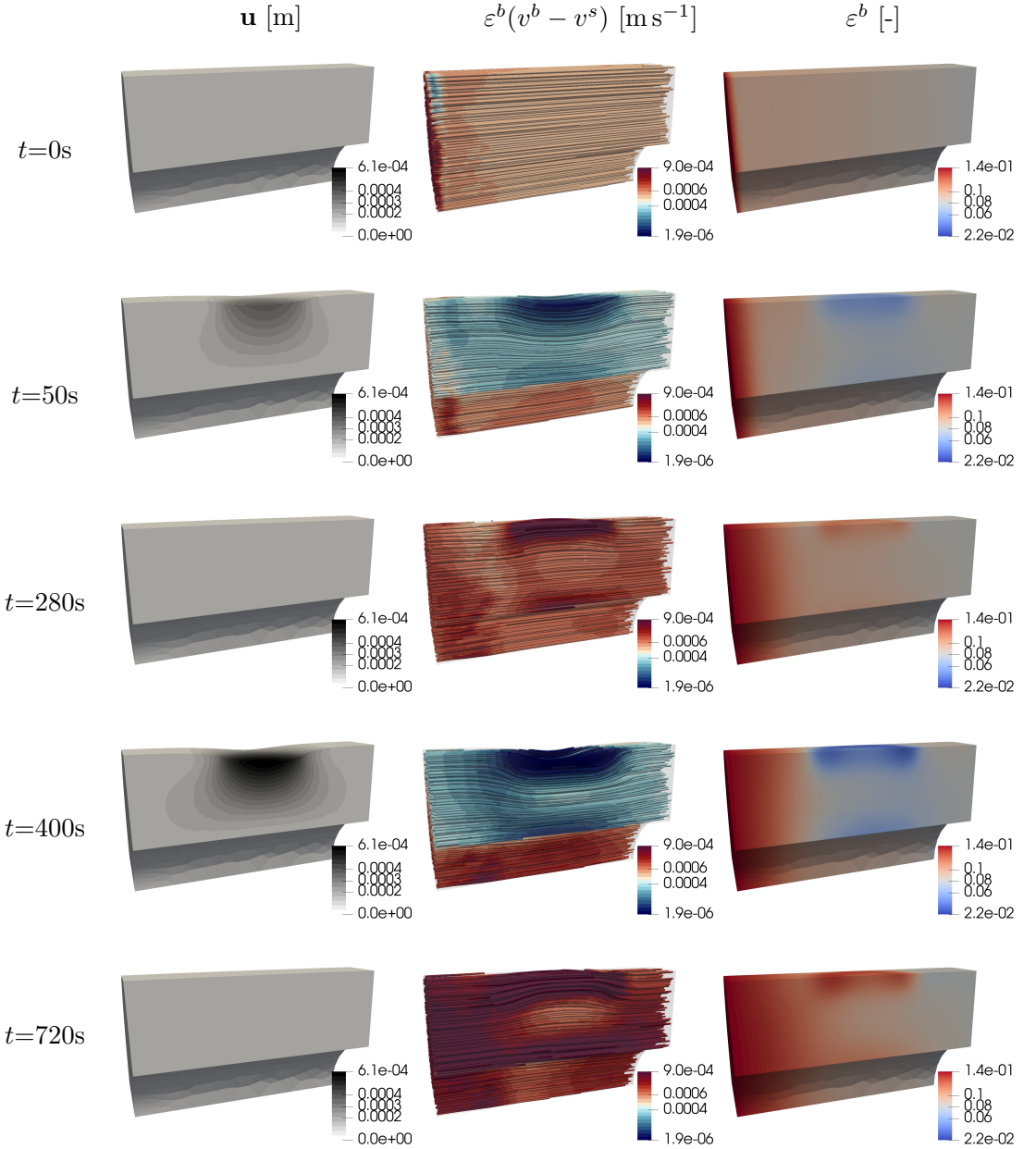


**Figure 30:** From left to right: displacement magnitude, blood flow, vascular porosity maps. The results represent the initial state, the first cycle ischaemia ( $t = 50$  s), the second hyperaemic peak ( $t = 280$  s), a maximum ischaemia ( $t = 400$  s) and the maximum hyperaemia ( $t = 720$  s). When indenting the skin, the flow is locally reduced and the vascular porosity decreases. Conversely, vasodilation is observed with an increase blood flow during and directly after the release of the load. During the indented phase, vasodilations seems to occur before the indented location.

## *9 In vivo evaluation of a two-compartment model*

contact force, skin temperature, and patient-specific characteristics such as tobacco use (Ajan et al. 2024; Kouadio et al. 2018; Nogami et al. 2019; Petrofsky and Berk 2012). Therefore, stringent calibration procedures and the control of experimental conditions are critical to ensuring the reproducibility and reliability of LDF measurements. To overcome these limitations, smokers were excluded from the study and the temperature was measured to limit bias in the analysis while ensuring a thermal stabilisation period prior to the start of the experiment. This ensures the reproducibility and reliability of the LDF measurements.

Although LDF has been used to diagnose micro-circulatory disorders, it is essential to consider the reference range and variability of the measured parameters to validly interpret LDF values in individual patients (Mrowietz et al. 2017). However, the LDF measurements allowed for the identification of values consistent with those reported in the literature, with an initial basal skin blood flow of  $24.1 \pm 15.3$  AU. Borchardt et al. 2017 reported similar basal skin blood flow values for the forearm. In their results, pressure-induced effects did not result in significant changes compared to basal blood flow from the skin. However, a significant increase of 105.5% was observed, from  $32.7 \pm 12.6$  AU to  $67.2 \pm 20.6$  AU, over a period of 1 hour after direct cold atmospheric plasma treatment for 270 s. Fei et al. 2018 reported forearm blood flow basal skin blood flow values of  $33 \pm 6.5$  AU measured by Laser Speckle Contrast Imaging (LSCI) and  $60 \pm 11.5$  AU measured by Laser Doppler Perfusion Imaging (LDPI). Changes in blood flow during iontophoresis showed an increase of  $724 \pm 412\%$  (LDPI) and  $259 \pm 87\%$  (LSCI) from basal skin blood flow.

In terms of fingertip blood perfusion, studies such as Saha et al. 2020 reported basal skin blood flow values around 20 AU. Volkov et al. 2017 described procedures including the recording of background perfusion and velocity (0.3 – 0.5 min), occlusion testing (1 – 1.5 min), and post-occlusion recordings (0.1 – 1 min), with occlusion pressure set at approximately 29.3 kPa. LDF amplitudes were also reported to vary between 10 and 60 AU for the fingers (Mrowietz et al. 2019).

The experiment also aligns with the literature on the observed behaviour. Similarly to Volkov et al. 2017, the load application induces a reduced LDF signal. When the load is released, strong reflux is observed. This reflux is called post-occlusive reactive hyperaemia (PORH) (Balasubramanian et al. 2021; Fuchs et al. 2017). Ostergren and Fagrell 1986 identified during the PORH a capillary blood velocity that reached a maximum of  $1.2 \pm 0.7$  mm s<sup>-1</sup> at  $7.8 \pm 2.4$  seconds after cuff release.

PORH is a subcategory of reactive hyperaemia (RH), which is a physiological response that leads to increased microvascular blood flow to the skin. Optical coherence tomography (OCT) has been used to visualise and quantify the microvascular changes of the skin in response to RH in humans, demonstrating an increase in microvascular diameter, flow rate, speed and density after a stimulus (Argarini et al. 2020; Wang-Evers et al. 2021). Four major factors have been proposed to be involved in the hyperaemic response: metabolic vasodilators, endothelial vasodilators, myogenic response, and sensory nerves (Cracowski et al. 2006). This hyperaemic state also explains the increase in temperature (thermal hyperaemia), since increased local blood flow to the skin leads to thermal hyperaemia (Basiladze et al. 2015; Choi et al. 2014; Golay et al. 2004; Horn et al. 2022; Leo et al. 2020; Rosenberry and Nelson 2020; Wong et al. 2006).

No significant differences were found between male and female populations for relative LDF variations with basal blood flow of the skin. This suggests that despite potential differences in absolute perfusion levels, the microvascular response to compressive loading and subsequent hyperaemia remains comparable between the sexes. The lack of significant differences ( $p > 0.3$  for all conditions) indicates that sex-related factors do not substantially influence relative ischaemic and hyperaemic responses, at least within the population studied. This finding is consistent with previous research suggesting that while baseline skin blood flow may vary due to differences in skin temperature, vascular tone, or hormonal influences, the fundamental regulatory mechanisms of reactive hyperaemia and ischaemic adaptation are preserved between sexes. Furthermore, the observed normal distribution of the results supports the robustness of the experimental design, strengthening the reliability of the findings. These results further highlight the importance of normalising the LDF values to basal blood flow, as absolute perfusion measurements alone may introduce variability that is not related to the actual microvascular response. This normalisation approach reduces inter-individual differences and allows for a more accurate comparison of vascular reactivity across different populations. Future studies with larger sample sizes and additional physiological parameters (e.g., hormone levels, vascular compliance) could provide further insight into possible subtle differences that were not detectable in the present study. However, within the current experimental framework, our findings suggest that the physiological response to compressive loading is largely independent of sex, reinforcing the validity of using mixed-sex data in similar studies.

## 9 *In vivo* evaluation of a two-compartment model

To reproduce the mechanical behaviour and micro-circulatory response of human skin *in vivo*, a two-compartment model inspired by Sciumè 2021 was developed, calculated in FEniCSx 0.9.0 and compared to the experiment. This model is based on the Thermodynamically Constrained Average Theory (TCAT) and accounts for both the fluid behaviour of the interstitial fluid and the vascular network, paving the way for the integration of biological exchange as proposed in Appendix B. Powered by the characteristic times of the experiment and a preliminary 1D consolidation problem in a column, the theory was simplified to provide a consistent comparison with the experiment. In addition, in the absence of data on the displacement field, no calibration was achievable, so parameters from the literature were used, and a sensitivity analysis was performed.

Sensitivity analysis revealed that three main parameters governed the response to blood flow. Young's modulus directly affected the displacement of the sample and, therefore, the level of occlusion. The other two parameters are related to the choice of exponent in the constitutive permeability law and the choice of compressibility of the vessel in the constitutive law of vascular porosity. This suggests that the choice and definition of the vascular porosity state law and the permeability state law are crucial for a physically relevant interpretation of the model. This can be explained in more detail by the non-Newtonian behaviour of blood. In fact, when blood is subjected to compressive loads, the deformation rates and the resulting shear stress can lead to changes in viscosity. At low deformation rates, cell aggregations increase viscosity, while at higher rates, these structures break down, leading to a decrease in viscosity (Javadi et al. 2023). The compressive load can also affect the formation of the cell-free layer (CFL) in micro-vessels, which influences blood flow and viscosity. Higher compressive loads can enhance the deformability of red blood cells, affecting CFL and overall blood rheology (Yalcin et al. 2015; Zhang 2011).

In the proposed study, three different simulations were further compared to the experiment to qualitatively assess the capacity of the model to reproduce the experiment. One of them allowed for a precise reproduction of the ischaemic plateau, whereas the two others highlighted the capacity to capture both ischaemia and hypoxia, supporting the capacity of this physically based model to account for skin micro-circulation. However, this study also supports the need to develop experimental procedures that monitor both mechanical fields (force/displacement) and fluid flows to further validate such models and inform their boundary conditions.

Therefore, experiment should concentrate on the explicit evaluation of skin fluids flow *in vivo*. Then, biochemistry and nutrient exchanges could be introduced and evaluated as proposed in the proof of concept of Appendix B.

## Conclusion

This study introduces a hierarchical modelling framework to integrate micro-circulation dynamics within a porous medium. The proposed theory conceptualises the interstitium as a biphasic system, distinguishing between the characteristic timescales of cells and the interstitial fluid. Appendix A extends the model to account for biological transport processes, such as oxygen diffusion.

To evaluate the model, a one-dimensional column consolidation test was performed. Initial results indicated that cell viscosity introduces an additional characteristic timescale, separate from that governed by interstitial fluid flow. Notably, when the cell viscosity is high and the timescales are short, the cells behave similarly to a solid.

Building on these insights, the model was simplified to correspond with an experimental study focused on healthy skin. A sensitivity analysis, based on material properties from the existing literature, identified three key parameters with strong interdependence: Young's modulus, the exponent of the permeability law, and the assumed compressibility of the vessel. Since displacement data was unavailable, parameter calibration was not performed, highlighting the need for further experimental studies to refine mechanical property estimates. However, the model successfully captured the qualitative features of both ischaemia and post-occlusive reactive hyperaemia within the experimental scope.

All numerical simulations were performed using the open-source software FEniCSx v0.9.0. To promote transparency and reproducibility, anonymised experimental data and associated finite element code have been openly shared on GitHub.

## Acknowledgments

This research was funded in whole or in part by the Luxembourg National Research Fund (FNR), grant reference No. 17013182. For the purpose of open access, the author has applied a Creative Commons Attribution 4.0 International (CC BY 4.0) licence to any Author-Accredited manuscript version arising from this submission.

The authors also acknowledge the use of the Cassiopee Arts et Métiers Institute of Technology HPC Centre made available for conducting the research reported in this article.

## Declarations

**Competing interests:** The authors declare that they have no known competing financial interests or personal relationships that could have appeared to influence the work reported in this article.

**Supplementary material:** The Python codes corresponding to the FEniCSx models and the experimental data of this article are made available at the following link: [Th0masLavigne/2-compartment-poromechanical-and-LDF-measurement.git](https://github.com/Th0masLavigne/2-compartment-poromechanical-and-LDF-measurement.git).

## Appendix A: Mono-phasic interstitium: Simplified Variational Form

The variational form is obtained considering  $(q^c, q^l, q^b, \mathbf{w})$  the test functions defined in the mixed space  $L_0^2(\Omega) \times L_0^2(\Omega) \times [H^1(\Omega)]^3$ . The solutions of the problem are the capillary pressure, the cell pressure, the blood pressure, and displacement of the solid:  $(p^l, p^b, \mathbf{u}^s)$ . The problem to be solved reads:

$$\mathbf{u}^s = \mathbf{u}_{\text{imposed}} \text{ on } \partial\Omega_u \quad (141)$$

$$p^\alpha = p_{\text{imposed}} \text{ on } \partial\Omega_p^\alpha \quad (142)$$

$$\begin{aligned} & \int_\Omega \frac{k^b}{\mu^b} \nabla p^b \nabla q^l d\Omega + \int_\Omega \frac{k^l}{\mu^l} \nabla p^l \nabla q^l d\Omega \\ & + \int_\Omega \nabla \cdot \left( \frac{D^s \mathbf{u}^s}{Dt} \right) q^l d\Omega = 0, \forall q^l \in L_0^2(\Omega) \end{aligned} \quad (143)$$

$$\begin{aligned} & \int_\Omega \tilde{C}_{e,p} \frac{D^s p^l}{Dt} q^b d\Omega - \int_\Omega \tilde{C}_{e,p} \frac{D^s p^b}{Dt} q^b d\Omega \\ & + \int_\Omega \frac{k^b}{\mu^b} \nabla p^b \nabla q^b d\Omega + \int_\Omega \varepsilon^b \nabla \cdot \left( \frac{D^s \mathbf{u}^s}{Dt} \right) q^b d\Omega = 0, \forall q^b \in L_0^2(\Omega) \end{aligned} \quad (144)$$

$$\begin{aligned} & \int_\Omega \mathbf{t}^{\text{eff}}(\mathbf{u}^s) : \nabla \mathbf{w} d\Omega - \int_\Omega (1 - \varepsilon^b) p^l \nabla \cdot \mathbf{w} d\Omega \\ & - \int_\Omega \varepsilon^b p^b \nabla \cdot \mathbf{w} d\Omega - \int_{\Gamma_s} \mathbf{t}^{\text{imposed}} \cdot \mathbf{w} d\Gamma_s = 0, \forall \mathbf{w} \in [H^1(\Omega)]^3 \end{aligned} \quad (145)$$

## Appendix B: Oxygen Biochemistry

Consider the exchange of oxygen between the blood compartment and cells in the extravascular space through the interstitial fluid. The idea is to establish the mass conservation equation of the blood with a mass exchange between the blood and the interstitial fluid and a consumption law by the cells as an extension of the model proposed by Sciumè 2021.

### Strong form

Let  $\omega^{O2,l}$  be the mass fraction of oxygen in the IF and  $\omega^{O2,b}$  the mass fraction of oxygen in the blood.  $\omega^{O2,l}$  is a new unknown in the problem to be computed. According to the formulas in Sciumè et al. 2021, the mass conservation of the species reads:

$$\begin{aligned} & \underbrace{\frac{\partial}{\partial t}(S^l \varepsilon \rho^l \omega^{O2,l})}_{\text{Accumulation rate}} + \underbrace{\nabla \cdot (S^l \varepsilon \rho^l \omega^{O2,l} \mathbf{v}^l)}_{\text{Outward of species advective transport}} \\ & + \underbrace{\nabla \cdot (S^l \varepsilon \rho^l \omega^{O2,l} \mathbf{u}^{O2,l})}_{\text{Outward of species diffusive transport}} - \underbrace{S^l \varepsilon r^{O2,l} \mathbf{u}^{O2,l}}_{\text{Intraphase reactive exchange of mass}} \\ & + \underbrace{\sum_{\kappa} M^{O2,l \rightarrow O2,\kappa}}_{\text{Intraphase mass transport of the species}} + \underbrace{\omega^{O2,l} \sum_{\kappa} M^{\kappa \rightarrow IF}}_{\text{Interphase mass transport}} = 0 \end{aligned} \quad (146)$$

In our case, this equation can be re-written:

$$\begin{aligned} & \underbrace{\frac{D^s}{Dt}(S^l \varepsilon \rho^l \omega^{O2,l})}_{\text{Accumulation rate}} + \underbrace{\nabla \cdot (S^l \varepsilon \rho^l \omega^{O2,l} (\mathbf{v}^l - \mathbf{v}^s))}_{\text{Infiltration}} \\ & + \underbrace{\nabla \cdot (S^l \varepsilon \rho^l \omega^{O2,l} \mathbf{u}^{O2,l})}_{\text{Diffusion}} + \underbrace{S^l \varepsilon \rho^l \omega^{O2,l} \nabla \cdot \mathbf{v}^s}_{\text{ECM deformation}} \\ & = \underbrace{M^{O2,b \rightarrow O2,l}}_{\text{Blood to IF transport}} - \underbrace{M^{O2,l \rightarrow O2,c}}_{\text{O2 consumption from the cells}} \end{aligned} \quad (147)$$

where the increase of oxygen from blood is driven by (exchange proportional to the

vessel wall area):

$$M^{O2,b \rightarrow O2,l} = h_v \varepsilon^b (\omega^{O2,b} - \omega^{O2,l}) \quad (148)$$

where  $\omega^{O2,b}$  is the mass fraction of oxygen within the blood and is assumed constant. The coefficient  $h_v$  is representative of the vessel wall permeability.

The consumption of oxygen from the cells is proportional to the fluid saturation in cells and is given by ( $\omega_{crit}$  is the hypoxia threshold obtained from Henry's law and  $\gamma_0$  relates to the cell metabolism):

- if  $\omega^{O2,l} \geq \omega_{crit}$ :

$$M^{O2,l \rightarrow O2,c} = \gamma_0 S^c \varepsilon \quad (149)$$

- if  $\omega^{O2,l} \leq \omega_{crit}$ :

$$M^{O2,l \rightarrow O2,c} = \gamma_0 S^c \varepsilon \left[ \frac{1}{2} \left( 1 - \cos \pi \frac{\omega^{O2,l}}{\omega_{crit}} \right) \right] \quad (150)$$

Introducing Fick's law, the diffusive flux of oxygen reads:

$$\omega^{O2,l} \mathbf{u}^{O2,l} = -D_{eff}^{O2,l} \nabla \omega^{O2,l} \quad (151)$$

where  $D_{eff}^{O2,l}$  is the effective diffusion coefficient of oxygen:

$$D_{eff}^{O2,l} = D_0^{O2,l} (\varepsilon^l)^\delta = D_0^{O2,l} (S^l \varepsilon)^\delta \quad (152)$$

where  $D_0^{O2,IF}$  is the oxygen diffusion coefficient in the bulk interstitial fluid and  $\delta$  is a coefficient related to the tortuosity of the medium.

## 9 In vivo evaluation of a two-compartment model

Considering a constant density  $\rho^l$ , the mass conservation becomes:

$$\begin{aligned} & S^l \varepsilon \frac{D^s}{Dt}(\omega^{O2,l}) + S^l \omega^{O2,l} \frac{D^s}{Dt}(\varepsilon) + \varepsilon \omega^{O2,l} \frac{D^s}{Dt}(S^l) \\ & - \nabla \cdot \left( \frac{k^l}{\mu^l} \omega^{O2,l} \nabla p^l \right) - \nabla \cdot (S^l \varepsilon D_{eff}^{O2,l} \nabla \omega^{O2,l}) \\ & + S^l \varepsilon \omega^{O2,l} \nabla \cdot \mathbf{v}^s = \frac{1}{\rho^l} \left( \frac{O2,b \rightarrow O2,l}{M} - \frac{O2,l \rightarrow O2,c}{M} \right) \end{aligned} \quad (153)$$

Using the divergence of a product rule, we get:

$$\nabla \cdot \left( \frac{k^l}{\mu^l} \omega^{O2,l} \nabla p^l \right) = \omega^{O2,l} \nabla \cdot \left( \frac{k^l}{\mu^l} \nabla p^l \right) + \frac{k^l}{\mu^l} \nabla \omega^{O2,l} \nabla p^l \quad (154)$$

Then, Equation 153 becomes:

$$\begin{aligned} & (1 - S^c) \varepsilon \frac{D^s}{Dt}(\omega^{O2,l}) \\ & + \omega^{O2,l} \underbrace{\left( \frac{D^s}{Dt}((1 - S^c)\varepsilon) - \nabla \cdot \left( \frac{k^l}{\mu^l} \nabla p^l \right) + (1 - S^c)\varepsilon \nabla \cdot \mathbf{v}^s \right)}_{(119) \Rightarrow =0} \\ & - \frac{k^l}{\mu^l} \nabla \omega^{O2,l} \nabla p^l - \nabla \cdot ((1 - S^c)\varepsilon D_{eff}^{O2,l} \nabla \omega^{O2,l}) \end{aligned} \quad (155)$$

$$\begin{aligned} & = \frac{1}{\rho^l} \left( \frac{O2,b \rightarrow O2,l}{M} - \frac{O2,l \rightarrow O2,c}{M} \right) \\ & (1 - S^c) \varepsilon \frac{D^s}{Dt}(\omega^{O2,l}) \\ & - \frac{k^l}{\mu^l} \nabla \omega^{O2,l} \nabla p^l - \nabla \cdot ((1 - S^c)\varepsilon D_{eff}^{O2,l} \nabla \omega^{O2,l}) \\ & = \frac{1}{\rho^l} \left( \frac{O2,b \rightarrow O2,l}{M} - \frac{O2,l \rightarrow O2,c}{M} \right) \end{aligned} \quad (156)$$

## Variational form

Consider  $(w_o)$  the test function defined in the space  $L_0^2(\Omega)$ . The following system of equations completes the system of equations in the previous section.

Consider  $(q^c, q^l, q^b, \mathbf{w}, w_o)$  the test functions defined in the mixed space  $L_0^2(\Omega) \times L_0^2(\Omega) \times [H^1(\Omega)]^3 \times L_0^2(\Omega)$ . The solutions of the problem are the capillary pressure, the cell pressure, the blood pressure, the displacement of the solid, and the fraction of the oxygen mass:  $(p^l, p^{lc}, p^b, \mathbf{u}^s, \omega^{O2,l})$ .

Using Equations 85, 111, 117, 121, and 156, the problem to be solved reads:

$$\mathbf{u}^s = \mathbf{u}_{\text{imposed}} \text{ on } \partial\Omega_u \quad (157)$$

$$p^\alpha = p_{\text{imposed}} \text{ on } \partial\Omega_p^\alpha \quad (158)$$

$$\begin{aligned} & \int_\Omega C_{m,c} \frac{D^s p^{lc}}{Dt} q^c d\Omega \\ & + \int_\Omega S^c \frac{k^b}{\mu^b} \nabla p^b \nabla q^c d\Omega \\ & + \int_\Omega \frac{k^c}{\mu^c} \nabla p^l \nabla q^c d\Omega \\ & - \int_\Omega \frac{k^c}{\mu^c} \nabla p^{lc} \nabla q^c d\Omega \\ & + \int_\Omega S^c \nabla \cdot \left( \frac{D^s \mathbf{u}^s}{Dt} \right) q^c d\Omega = 0, \forall q^c \in L_0^2(\Omega) \end{aligned} \quad (159)$$

$$\begin{aligned} & \int_\Omega \frac{k^b}{\mu^b} \nabla p^b \nabla q^l d\Omega \\ & + \int_\Omega \left[ \frac{k^c}{\mu^c} + \frac{k^l}{\mu^l} \right] \nabla p^l \nabla q^l d\Omega \\ & - \int_\Omega \frac{k^c}{\mu^c} \nabla p^{lc} \nabla q^l d\Omega \\ & + \int_\Omega \nabla \cdot \left( \frac{D^s \mathbf{u}^s}{Dt} \right) q^l d\Omega = 0, \forall q^l \in L_0^2(\Omega) \end{aligned} \quad (160)$$

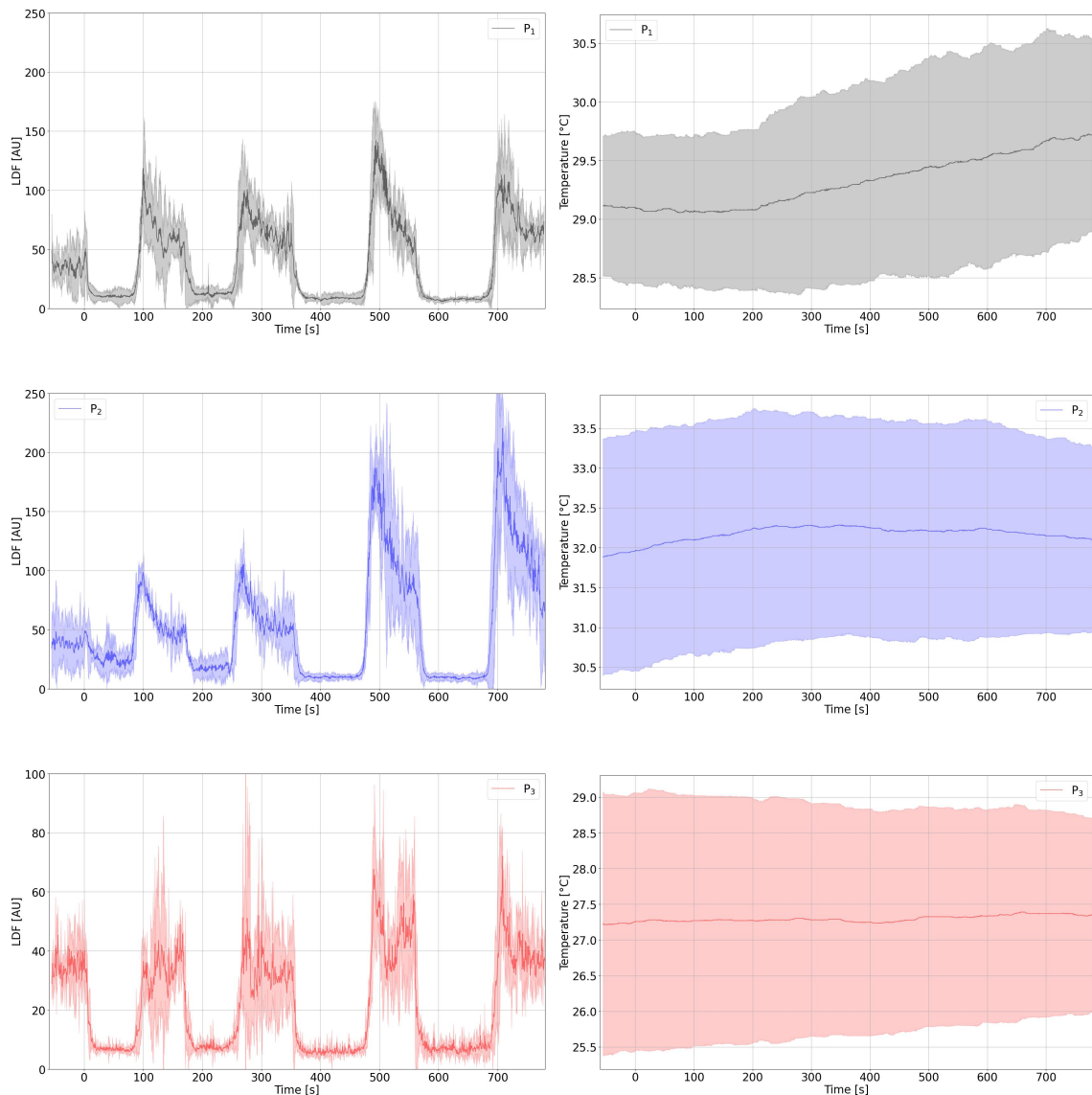
$$\begin{aligned}
 & \int_{\Omega} C_{e,p} \frac{\mathrm{D}^s p^l}{\mathrm{D}t} q^b \mathrm{d}\Omega \\
 & - \int_{\Omega} C_{e,p} C_{state} \frac{\mathrm{D}^s p^{lc}}{\mathrm{D}t} q^b \mathrm{d}\Omega \\
 & - \int_{\Omega} C_{e,p} \frac{\mathrm{D}^s p^b}{\mathrm{D}t} q^b \mathrm{d}\Omega \\
 & + \int_{\Omega} \frac{k^b}{\mu^b} \nabla p^b \nabla q^b \mathrm{d}\Omega \\
 & + \int_{\Omega} \varepsilon^b \nabla \cdot \left( \frac{\mathrm{D}^s \mathbf{u}^s}{\mathrm{D}t} \right) q^b \mathrm{d}\Omega = 0, \forall q^b \in L_0^2(\Omega)
 \end{aligned} \tag{161}$$

$$\begin{aligned}
 & \int_{\Omega} \mathbf{t}^{\text{eff}}(\mathbf{u}^s) : \nabla \mathbf{w} \mathrm{d}\Omega \\
 & - \int_{\Omega} (1 - \varepsilon^b) (p^l - S^c p^{lc}) \nabla \cdot \mathbf{w} \mathrm{d}\Omega \\
 & - \int_{\Omega} \varepsilon^b p^b \nabla \cdot \mathbf{w} \mathrm{d}\Omega \\
 & - \int_{\Gamma_s} \mathbf{t}^{\text{imposed}} \cdot \mathbf{w} \mathrm{d}\Gamma_s = 0, \forall \mathbf{w} \in [H^1(\Omega)]^3
 \end{aligned} \tag{162}$$

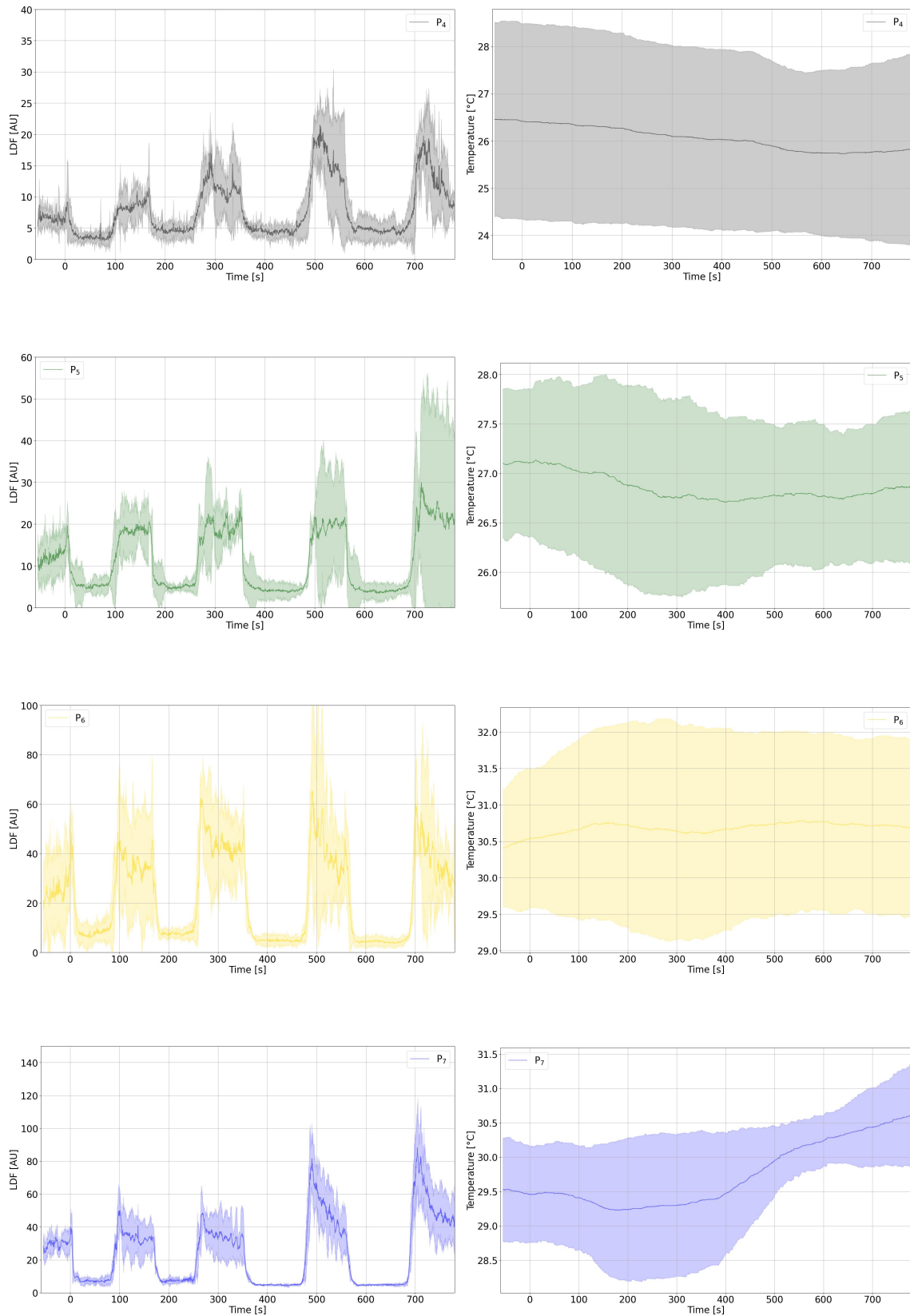
$$\begin{aligned}
 & \int_{\Omega} (1 - S^c) \varepsilon \frac{\mathrm{D}^s}{\mathrm{D}t} (\omega^{O2,l}) w_o \mathrm{d}\Omega \\
 & - \int_{\Omega} \frac{k^l}{\mu^l} \nabla \omega^{O2,l} \nabla p^l w_o \mathrm{d}\Omega \\
 & + \int_{\Omega} (1 - S^c) \varepsilon D_{eff}^{O2,l} \nabla \omega^{O2,l} \nabla w_o \mathrm{d}\Omega \\
 & = \int_{\Omega} \frac{1}{\rho^l} \left( M^{O2,b \rightarrow O2,l} - M^{O2,l \rightarrow O2,c} \right) w_o \mathrm{d}\Omega, \forall w_o \in L_0^2(\Omega)
 \end{aligned} \tag{163}$$

## Appendix C: Individual LDF signals for the 10 subjects

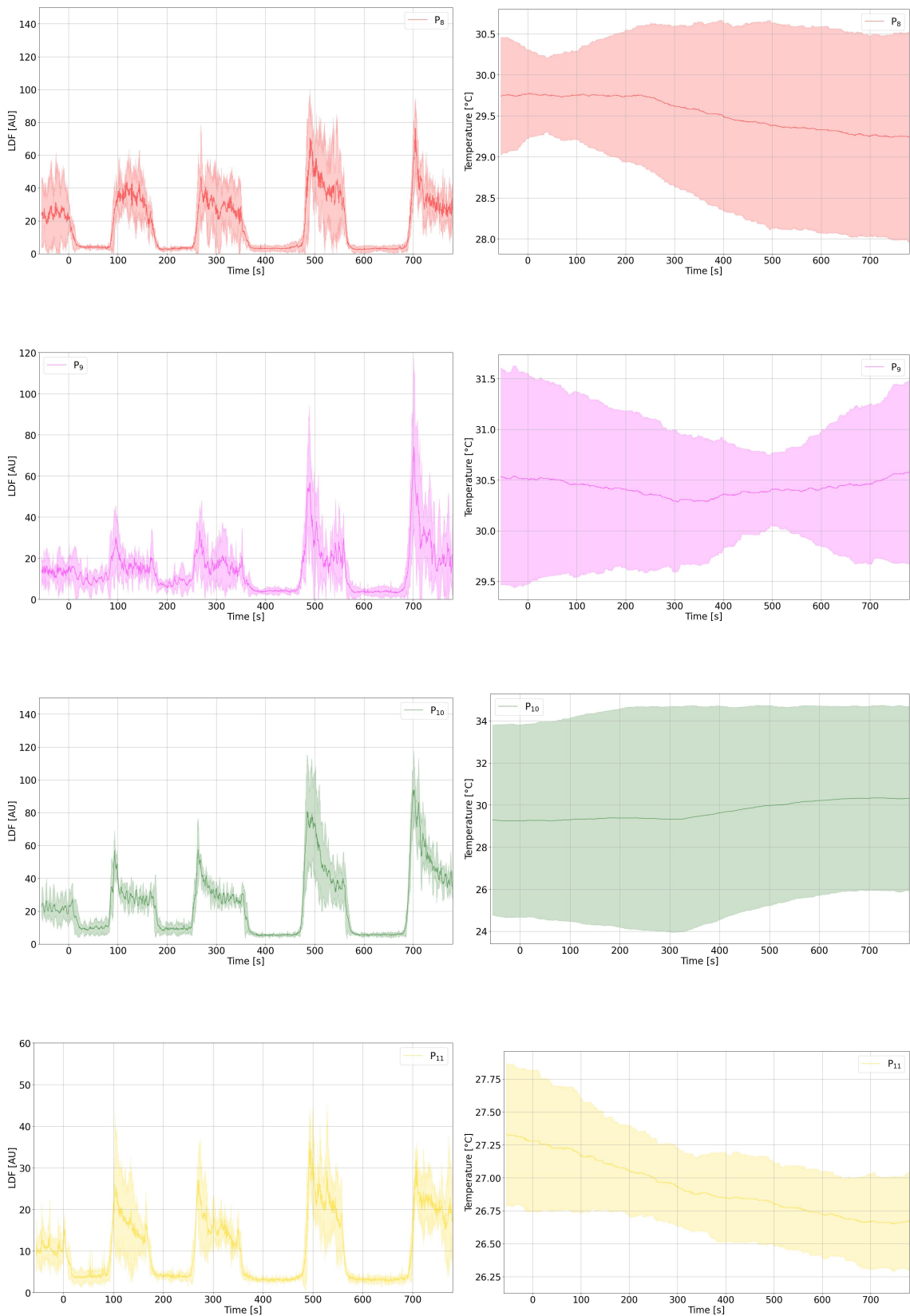
This appendix provides the median LDF and temperature signals with the IQR corridor for each of the patients.



## 9 In vivo evaluation of a two-compartment model



## 9 In vivo evaluation of a two-compartment model



## Appendix D: Sensitivity Curves

This appendix provides the sensitivity curves for each parameter (first-order sensitivity) in Figure 31.

The analysis reveals that an increase in Young's modulus leads to a reduction in displacement, thereby decreasing the ischaemic response. In contrast, increasing the hydraulic permeability of the interstitial fluid and the compressibility of the vessel tends to alleviate ischaemia and enhance the hyperaemic response. In contrast, an increase in blood hydraulic permeability results in a diminished hyperaemic response. Both ischaemic and hyperaemic responses are further amplified by an increase in the exponent  $\alpha$ . Interestingly, the Young modulus mainly impacts the displacement magnitude, whereas the other parametric factor played an important role in the hysteresis response of the model in the flux-displacement curves.

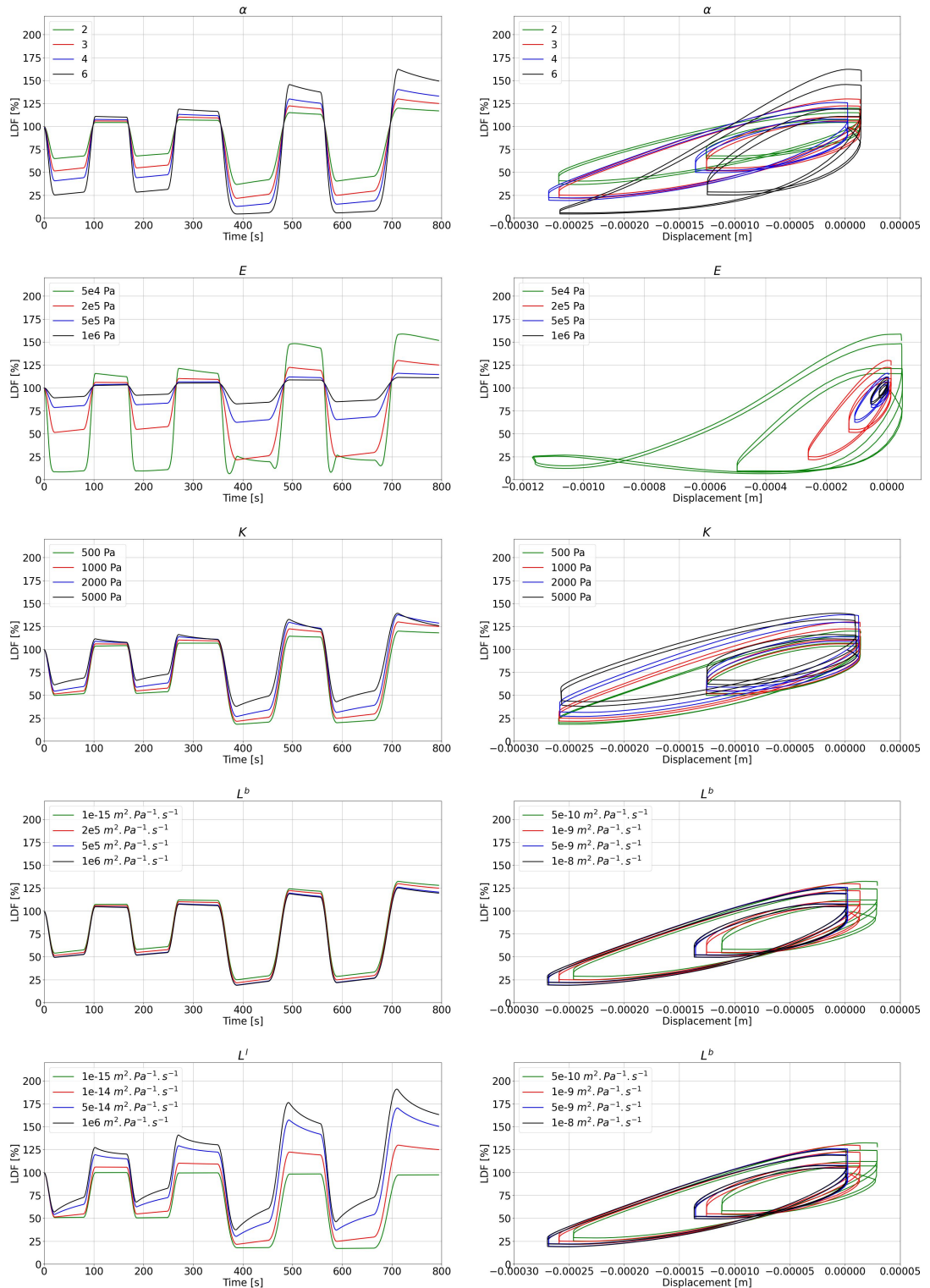


**Figure 31:** Impact of the parameters on the model output: first-order sensitivity. Each parameter was independently varied to study the impact on the model response.

## Appendix E: Parallel environment install

This procedure was used to install FEniCSx on the HPC Cassiopee (Red Hat Enterprise Linux 8.10).

### Install

- Get version 0.23.1 of spack:

```
1 wget https://github.com/spack/spack/releases/download/
2 v0.23.1/spack-0.23.1.tar.gz
```

- untar the archive:

```
1 tar -xf spack-0.23.1.tar.gz
```

- Optional: disable the local configuration of spack (current user home directory). Useful if you have multiple versions of spack

```
1 export SPACK_DISABLE_LOCAL_CONFIG=true
```

- activate spack:

```
1 source spack-0.23.1/share/spack/setup-env.sh
```

- add system compiler to spack (need to be installed in your os):

```
1 spack compiler find
```

- optional: add a decent compiler (useful if you have an old distribution) and add it as compiler to spack:

```
1 spack install gcc@12
2 spack compiler find $(spack location -i gcc@12)
```

- create a spack environment (useful if you want to load several packages at one time):

```
1 spack env create MyFenicsxEnv
```

- activate the environment, add some packages, and install them:

```

1 spack env activate MyFenicsxEnv
2 spack add petsc +fortran +mumps +trilinos +superlu-dist
3 spack add python
4 spack add py-fenics-dolfinx@0.9.0
5 spack add py-numpy
6 spack add py-matplotlib
7 spack add py-pandas
8 spack add py-gmsh
9 spack install

```

Congratulation, you have installed fenicsx 0.9.0, working with mpi!

- create the porous\_fenicsx package:

```

1 cd $PATH/porous_fenicsx
2 python -m pip install .

```

- deactivate your environment:

```
1 spack env deactivate
```

## Use

- activate spack in your session (can be added to your .bashrc):

```
1 source FullPathToSpack/share/spack/setup-env.sh
```

- activate your environment:

```
1 spack env activate MyFenicsxEnv
```

- launch your script in parallel (replace NCPUs with the number of CPUs you want):

```
1 mpirun -n NCPUs python myscript.py
```

- deactivate your environment:

```
1 spack env deactivate
```



## Part V

Towards a better control of  
boundary conditions: method for  
phantom generation and *in silico*  
evaluation



# 10 Towards a better control of boundary conditions: phantoms and *in silico* evaluation

## Table of Contents

---

10.1 Synopsis (FR) . . . . .	209
10.2 Synopsis (EN) . . . . .	211
10.3 Article . . . . .	213

---

### 10.1 Synopsis (FR)

#### Synopsis

L'identification des relations constitutives (évolution de la porosité vasculaire) ainsi que l'identification des paramètres matériaux demeurent un challenge. En effet, les méthodes de calibration ne convergent pas forcément vers une solution unique et, suivant les hypothèses de modélisation, les ordres de grandeurs de certains paramètres, comme la perméabilité, possèdent une grande incertitude.

Cette étude introduit une approche numérique pour l'évaluation de la perméabilité des structures poreuses synthétiques non périodiques, en proposant une méthodologie systématique et efficace pour l'analyse du transport des fluides dans ces milieux complexes. Une méthode numérique a été développée afin de générer des géométries aléatoirement organisées avec une porosité contrôlée, puis adaptées aux simulations de dynamique des fluides. Cette approche permet une évaluation complète de la perméabilité en combinant la génération automatisée de géométries, des simulations numériques haute fidélité et des techniques d'estimation statistique de la perméabilité.

Le processus de génération des structures poreuses 3D repose sur des outils open-source, notamment le logiciel cristallographique Neper et la bibliothèque de maillage Python Pymesh. Le procédé commence par la tessellation d'un domaine cylindrique (diamètre : 24 mm, hauteur : 41 mm), où un nombre défini de sous-domaines sert à structurer la géométrie initiale. Chaque arête définissant un bord de sous-domaine est substituée par des cylindres afin de construire l'échafaudage poreux. Pour assurer des transitions fluides aux bords de l'échantillon, des sphères supplémentaires sont placées aux noeuds de tessellation, et un tube externe crée une région confinée pour l'écoulement du fluide. La géométrie finale est traitée à l'aide de la géométrie solide constructive (CSG) afin d'obtenir un maillage de surface bien défini, puis voxelisée pour permettre les simulations numériques. La voxelisation offre une flexibilité dans la définition de la résolution et de la taille des voxels, garantissant ainsi la compatibilité avec la méthode Entropically Damped Artificial Compressibility (EDAC) utilisée pour l'évaluation de la perméabilité. Les coordonnées et les métadonnées des matériaux de la structure voxelisée sont exportées pour être utilisées lors de la phase de simulation.

Les simulations numériques s'appuient sur la formulation EDAC, qui permet une modélisation explicite des écoulements incompressibles dans des structures poreuses complexes. La méthode Discretisation-Corrected Particle Strength Exchange (DC-PSE) est employée afin d'améliorer la précision dans la résolution des équations gouvernantes. Ces simulations permettent d'évaluer les interactions fluide-structure ainsi que les propriétés de perméabilité à travers divers régimes d'écoulement. Pour caractériser la perméabilité effective des structures poreuses générées, deux critères clés sont analysés : (i) le nombre de Reynolds  $Re \ll 1$ , garantissant que le système fonctionne dans le régime d'écoulement rampant, et (ii) la variation de la vorticité

normalisée  $\Delta\omega^* \ll 1$ , qui doit rester suffisamment faible pour maintenir une relation linéaire entre le champ de vitesse et le gradient de pression. Le premier critère est contrôlé par l'ajustement de la pression d'entrée, tandis que le second dépend de la longueur caractéristique  $l_c$  nécessaire à la normalisation de la vorticité. Une fois ces deux conditions remplies, la perméabilité est déterminée en minimisant le résidu de la méthode pseudo-inverse de Moore-Penrose, avec un échantillonnage de Monte-Carlo renforçant la stabilité et la robustesse du processus d'estimation.

Cette méthodologie établit une base pour l'identification de la perméabilité *in silico* et facilite la comparaison directe avec des données expérimentales. L'étude met en évidence le potentiel de l'impression 3D pour la validation, permettant la fabrication de structures poreuses synthétiques aux propriétés de perméabilité précises et reproductibles. Les travaux futurs exploreront les implications cliniques de cette recherche, notamment le développement de matériaux biocompatibles imprimés en 3D pour des applications médicales, telles que les échafaudages pour l'ingénierie tissulaire et les implants biomédicaux. Le cadre proposé constitue un outil polyvalent pour les chercheurs en ingénierie, en biomécanique et en science des matériaux, facilitant l'optimisation des structures poreuses pour diverses applications industrielles et médicales.

*Les encadrants de la thèse n'apparaissent pas dans cet article par choix. N'ayant pas contribué à ce travail, qui constitue une réflexion menée parallèlement à l'orientation principale de la thèse, ils ont, par conséquent, décidé de ne pas figurer sur ce document.*

## 10.2 Synopsis (EN)

The identification of constitutive relationships (such as the evolution of vascular porosity) as well as material parameter estimation remains a significant challenge. Indeed, calibration methods do not necessarily converge to a unique solution, and depending on the modeling assumptions, the orders of magnitude of certain parameters—such as permeability—can exhibit considerable uncertainty.

This study introduces a numerical approach to the evaluation of permeability in non-periodic synthetic porous structures, providing a systematic and efficient methodology for analysing fluid transport in complex media. A numerical method was

developed to generate random microstructures with controlled porosity distributions, which were then adapted for fluid dynamics simulations using the particles method. The proposed approach enables a comprehensive assessment of permeability using a combination of automated geometric generation, high-fidelity numerical simulations, and statistical permeability estimation techniques.

The pipeline for generating 3D porous structures is based on open-source computational tools, including the crystallographic software Neper and the Python meshing library Pymesh. The process begins with the tessellation of a cylindrical domain (diameter: 24 mm, height: 41 mm), where the expected number of seeds defines the initial geometric structure. Each of the edges describing a seed border is replaced with cylinders to construct the porous scaffold. To ensure smooth transitions at the domain boundaries, additional spheres are placed on the tessellation nodes, and an external tube creates a confined region for fluid flow. The final geometry is processed using Constructive Solid Geometry (CSG) to achieve a well-defined surface mesh, which is subsequently voxelised to allow for numerical simulations. The voxelisation process provides flexibility in defining resolution and voxel size, ensuring compatibility with the Entropically Damped Artificial Compressibility (EDAC) method used for the evaluation of permeability. The coordinates and material tags of the voxelised structure are exported for use in the simulation phase.

The numerical simulations are based on the EDAC formulation, which allows explicit simulation of the flow of incompressible fluid in highly complex porous structures. The Discretisation-Corrected Particle Strength Exchange (DC-PSE) method is employed to enhance the accuracy in solving the governing equations. These simulations assess fluid-structure interactions via Brinkman penalisation, and macroscopic permeability estimation in various flow regimes. To characterise the effective permeability of the generated porous structures, two key criteria are analysed: (i) Reynolds number  $Re \ll 1$ , ensuring that the system operates within the creeping flow regime, and (ii) variation of normalised vorticity  $\Delta\omega^* \ll 1$ , which must remain sufficiently small to maintain a linear relationship between velocity and pressure gradients (i.e. the creeping regime). The first criterion is controlled by adjusting the inlet pressure, while the second depends on the characteristic length  $l_c$  required for vorticity normalisation. Once both conditions are satisfied, the permeability is determined by minimising the residual of the Moore-Penrose pseudo-inverse method, with Monte Carlo sampling enhancing the stability and robustness of the estimation process

enforcing the physical consistency of the second order permeability tensor.

This methodology establishes a foundation for *in silico* permeability identification and facilitates direct comparisons with experimental data. The study highlights the potential of 3D printing for validation, allowing the fabrication of synthetic porous structures with precise and reproducible permeability properties. Future work will explore the clinical implications of this research, particularly in the development of biocompatible 3D-printed materials for medical applications, including scaffolds for tissue engineering and biomedical implants. The proposed framework provides a versatile tool for researchers in engineering, biomechanics, and materials science, enabling the optimisation of porous structures for diverse industrial and healthcare applications.

*The thesis supervisors do not appear in this article by choice. They did not contribute to this work, which was a perspective developed independently alongside the primary direction of the thesis. Consequently, they chose not to be listed as authors on the document.*

### 10.3 Article

This work was made available as a pre-print in 2025 on Arxiv (<https://doi.org/10.48550/arXiv.2502.14518>). Evaluation of the permeability in the other directions is currently being assessed for completion.

Contribution (CRediT author statement)

Conceptualisation, Methodology, Investigation, Software, Writing – original draft.

# Synthetic Porous Microstructures: Automatic Design, Simulation, and Permeability Analysis.

Thomas Lavigne<sup>a,b,c</sup>, Camilo A. Suarez - Afanador<sup>a</sup>, Anas Obeidat<sup>a</sup>, Stéphane Urcun<sup>a,\*</sup>

<sup>a</sup> Institute of Computational Engineering, Department of Engineering, University of Luxembourg,  
2 place de l'université, Esch-sur-Alzette, L-4365, Luxembourg, <sup>b</sup> Arts et Metiers Institute of  
Technology, IBHGC, 151 bd de l'hôpital, Paris, 75013, France, <sup>c</sup> Arts et Metiers Institute of  
Technology, Univ. of Bordeaux, CNRS, Bordeaux INP, INRAE, I2M Bordeaux, Avenue  
d'Aquitaine, Pessac, 33607, France

---

## Abstract:

This study introduces an open-source computational framework for the generation and permeability evaluation of synthetic porous media. The proposed methodology integrates crystallographic and meshing tools to construct controlled microstructures with tunable porosity, facilitating seamless transitions from geometric modelling to computational domains for numerical simulations. The generated structures are analysed through fluid-structure interaction (FSI) simulations, leveraging the Entropically Damped Artificial Compressibility (EDAC) formulation in conjunction with the Discretisation-Corrected Particle Strength Exchange (DC-PSE) method.

A novel approach for the numerical estimation of the macroscopic permeability tensor is presented, employing a stochastic upscaling technique inspired by the volume averaging method. To validate the framework, we investigate the transition between creeping and non-Darcy flow regimes through parametric permeability studies, utilizing a one-dimensional approach for practical benchmarking.

The results establish a foundation for experimental validation and provide insights into the customised design of porous structures for engineering and biomedical applications, offering a versatile tool for research in fluid transport and porous media mechanics.

**Keywords:** Porous media; Permeability; Computational Fluid Dynamics; Homogenisation; Fluid-Structure Interaction

---

## Introduction

Porous media, whether natural or synthetic, encompass a diverse range of materials, including natural substances such as soil, rock, sponges, and wood, as well as biological tissues such as trabecular bone and menisci. In addition, engineered porous structures, such as foams, concrete, electrospun fibre networks, titanium-printed scaffolds for tissue engineering and paper-based materials, have expanded the functional applications of porous media Ashby et al. 2000; Banhart 2001; J.Gibson and M. F 1999. These materials share a distinctive combination of advantageous physical properties, including low weight, high permeability, large surface area to volume ratio, initial stiffness, energy absorption capacity and capillary-driven liquid attraction Bhattacharya et al. 2002; Boomsma and Poulikakos 2002; Lage et al. 1996.

Because of these properties, porous media are employed in diverse applications, such as shock absorption, load-bearing components, heat exchangers, catalysts, fluid mixing, and solid lubrication. Fundamentally, all porous materials consist of a solid framework interspersed with interconnected voids that enable fluid transport Cowin 1985. The interaction between the solid structure and the fluid that flows through it often leads to complex behaviours, particularly when considering how fluid dynamics influence the mechanical properties of the medium Boutin and Auriault 1991. These phenomena, collectively referred to as fluid-structure interactions (FSIs), are of critical importance in multiple fields, including biomechanics, materials science, and engineering Biot 1956.

While natural porous materials exhibit remarkable multifunctionality, their intricate microstructures pose significant challenges for analysis and simulation. First, accurately modelling their complex, heterogeneous architecture requires computationally intensive simulations for both fluid and solid mechanics. Second, their microstructural variability, which differs spatially within the same sample and between different samples, introduces uncertainties that complicate deterministic modelling and prediction.

This inherent randomness can be a limiting factor in industrial applications. For instance, open-cell metal foams offer substantial advantages in automotive engineering, yet inconsistencies in their microstructure, even under identical manufacturing conditions, hinder their widespread adoption. To overcome these limitations, synthetic porous media have emerged as an alternative, offering the advantage of con-

## 10 Numerical phantoms and *in silico* evaluation

trolled fabrication processes Bear 1972a. By designing synthetic porous materials with customised pore size, distribution, and connectivity, researchers and industry professionals can optimise these structures for specific applications. As a result, synthetic porous media are being increasingly used in sectors such as water purification, petrochemistry, and acoustics Adler 1992; Allard and Atalla 2009; Bear 1972b; Tien 1993.

In biomechanics, the variability in natural porous structures, such as knee menisci, complicates personalised medical treatments, as their microstructure differs between individuals. The ability to fabricate synthetic porous materials with precise and reproducible properties enhances the reliability of the investigation and ensures consistent quality in medical implants, thus improving patient outcomes Wu and Zhang 2016. Furthermore, conducting *in vivo* biomechanical experiments presents challenges related to sample geometry, boundary conditions, and mechanical response measurements. This introduces multiple sources of uncertainty, raising concerns about the robustness of the derived conclusions. A promising alternative involves the use of synthetic porous materials as standardised experimental models, combined with *in silico* simulations. Since the physical domain of a synthetic porous medium, its geometry and porosity are well defined, initial constitutive parameters can be accurately determined, either through computational modelling or experimental validation. Furthermore, synthetic porous media facilitate the isolation of specific variables in scientific studies, a task often complicated by the inherent variability of natural samples. They can also be engineered to replicate pathological conditions, supporting targeted therapeutic research and intervention strategies Martínez-Hernández et al. 2007.

With respect to the synthetic generation of porous media, previous studies have focused on deterministic replication of porous structures using idealised repetitive units. These models include uniformly arranged sphere beds Krishnan et al. 2006, cubic unit cells composed of 65 square cylinders Boomsma and Poulikakos 2001; Plessis et al. 1994, and diamond-configured cells with vertical and horizontally connected micro-cylinders Bai et al. 2012. A representative elementary volume (REV) provides a more realistic depiction of microstructural porosity Boomsma and Poulikakos 2002; Hil 1963; Plessis et al. 1994, requiring fewer adjustments compared to idealised models Boomsma and Poulikakos 2001; Krishnan et al. 2006; Plessis et al. 1994.

Various computational methods have been developed to analyse fluid transport and heat transfer in porous media. Aarnes and Efendiev 2008 introduced mixed multiscale finite element methods (MsFEM) to solve stochastic flow equations with permeability-dependent basis functions, enabling large-scale solutions. Ganapathysubramanian and Zabaras 2009 proposed a multiscale stochastic model that captures unpredictable subgrid-scale permeability variations using a reduced-order approach based on statistical data. Biswal et al. 2011 developed a multiscale framework to characterise porous media at varying levels of detail, accommodating a range of pore sizes. More recently, Vazic et al. 2022 investigated the impact of the micropore structure on the performance of porous material using higher-order modelling techniques. In the context of subsurface flow, Dostert et al. 2008 proposed an efficient sampling method to quantify uncertainty in permeability distributions, leveraging coarse-scale models and sparse interpolation to approximate posterior distributions.

Building upon these advancements, the present study aims to develop a streamlined methodology for the generation of random porous microstructures using a combination of open-source Python, POV-Ray SDL, and C++ libraries. This approach takes advantage of highly optimised computational functions, allowing for efficient automation of the generation process. Furthermore, we establish a framework for estimating macroscopic permeability tensors by conducting fluid-structure interaction simulations, following the methodology proposed by Whitaker 1998 and refined by Scandelli et al. 2022.

## Methodology

### Generation of synthetic samples

The pipeline developed for the generation of synthetic geometries, as illustrated in Figure 32, leverages the open-source crystallographic software Neper Quey et al. 2011 in combination with the open-source Python meshing library Pymesh Zhou 2019. This integrated approach ensures efficient and precise control over geometric and meshing parameters. The complete set of scripts and codes used for mesh generation is provided as supplementary material to facilitate reproducibility and further research.

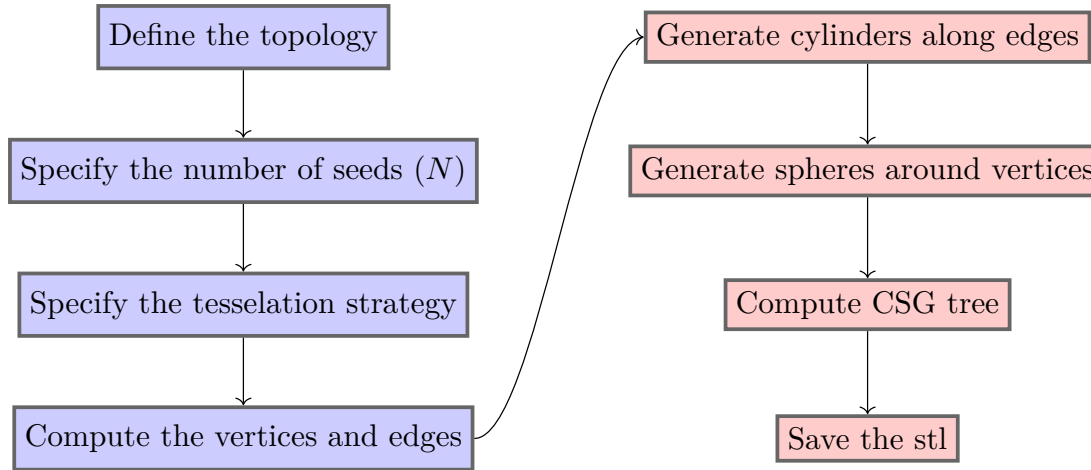


**Figure 32:** Graphical Representation of the Workflow for Porous Scaffold Generation. Blue elements indicate the Neper environment, while red elements represent the Pymesh environment.

The topology of the porous medium, *i.e.*, the spatial domain occupied by the porous scaffold, was first defined (Algorithm 1). Standard geometric shapes such as cylinders, prisms, and tori are available as predefined options. However, more complex geometries can also be generated through transformations, including Boolean operations. In this study, the porous medium was confined within a cylindrical domain with a diameter of 24 mm and a height of 40 mm.

The macroscopic porosity ( $\phi$ ) of the domain was determined by a single parameter: the number of seeds  $N$ , which corresponds to the target number of tessellation cells. To illustrate the functionality of the generation process, four cases with varying seed numbers were calculated:  $N = 1500, 2000, 2500, 3000$ . In addition, a morphological rule governing the tessellation process was specified, allowing customisation according to statistical constraints, Voronoi tessellation principles, or other user-defined criteria. Depending on the chosen approach, the resulting scaffold could exhibit either a controlled, regular pore size or a more randomly distributed microstructure. In the present work, a logarithmic normal sphericity law was applied to ensure a relatively uniform pore-size distribution. Based on these parameters, a set of vertices and edges was generated and stored in a “.tess” file, representing the tessellation output.

After generation, the vertices and edges from the “.tess” file were imported into the Pymesh environment (Algorithm 2). Then a cylindrical structure was assigned

---

**Algorithm 1:** NEPER: Generate a domain and its corresponding tessellation

---

**input :** Geometric specifications**output:** Tessellation file

```

1  $N \leftarrow \{1500, 2000, 2500, 3000\};$ 
2  $L_z \leftarrow 4.0 \times 10^{-2} \text{m};$ 
3  $r \leftarrow 1.2 \times 10^{-2} \text{m};$ 
4 DOMAIN  $\leftarrow \text{"cylinder}(L_z, 2 * r)";$ 
5 Law  $\leftarrow \text{"diameq:dirac(1),1-sphericity:lognormal(0.145,0.03)"};$ 
6 if  $\exists \text{ output.tess}$  then
7   | Pass
8 else
9   | output.tess  $\leftarrow \text{neper -T -n } \$N \text{ -morpho } \$Law \text{ -domain } \$DOMAIN$ 

```

---

along each edge, with a fixed radius of 0.5 mm. The methodology can be extended to incorporate variable radii by defining a function that adjusts the radius based on the distance between the connected vertices, ensuring proportional scaling across the structure. To maintain a smooth and continuous scaffold geometry, spherical elements were added at the boundary vertices, preventing abrupt discontinuities. In addition, an external cylindrical tube was introduced, creating a 10 mm chamber on either side of the sample to define a confined region for fluid flow. Given the high number of generated elements, a Constructive Solid Geometry (CSG) tree was employed to perform Boolean operations, resulting in a well-defined and unified surface mesh.

Once the porous scaffold was created, it was saved as a ".stl" file—whether generated via the aforementioned pipeline or obtained from the segmentation of a micro-CT image. This geometry was then processed using the numpy-stl library, which ensured the correct orientation of surface normals. A set of custom functions, based on the prior stl-to-voxel library Pedrekoff 2015, was implemented to convert the mesh into a voxel-based representation. Users can define the desired voxel resolution ( $N_x \times N_y \times N_z$  voxels) or specify a fixed voxel size, depending on computational requirements.

For synthetic porous media, additional considerations were necessary to ensure that the fluid remained within the confined region. Specifically, voxels located outside the external cylindrical boundary were removed to prevent undesired flow artifacts. This step was feasible due to the well-defined dimensions of the domain. A similar adjustment may be required when replicating an experimental set-up with an

---

**Algorithm 2:** Pymesh: Create the porous scaffold

---

```

input : output.tess to load the vertices and edges (parsing)
output: Mesh of the porous scaffold

1 N ← {1500, 2000, 2500, 3000};
2 rad ←  $5 \times 10^{-4}$ m;
3 list ← [ ];
4 i ← 0;
5 v, e ← M([x,y,z]), M([v(i), v(j)]);           ▷ vertices and edges;
6 while  $i \leq \text{len}(e)$  do
7   cylinder ← pymesh.generate_cylinder(v[e[0]], v[e[1]], radius, radius);
8   list ← [list, cylinder];
9   i ← i + 1;
10 i ← 0;
11 while  $i \leq \text{len}(v)$  do
12   if  $v$  on boundary then
13     sphere ← pymesh.generate_icosphere(radius, v[i]);
14     list ← [list, sphere];
15   i ← i + 1;
16 list ← [list, tube];                         ▷ tube generated with Pymesh;
17 mesh ← CSG tree;                           ▷ boolean operations between all parts

```

---

external boundary, but it can be omitted in other cases.

Following voxelisation, the voxel coordinates and their corresponding material tags were exported to separate files, facilitating domain creation in subsequent processing steps (Algorithm 3). The resulting microstructures are presented in the implementation section (Section 18).

## Governing equations and mathematical modelling of fluid/structure interactions

For clarity and convenience, we provide a brief overview of the fundamental concepts underlying the governing equations. Readers seeking a more comprehensive examination of the Entropy-Density Approximate Compressibility (EDAC) formulation in conjunction with the Discretization-Corrected Particle Strength Exchange (DC-PSE) method are encouraged to refer to Singh et al. 2023.

---

**Algorithm 3:** STL-2-Voxel: Transform the mesh.stl to a particle space

---

**input :** Mesh of the porous scaffold  
**output:** Particle space

```

1  $x, y, z \leftarrow 0, 0, 0;$ 
2  $\min, \max \leftarrow \text{mesh spatial limits};$ 
3  $vx_{size} \leftarrow 1 \times 10^{-3};$ 
4  $ROI \leftarrow \max - \min;$ 
5  $idx \leftarrow \text{argmax}(ROI);$ 
6  $res \leftarrow \text{int}\left(\frac{ROI[idx]}{vx_{size}}\right)$   $\triangleright$  expected resolution;
7  $voxels, scale, shift \leftarrow \text{stltovoxel.convert(mesh, resolution=}res - 1\text{)};$ 
8 while  $z \leq voxels.shape[0]$  do
9   while  $y \leq voxels.shape[1]$  do
10    while  $x \leq voxels.shape[2]$  do
11      write  $[x, y, z]/scale$  in coord.txt;  $\triangleright$  sphere center;
12      if point  $\notin$  confined well then
13        write 3 tag.txt;
14      else
15        write voxels[z][y][x] tag.txt;
16       $x \leftarrow x + 1;$ 
17     $y \leftarrow y + 1;$ 
18   $z \leftarrow z + 1;$ 
```

---

**Entropically Damped Artificial Compressibility (EDAC) formulation**

In the field of simulating the incompressible Navier-Stokes equations, Clausen 2013 introduced the EDAC method, which allows for the explicit simulation of these equations. The EDAC formulation incorporates an additional governing equation for the evolution of pressure  $p$  (Equation 165), derived from the thermodynamic properties of the system while ensuring a fixed density  $\rho$ . This method demonstrates convergence to the incompressible Navier-Stokes (INS) equations at low Mach numbers and maintains consistency across a broad range of Reynolds numbers, from low to high. The momentum equation and the pressure evolution equation within the Eulerian frame of reference,

$$\rho \frac{du_i}{dt} + u_j \frac{\partial u_i}{\partial x_j} = - \frac{\partial p}{\partial x_i} + \frac{\partial \tau_{ij}}{\partial x_j} \quad (164)$$

$$\frac{dp}{dt} + u_i \frac{\partial p}{\partial x_i} = -c_s^2 \rho_o \frac{\partial u_i}{\partial x_i} + \nu \frac{\partial^2 p}{\partial x_i \partial x_i}, \quad (165)$$

$$\tau_{ij} = \mu \left( \frac{\partial u_i}{\partial x_j} + \frac{\partial u_j}{\partial x_i} - \frac{2}{3} \delta_{ij} \frac{\partial u_k}{\partial x_k} \right), \quad (166)$$

where  $u$  is the velocity vector field,  $p$  is the pressure field,  $t$  is time,  $\tau$  is the shear stress,  $\mu$  is the dynamic viscosity, and  $c_s$  is the speed of sound.

Equation 164 corresponds to the equation that governs momentum conservation, while Equation 165 represents the EDAC formulation for the evolution of pressure. This formulation introduces entropy as a means of damping pressure oscillations. A comprehensive derivation, along with the physical model of the EDAC formulation, is extensively detailed in Clausen's work Clausen 2013. In summary, starting from the compressible Navier-Stokes equations, we derive the pressure evolution equation using mass conservation, entropy balance, and thermodynamics, introducing temperature as a variable and adding an entropy constraint. Clausen resolves the issue of density fluctuations by linking density directly to pressure and temperature, simplifying the model to explicitly relate temperature to pressure in Equation 165. Hence, allowing for explicit pressure evolution.

In this study, the EDAC equations are coupled with Brinkman penalisation, as explained in the reference Obeidat et al. 2020; Obeidat and Bordas 2019, for the simulation of fluid flow in intricate geometries. This approach involves the implicit penalisation of the computational domain, achieved by employing an indicator function  $\chi$  that identifies the areas occupied by the solid geometry denoted  $O$ .

$$\chi(x) = \begin{cases} 1 & \text{if } x \in O, \\ 0 & \text{otherwise.} \end{cases} \quad (167)$$

A penalty term is added to the momentum equation (implicit penalisation). The penalized conservation of momentum equation is:

$$\rho \frac{du_i}{dt} + u_j \frac{\partial u_i}{\partial x_j} = - \frac{\partial p}{\partial x_i} + \frac{\partial \tau_{ij}}{\partial x_j} - \frac{\chi}{\eta} (u_i - u_{(oq)i}) \quad (168)$$

Where,  $u_{(oq)i}$  is the velocity of the solid body,  $\eta = \alpha\phi$  is the normalized viscous permeability and  $\phi$  is the porosity. Note that  $0 < \phi < 1$  and  $0 < \eta \ll 1$ .

### The Discretization-Corrected Particle Strength Exchange (DC-PSE) formulation

DC-PSE is a numerical technique utilised to discretise differential operators when dealing with unevenly distributed collocation points Schrader et al. 2010. It initially emerged as an enhancement to the traditional Particle Strength Exchange (PSE) method Degond and Mas-Gallic 1989; Eldredge et al. 2002, with the aim of decreasing the integration error when the coordinate points are placed irregularly. However, from a mathematical point of view, it essentially represents an extension of finite differences Schrader et al. 2010. The group of collocation methods within the PSE/DC-PSE category employs mollification, utilising a symmetric smoothing kernel  $\eta\epsilon()$ , to approximate continuous functions  $f_\epsilon(\vec{x})$  that are sufficiently smooth, as:

$$f(\vec{x}) \approx f_\epsilon(\vec{x}) = \int_{\Omega} f(\vec{y})\eta_\epsilon(\vec{x} - \vec{y})d\vec{y}, \quad (169)$$

where  $\epsilon$  is the smoothing length or the width of the kernel. In DC-PSE the linear system is solved locally to each particle in order to determine the kernel weights in a way that they locally satisfy the discrete moment conditions to the desired order of convergence. This allows DC-PSE to directly satisfy the discrete-moment conditions on particle distribution rustling, avoiding quadrature error.

The most commonly used DC-PSE kernels are of the form

$$\eta(\vec{x}) = \begin{cases} \sum_{i,j}^{i+j < r+m+n} a_{i,j} x^i y^j e^{-x^2-y^2} & \sqrt{x^2 + y^2} < r_c \\ 0 & \text{otherwise,} \end{cases} \quad (170)$$

where the polynomial coefficients  $a_{i,j}$  are determined from the discrete moment conditions

$$Z^{i,j}(\vec{x}_p) = \begin{cases} i!j!(-1)^{i+j} & i = m, j = n \\ 0 & \alpha_{\min} < i + j < r + m + n \\ < \infty & \text{otherwise.} \end{cases} \quad (171)$$

$\alpha_{min}$  is 0 for odd and 1 for even operators, and the discrete moments  $Z^{i,j}$  are defined as

$$Z^{i,j}(\vec{x}_p) = \sum_{\vec{x}_q \in \mathcal{N}(\vec{x}_p)} \frac{(x_p - x_q)^i (y_p - y_q)^j}{\epsilon(\vec{x}_p)^{i+j}} \eta \left( \frac{\vec{x}_p - \vec{x}_q}{\epsilon(\vec{x}_p)} \right). \quad (172)$$

This not only leads to operator discretizations that are consistent on (almost<sup>1</sup>) all particle distributions, but also relaxes the overlap condition of PSE to the less restrictive requirement

$$\frac{h(\vec{x}_p)}{\epsilon(\vec{x}_p)} \in \mathcal{O}(1), \quad (173)$$

that is, the ratio of the kernel width  $\epsilon$  and the inter-particle spacing  $h$  has to be bounded by an arbitrary constant as  $h \rightarrow 0$ .

## Numerical evaluation of the permeability of the medium

### Theoretical hypotheses and validity criteria

In this section, we analyse the existence of an effective permeability tensor  $\tilde{\mathbf{K}}$  for a non-periodic synthetic porous medium generated following the methodology presented in Section 10.3. The EDAC solver for DC-PSE Singh et al. 2023 is used to model the three-dimensional incompressible viscous fluid flow within the synthetic porous medium by solving the EDAC formulation as described in Section 18. This simulation scenario is in agreement with the formulation of the effective (or macroscopic) permeability tensor from *The Method of Volume Averaging* Whitaker 1998 which is the main reference work for further derivations. In the case of non-periodic microstructures, to determine the applicability of the above work in simulations, the recent work in Scandelli et al. 2022 is used as a complementary reference, since it presents an extensive review of the literature, several application cases, and introduces a supplementary criterion verifying ideal conditions for such estimations.

---

<sup>1</sup>DC-PSE fails on particle distributions where particle positions in the neighbourhood are linearly dependent. In such cases, the linear system for the kernel weights does not have full rank and cannot be solved.

Within this framework, we assume that the observed medium can be macroscopically described by a Darcy relationship, which represents a linear dependency of the macroscopic physical fields, the spatial average of the velocity and the gradient of pressure distributions. This relation is expressed via the macroscopic Darcy's law obtained by the volume averaging method for non-slip condition on the interphase fluid/solid, as it is described in Howes and Whitaker 1985; Whitaker 1986; Whitaker 1998:

$$\langle u \rangle = -\tilde{\mathbf{K}} \frac{\nabla \langle p \rangle}{\mu \Phi} = -\tilde{\mathbf{K}} \frac{\langle \nabla p \rangle}{\mu \Phi} \quad (174)$$

Where  $\langle f \rangle$  is the spatial average of a function  $f(x)$  in a domain  $\Omega$  defined as:

$$\langle f \rangle = \frac{1}{||\Omega||} \int_{\Omega} f(x) d\Omega, \quad (175)$$

and  $u, p$  are the velocity and pressure fields respectively,  $\tilde{\mathbf{K}}$  the macroscopic permeability tensor,  $\mu$  the dynamic viscosity,  $\Phi$  the macroscopic porosity. For such relationships to hold, it is necessary to verify that the flow can be considered to be in the so-called "creeping regime", in which non-linear inertial effects are negligible (from a macroscopic point of view), and thus a linearity of the macroscopic fields can be considered. For this, the main parameter to consider is the Reynolds number ( $Re$ ) and additionally the normalised vorticity criterion ( $w^*$ ) introduced in Scandelli et al. 2022. The explicit form of these two parameters is presented below:

$$Re = \frac{\rho \langle \mathbf{u} \rangle l_c}{\mu}, \text{ and, } w^* = \frac{wl_c}{||\langle \mathbf{u} \rangle||} = \frac{(\nabla \times \mathbf{u})l_c}{||\langle \mathbf{u} \rangle||}. \quad (176)$$

Following the methodology of *volume averaging* Whitaker 1998, we consider a Representative Elementary Volume (REV) as a subset of the macro-domain holding the same porosity of the entire domain, which verifies the linearity requirements of Scandelli-Whitaker. However, periodic boundary conditions are not valid in the studied cases as the random microstructures of Section 10.3 are the geometrical support for the simulations. Therefore, we compute for each REV in a set of sample REVs the effective permeability tensor as follows:

$$\langle u_i \rangle = -\frac{\kappa_{ij}(x_i)}{\mu \Phi} \nabla \langle p(x_i) \rangle \quad (177)$$

Given that for each point of a REV we know the velocity and pressure field, we need

to compute  $\kappa_{ij}$  the effective permeability tensor of an intermediate scale created by the spatial distribution of REVs accounting for the different distributions of the microscopic fields, but to do this, we first have to take into account that the number of equations from the above linear system is less than the required for the calculation of the elements in this tensor. To be able to estimate a solution for such a system, we assume that there is no fracture in the domain and conservation of momentum that leads to symmetry and positive definite properties of the tensor Pouya and Courtois 2002a. The initial Darcy problem within the fluid phase (i.e.  $\chi(x_i) = 0$ ) reads:

$$\begin{aligned} & \text{Given } \{u_i(x_i), p(x_i)\}: \\ & \text{Find } \kappa_{ij}(x_i) \forall x_i \in \Omega_{REV}, \langle u_i \rangle = -\frac{\kappa_{ij}(x_i)}{\mu\Phi} \nabla \langle p(x_i) \rangle, \chi(x_i) = 0 \end{aligned} \quad (178)$$

To simplify the notation, let us introduce the average material pressure gradient vector  $\langle p_i^*(x_i) \rangle = (\mu\Phi)^{-1} \langle \nabla p(x_i) \rangle$  to rewrite the above local Darcy law,

$$\langle u_i \rangle = \kappa_{ij} \langle p_j^* \rangle, \quad (179)$$

and, to ease the formulation we adopt a matrix-vector notation with vectors represented by the column matrix of dimensions  $\dim(u) = (3, 1)$ , and the local permeability tensor a square matrix of dimensions  $\dim(\boldsymbol{\kappa}) = (3, 3)$ :

$$\langle \mathbf{u} \rangle = \boldsymbol{\kappa} \langle \mathbf{p}^* \rangle \quad (180)$$

The effective permeability tensor  $\boldsymbol{\kappa}$  being symmetric by definition (i.e.  $\boldsymbol{\kappa} = \boldsymbol{\kappa}^T$ ) the number of independent coefficients to compute is 6, therefore the linear system of three equations relating the 6 coefficients is undetermined and the solution cannot be directly obtained. To overcome this issue, one should refer to Scandelli et al. 2022, in which 3 compatible simulations are used to recover the elements of the effective permeability tensor (see also Lang et al. 2014; Pouya and Courtois 2002b).

**Vorticity criterion** As mentioned above, to start the exploratory analysis of the existence of a macroscopic permeability tensor  $\tilde{K}$ , first, one must observe the distribution of the norm of the vorticity vector ( $\|\mathbf{w}\| = \|\nabla \times \mathbf{u}\|$ ) that verifies the pertinence of such computation via the supplementary indicator of the presence

of the creeping regime introduced in Scandelli et al. 2022, that in the case of the reference article, is given by comparisons for different Reynolds numbers using a dimensionless vorticity (weighted by up-scaling parameters) with respect to a reference state, validating the Darcy-like flow, and therefore, verifying the validity of a macroscopic permeability tensor following Whitaker 1998.

**Parametric up-scaling** The following steps represent a deductive approach to identify the parameter  $l_c$ , a characteristic length that preserves the so-called representativeness of the macroscopic medium, describing a domain decomposition in which the elements are rich enough (from a statistical point of view) to be a simplified representation of the entire domain. Since the effective permeability tensor is a function of the porosity volume fraction, the macroscopic volume fraction  $\phi$  is used here as a parameter to guide the choice of  $l_c$  for the example microstructure. At this point, a first arbitrary choice is made; this is the shape of the subdomains. For the present study, cuboid subdomains are chosen to facilitate the numerical implementation since the subdomains are represented by structured meshes (as a consequence of the voxelisation process for simulations). First, the distribution of local porosity is observed for a set of test characteristic lengths, and the parameter is chosen such that the obtained distribution is a Gaussian-like distribution centred close to the expected volume fraction, and the dispersion around the mean is symmetric and of reasonable amplitude. The corresponding values are discussed in Section 18.

### Stochastic approximation of the macroscopic effective permeability

Following Scandelli et al. 2022, we are able to compute an approximation of the effective permeability tensor  $\kappa$  of the “intermediate” scale for a given REV, which in terms of the spatial distribution is characterised by its centroid. The domain decomposition led by  $l_c$  ensures the representativeness of the medium, and thus a smooth decomposition is capable of considering every material point within the domain as a potential centroid of an REV. Moreover, such decomposition allows the REVs to overlap mapping in a smooth way the changes of the distributions of the “moving” REV sampling. Thus, the macroscopic permeability tensor can be obtained via stochastic upscaling using Monte Carlo integration, which gives as a result an effective behaviour that takes into account the local porosity statistics of the random porous medium.

## Implementation

### Sample Geometries generation

The four geometries described in Section 10.3 were generated. The volume of the domain envelope was 20,125.83 mm<sup>3</sup>. This value was also used to estimate the porosity of the medium after the computation. The number of cylinders and spheres generated, the computation times, and porosity are provided in Table 19. Figure 33 shows an example of the entire STL geometry in its confined configuration used in simulations to ensure the flow direction in the chosen principal direction (co-linear to the principal axis of the cylinder), and Figure 34 shows the final network for each number of seeds. On the left-hand side, a clipped 3D-like image is presented within a 2D projection of the medial plane (in white) and its corresponding voxelised version for simulations at the right-hand side. The black voxels are void, whereas the grey voxels are the solid phase.

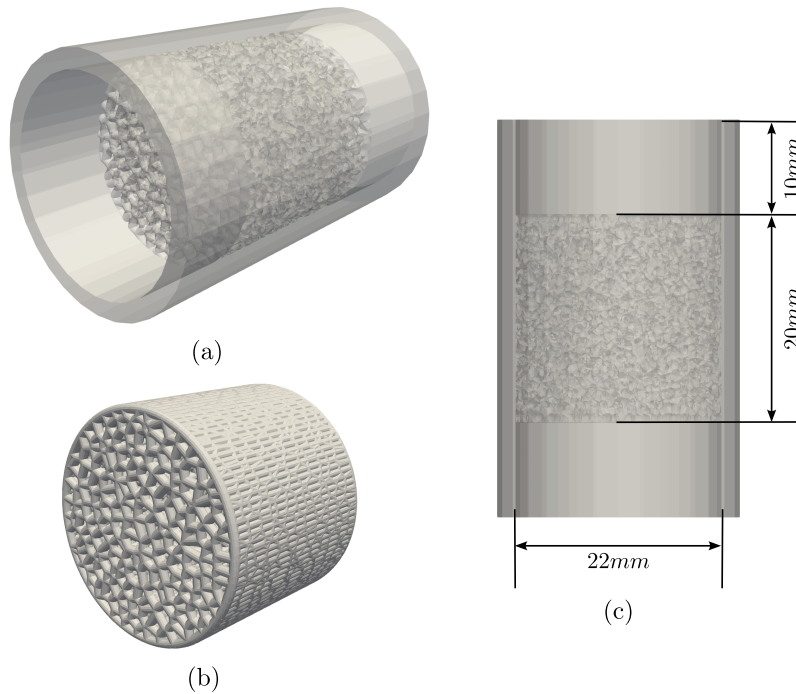


**Figure 33:** Sample Microstructure  $N = 3000$ . (a) A 3D isometric representation of the generated STL geometry, (b) a closer view to the inner porous network inserted in the cylindrical domain for simulations, and (c) the dimensions of the confined well configuration for simulations on a 2D projection of the domain.

An increasing number of seeds resulted in an increasing number of cylinders/spheres.

Seeds [ - ]	Porosity [ - ]	Cylinders/spheres [ - ]	Time (CSG tree) [ h.m.s ]	Time (voxelising) [ m.s ]
1500	29.31%	19714/656	08h 11min	09min 12s
2000	22.40%	26126/778	10h 37min	13min 23s
2500	17.43%	32674/870	13h 05min	16min 54s
3000	10.13%	37957/943	17h 46min	22min 03s

**Table 19:** Geometrical and computational information of the generated synthetic samples. The voxelising time is provided for a required resolution of  $N_x \times N_y \times N_z = 80 \times 80 \times 160$  voxels.

Therefore, more elements that interact all together were present in the CSG tree, leading to larger computation times. Depending on geometric choices and the number of seeds, the porosity of the scaffolds varied approximately from 10% to 30 %, as can also be observed in Figure 34.

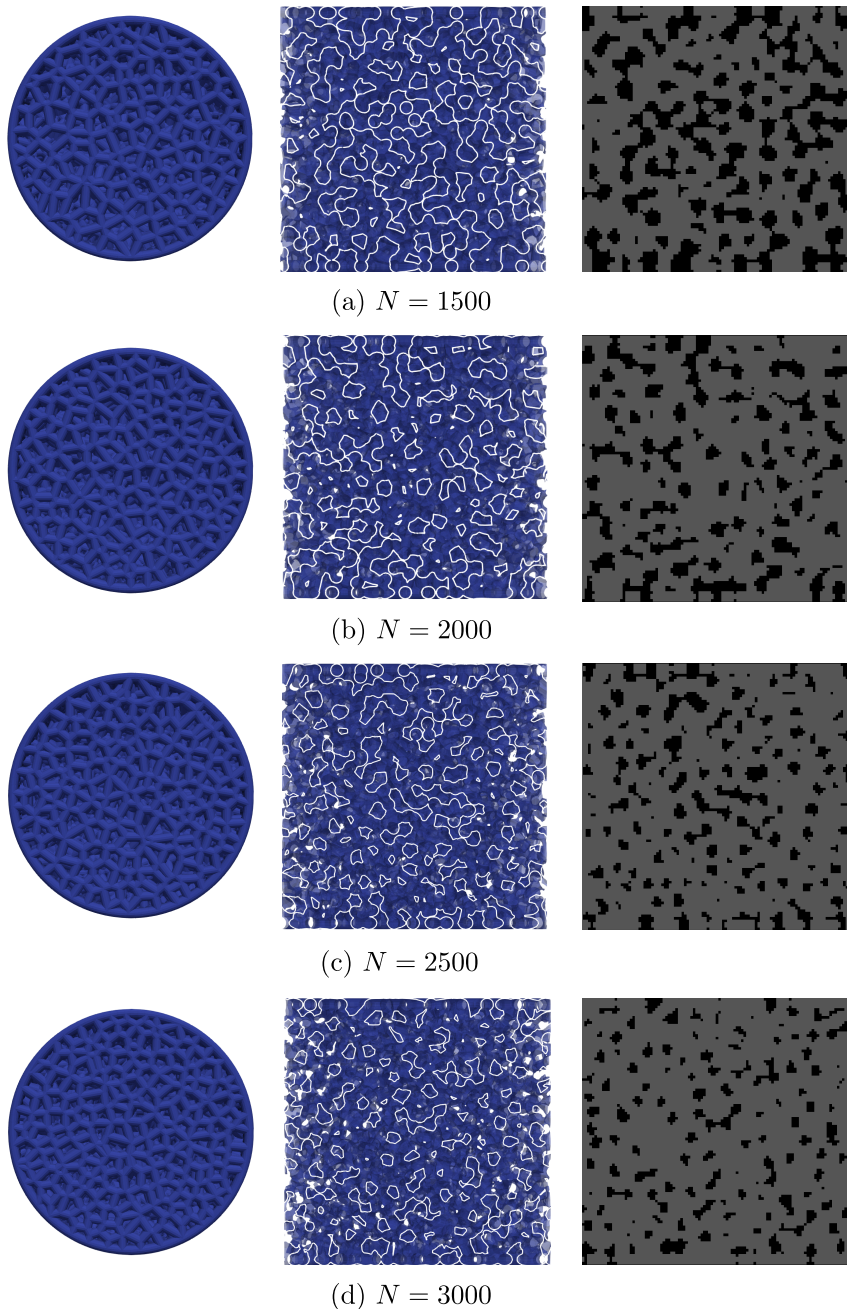


**Figure 34:** Resulting geometries for  $N = 1500, 2000, 2500, 3000$  seeds. First a top view of the inner porous network, in the middle, both, a 3D projection of a half view and central slice are provided to represent the porous network. And its corresponding voxelised representation is shown at the right-hand side. Only the confined porous network is presented.

## Fluid/Structure interactions simulations

In this section, only a single microstructure is used to present the simulation scenario, the one identified by the seeding number  $N = 3000$ , since the main goal of this section is to serve as an application example for the methodology and no direct practical application is considered. The following is intended to present the general methodology without further analysis in the physical fields resulting from the simulation.

Here we consider the numerical implementation of the incompressible fluid flow simulations using previous section synthetic porous microstructures. The numerical implementation is achieved using the open-source C++ library OpenFPM, which already integrates the DC-PSE framework.

Regarding the numerical setup for the simulations, first, since one of the goals is to estimate the macroscopic permeability of the medium according to Whitaker 1998, the non-slip condition on the fluid/structure of the interphase was defined, which represents the rigid behaviour of the solid phase. A test pressure of 9.93 Pa was defined as the reference pressure, and the controlled boundary condition for the parametric study was the inlet pressure, chosen so that the actual controlled parameter was the pressure difference between the inlet and outlet cross sections of the cylindrical geometry (see Fig. 33). The purpose of such a study is to observe the changes in the permeability of the sample for different Reynolds numbers as the velocity profile is affected by the imposed inlet pressure. The discrete interval of the imposed pressure difference for the parametric study was:

$$\Delta p = \{5e-6, 1e-5, 5e-5, 1e-4, 5e-4, 1e-3, 5e-3, 1e-2, 5e-2, 1e-1, 5e-1, 1e0\} [\text{Pa}]$$

The output of the simulations are the velocity,  $u_i(x_i)$ , and pressure,  $p(x_i)$  fields. This output data is the input that will be used to analyse the existence of a macroscopic permeability tensor ( $\tilde{\mathbf{K}}$ ), an example of such data for an input pressure  $p = 10.03$  Pa (i.e.  $\Delta p = 1e-2$  Pa) is presented in Fig. 35, which only shows the physical fields for the fluid phase, and in the form of histograms in Fig. 36. The latter showing the principal direction of the fluid (i.e.,  $e_3$  or  $z$  axis, histograms in green) where changes in pressure and velocity exhibit skewed distributions, while the rest of the components are represented by Gaussian-like distributions centred close to zero. In

Fig. 35, the norm of the velocity field show a non-linear evolution of the magnitude in the principal direction ( $z$  axis) while the distributions in the other two principal directions appear more or less homogeneous for a given cross section. The pressure field, in contrast, exhibits a linear-like evolution from the higher input pressure to the lower outlet pressure.

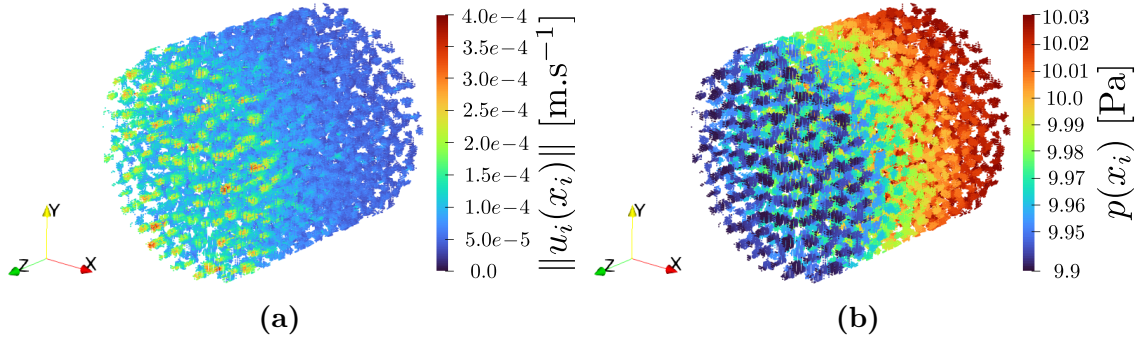


**Figure 35:** Example output fields R.O.I. (i.e. the porous network): (a) velocity norm distribution and (b) pressure distribution. For visualization only liquid sub-domain is shown (i.e.  $\chi(x_i) = 0$ ).

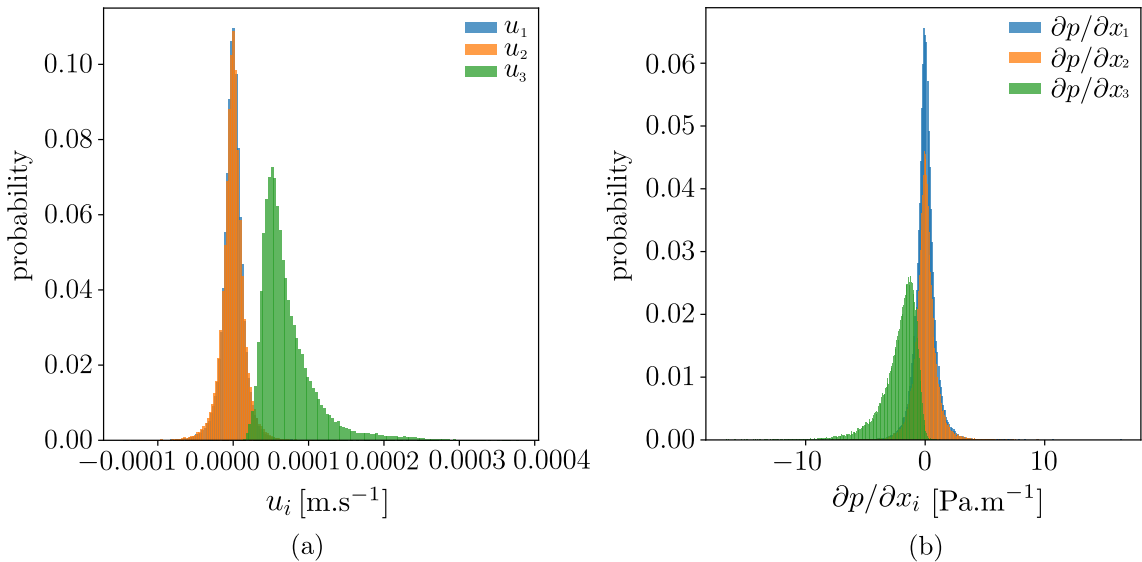


**Figure 36:** Example output fields R.O.I. (i.e. the porous network) Histograms: (a) velocity distribution and (b) pressure distribution.

## Permeability evaluation

### Verification of theoretical hypotheses and criteria

**Verification of creeping regime** In the present work, the distribution of the norm of the vorticity vector in its original form is considered as a primary indicator of such regime and further verifications are given by the distribution of the main parameter of the creeping flow, the Reynolds number itself (see Fig. 37). This is because the methodology to compute the upscaling parameters is subject to arbitrary choices, including the spatial average and characteristic length within a representative elementary volume.

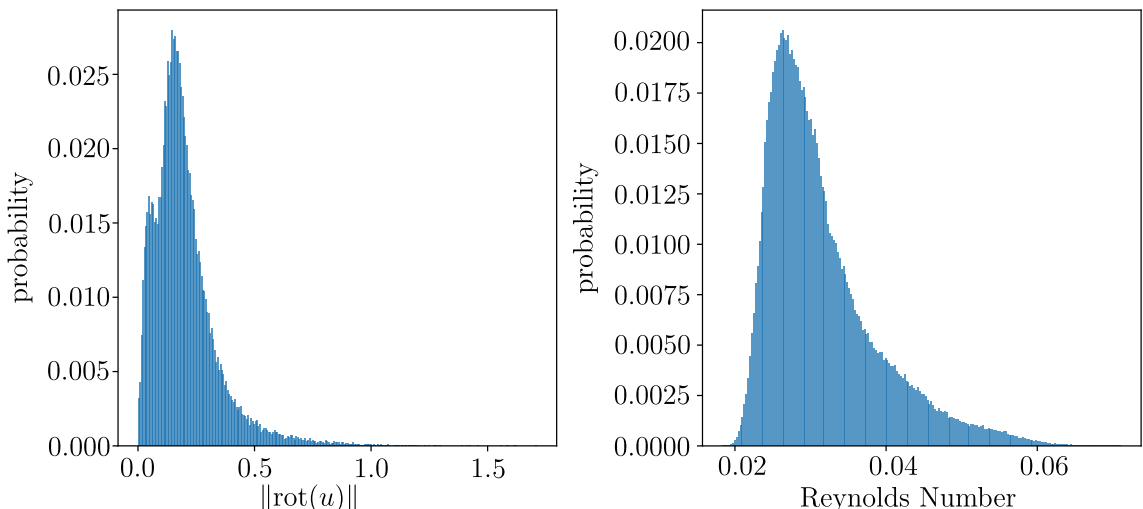


**Figure 37:** Distribution of creeping regime parameters for the example case, inlet pressure  $p = 10.003$  Pa. (a) The norm of the vorticity vector, and (b) The Reynolds number.

The figure above shows the evidence of the creeping regime for the reference example, the Reynolds number distribution follows the creeping regime condition  $Re < 0.5$  Agnaou et al. 2017; Dybbs and Edwards 1984; Scandelli et al. 2022. Both with the norm of the vorticity distribution ( $\|\mathbf{w}(\mathbf{x})\|$ ) suggest a linearity of the relationship between the macroscopic pressure gradient and the velocity, where low vorticity values can be used as arguments for low non-linear and localised effects of the viscous flow due to higher local velocity profiles.

**Identification of the characteristic length** In Fig. 38 one can observe the obtained volume fraction distributions for some examples of characteristic lengths, the

magnitude of which is computed as a fraction of the total length of the macroscopic domain (i.e.,  $L$ ). As can be expected, as the characteristic length of the REV gets closer to the total length, the distribution starts to align with the expected volume fraction value (represented by the red dashed line). In order to maintain scale separation of the observed set of REVs, the maximum fraction of the total length is set to  $l_c = 0.2L$  with the mean volume fraction  $\bar{\phi} \simeq 0.1265$  (with  $\Delta\phi \simeq 0.004$  from the macroscopic volume fraction) and with the 70% of the data inside a symmetric extension of one standard deviation.

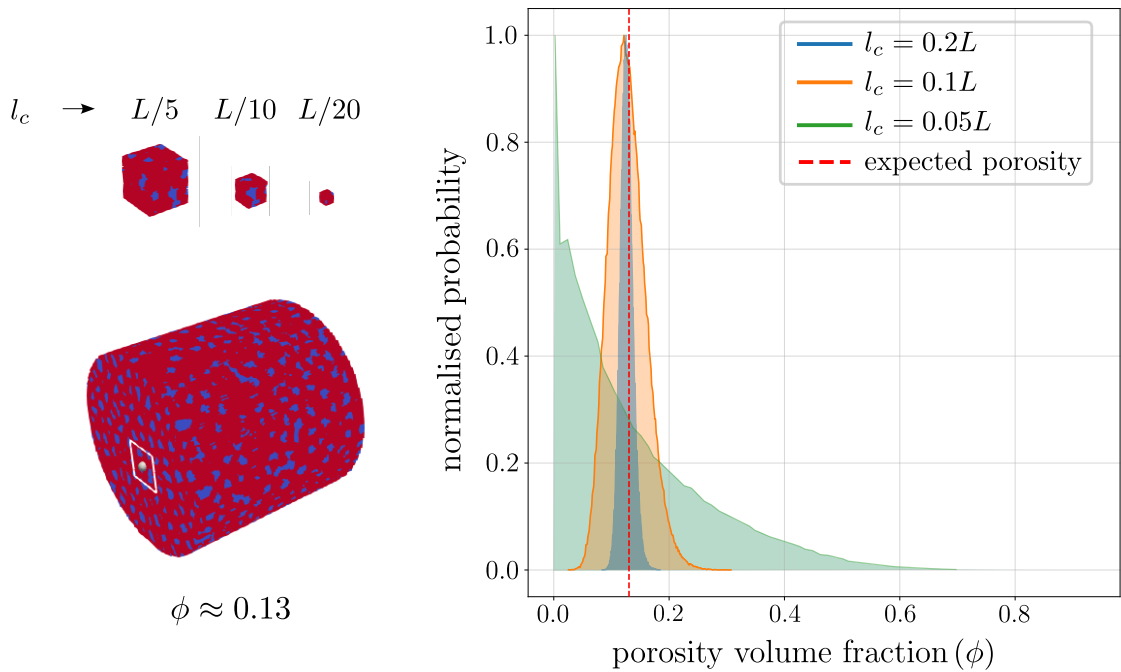


**Figure 38:** Volume fraction distributions for sample characteristic lengths

## A One-dimension approximation for experimental comparisons

Since this study presents simulations to illustrate the capabilities of the proposed methodology, the three-dimensional permeability tensor is not explicitly addressed in the implementation, we propose here a one-dimensional approximation that serves as a link between simulations and actual experimental setups. As can be observed in Fig. 39, in a basic scenario the pressure gradient is only accessible for the direction which is collinear to the principal direction of the fluid flow (i.e. the  $z$  direction from the conventions adopted previously); thus for a quasi-static established regime

characterised by low Reynolds number, one is able to estimate the permeability of the porous medium by computing the pressure difference from input to output.



**Figure 39:** Example of an experimental setup compatible with an instrumented micro-CT scanner, for permeability evaluation.

As mentioned above, the simulation scenario adopted in the present study is consistent with the criteria defined in Scandelli et al. 2022 for non-periodic microstructures; therefore, we can directly obtain a first approximation of the permeability in the  $\mathbf{z}$  (or  $\mathbf{e}_3$ ) direction (i.e.  $\bar{\mathbf{K}}_{33}$ ) by assuming that the pressure field is constant at each infinitesimal cross section (i.e.  $p(x_i) = p(x_3)$ ).

$$\bar{\mathbf{K}}_{33} \approx -\mu\phi \left( \frac{\Delta p}{\Delta z} \right)^{-1} \langle u_3 \rangle, \quad (181)$$

Where  $\Delta p$  represents the difference in pressure between the mean pressure of the inlet and outlet cross sections,  $\Delta z$ , the length of the porous medium under testing, and recalling from previous sections,  $\langle u_3 \rangle$  the mean velocity of the fluid in the third direction (or the effective velocity in  $z$  direction),  $\mu$ , the dynamic viscosity of the fluid, here the water (0.001 Pa.s), and  $\phi$ , the macroscopic volume fraction of porosity. The above equation is in fact equivalent to the earliest historical studies from Darcy 1856. In Fig. 40 we can observe the evolution of permeability as a function of the Reynolds number (indicator of the presence of the creeping regime) and inlet pressure (the controlled parameter of the subsequent simulations). In this figure, we can observe the transition from a linear-dominated regime to a more chaotic and turbulent one, as evidenced by the plateau-like behaviour of the left side (low Reynolds number zone), where the calculated parameter seems to be close to reaching a stable value. As the inlet pressure increases (as well as the Reynolds

number) non-linear effects become more dominant and the Darcy-like assumption becomes invalid, which can be verified by the monotonic decrease on the right-hand side, suggesting that at higher pressure states the notion of permeability from a macroscopic Darcy law no longer holds. These observations are consistent with Scandelli et al. 2022; Whitaker 1998.

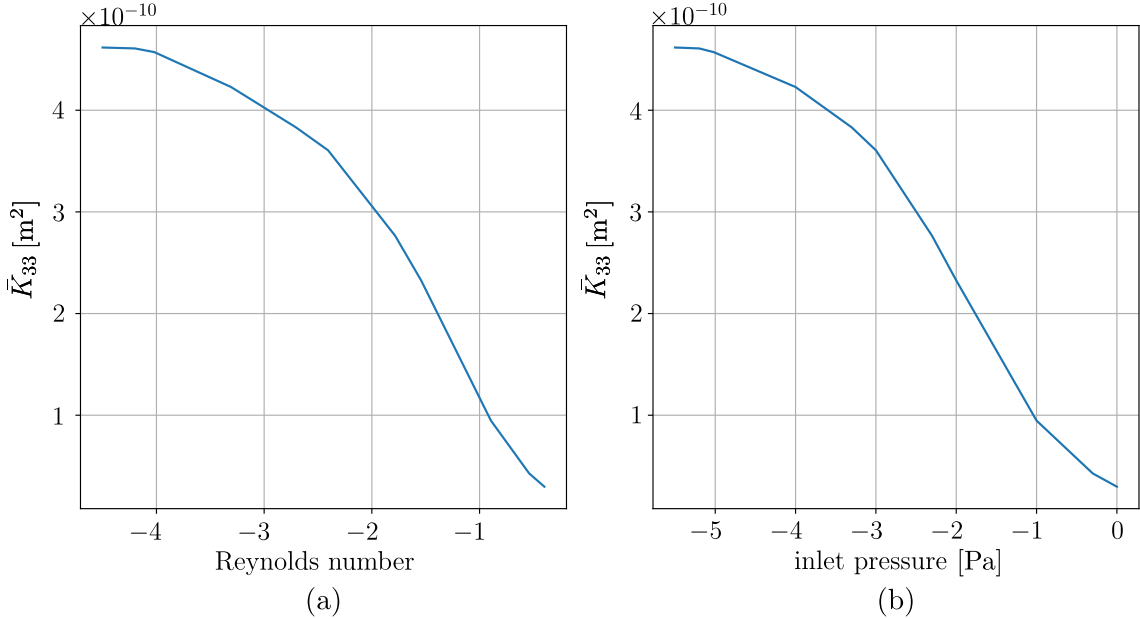


**Figure 40:** Evolution of the principal direction permeability  $\bar{K}_{33}$ , at the left side in function of the decimal logarithm of the Reynolds number and at the right-hand side, in function of the decimal logarithm of the imposed inlet pressure.

## Discussion

In this study, we have introduced a comprehensive methodology for generating synthetic porous media along with a direct computational pipeline that seamlessly integrates these structures into fluid-structure interaction simulations. This pipeline facilitates the transition from STL geometries to voxel-based domains and enables numerical simulations using the C++ library OpenFPM. Through this framework, we have directly implemented the model described in Section 18. Furthermore, we have established a foundation for the analysis and estimation of the permeability of these synthetic samples, following the approaches of Whitaker 1986; Whitaker 1998, and linking these estimates with the experimental evaluation. The ultimate goal

is to provide parametric control over porous structures for real-world applications, such as prosthetics.

Using four different configurations of synthetic porous media (seed numbers: 1500, 2000, 2500, and 3000), the Constructive Solid Geometry (CSG) workflow generated structures with porosities ranging from approximately 10% to 30%. Higher seed numbers resulted in more intricate geometries, leading to increased computational times, with the 3000-seed case requiring nearly 18 hours for CSG processing. Following voxelisation, numerical simulations using Entropically Damped Artificial Compressibility (EDAC) and discretisation-corrected particle strength exchange (DC-PSE) methods revealed that at low Reynolds numbers ( $\text{Re} < 0.5$ ), the flow exhibited Darcy-like behaviour with negligible inertial effects. The estimated permeability plateaued under creeping flow conditions, demonstrating a linear relationship between the mean fluid velocity and the applied pressure gradient. However, as the inlet pressure increased, the non-linear effects became more pronounced, causing deviations from Darcy's law. These findings highlight the robustness of the proposed pipeline in capturing different levels of porosity and the transition from creeping to more complex flow regimes within synthetic porous media.

Finally, we consider the full determination of the permeability tensor. This requires modifications to the generated microstructures to adjust the principal direction of fluid flow, along with refinements to the boundary condition to ensure consistency across successive simulations. Following the approaches outlined in Lang et al. 2014; Pouya and Courtois 2002a; Scandelli et al. 2022, we propose to construct a linear system with a unique solution that allows the explicit formulation of the second-order effective permeability tensor for a given porous medium.

## Declaration of Competing Interest

Authors have no conflicts of interest to report.

**Supplementary material:** The codes corresponding to the generation of the porous medium of this article are available at the following link: [https://github.com/ThomasLavigne/Porous\\_media\\_Generation.git](https://github.com/ThomasLavigne/Porous_media_Generation.git).

## Acknowledgment

This research was funded in whole, or in part, by the Luxembourg National Research Fund (FNR), grant reference No. 17013182. For the purpose of open access, the author has applied a Creative Commons Attribution 4.0 International (CC BY 4.0) license to any Author Accepted Manuscript version arising from this submission.

# **Part VI**

## **General conclusion and perspectives**



# General Conclusion and perspectives

This thesis set out to advance the field of poromechanics, with a particular emphasis on its application to human skin. Through a comprehensive and interdisciplinary approach, we developed a robust framework encompassing theoretical derivations, computational modelling, variance-based sensitivity analysis, gradient-based parameter calibration, experimental design, and, model evaluation using experimental data. A modular and hierarchical porous model was proposed and evaluated to assess its capability in capturing both the apparent mechanical behaviour of human skin *in vivo* and the dynamics of blood micro-circulation under mechanical loading. While damage processes were not yet incorporated, the groundwork laid here offers a clear path toward coupling mechanical and biological factors—crucial for understanding the mechanisms underlying the onset of skin damage.

This work provides a solid foundation for future research, bridging mechanics and physiology, and opens new avenues for the development of predictive, patient-specific skin models in biomedical applications.

## Theoretical and Computational Foundation

The theoretical model presented in this thesis is thoroughly developed, with a detailed step-by-step tutorial for implementation in the open-source software FEniCSx. This resource is pivotal for enabling researchers and practitioners to replicate and build on our work. Throughout the course of this Ph.D., the computational framework has been continually updated to maintain compatibility with the latest software versions, ensuring its longevity and functionality in the evolving landscape of computational mechanics. The models have been framed within the general theoretical

## *General conclusion and perspectives*

context of TCAT (Thermodynamically Constrained Averaging Theory), which provides a systematic and rigorous formulation of conservation laws at different scales (pore, REV, etc.) while accounting for multiphysics couplings. However, despite its conceptual richness, TCAT remains challenging to implement directly in finite element software. The use of FEniCSx facilitated the direct translation of the mathematical formulas to the numerical environment.

By adopting open-source tools like FEniCSx, we promote reproducibility, transparency, and global collaboration in scientific research. Furthermore, using our GitHub repositories, researchers worldwide can freely access, modify, and build upon our work, ensuring that our contributions to poromechanics continue to evolve and adapt to new challenges. This approach democratises access to advanced computational methods, encouraging worldwide contributions that will further enhance and expand the scope of poromechanics research. This objective was already reached as part of the Ph.D., when international Ph.D. students (A. Kerachni on foetal brain growth and R. Collet on the study of breast chemotherapeutic treatment) reached out to us for help in the implementation of their models in FEniCSx.

## **Model evaluation and Sensitivity Analysis**

A central component of this work has been the evaluation of the developed models. Where applicable, our models were compared with experimental data and benchmark studies to assess their accuracy and predictive capabilities. Such evaluation efforts are crucial to bridge the gap between theoretical advances and practical applications in clinical settings. A variance-based sensitivity analysis was performed to identify the key parameters that influence the model's behaviour, providing critical insights into the underlying mechanics of the poromechanics of the human skin. This analysis not only deepens our understanding of the system, but also guides future experimental and modelling efforts by pinpointing the most influential factors.

To optimise the model parameters, gradient-based calibration techniques were applied, refining the predictive capabilities of the model and aligning the simulated results with empirical observations. These improvements are vital for the potential integration of these models into clinical workflows, where reliability and precision are paramount.

## Proof-of-Concept on a simplified Model and Clinical Relevance

Building upon this comprehensive foundation, a simplified proof of concept model was developed to simulate the time-dependent mechanical response of the human skin. This model used unpublished *in vivo* experimental data from a single patient, allowing comparison with clinically relevant data. The experimental data was obtained through a series of controlled extension tests, which provided insight into responses to stress-relaxation and skin creep.

The model effectively captured complex skin behaviours, including inherent time-dependent behaviour and non-linear stress-strain relationships, both well-documented in dermatological research. Estimation of parameters revealed values consistent with the existing literature, further confirming the credibility of the model. This proof-of-concept work sets the stage for future research that aims to refine the model to account for patient-specific variability, such as age, hydration, and skin thickness, as well as evaluating it across a wider cohort of subjects. Despite the limited dataset, the model demonstrated strong correlations with expected physiological responses, evaluating its clinical relevance.

## Advancing Biological Complexity and Vascular Modelling

Looking ahead, several exciting avenues for future research are identified. One key direction is the introduction of more complex biological exchanges into the model such as proposed by Buganza Tepole and Kuhl 2014.

As part of this Ph.D. work, we included a vascular compartment for future integration of chemo-bio-mechanical coupling, offering a more comprehensive framework for understanding the complex interactions within human skin. As outlined in Appendix A of Part IV, the nutrient supply would then be correlated with blood flow within the model, thereby enhancing our mechanistic understanding of chemo-bio-mechanical interactions. An extensive theoretical framework for a two-compartment model was introduced and compared with experimental blood flow measurements

## *General conclusion and perspectives*

using Laser Doppler Flowmetry (LDF). A biphasic interstitium was incorporated to account for both the cellular and interstitial fluid phases. However, because of the characteristic time scale of the experiment, the model was simplified, assuming that cells behave as solids within the experimental time frame. At longer timescales, consistent with previous studies (Buganza Tepole and Kuhl 2014), the cells could exhibit a highly viscous fluid-like behaviour. The variance-based sensitivity revealed a strong coupling for the influence of the material parameters on blood flow, highlighting the dominant contribution of the solid stiffness, the vessel bulk modulus and the choice of the vascular permeability/porosity relationship. In an effort to assess clinical relevance, the model output was compared with the experimental data set. Interestingly, the model demonstrated its potential to capture ischaemic and hyperaemic responses of human skin using literature-based parameters.

Future efforts will focus on refining this vascular model by incorporating additional physiological complexities, such as autoregulatory mechanisms and vessel compliance. This would allow for a more accurate representation of tissue perfusion, particularly in conditions such as diabetes and peripheral artery disease, where microvascular dysfunction plays a crucial role.

## **Computational Calibration, Evaluation and Clinical Integration**

As the model becomes more sophisticated, computational efficiency remains a critical challenge. Currently, a 250,000-element sample discretising the two-compartment model requires approximately two hours per time step on a modern CPU, which can be reduced to 15 minutes using 16 CPUs, leading to a total computation time of eight days. Consequently, parameter calibration can span several weeks, which is not feasible within clinical time constraints. Potential strategies to reduce computation time include employing locally refined meshes, exploiting geometric symmetries, adopting linearised constitutive relationships, and simplifying the number of modelled phenomena. However, achieving real-time computation on the organ scale remains a significant hurdle. Optimising the model to allow real-time simulations will be essential for clinical applications, such as personalised treatment planning and intraoperative decision making. Machine learning techniques could play a key

role in improving model performance (Dehghani and Zilian 2023) by identifying key parameters and facilitating the optimisation process. The use of parallel computing frameworks, such as GPU acceleration and distributed cloud computing, will be instrumental in handling the computational demands of patient-specific models.

In addition, to further evaluate the model, additional experimental data should be gathered. Despite these promising developments, challenges remain to control boundary conditions. The proof-of-concept studies conducted thus far have been evaluated using partial and surface-level data, highlighting the inherent complexity in obtaining comprehensive one-to-one calibration. Determining the precise pressures required to maintain specific blood flow rates remains computationally demanding. The interplay of mechanical, biological, and computational factors introduces additional layers of uncertainty, necessitating more robust and adaptive modelling approaches. In addition, techniques such as line-confocal optical coherence tomography (LC-OCT) could provide valuable 3D displacement maps for full-field displacement evaluation, potentially in conjunction with digital volume correlation methods. However, LCOCT is depth limited, restricting its application to superficial layers of tissue, and while magnetic resonance imaging (MRI) could offer deeper insights, it lacks the dynamic capabilities of LC-OCT. Hybrid imaging strategies that combine the high spatial resolution of LC-OCT with the volumetric coverage of MRI may offer a more comprehensive understanding, although at the cost of increased complexity and resource requirements. Furthermore, displacement data alone is insufficient; it must be supplemented with reaction load measurements for pressure evaluation and perfusion assessments to evaluate blood flow. Advanced sensor technologies, such as flexible pressure transducers and fibre-optic sensors, could improve the accuracy of measurement, providing real-time feedback to refine boundary condition estimates. Trans-cutaneous oxygen pressure measurements could also provide insight into tissue oxygenation, although a direct comparison with modelled oxygen concentrations remains a challenge.

## **Towards Phantom Based Verification Procedures**

As previously introduced, the complexity of accurately defining boundary conditions, such as blood flow rates and pressures, remains a major hurdle. Moving towards

## General conclusion and perspectives

phantom based methods would allow to evaluate the mathematical constitutive relationships. Such methods seem necessary to evaluate empirical relationships such as the vascular permeability constitutive law.

A potential approach to address part of these challenges would be to integrate *in silico* and *ex vivo* (digital volume correlation) experiments using synthetic phantoms. As proposed in Part V, the porous cylinders were automatically generated via a Python pipeline, with fluid flow applied to estimate the permeability values relative to the deformed state. The intention was to 3D print these samples and evaluate them using the instrumented microCT imaging at LMPS for single- and two-compartment samples. An experimental bench compatible with experimental constraints was designed in Figure 41. However, due to experimental constraints and limitations in the microCT setup, the 3D printing approach proved unsatisfactory, leading to the abandonment of this experimental avenue within the time frame of this Ph.D.

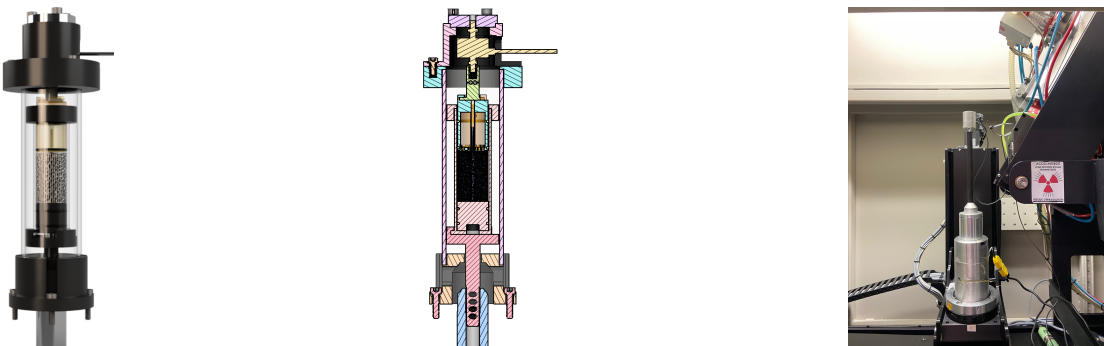


**Figure 41:** Designed experimental bench including a computed 3D sample (left), cut view in the middle plane of the assembly (centre), and experimental set-up in the instrumented micro-CT-scanner at Laboratoire de Mécanique Paris-Saclay (right).

As an alternative, efforts were concentrated on the *in silico* pipeline, highlighting potential areas for refinement in computational modelling and paving the way for extension in the development of experimental setups that inform the management of boundary conditions and the measurements of permeability. The use of advancements in additive manufacturing technologies and improving experimental protocols may eventually enable the successful implementation of the originally proposed approach.

## Moving Towards Personalised Medicine

A major challenge in the transition to clinical applications is the development of patient-specific models that account for variability in skin properties between individuals. Generating realistic patient-specific meshes and calibrating the model to individual parameters presents significant computational challenges, particularly for large-scale simulations. Generating realistic multi-domain conformal meshes is inherently complex, and to date, only simplified geometries have been considered. Patient-specific geometries often require a large number of elements, resulting in substantial computational demands. The integration of machine learning could offer solutions for dynamic mesh optimisation and prediction of parameter distributions, reducing the computational burden and allowing for real-time simulations that could be used by clinicians.

Furthermore, to bring this model into clinical practice, robust verification and evaluation procedures are needed to ensure its accuracy and reliability. The use of high-resolution magnetic resonance imaging and CT scans, along with real-time data from wearable sensors, will enable the model to provide more precise information on skin health and disease progression. However, beyond technical considerations, there are significant challenges related to data privacy, standardisation, and regulatory compliance. The implementation of personalised medicine frameworks must adhere to stringent data protection regulations, which require secure data handling and anonymisation protocols. In addition, the establishment of standardised workflows and interoperability between different computational tools and clinical systems is essential to facilitate widespread adoption in healthcare settings. In summary, while substantial progress has been made in developing computational frameworks for personalised medicine, several hurdles remain. Addressing computational efficiency, data integration, model evaluation, and regulatory compliance will be crucial to transitioning these frameworks from research environments to routine.

## **Expanding Model Capabilities: Damage and remodelling**

Another key focus for future work is the incorporation of skin damage and remodelling processes, fundamental aspects of skin behaviour that have not yet been addressed in the current model, since the priority has been to establish the physiological relevance of the model before introducing additional complexity. By introducing sub-models simulating injury, wound healing, and ageing, the model could predict long-term changes in skin structure and function, offering valuable insights for clinical treatments. Investigating the interactions between mechanical loading, microvascular dynamics, and biochemical signals in these contexts could provide valuable information for clinical decision-making and therapeutic interventions.

Future research should also explore the inclusion of biochemical factors such as inflammatory responses and cellular signalling pathways, which are essential to understand skin health and disease progression. The model could be expanded to address a wider range of dermatological conditions, such as diabetic foot ulcers and venous leg ulcers, and assess the viability of skin grafts.

## **Conclusion: An Interdisciplinary Approach to Skin Biomechanics**

In conclusion, the work presented in this thesis lays a solid foundation for the development of a multi-compartment porous media mechanics model for skin. Special care was taken to enhance the reproducibility of the studies, with guidance provided through open-access tutorials and workshops, as well as a Python package accompanied by a theoretical guide in the last GitHub repository. However, significant work remains to be done. Overcoming challenges related to computational efficiency, data integration, and model evaluation will be critical to ensuring clinical applicability of the model. Future research should focus on advancing these aspects, integrating machine learning, experimental evaluation, and clinical collaboration to develop personalised predictive models.

## *General conclusion and perspectives*

Furthermore, the integration of a vascular compartment for chemo-bio-mechanical interactions marks a significant advancement in tissue engineering and biomechanics. By bridging the gap between theoretical modelling and experimental data, this work has the potential to provide valuable information on the complex interactions between biological, chemical, and mechanical factors that govern tissue function and adaptation.

Ultimately, the fusion of computational modelling, experimental research, and clinical expertise presents a promising path forward for personalised dermatological treatments. This interdisciplinary approach improves our understanding of skin biomechanics and offers new possibilities for the management of skin-related medical conditions. The collaborative nature of this research, which involves expertise in materials science, bioengineering, clinical dermatology, and computational mechanics, has the potential to redefine the modelling and treatment of skin disorders. It could lead to innovative therapeutic strategies, personalised medicine, and improved patient outcomes. Future studies should aim to incorporate this framework into clinical tools and diagnostic devices, facilitating a smooth transition from theory to practice.



## **Scientific contributions**



# Scientific Contributions

## Articles

- Digital Volume Correlation for large deformations of soft tissues: Pipeline and proof of concept for the application to breast *ex vivo* deformations, 30 September 2022, Lavigne et al. 2022a,
- Identification of material parameters and traction field for soft bodies in contact, 1 March 2023, Lavigne et al. 2023a,
- Single and bi-compartment poro-elastic model of perfused biological soft tissues: FEniCSx implementation and tutorial, Lavigne et al. 2023b,
- Poromechanical modelling of the time-dependent response of *in vivo* human skin during extension, Lavigne et al. 2024,
- Hierarchical poromechanical approach to investigate the impact of mechanical loading on human skin micro-circulation, Lavigne et al. 2025b,
- Synthetic porous media generation, Lavigne et al. 2025a,
- MRI-based computational modeling of human cortical folding, Kerachni et al. 2024 (co-author), [https://www.scipedia.com/public/Kerachni\\_et\\_al\\_2024a](https://www.scipedia.com/public/Kerachni_et_al_2024a)
- Patient-specific breast tumour modelling to predict response to neoadjuvant chemotherapy, Collet et al. (co-author, in progress),
- A mathematical model for two-phase flow in confined environments: numerical solution and validation, Sciumè et al. (co-author, under review),
- Physics-informed Dynamic Graph Convolutional Neural Network with Curriculum Learning for Pore-scale Flow Simulations, Rajabi et al. (co-author, in progress), <https://hdl.handle.net/10993/57127>.

## **Congresses, conferences and seminars:**

- Journée scientifique de la F2M-MSP, Oral Communication: Multiscale Modelling of the muscle, 13<sup>th</sup> of February 2023, F2M - Jussieu Paris,
- Journée scientifique - Biomécanique et biomatériaux - de la F2M-MSP, Oral Communication: Modélisation poro-élastique de la peau humaine *in vivo*, 4<sup>th</sup> of April 2024, F2M - Polytechnique Saclay,
- British Society for Strain Measurement, Oral Communication: FE-based Heterogeneous Digital Volume Correlation to Measure Large Deformations of Breast's Soft Tissues, Glasgow, August 2023,
- International Symposium on Computer Methods in Biomechanics and Biomedical Engineering, Participating in the organising and Poster presentation: 'On the feasibility of using FE-based Digital Volume Correlation to map breast deformation', Paris May 2023,
- Interpore BeneLux 2024, Poster Presentation: Poromechanics to account for the time-dependent behaviour of human skin during extension tests,
- Interpore BeneLux 2024, co-author Poster Presentation: Image informed breast tumour models to predict the outcome of neoadjuvant chemotherapy,
- PhD Day: Poster Presentation at the Doctoral Programme in Complex Systems Science, Poromechanics to account for the interplay between the mechanical and biological responses for the human skin, Best Poster Award, rank 2nd, Luxembourg, June 2024,
- Workshop organiser and animator on the use of GMSH and FEniCSx. I2M Bordeaux. September 2024
- EPUAP, Oral communication, Lausanne, September 2024: Poro-elasticity to capture the time-dependent mechanical behaviour of *in vivo* human skin during an extension test, Lausanne, Switzerland, 2024.

## **GitHub Repositories:**

- Dolfinx\_Porous\_Media at [https://github.com/ThomasLavigne/Dolfinx\\_Porous\\_Media.git](https://github.com/ThomasLavigne/Dolfinx_Porous_Media.git),

- FEniCSx\_GMSH\_tutorials at [https://github.com/ThomasLavigne/FEniCSx\\_GMSH\\_tutorials.git](https://github.com/ThomasLavigne/FEniCSx_GMSH_tutorials.git),
- Skin\_porous\_modelling at [https://github.com/ThomasLavigne/Skin\\_porous\\_modelling.git](https://github.com/ThomasLavigne/Skin_porous_modelling.git),
- 2-compartment-poromechanical-and-LDF-measurement at <https://github.com/ThomasLavigne/2-compartment-poromechanical-and-LDF-measurement.git>,
- Synthetic Porous Media Generation at [https://github.com/ThomasLavigne/Porous\\_media\\_Generation.git](https://github.com/ThomasLavigne/Porous_media_Generation.git).

## Others:

- Development of codes from tutorials up to the development of a small python package for porous media modelling using FEniCSx,
- Reviews for *Journal of Biomechanics* and *Applied Mathematical Modelling*,
- International exchange, sharing of the PhD work and brain mechanics. December 2024, LKM, Erlangen, Germany,
- Help in the computational supervision of Matthieu Lacour M2 Internship at I2M on micro-fluidic chips design,
- 75h teaching including Mathematics (L3), Basics in Solid Mechanics (M1), Finite Element Modelling (M1), and Dynamics (M2),
- Management of the lab website and youtube channel (Luxembourg).



## Bibliography



# Bibliography

- 3DS Dassault Softwares (n.d.). <https://www.autodesk.com/fr/products/fusion-360/>.
- Aarnes, J. E. and Y. Efendiev (2008). “Mixed Multiscale Finite Element Methods for Stochastic Porous Media Flows”. In: *SIAM Journal on Scientific Computing* 30.5, pp. 2319–2339.
- Abbasi, N. R., H. M. Shaw, D. S. Rigel, R. J. Friedman, W. H. McCarthy, I. Osman, A. W. Kopf, and D. Polsky (2004). “Early Diagnosis of Cutaneous Melanoma: Revisiting the ABCD Criteria”. In: *JAMA* 292.22, p. 2771.
- Abdo, J. M., N. A. Sopko, and S. M. Milner (2020). “The applied anatomy of human skin: A model for regeneration”. In: *Wound Medicine* 28, p. 100179.
- Abyaneh, M.-A. Y., R. Griffith, L. Falto-Aizpurua, and K. Nouri (2014). “Famous Lines in History: Langer Lines”. In: *JAMA Dermatology* 150.10, p. 1087.
- AceFEM/AceGen (n.d.). <http://symech.fgg.uni-lj.si/>.
- Adler, P. (1992). *Porous Media: Geometry and Transports*. Butterworth-Heinemann.
- Agache, P. G., C. Monneur, J. L. Leveque, and J. De Rigal (1980). “Mechanical properties and Young’s modulus of human skin in vivo”. In: *Archives of Dermatological Research* 269, pp. 221–232.
- Agnaou, M., D. Lasseux, and A. Ahmadi (2017). “Origin of the inertial deviation from Darcy’s law: An investigation from a microscopic flow analysis on two-dimensional model structures”. In: *Physical Review E* 96 (4), p. 43105.
- Ajan, A., K. Roberg, I. Fredriksson, and J. Abtahi (2024). “Reproducibility of Laser Doppler Flowmetry in gingival microcirculation. A study on six different protocols”. In: *Micovascular Research* 153. Cited by: 0.

## Bibliography

- Alexander, H. and T. Cook (1977). "Accounting for natural tension in the mechanical testing of human skin". In: *Journal of Investigative Dermatology* 69.3, pp. 310–314.
- Allard, J. F. and N. Atalla (2009). *Propagation of Sound in Porous Media: Modelling Sound Absorbing Materials*. 2nd ed. John Wiley & Sons.
- Alnæs, M., J. Blechta, J. Hake, A. Johansson, B. Kehlet, A. Logg, C. Richardson, J. Ring, M. E. Rognes, and G. N. Wells (2015). "The FEniCS Project Version 1.5". en. In: *Archive of Numerical Software* Vol 3.
- Alnæs, M. S., A. Logg, K. B. Ølgaard, M. E. Rognes, and G. N. Wells (2014). "Unified Form Language: A Domain-Specific Language for Weak Formulations of Partial Differential Equations". In: *ACM Trans. Math. Softw.* 40.2.
- An, L., J. Qin, and R. K. Wang (2010). "Ultrahigh sensitive optical microangiography for in vivo imaging of microcirculations within human skin tissue beds". In: *Optics Express* 18.8, p. 8220.
- Annaidh, A. N., K. Bruyère, M. Destrade, M. D. Gilchrist, and M. Otténio (2012). "Characterization of the anisotropic mechanical properties of excised human skin". In: *Journal of the Mechanical Behavior of Biomedical Materials* 5.1, pp. 139–148.
- ANSYS (n.d.). <https://www.ansys.com>.
- Anthony, D., S. Parboreeah, M. Saleh, and P. Papanikolaou (2008). "Norton, Waterlow and Braden scores: a review of the literature and a comparison between the scores and clinical judgement". In: *Journal of Clinical Nursing* 17.5, pp. 646–653.
- Antonova, N. (2012). "On some mathematical models in hemorheology". In: *Biotechnology and Biotechnological Equipment* 26.5. Cited by: 14; All Open Access, Bronze Open Access, pp. 3286–3291.
- Argarini, R., K. J. Smith, H. H. Carter, L. H. Naylor, R. A. McLaughlin, and D. J. Green (2020). "Visualizing and quantifying the impact of reactive hyperemia on cutaneous microvessels in humans". In: *Journal of Applied Physiology* 128.1, pp. 17–24.

- Argoubi, M. and A. Shirazi-Adl (1996). “Poroelastic creep response analysis of a lumbar motion segment in compression”. In: *Journal of Biomechanics* 29.10, pp. 1331–1339.
- Armstrong, B. K. and A. Kricker (1995). “Skin Cancer”. In: *Dermatologic Clinics* 13.3, pp. 583–594.
- Arndt, D., W. Bangerth, M. Bergbauer, M. Feder, M. Fehling, J. Heinz, T. Heister, L. Heltai, M. Kronbichler, M. Maier, P. Munch, J.-P. Pelteret, B. Turcksin, D. Wells, and S. Zampini (2023). “The deal.II Library, Version 9.5”. In: *Journal of Numerical Mathematics* 31.3, pp. 231–246.
- Arndt, D., W. Bangerth, D. Davydov, T. Heister, L. Heltai, M. Kronbichler, M. Maier, J.-P. Pelteret, B. Turcksin, and D. Wells (2021). “The deal.II finite element library: Design, features, and insights”. In: *Computers & Mathematics with Applications* 81, pp. 407–422.
- Ashby, M., A. Evans, N. A., L. J. Gibson, J. W. Hutchinson, and H. J. G. W. and (2000). “Metal Foams: A Design Guide,” in: *Butterworth-Heinemann*.
- Ateshian, G. A. (2009). “The role of interstitial fluid pressurization in articular cartilage lubrication”. In: *Journal of Biomechanics* 42.9, pp. 1163–1176.
- Aukland, K. and G. Nicolaysen (1981). “Interstitial fluid volume: local regulatory mechanisms.” In: *Physiological Reviews* 61.3, pp. 556–643.
- Autodesk Fusion 360* (n.d.). <https://www.3ds.com/>.
- Avram, A. S., M. M. Avram, and W. D. James (2005). “Subcutaneous fat in normal and diseased states”. In: *Journal of the American Academy of Dermatology* 53.4, pp. 671–683.
- Ayadh, M., A. Guillermin, M.-A. Abellan, A. Bigouret, and H. Zahouani (2023). “The assessment of natural human skin tension orientation and its variation according to age for two body areas: Forearm and thigh”. In: *Journal of the Mechanical Behavior of Biomedical Materials* 141, p. 105798.
- Ayello, C. H. L. E. A. (2008). “Patient Safety and Quality: An Evidence-Based Handbook for Nurses.” In: NIH. Chap. 12.

## Bibliography

- Bader, D. and P. Bowker (1983). "Mechanical characteristics of skin and underlying tissues in vivo". In: *Biomaterials* 4.4, pp. 305–308.
- Bai, Y., D. Sun, J. Lin, D. Kennedy, and F. Williams (2012). "Numerical aerodynamic simulations of a NACA airfoil using CFD with block-iterative coupling and turbulence modelling". In: *International Journal of Computational Fluid Dynamics* 26.2, pp. 119–132.
- Balasubramanian, G. V., N. Chockalingam, and R. Naemi (2021). "The Role of Cutaneous Microcirculatory Responses in Tissue Injury, Inflammation and Repair at the Foot in Diabetes". In: *Frontiers in Bioengineering and Biotechnology* 9.
- Banhart, J. (2001). "Manufacture, Characterization and Application of Cellular Metals and Metal Foams". In: *Prog. Mater. Sci.* 46, pp. 559–632.
- Baran, U., W. J. Choi, and R. K. Wang (2015). "Potential use of <scp>OCT</scp>-based microangiography in clinical dermatology". In: *Skin Research and Technology* 22.2, pp. 238–246.
- Baratta, I. A., J. P. Dean, J. S. Dokken, M. Habera, J. S. Hale, C. N. Richardson, M. E. Rognes, M. W. Scroggs, N. Sime, and G. N. Wells (2023). *DOLFINx: The next generation FEniCS problem solving environment*. en.
- Bartek, M. J., J. A. Labudde, and H. I. Maibach (1972). "Skin Permeability In Vivo: Comparison in Rat, Rabbit, Pig and Man". In: *Journal of Investigative Dermatology* 58.3, pp. 114–123.
- Basiladze, T., G. Bekaia, N. Gongadze, and N. Mitagvaria (2015). "Possible mechanism of hyperemia in the skin caused by non-painful mechanical pressure". In: *Georgian medical news* 238. Cited by: 0, pp. 83–88.
- Bauer, D., R. Grebe, and A. Ehrlacher (2005). "First phase microcirculatory reaction to mechanical skin irritation: a three layer model of a compliant vascular tree". In: *Journal of Theoretical Biology* 232.2, pp. 249–260.
- Bear, J. (1972a). *Dynamics of Fluids in Porous Media*. American Elsevier.
- Bear, J. (1972b). *Dynamics of Fluids in Porous Media*. American Elsevier Publishing Company.

- Benítez, J. M. and F. J. Montáns (2017). “The mechanical behavior of skin: Structures and models for the finite element analysis”. In: *Computers & Structures* 190, pp. 75–107.
- Bennett, G., C. Dealey, and J. Posnett (2004). “The cost of pressure ulcers in the UK”. In: *Age and Ageing* 33.3, pp. 230–235. eprint: <https://academic.oup.com/ageing/article-pdf/33/3/230/49574/afh086.pdf>.
- Bera, K., A. Kiepas, I. Godet, Y. Li, P. Mehta, B. Ifemembu, C. D. Paul, A. Sen, S. A. Serra, K. Stoletov, J. Tao, G. Shatkin, S. J. Lee, Y. Zhang, A. Boen, P. Mistriotis, D. M. Gilkes, J. D. Lewis, C.-M. Fan, A. P. Feinberg, M. A. Valverde, S. X. Sun, and K. Konstantopoulos (2022). “Extracellular fluid viscosity enhances cell migration and cancer dissemination”. In: *Nature* 611.7935, pp. 365–373.
- Bergstrom, N. et al. (1987). “The Braden Scale for predicting pressure sore risk”. In: *Nurs res* 36.4, pp. 205–210.
- Bhattacharya, A., V. V. Calmudi, and R. . Mahajan (2002). “Thermophysical properties of high porosity metal foams”. In: *International Journal of Heat and Mass Transfer* 45, pp. 1017–1031.
- Biot, M. (1956). “Theory of propagation of elastic waves in a fluid-saturated porous solid. I. Low-frequency range”. In: *The Journal of the Acoustical Society of America* 28.2, pp. 168–178.
- Biot, M. A. (1941). “General theory of three-dimensional consolidation”. In: *Journal of applied physics* 12.2, pp. 155–164.
- Birkebaek, N., A. Johansen, and J. Solvig (1998). “Cutis/subcutis thickness at insulin injection sites and localization of simulated insulin boluses in children with Type 1 diabetes mellitus: need for individualization of injection technique?” In: *Diabetic Medicine* 15.11, pp. 965–971.
- Biswal, B., P.-E. Oren, R. J. Held, S. Bakke, and R. Hilfer (2011). “MODELING OF MULTISCALE POROUS MEDIA”. In: *Image Analysis & Stereology* 28.1.
- Boomsma, K. and D. Poulikakos (2001). “On the Effective Thermal Conductivity of a Three-Dimensionally Structured Fluid-Saturated Metal Foam”. In: *Int. J. Heat Mass Transfer* 44, pp. 827–836.

## Bibliography

- Boomsma, K. and D. Poulikakos (2002). "The effects of compression and pore size variations on the liquid flow characteristics of metal foams". In: *Journal of Fluids Engineering* 124, pp. 263–272.
- Borchardt, T., J. Ernst, A. Helmke, M. Tanyeli, A. F. Schilling, G. Felmerer, and W. Viöl (2017). "Effect of direct cold atmospheric plasma (di<scp>CAP</scp>) on microcirculation of intact skin in a controlled mechanical environment". In: *Microcirculation* 24.8.
- Bosboom, E., M. Hesselink, C. Oomens, C. Bouten, M. Drost, and F. Baaijens (2001). "Passive transverse mechanical properties of skeletal muscle under in vivo compression". In: *Journal of Biomechanics* 34.10, pp. 1365–1368.
- Boutin, C. and J. Auriault (1991). "Dynamic behaviour of porous media saturated by a Newtonian fluid: I. Inertial effects". In: *International Journal of Engineering Science* 29.1, pp. 81–93.
- Boyer, G., H. Zahouani, A. L. Bot, and L. Laquieze (2007). "In vivo characterization of viscoelastic properties of human skin using dynamic micro-indentation". In: *2007 29th Annual International Conference of the IEEE Engineering in Medicine and Biology Society*. IEEE.
- Braverman, I. M. (1989). "Ultrastructure and Organization of the Cutaneous Microvasculature in Normal and Pathologic States". In: *Journal of Investigative Dermatology* 93.2, S2–S9.
- Breuls, R. G. M., C. V. C. Bouten, C. W. J. Oomens, D. L. Bader, and F. P. T. Baaijens (2003). "A Theoretical Analysis of Damage Evolution in Skeletal Muscle Tissue With Reference to Pressure Ulcer Development". In: *Journal of Biomechanical Engineering* 125.6, pp. 902–909.
- Breuls, R. G. M., B. G. Sengers, C. W. J. Oomens, C. V. C. Bouten, and F. P. T. Baaijens (2002). "Predicting Local Cell Deformations in Engineered Tissue Constructs: A Multilevel Finite Element Approach". In: *Journal of Biomechanical Engineering* 124.2, pp. 198–207.
- Budday, S., T. C. Ovaert, G. A. Holzapfel, P. Steinmann, and E. Kuhl (2019). "Fifty Shades of Brain: A Review on the Mechanical Testing and Modeling of Brain

- Tissue”. In: *Archives of Computational Methods in Engineering* 27.4, pp. 1187–1230.
- Buganza Tepole, A. and E. Kuhl (2014). “Computational modeling of chemo-bio-mechanical coupling: a systems-biology approach toward wound healing”. In: *Computer Methods in Biomechanics and Biomedical Engineering* 19.1, pp. 13–30.
- Bulle, R. (2022). “A posteriori error estimation for finite element approximations of fractional Laplacian problems and applications to poro-elasticity”. Theses. Université Bourgogne Franche-Comté ; Université du Luxembourg.
- Bulle, R., G. Alotta, G. Marchiori, M. Berni, N. F. Lopomo, S. Zaffagnini, S. P. A. Bordas, and O. Barrera (2021). “The Human Meniscus Behaves as a Functionally Graded Fractional Porous Medium under Confined Compression Conditions”. In: *Applied Sciences* 11.20, p. 9405.
- Burns, T., S. M. Breathnach, N. H. Cox, and C. Griffiths, eds. (2010). *Rook’s textbook of dermatology*. en. 8th ed. Chichester, England: Wiley-Blackwell.
- Caon, M. (2020). “Homeostasis”. In: *Examination Questions and Answers in Basic Anatomy and Physiology*. Springer International Publishing, pp. 173–183.
- Carrasco-Mantis, A., T. Randelovic, H. Castro-Abril, I. Ochoa, M. Doblaré, and J. A. Sanz-Herrera (2023). “A mechanobiological model for tumor spheroid evolution with application to glioblastoma: A continuum multiphysics approach”. In: *Computers in Biology and Medicine* 159, p. 106897.
- CAST3M (n.d.). <https://www-cast3m.cea.fr/index.php>.
- Ceelen, K., A. Stekelenburg, S. Loerakker, G. Strijkers, D. Bader, K. Nicolay, F. Baaijens, and C. Oomens (2008). “Compression-induced damage and internal tissue strains are related”. In: *Journal of Biomechanics* 41.16, pp. 3399–3404.
- Chambert, J., T. Lihoreau, S. Joly, B. Chatelain, P. Sandoz, P. Humbert, E. Jacquet, and G. Rolin (2019). “Multimodal investigation of a keloid scar by combining mechanical tests in vivo with diverse imaging techniques”. In: *Journal of the Mechanical Behavior of Biomedical Materials* 99, pp. 206–215.

## Bibliography

- Chaudhuri, O., J. Cooper-White, P. A. Janmey, D. J. Mooney, and V. B. Shenoy (2020). “Effects of extracellular matrix viscoelasticity on cellular behaviour”. In: *Nature* 584.7822, pp. 535–546.
- Choi, P. J., V. E. Brunt, N. Fujii, and C. T. Minson (2014). “New approach to measure cutaneous microvascular function: an improved test of NO-mediated vasodilation by thermal hyperemia”. In: *Journal of Applied Physiology* 117.3, pp. 277–283.
- Clausen, J. . (2013). “Entropically damped form of artificial compressibility for explicit simulation of incompressible flow”. In: *Phys. Rev.* 87.1, p. 013309.
- Coleman, S., C. Gorecki, E. A. Nelson, S. J. Closs, T. Defloor, R. Halfens, A. Farrin, J. Brown, L. Schoonhoven, and J. Nixon (2013). “Patient risk factors for pressure ulcer development: Systematic review”. In: *International Journal of Nursing Studies* 50.7, pp. 974–1003.
- Coleman, S., J. Nixon, J. Keen, L. Wilson, E. McGinnis, C. Dealey, N. Stubbs, A. Farrin, D. Dowding, J. M. Schols, J. Cuddigan, D. Berlowitz, E. Jude, P. Vowden, L. Schoonhoven, D. L. Bader, A. Gefen, C. W. Oomens, and E. A. Nelson (2014). “A new pressure ulcer conceptual framework”. In: *Journal of Advanced Nursing* 70.10, pp. 2222–2234.
- Comsol (n.d.). <https://www.comsol.com/>.
- Connesson, N., N. Briot, P. Y. Rohan, P. A. Barraud, S. A. Elahi, and Y. Payan (2023). “Bilayer Stiffness Identification of Soft Tissues by Suction”. In: *Experimental Mechanics* 63.4, pp. 715–742.
- Connor, J. J. and C. A. Brebbia (2013). *Finite element techniques for fluid flow*. Newnes.
- Cornillon, C., B. Keenan, C. Vergari, and P.-Y. Rohan (2023). “Impact of material properties in the simulated tissue response in heel pressure ulcer prevention: a preliminary study”. In: *Journal of Wound Care* 32.9, pp. 558–559.
- Cornillon, C., A. Segain, M. Abou Karam, H. Pillet, P.-Y. Rohan, and G. Sciumè (2024). “A Preliminary Inverse Optimization Method for the Identification of Muscle and Adipose Material Properties in the Context of Pressure Ulcers”. In.

- Cowin, S. (1985). "Mechanical properties of porous media". In: *Journal of Biomechanics* 18.5, pp. 312–318.
- Cracowski, J.-L., C. T. Minson, M. Salvat-Melis, and J. R. Halliwill (2006). "Methodological issues in the assessment of skin microvascular endothelial function in humans". In: *Trends in Pharmacological Sciences* 27.9, pp. 503–508.
- Crichton, M. L., X. Chen, H. Huang, and M. A. Kendall (2013). "Elastic modulus and viscoelastic properties of full thickness skin characterised at micro scales". In: *Biomaterials* 34.8, pp. 2087–2097.
- Darcy, H. (1856). *Les fontaines publiques de Dijon*.
- Degond, P. and S. Mas-Gallic (1989). "The weighted particle method for convection-diffusion equations. Part 1: The case of an isotropic viscosity". In: *Mathematics of Computation* 53.188. Oct, pp. 485–507.
- Dehghani, H. and A. Zilian (2023). "Finite strain poro-hyperelasticity: an asymptotic multi-scale ALE-FSI approach supported by ANNs". In: *Computational Mechanics* 71.4, pp. 695–719.
- Detournay, E. and A. H.-D. Cheng (1993). *Fundamentals of poroelasticity*. Elsevier, pp. 113–171.
- Diegel, K. L., D. M. Danilenko, and Z. W. Wojcinski (2018). "The Integumentary System". In: *Fundamentals of Toxicologic Pathology*. Elsevier, pp. 791–822.
- Diridollou, S., F. Patat, F. Gens, L. Vaillant, D. Black, J. M. Lagarde, Y. Gall, and M. Berson (2000). "In vivo model of the mechanical properties of the human skin under suction". In: *Skin Research and Technology* 6.4, pp. 214–221.
- Doll, S. and K. Schweizerhof (2000). "On the development of volumetric strain energy functions". In: *Journal of Applied Mechanics* 67.1, pp. 17–21.
- Dostert, P., Y. Efendiev, and T. Hou (2008). "Multiscale finite element methods for stochastic porous media flow equations and application to uncertainty quantification". In: *Computer Methods In Applied Mechanics and Engineering* 197.43, pp. 3445–3455.
- Dubois, A., O. Levecq, H. Azimani, D. Siret, A. Barut, M. Suppa, V. del Marmol, J. Malvehy, E. Cinotti, P. Rubegni, and J.-L. Perrot (2018). "Line-field confo-

## Bibliography

- cal optical coherence tomography for high-resolution noninvasive imaging of skin tumors”. In: *Journal of Biomedical Optics* 23.10, p. 106007.
- Durand, S., B. Fromy, P. Bouyé, J. Saumet, and P. Abraham (2002). “Vasodilatation in response to repeated anodal current application in the human skin relies on aspirin-sensitive mechanisms”. In: *The Journal of physiology* 540.1, pp. 261–269.
- Dwivedi, K. K., P. Lakhani, S. Kumar, and N. Kumar (2022). “Effect of collagen fibre orientation on the Poisson’s ratio and stress relaxation of skin: an ex vivo and in vivo study”. In: *Royal Society Open Science* 9.3.
- Dybbs, A. and R. V. Edwards (1984). “A New Look at Porous Media Fluid Mechanics — Darcy to Turbulent”. In: *NATO ASI Series, Series E: Applied Sciences* (82), pp. 199–256.
- Ehlers, W. and B. Markert (2001). “A Linear Viscoelastic Biphasic Model for Soft Tissues Based on the Theory of Porous Media”. In: *Journal of Biomechanical Engineering* 123.5, pp. 418–424.
- Eldredge, J. D., A. Leonard, and T. Colonius (2002). “A General Deterministic Treatment of Derivatives in Particle Methods”. In: *Journal of Computational Physics* 180.2, pp. 686–709.
- Elleuch, K., R. Elleuch, and H. Zahouani (2006). “Comparison of elastic and tactile behavior of human skin and elastomeric materials through tribological tests”. In: *Polymer Engineering & Science* 46.12, pp. 1715–1720.
- Elouneg, A., J. Chambert, A. Lejeune, Q. Lucot, E. Jacquet, and S. Bordas (2023). “Anisotropic mechanical characterization of human skin by in vivo multi-axial ring suction test”. In: *Journal of the Mechanical Behavior of Biomedical Materials* 141, p. 105779.
- Elouneg, A. (2023). “In vivo mechanical characterization of soft tissues : application to human skin and keloid”. Theses. Université Bourgogne Franche-Comté ; Université du Luxembourg, pp. 99–101.
- Elouneg, A., D. Sutula, J. Chambert, A. Lejeune, S. Bordas, and E. Jacquet (2021). “An open-source FEniCS-based framework for hyperelastic parameter estimation from noisy full-field data: Application to heterogeneous soft tissues”. In: *Computers & Structures* 255, p. 106620.

- Escoffier, C., J. de Rigal, A. Rochefort, R. Vasselet, J.-L. Léve^que, and P. G. Agache (1989). "Age-related mechanical properties of human skin: An in vivo study". In: *Journal of Investigative Dermatology* 93.3, pp. 353–357.
- Eshel, H. and Y. Lanir (2001). "Effects of Strain Level and Proteoglycan Depletion on Preconditioning and Viscoelastic Responses of Rat Dorsal Skin". In: *Annals of Biomedical Engineering* 29.2, pp. 164–172.
- Eskandari, M. and E. Kuhl (2015). "Systems biology and mechanics of growth". en. In: *Wiley Interdiscip. Rev. Syst. Biol. Med.* 7.6, pp. 401–412.
- Fagrell, B., A. Fronek, and M. Intaglietta (1977). "A microscope-television system for studying flow velocity in human skin capillaries". en. In: *Am. J. Physiol. Heart Circ. Physiol.* 233.2, H318–H321.
- Fang, Y., J. Cui, J. Xu, J. Ma, Z. Liu, and H. Zhang (2024). "Research progress and clinical application of laser Doppler blood flow measurement technology". In: vol. 13182. Cited by: 0.
- Farkas, K., E. Kolossváry, Z. Járai, J. Nemcsik, and C. Farsang (2004). "Non-invasive assessment of microvascular endothelial function by laser Doppler flowmetry in patients with essential hypertension". In: *Atherosclerosis* 173.1, pp. 97–102.
- Fedorovich, A., O. Drapkina, K. Pronko, V. Sinopalnikov, and V. Zemskov (2018). "Telemonitoring of capillary blood flow in the human skin: New opportunities and prospects". In: *Clinical Practice*.
- Fehervary, H., L. Maes, J. Vastmans, G. Kloosterman, and N. Famaey (2020). "How to implement user-defined fiber-reinforced hyperelastic materials in finite element software". In: *Journal of the Mechanical Behavior of Biomedical Materials* 110, p. 103737.
- Fei, W., S. Xu, J. Ma, W. Zhai, S. Cheng, Y. Chang, X. Wang, J. Gao, H. Tang, S. Yang, and X. Zhang (2018). "Fundamental supply of skin blood flow in the Chinese Han population: Measurements by a full-field laser perfusion imager". In: *Skin Research and Technology* 24.4. Cited by: 1, pp. 656–662.
- Filatova, O., A. Sidorenko, and S. Agarkova (2015). "The Rheological Properties of Blood Depending on Age and Sex". In: *Fiziologiya cheloveka* 41.4. Cited by: 8, pp. 110–118.

## Bibliography

- Finlay, B. (1970). "Dynamic mechanical testing of human skin 'in vivo'". In: *Journal of biomechanics* 3.6, pp. 557–568.
- Flynn, C. and B. A. O. McCormack (2008). "Finite element modelling of forearm skin wrinkling". In: *Skin Research and Technology* 14.3, pp. 261–269.
- Flynn, C., A. Taberner, and P. Nielsen (2010). "Mechanical characterisation of in vivo human skin using a 3D force-sensitive micro-robot and finite element analysis". In: *Biomechanics and Modeling in Mechanobiology* 10.1, pp. 27–38.
- Folgosi-Correa, M. S. and G. E. C. Nogueira (2012). "Time of correlation of low-frequency fluctuations in the regional laser Doppler flow signal from human skin". In: *Biophotonics: Photonic Solutions for Better Health Care III*. Ed. by J. Popp, W. Drexler, V. V. Tuchin, and D. L. Matthews. Vol. 8427. SPIE, p. 84272D.
- Franceschini, G., D. Bigoni, P. Regitnig, and G. Holzapfel (2006). "Brain tissue deforms similarly to filled elastomers and follows consolidation theory". In: *Journal of the Mechanics and Physics of Solids* 54.12, pp. 2592–2620.
- Francisco, M. A. and C. T. Minson (2018). "Cutaneous active vasodilation as a heat loss thermoeffector". In: *Handbook of Clinical Neurology* 156. Cited by: 21, pp. 193–209.
- Fredriksson, I., M. Larsson, and T. Strömberg (2009). "Measurement depth and volume in laser Doppler flowmetry". In: *Microvascular Research* 78.1, pp. 4–13.
- FreeCAD* (n.d.). <https://www.freecad.org/>.
- Fromy, B., P. Abraham, and J.-L. Saumet (1998). "Non-nociceptive capsaicin-sensitive nerve terminal stimulation allows for an original vasodilatory reflex in the human skin". In: *Brain Research* 811.1-2, pp. 166–168.
- Fromy, B., P. Abraham, and J.-L. Saumet (2000). "Progressive calibrated pressure device to measure cutaneous blood flow changes to external pressure strain". In: *Brain Research Protocols* 5.2, pp. 198–203.
- Fu, J., M. Ni, W. Chai, X. Li, L. Hao, and J. Chen (2019). "Synovial Fluid Viscosity Test is Promising for the Diagnosis of Periprosthetic Joint Infection". In: *The Journal of Arthroplasty* 34.6, pp. 1197–1200.

## Bibliography

- Fuchs, D., P. P. Dupon, L. A. Schaap, and R. Draijer (2017). “The association between diabetes and dermal microvascular dysfunction non-invasively assessed by laser Doppler with local thermal hyperemia: a systematic review with meta-analysis”. In: *Cardiovascular Diabetology* 16.1.
- Fukumura, D. and R. K. Jain (2007). “Tumor microvasculature and microenvironment: Targets for anti-angiogenesis and normalization”. In: *Microvascular Research* 74.2. Therapeutic Applications of Angiogenesis and Anti-angiogenesis, pp. 72–84.
- Gaboriau, H. P. and C. S. Murakami (2001). “Skin anatomy and flap physiology”. In: *Otolaryngologic Clinics of North America* 34.3, pp. 555–569.
- Gallagher, A., A. Ní Annaidh, K. Bruyère, M. Otténio, H. Xie, and M. Gilchrist (2012). “Dynamic tensile properties of human skin”. In: *IRCOBI conference*. Vol. 59. International Research Council on the Biomechanics of Injury Dublin (Ireland), pp. 494–502.
- Ganapathysubramanian, B. and N. Zabaras (2009). “A stochastic multiscale framework for modeling flow through random heterogeneous porous media”. In: *Journal of Computational Physics* 228.2, pp. 591–618.
- Gawkrodger, D. and M. R. Ardern-Jones (2020). *Dermatology*. en. 7th ed. Illustrated Colour Text. London, England: Elsevier Health Sciences.
- Ge, M., L. Gu, J. He, R. Xue, S. Yang, C. Wang, and H. Fu (2013). “Normal reference value of whole blood viscosity (230s<sup>-1</sup>) of old women and geographical factors”. In: *Experimental Gerontology* 48.12, pp. 1449–1454.
- Gefen, A., D. M. Brienza, J. Cuddigan, E. Haesler, and J. Kottner (2022). “Our contemporary understanding of the aetiology of pressure ulcers/pressure injuries”. en. In: *Int. Wound J.* 19.3, pp. 692–704.
- Gerhardt, L.-C., J. Schmidt, J. Sanz-Herrera, F. Baaijens, T. Ansari, G. Peters, and C. Oomens (2012). “A novel method for visualising and quantifying through-plane skin layer deformations”. In: *Journal of the Mechanical Behavior of Biomedical Materials* 14, pp. 199–207.
- Geuzaine, C. and J.-F. Remacle (2020). *Gmsh*. Version 4.6.0.

## Bibliography

- Geuzaine, C. and J.-F. Remacle (2009). “Gmsh: A 3-D finite element mesh generator with built-in pre- and post-processing facilities”. In: *International Journal for Numerical Methods in Engineering* 79.11, pp. 1309–1331.
- Giavazzi, S., M. F. Ganatea, M. Trkov, P. Sustarsic, and T. Rodic (2010). “Inverse determination of viscoelastic properties of human fingertip skin”. In: *Materials and Geoenvironment* 57.1, p. 16.
- Gibson, T., H. Stark, and J. Evans (1969). “Directional variation in extensibility of human skin in vivo”. In: *Journal of Biomechanics* 2.2, pp. 201–204.
- Gimlich, O. A., J. Singh, J. Bismuth, D. J. Shah, and G. Brunner (2019). “Magnetic resonance imaging based modeling of microvascular perfusion in patients with peripheral artery disease”. In: *Journal of Biomechanics* 93, pp. 147–158.
- Golay, S., C. Haeberli, A. Delachaux, L. Liaudet, P. Kucera, B. Waeber, and F. Feihl (2004). “Local heating of human skin causes hyperemia without mediation by muscarinic cholinergic receptors or prostanoids”. In: *Journal of Applied Physiology* 97.5, pp. 1781–1786.
- Gonzalez-Molina, J., X. Zhang, M. Borghesan, J. Mendonça da Silva, M. Awan, B. Fuller, N. Gavara, and C. Selden (2018). “Extracellular fluid viscosity enhances liver cancer cell mechanosensing and migration”. In: *Biomaterials* 177, pp. 113–124.
- Gosz, M. R. (2017). *Finite element method: applications in solids, structures, and heat transfer*. CRC Press.
- Grahame, R. and P. Holt (1969). “The Influence of Ageing on the in vivo Elasticity of Human Skin”. In: *Gerontology* 15.2–3, pp. 121–139.
- Gray, W. G. and C. T. Miller (2014). *Introduction to the Thermodynamically Constrained Averaging Theory for Porous Medium Systems*. Springer International Publishing.
- Greiner, A., N. Reiter, F. Paulsen, G. A. Holzapfel, P. Steinmann, E. Comellas, and S. Budday (2021). “Poro-Viscoelastic Effects During Biomechanical Testing of Human Brain Tissue”. In: *Frontiers in Mechanical Engineering* 7.

- Groves, R. B., S. A. Coulman, J. C. Birchall, and S. L. Evans (2013). “An anisotropic, hyperelastic model for skin: Experimental measurements, finite element modelling and identification of parameters for human and murine skin”. In: *Journal of the Mechanical Behavior of Biomedical Materials* 18, pp. 167–180.
- Guéguen, Y., L. Dormieux, and M. Boutéca (2004). “Fundamentals of Poromechanics”. In: *Mechanics of Fluid-Saturated Rocks*. Elsevier, pp. 1–54.
- Haagenson, R., H. Rajaram, and J. Allen (2020). “A generalized poroelastic model using FEniCS with insights into the Noordbergum effect”. In: *Computer Methods in Applied Mechanics and Engineering* 135, p. 104399.
- Han, D., Z. Huang, E. Rahimi, and A. M. Ardekani (2023). “Solute Transport across the Lymphatic Vasculature in a Soft Skin Tissue”. In: *Biology* 12.7, p. 942.
- Hansen, K. L. and J. F. Carlsen (2021). “New Trends in Vascular Imaging”. In: *Diagnostics* 11.1, p. 112.
- Hargens, A. R., J. B. Cologne, F. J. Menninger, J. S. Hogan, B. J. Tucker, and R. M. Peters (1981). “Normal transcapillary pressures in human skeletal muscle and subcutaneous tissues”. In: *Microvascular research* 22.2, pp. 177–189.
- Hartmann, F. and C. Katz (2013). *Structural analysis with finite elements*. Springer Science & Business Media.
- Hasselbring, W., L. Carr, S. Hettrick, H. Packer, and T. Tiropanis (2020). “Open Source Research Software”. In: *Computer* 53.8, pp. 84–88.
- Hendriks, F. M., D. Brokken, J. T. W. M. V. Eemeren, C. W. J. Oomens, F. P. T. Baaijens, and J. B. A. M. Horsten (2003). “A numerical-experimental method to characterize the non-linear mechanical behaviour of human skin”. In: *Skin Research and Technology* 9.3, pp. 274–283.
- Hendriks, F. M., D. Brokken, C. W. J. Oomens, and F. P. T. Baaijens (2004). “Influence of hydration and experimental length scale on the mechanical response of human skin in vivo, using optical coherence tomography”. In: *Skin Research and Technology* 10.4, pp. 231–241.

## Bibliography

- Hermann, M., K. Bachus, G. Gibson, and R. D. Oleschuk (2019). “Low sample consuming, portable viscometer based on laplace-induced-pumping and refraction for hemorheology”. In: Cited by: 0, pp. 1442–1443.
- Hervas-Raluy, S., B. Wirthl, P. E. Guerrero, G. Robalo Rei, J. Nitzler, E. Coronado, J. Font de Mora Sainz, B. A. Schrefler, M. J. Gomez-Benito, J. M. Garcia-Aznar, and W. A. Wall (2023). “Tumour growth: An approach to calibrate parameters of a multiphase porous media model based on in vitro observations of Neuroblastoma spheroid growth in a hydrogel microenvironment”. In: *Computers in Biology and Medicine* 159, p. 106895.
- Hil, R. (1963). “Elastic properties of reinforced solids: some theoretical principles”. In: *Journal of the Mechanics and Physics of Solids* 11.5, pp. 357–372.
- Holowatz, L. A. and W. L. Kenney (2010). “Peripheral mechanisms of thermoregulatory control of skin blood flow in aged humans”. In: *Journal of Applied Physiology* 109.5, pp. 1538–1544.
- Holzapfel, G. A. (2002). *Nonlinear solid mechanics: a continuum approach for engineering science*.
- Horgan, C. O. and G. Saccomandi (2004). “Constitutive Models for Compressible Nonlinearly Elastic Materials with Limiting Chain Extensibility”. In: *Journal of Elasticity* 77.2, pp. 123–138.
- Horn, A. G., K. M. Schulze, R. E. Weber, T. J. Barstow, T. I. Musch, D. C. Poole, and B. J. Behnke (2022). “Post-occlusive reactive hyperemia and skeletal muscle capillary hemodynamics”. In: *Microvascular Research* 140, p. 104283.
- Hoskins, P. R., P. V. Lawford, and B. J. Doyle, eds. (2017). *Cardiovascular Biomechanics*. Springer International Publishing.
- Hosseini-Farid, M., M. Ramzanpour, J. McLean, M. Ziejewski, and G. Karami (2020). “A poro-hyper-viscoelastic rate-dependent constitutive modeling for the analysis of brain tissues”. In: *Journal of the Mechanical Behavior of Biomedical Materials* 102, p. 103475.
- Howes, F. A. and S. Whitaker (1985). “The spatial averaging theorem revisited”. In: *Chemical Engineering Science* 40 (8), pp. 1387–1392.

- Hrennikoff, A. (1941). "Solution of Problems of Elasticity by the Framework Method". In: *Journal of Applied Mechanics* 8.4, A169–A175.
- Hsu, Y.-C. and E. Fuchs (2021). "Building and Maintaining the Skin". In: *Cold Spring Harbor Perspectives in Biology* 14.7, a040840.
- Humbert, P., F. Fanian, H. I. Maibach, and P. Agache, eds. (2017). *Agache's Measuring the Skin – Non-invasive Investigations, Physiology, Normal Constants*. Second. Switzerland: Springer International Publishing.
- Humeau-Heurtier, A., E. Guerreschi, P. Abraham, and G. Mahé (2013). "Relevance of Laser Doppler and Laser Speckle Techniques for Assessing Vascular Function: State of the Art and Future Trends". In: *IEEE Transactions on Biomedical Engineering* 60.3, pp. 659–666.
- Humphrey, J. D. and S. L. O'Rourke (2015). *An Introduction to Biomechanics*. Springer New York.
- Hwang, J. and W. Lord (1974). "Finite element analysis of the magnetic field distribution inside a rotating ferromagnetic bar". In: *IEEE Transactions on Magnetics* 10.4, pp. 1113–1118.
- Ibrahim, M. M. (2009). "Subcutaneous and visceral adipose tissue: structural and functional differences". In: *Obesity Reviews* 11.1, pp. 11–18.
- Iwanowska-Chomiak, B. and A. Walicka (2019). "Mass Transport Through Interstitial Structures". In: *International Journal of Applied Mechanics and Engineering* 24.4, pp. 66–91.
- J.Gibson, L. and A. M. F (1999). "Cellular Solids: Structure and Properties". In: *Cambridge University Press*.
- Jacquet, E., J. Chambert, J. Pauchot, and P. Sandoz (2017a). "Intra- and inter-individual variability in the mechanical properties of the human skin from in vivo measurements on 20 volunteers". In: *Skin Research and Technology* 23.4, pp. 491–499.
- Jacquet, E., S. Joly, J. Chambert, K. Rekik, and P. Sandoz (2017b). "Ultra-light extensometer for the assessment of the mechanical properties of the human skin

## Bibliography

- in vivo”. In: *Skin Research and Technology* 23.4, pp. 531–538. eprint: {<https://onlinelibrary.wiley.com/doi/pdf/10.1111/srt.12367>}.
- Jasaitiene, D., S. Valiukeviciene, G. Linkeviciute, R. Raisutis, E. Jasiuniene, and R. Kazys (2011). “Principles of high-frequency ultrasonography for investigation of skin pathology”. In: *Journal of the European Academy of Dermatology and Venereology* 25.4, pp. 375–382.
- Javadi, E., M. J. Armstrong, and S. Jamali (2023). “A fully physiologically-informed time- and rate-dependent hemorheological constitutive model”. In: *Journal of Rheology* 67.3. Cited by: 1; All Open Access, Bronze Open Access, pp. 775–788.
- Jiang, X., E. C. Wilkirson, A. O. Bailey, W. K. Russell, and P. B. Lillehoj (2024). “Microneedle-based sampling of dermal interstitial fluid using a vacuum-assisted skin patch”. In: *Cell Reports Physical Science* 5.6, p. 101975.
- Jo, S. J. and O. S. Kwon (2012). “Structure and Function of Skin: The Application of THz Radiation in Dermatology”. In: *Convergence of Terahertz Sciences in Biomedical Systems*. Springer Netherlands, pp. 281–299.
- Johnson, J. M. and D. L. Kellogg Jr. (2010). “Local thermal control of the human cutaneous circulation”. In: *Journal of Applied Physiology* 109.4. Cited by: 212; All Open Access, Green Open Access, pp. 1229–1238.
- Johnson, R. S., J. Titze, and R. Weller (2016). “Cutaneous control of blood pressure”. In: *Current Opinion in Nephrology and Hypertension* 25.1, pp. 11–15.
- Joodaki, H. and M. B. Panzer (2018). “Skin mechanical properties and modeling: A review”. In: *Proceedings of the Institution of Mechanical Engineers, Part H: Journal of Engineering in Medicine* 232.4, pp. 323–343.
- Joodat, S., K. Nakshatrala, and R. Ballarini (2018). “Modeling flow in porous media with double porosity/permeability: A stabilized mixed formulation, error analysis, and numerical solutions”. In: *Computer Methods in Applied Mechanics and Engineering* 337, pp. 632–676.
- Jor, J. W., M. D. Parker, A. J. Taberner, M. P. Nash, and P. M. Nielsen (2013). “Computational and experimental characterization of skin mechanics: identifying current challenges and future directions”. In: *WIREs Systems Biology and Medicine* 5.5, pp. 539–556.

- Kaelo, P. and M. M. Ali (2006). "Some Variants of the Controlled Random Search Algorithm for Global Optimization". In: *Journal of Optimization Theory and Applications* 130.2, pp. 253–264.
- Kallepalli, A., J. Halls, D. B. James, and M. A. Richardson (2022). "An ultrasonography-based approach for tissue modelling to inform photo-therapy treatment strategies". In: *Journal of Biophotonics* 15.4.
- Kalra, A. and A. Lowe (2016). "Mechanical Behaviour of Skin: A Review". In: *Journal of Material Science & Engineering* 5.4.
- Kanitakis, J. (2002). "Anatomy, histology and immunohistochemistry of normal human skin". In: *European journal of dermatology* 12.4, pp. 390–401.
- Kazemi, M., Y. Dabiri, and L. P. Li (2013). "Recent Advances in Computational Mechanics of the Human Knee Joint". In: *Computational and Mathematical Methods in Medicine* 2013, pp. 1–27.
- Kelly, R. I., R. Pearse, R. H. Bull, J.-L. Leveque, J. de Rigal, and P. S. Mortimer (1995). "The effects of aging on the cutaneous microvasculature". In: *Journal of the American Academy of Dermatology* 33.5, pp. 749–756.
- Khaothong, K. (2010). "In Vivo Measurements of the Mechanical Properties of Human Skin and Muscle by Inverse Finite Element Method Combined with the Indentation Test". In: *IFMBE Proceedings*. Springer Berlin Heidelberg, pp. 1467–1470.
- Khatyr, F., C. Imberdis, P. Vescovo, D. Varchon, and J.-M. Lagarde (2004). "Model of the viscoelastic behaviour of skin in vivo and study of anisotropy". In: *Skin Research and Technology* 10.2, pp. 96–103.
- Khounouf, R., D. Karasneh, E. Abdulhay, A. Abdelhay, W. Sheng, and Z. H. Fan (2019). "Microfluidics-based device for the measurement of blood viscosity and its modeling based on shear rate, temperature, and heparin concentration". In: *Biomedical Microdevices* 21.4.
- Kim, H., Y. I. Cho, D.-H. Lee, C.-M. Park, H.-W. Moon, M. Hur, J. Q. Kim, and Y.-M. Yun (2013). "Analytical performance evaluation of the scanning capillary tube viscometer for measurement of whole blood viscosity". In: *Clinical Biochemistry* 46.1–2, pp. 139–142.

## Bibliography

- Kim, J., J.-Y. Lee, and E. Lee (2020). "Risk factors for newly acquired pressure ulcer and the impact of nurse staffing on pressure ulcer incidence". In: *Journal of Nursing Management* 30.5.
- Kim, J. Y. and H. Dao (2023). *Physiology, Integument*. StatPearls Publishing, Treasure Island (FL).
- Klee, S. K., M. Farwick, and P. Lersch (2007). *The effect of sphingolipids as a new therapeutic option for acne treatment*. Cited by: 10, pp. 155–165.
- Kouadio, A. A., F. Jordana, N. J. Koffi, P. Le Bars, and A. Soueidan (2018). "The use of laser Doppler flowmetry to evaluate oral soft tissue blood flow in humans: A review". In: *Archives of Oral Biology* 86. Cited by: 37, pp. 58–71.
- Koys, T. M. and T. D. Nguyen (2012). "Modeling the Anisotropic Properties of Human Skin Tissues". In: *ASME 2012 Summer Bioengineering Conference, Parts A and B*. SBC2012. American Society of Mechanical Engineers.
- Kremheller, J., A.-T. Vuong, B. A. Schrefler, and W. A. Wall (2019). "An approach for vascular tumor growth based on a hybrid embedded/homogenized treatment of the vasculature within a multiphase porous medium model". In: *International Journal for Numerical Methods in Biomedical Engineering* 35.11.
- Krishnan, S., J. Y. Murthy, and S. V. Garimella (2006). "Direct Simulation of Transport in Open-Cell Metal Foam". In: *ASME J. Heat Transfer* 128, pp. 793–799.
- Kubli, S., B. Waeber, A. Dalle-Ave, and F. Feihl (2000). "Reproducibility of laser Doppler imaging of skin blood flow as a tool to assess endothelial function". In: *Journal of cardiovascular pharmacology* 36.5, pp. 640–648.
- Lademann, J., M. E. Darvin, M. C. Meinke, and S. Jung (2022). "Correlation between Blood Flow and Various Physiological Parameters in Human Skin". In: *Journal of Biomedical Photonics & Engineering* 8.4, p. 040508.
- Lage, J. L., A. Weinert, and D. C. Price (1996). "Numerical study of a low permeability microporous heat sink for cooling phased-array radar systems". In: *International Journal of Heat and Mass Transfer* 39, pp. 3633–3647.

- Lakhani, P., K. K. Dwivedi, A. Parashar, and N. Kumar (2021). “Non-Invasive in Vivo Quantification of Directional Dependent Variation in Mechanical Properties for Human Skin”. In: *Frontiers in Bioengineering and Biotechnology* 9.
- Lang, P. S., A. Paluszny, and R. W. Zimmerman (2014). “Permeability tensor of three-dimensional fractured porous rock and a comparison to trace map predictions”. In: *Journal of Geophysical Research: Solid Earth* 119.8, pp. 6288–6307. eprint: <https://agupubs.onlinelibrary.wiley.com/doi/pdf/10.1002/2014JB011027>.
- Lanir, Y. (1983). “Constitutive equations for fibrous connective tissues”. In: *Journal of biomechanics* 16.1, pp. 1–12.
- Lanotte, L., J. Mauer, S. Mendez, D. A. Fedosov, J.-M. Fromental, V. Claveria, F. Nicoud, G. Gompper, and M. Abkarian (2016). “Red cells’ dynamic morphologies govern blood shear thinning under microcirculatory flow conditions”. In: *Proceedings of the National Academy of Sciences of the United States of America* 113.47. Cited by: 182; All Open Access, Bronze Open Access, Green Open Access, pp. 13289–13294.
- Lavigne, T., S. Bordas, and J. Lengiewicz (2023a). “Identification of material parameters and traction field for soft bodies in contact”. In: *Computer Methods in Applied Mechanics and Engineering* 406, p. 115889.
- Lavigne, T., A. Mazier, A. Perney, S. Bordas, F. Hild, and J. Lengiewicz (2022a). “Digital Volume Correlation for large deformations of soft tissues: Pipeline and proof of concept for the application to breast ex vivo deformations”. In: *Journal of the Mechanical Behavior of Biomedical Materials* 136, p. 105490.
- Lavigne, T., G. Sciumè, S. Laporte, H. Pillet, S. Urcun, B. Wheatley, and P.-Y. Rohan (2022b). “Société de Biomécanique Young Investigator Award 2021: Numerical investigation of the time-dependent stress-strain mechanical behaviour of skeletal muscle tissue in the context of pressure ulcer prevention”. In: *Clinical Biomechanics* 93, p. 105592.
- Lavigne, T., C. A. S. Afanador, A. Obeidat, and S. Urcun (2025a). *Synthetic Porous Microstructures: Automatic Design, Simulation, and Permeability Analysis*. arXiv: 2502.14518 [q-bio.T0].

## Bibliography

- Lavigne, T., S. Urcun, B. Fromy, A. Josset-Lamaugarny, A. Lagache, C. A. Suarez-Afanador, S. P. A. Bordas, P.-Y. Rohan, and G. Sciumè (2025b). “Hierarchical poromechanical approach to investigate the impact of mechanical loading on human skin micro-circulation”. In: *International Journal for Numerical Methods in Biomedical Engineering*.
- Lavigne, T., S. Urcun, E. Jacquet, J. Chambert, A. Elouneig, C. A. Suarez-Afanador, S. P. A. Bordas, G. Sciumè, and P.-Y. Rohan (2024). *Poromechanical modelling of the time-dependent response of in vivo human skin during extension*.
- Lavigne, T., S. Urcun, P.-Y. Rohan, G. Sciumè, D. Baroli, and S. P. Bordas (2023b). “Single and bi-compartment poro-elastic model of perfused biological soft tissues: FENiCSx implementation and tutorial”. In: *Journal of the Mechanical Behavior of Biomedical Materials* 143, p. 105902.
- Lenasi, H. (2011). “Assessment of human skin microcirculation and its endothelial function using laser Doppler flowmetry”. In: *Science, Technology and Medicine open access conten* 13, pp. 271–296.
- Leng, Y., M. de Lucio, and H. Gomez (2021). “Using poro-elasticity to model the large deformation of tissue during subcutaneous injection”. In: *Computer Methods in Applied Mechanics and Engineering* 384, p. 113919.
- Leo, F., T. Krenz, G. Wolff, M. Weidenbach, C. Heiss, M. Kelm, B. Isakson, and M. M. Cortese-Krott (2020). “Assessment of tissue perfusion and vascular function in mice by scanning laser Doppler perfusion imaging”. In: *Biochemical Pharmacology* 176, p. 113893.
- Levick, J. R. (1987). “FLOW THROUGH INTERSTITIUM AND OTHER FIBROUS MATRICES”. In: *Quarterly Journal of Experimental Physiology* 72.4, pp. 409–437.
- Levy, A., M. B.-O. Frank, and A. Gefen (2015). “The biomechanical efficacy of dressings in preventing heel ulcers”. In: *Journal of Tissue Viability* 24.1, pp. 1–11.
- Lewis, R. W., K. Morgan, H. Thomas, and K. N. Seetharamu (1996). *The finite element method in heat transfer analysis*. John Wiley & Sons.

## Bibliography

- Lewis, R. W., P. Nithiarasu, and K. N. Seetharamu (2004). *Fundamentals of the finite element method for heat and fluid flow*. John Wiley & Sons.
- Li, Y., N. Liu, N. Xie, Z. Wei, X. Liang, and F. Xu (2024). “Extracellular fluid viscosity: a new physical cue in cell biology”. In: *Acta Mechanica Sinica* 40.5.
- Liao, F., S. Burns, and Y.-K. Jan (2013). “Skin blood flow dynamics and its role in pressure ulcers”. In: *Journal of Tissue Viability* 22.2, pp. 25–36.
- Liu, P., T. Zhang, and Y. Huang (2024). “Three-dimensional model of normal human dermal tissue using serial tissue sections”. In: *Frontiers in Bioengineering and Biotechnology* 12. Cited by: 1; All Open Access, Gold Open Access, Green Open Access.
- Loerakker, S., E. Manders, G. J. Strijkers, K. Nicolay, F. P. T. Baaijens, D. L. Bader, and C. W. J. Oomens (2011). “The effects of deformation, ischemia, and reperfusion on the development of muscle damage during prolonged loading”. In: *Journal of Applied Physiology* 111.4, pp. 1168–1177.
- Loerakker, S., A. Stekelenburg, G. J. Strijkers, J. J. M. Rijpkema, F. P. T. Baaijens, D. L. Bader, K. Nicolay, and C. W. J. Oomens (2010). “Temporal Effects of Mechanical Loading on Deformation-Induced Damage in Skeletal Muscle Tissue”. In: *Annals of Biomedical Engineering* 38.8, pp. 2577–2587.
- Logg, A., K.-A. Mardal, and G. Wells (2012). *Automated Solution of Differential Equations by the Finite Element Method: The FEniCS Book*. Vol. 84. Lecture Notes in Computational Science and Engineering. Springer.
- Lucio, M. de, Y. Leng, A. Hans, I. Bilionis, M. Brindise, A. M. Ardekani, P. P. Vlachos, and H. Gomez (2023). “Modeling large-volume subcutaneous injection of monoclonal antibodies with anisotropic porohyperelastic models and data-driven tissue layer geometries”. In: *Journal of the Mechanical Behavior of Biomedical Materials* 138, p. 105602.
- Lucio, M. de, Y. Leng, H. Wang, P. P. Vlachos, and H. Gomez (2024). “Modeling drug transport and absorption in subcutaneous injection of monoclonal antibodies: Impact of tissue deformation, devices, and physiology”. In: *International Journal of Pharmaceutics* 661, p. 124446.

## Bibliography

- Lustig, A., R. Margi, A. Orlov, D. Orlova, L. Azaria, and A. Gefen (2021). “The mechanobiology theory of the development of medical device-related pressure ulcers revealed through a cell-scale computational modeling framework”. In: *Biomechanics and Modeling in Mechanobiology* 20.3, pp. 851–860.
- Lyon, C. C., J. Kulkarni, E. Zimersonc, E. Van Ross, and M. H. Beck (2000). “Skin disorders in amputees”. In: *Journal of the American Academy of Dermatology* 42.3, pp. 501–507.
- Mano, M. et al. (2003). “Finite element method”. In.
- Marino, M. (2018). “Constitutive Modeling of Soft Tissues”. In: Elsevier, pp. 81–110.
- Martínez-Hernández, A., C. Velasco-Santos, M. De-Icaza, and V. Castaño (2007). “Microstructural characterisation of carbon nanotube composites”. In: *Composite Interfaces* 14.7-9, pp. 753–766.
- Mascheroni, P., C. Stigliano, M. Carfagna, D. P. Boso, L. Preziosi, P. Decuzzi, and B. A. Schrefler (2016). “Predicting the growth of glioblastoma multiforme spheroids using a multiphase porous media model”. In: *Biomechanics and Modeling in Mechanobiology* 15.5, pp. 1215–1228.
- Mazier, A., S. E. Hadramy, J.-N. Brunet, J. S. Hale, S. Cotin, and S. P. A. Bordas (2022). *SOniCS: Develop intuition on biomechanical systems through interactive error controlled simulations*.
- Mazier, A., S. Ribes, B. Gilles, and S. P. Bordas (2021). “A rigged model of the breast for preoperative surgical planning”. In: *Journal of Biomechanics* 128, p. 110645.
- Meijer, R., L. F. A. Douven, and C. W. J. OOMENS (1999). “Characterisation of Anisotropic and Non-linear Behaviour of Human SkinIn Vivo”. In: *Computer Methods in Biomechanics and Biomedical Engineering* 2.1, pp. 13–27.
- Mellor, R. H., N. L. Bush, A. W. B. Stanton, J. C. Bamber, J. R. Levick, and P. S. Mortimer (2004). “Dual-Frequency Ultrasound Examination of Skin and Subcutis Thickness in Breast Cancer-Related Lymphedema”. In: *The Breast Journal* 10.6, pp. 496–503.

- Meulenbelt, H. E., J. H. Geertzen, M. F. Jonkman, and P. U. Dijkstra (2009). “Determinants of Skin Problems of the Stump in Lower-Limb Amputees”. In: *Archives of Physical Medicine and Rehabilitation* 90.1, pp. 74–81.
- Millet, C., M. Roustit, S. Blaise, and J. Cracowski (2011). “Comparison between laser speckle contrast imaging and laser Doppler imaging to assess skin blood flow in humans”. In: *Microvascular research* 82.2, pp. 147–151.
- Mithraratne, K., H. Ho, P. Hunter, and J. Fernandez (2012). “Mechanics of the foot Part 2: A coupled solid-fluid model to investigate blood transport in the pathologic foot”. In: *International Journal for Numerical Methods in Biomedical Engineering* 28.10. Cited by: 17, pp. 1071–1081.
- Mitragotri, S., Y. G. Anissimov, A. L. Bunge, H. F. Frasch, R. H. Guy, J. Hadgraft, G. B. Kasting, M. E. Lane, and M. S. Roberts (2011). “Mathematical models of skin permeability: An overview”. In: *International Journal of Pharmaceutics* 418.1, pp. 115–129.
- Moore, Z., P. Avsar, L. Conaty, D. H. Moore, D. Patton, and T. O’Connor (2019). “The prevalence of pressure ulcers in Europe, what does the European data tell us: a systematic review”. In: *Journal of Wound Care* 28.11, pp. 710–719.
- Mrowietz, C., R. Franke, G. Pindur, R. Sternitzky, F. Jung, and U. Wolf (2019). “Evaluation of Laser-Doppler-Fluxmetry for the diagnosis of microcirculatory disorders”. In: *Clinical Hemorheology and Microcirculation* 71.2. Cited by: 12, pp. 129–135.
- Mrowietz, C., R. Franke, G. Pindur, U. Wolf, and F. Jung (2017). “Reference range and variability of Laser-Doppler-Fluxmetry”. In: *Clinical Hemorheology and Microcirculation* 67.3-4. Cited by: 8, pp. 347–353.
- Mukhina, E., P.-Y. Rohan, N. Connesson, and Y. Payan (2020). “Calibration of the fat and muscle hyperelastic material parameters for the assessment of the internal tissue deformation in relation to pressure ulcer prevention”. In: *Computer Methods in Biomechanics and Biomedical Engineering* 23.sup1, S197–S199.
- Muramoto, Y., N. Takahashi, N. Kamata, and Y. Nagasaka (2010). “Development of High-Speed Sensing Technique for Blood Viscosity with Micro-Liter Sample Vol-

## Bibliography

- ume(Thermal Engineering)”. In: *TRANSACTIONS OF THE JAPAN SOCIETY OF MECHANICAL ENGINEERS Series B* 76.768, pp. 1290–1296.
- Nader, E., S. Skinner, M. Romana, R. Fort, N. Lemonne, N. Guillot, A. Gauthier, S. Antoine-Jonville, C. Renoux, M.-D. Hardy-Dessources, E. Stauffer, P. Joly, Y. Bertrand, and P. Connes (2019). “Blood rheology: Key parameters, impact on blood flow, role in sickle cell disease and effects of exercise”. In: *Frontiers in Physiology* 10.OCT. Cited by: 281; All Open Access, Gold Open Access, Green Open Access.
- Nakagawa, N., M. Matsumoto, and S. Sakai (2010). “In vivo measurement of the water content in the dermis by confocal Raman spectroscopy”. In: *Skin Research and Technology* 16.2, pp. 137–141.
- NGSolve (n.d.). <https://ngsolve.org/>.
- Nguyen-Tu, M.-S., A.-L. Begey, J. Decrops, J. Boizot, P. Sommer, B. Fromy, and D. Sigaudo-Roussel (2013). “Skin microvascular response to pressure load in obese mice”. In: *Microvascular Research* 90, pp. 138–143.
- Nickoloff, B. J., J.-Z. Qin, and F. O. Nestle (2007). “Immunopathogenesis of Psoriasis”. In: *Clinical Reviews in Allergy & Immunology* 33.1–2, pp. 45–56.
- Nierop, B. J. van, A. Stekelenburg, S. Loerakker, C. W. Oomens, D. Bader, G. J. Strijkers, and K. Nicolay (2010). “Diffusion of water in skeletal muscle tissue is not influenced by compression in a rat model of deep tissue injury”. In: *Journal of Biomechanics* 43.3, pp. 570–575.
- Nogami, H., K. Komatsutani, T. Hirata, and R. Sawada (2019). “Integrated laser Doppler blood flowing combining optical contact force”. In: Cited by: 2, pp. 287–290.
- Obeidat, A., T. Andreas, S. P. A. Bordas, and A. Ziliana (2020). “Discrete filters for viscous compressible high Reynolds flows in industrial complex geometry using a hybrid remeshed particle hydrodynamics method”. In.
- Obeidat, A. and S. P. A. Bordas (2019). “An implicit boundary approach for viscous compressible high Reynolds flows using a hybrid remeshed particle hydrodynamics method”. In: *Journal of Computational Physics* 391, pp. 347–364.

- Oftadeh, R., M. Azadi, M. Donovan, J. Langer, I.-C. Liao, C. Ortiz, A. J. Grodzinsky, and G. S. Luengo (2023). “Poroelastic behavior and water permeability of human skin at the nanoscale”. In: *PNAS Nexus* 2.8. Ed. by A. Guadagnini.
- Oftadeh, R., B. K. Connizzo, H. T. Nia, C. Ortiz, and A. J. Grodzinsky (2018). “Biological connective tissues exhibit viscoelastic and poroelastic behavior at different frequency regimes: Application to tendon and skin biophysics”. In: *Acta Biomaterialia* 70, pp. 249–259.
- Ogawa, R., K. Okai, F. Tokumura, K. Mori, Y. Ohmori, C. Huang, H. Hyakusoku, and S. Akaishi (2012). “The relationship between skin stretching/contraction and pathologic scarring: the important role of mechanical forces in keloid generation”. In: *Wound Repair and Regeneration* 20.2, pp. 149–157.
- Ogien, J., O. Levecq, H. Azimani, and A. Dubois (2020). “Dual-mode line-field confocal optical coherence tomography for ultrahigh-resolution vertical and horizontal section imaging of human skin in vivo”. In: *Biomedical Optics Express* 11.3, p. 1327.
- Oomens, C. W. J., D. H. Van Campen, H. J. Grootenboer, and L. J. De Boer (1985). “Experimental and Theoretical Compression Studies on Porcine Skin”. In: *Biomechanics: Current Interdisciplinary Research*. Springer Netherlands, pp. 227–232.
- Oomens, C., D. van Campen, and H. Grootenboer (1987a). “In vitro compression of a soft tissue layer on a rigid foundation”. In: *Journal of Biomechanics* 20.10, pp. 923–935.
- Oomens, C., D. van Campen, and H. Grootenboer (1987b). “A mixture approach to the mechanics of skin”. In: *Journal of Biomechanics* 20.9, pp. 877–885.
- Oomens, C. W. J., D. L. Bader, S. Loerakker, and F. Baaijens (2014). “Pressure Induced Deep Tissue Injury Explained”. In: *Annals of Biomedical Engineering* 43.2, pp. 297–305.
- Oomens, C. W., M. van Vijven, and G. W. Peters (2017). “Chapter 16 - Skin Mechanics”. In: *Biomechanics of Living Organs*. Ed. by Y. Payan and J. Ohayon. Vol. 1. Translational Epigenetics. Oxford: Academic Press, pp. 347–357.

## Bibliography

- Ortiz-Prado, E., J. F. Dunn, J. Vasconez, D. Castillo, and G. Viscor (2019). “Partial pressure of oxygen in the human body: a general review”. In: *American journal of blood research* 9.1, p. 1.
- Ostergren, J. and B. Fagrell (1986). “Skin capillary blood cell velocity in man. Characteristics and reproducibility of the reactive hyperemia response.” In: *International journal of microcirculation, clinical and experimental* 5.1, pp. 37–51.
- Ottenio, M., D. Tran, A. N. Annaidh, M. D. Gilchrist, and K. Bruyère (2015). “Strain rate and anisotropy effects on the tensile failure characteristics of human skin”. In: *Journal of the Mechanical Behavior of Biomedical Materials* 41, pp. 241–250.
- Padula, W. V. and B. A. Delarmente (2019). “The national cost of hospital-acquired pressure injuries in the United States”. In: *International Wound Journal* 16.3, pp. 634–640.
- Pailler-Mattei, C., S. Bec, and H. Zahouani (2008). “In vivo measurements of the elastic mechanical properties of human skin by indentation tests”. In: *Medical Engineering & Physics* 30.5, pp. 599–606.
- Pailler-Mattéi, C. and H. Zahouani (2004). “Study of adhesion forces and mechanical properties of human skin in vivo”. In: *Journal of Adhesion Science and Technology* 18.15–16, pp. 1739–1758.
- Pancorbo-Hidalgo, P. L., F. P. Garcia-Fernandez, I. M. Lopez-Medina, and C. Alvarez-Nieto (2006). “Risk assessment scales for pressure ulcer prevention: a systematic review”. In: *Journal of Advanced Nursing* 54.1, pp. 94–110.
- Pao-La-Or, P., A. Isaramongkolrak, and T. Kulworawanichpong (2010). “Finite Element Analysis of Magnetic Field Distribution for 500-kV Power Transmission Systems.” In: *Engineering Letters* 18.1.
- Parvizi, A., S. Haddadi, A. Mollaei, P. Ghorbani Vajargah, P. Takasi, M. Firooz, S. J. Hosseini, R. Farzan, and S. Karkhah (2023). “A systematic review of nurses’ knowledge and related factors towards the prevention of medical device-related pressure ulcers”. In: *International Wound Journal* 20.7, pp. 2843–2854. eprint: <https://onlinelibrary.wiley.com/doi/pdf/10.1111/iwj.14122>.
- Pasquet, P. (1999). *CALCULS MECANIQUES - I. MECANIQUE DES STRUCTURES* - I. Cast3M200, PhP. The address of the publisher.

- Pedanekar, T., R. Kedare, and A. Sengupta (2018). “Monitoring tumor progression by mapping skin microcirculation with laser Doppler flowmetry”. In: *Lasers in Medical Science* 34.1, pp. 61–77.
- Pedrekoff, C. (2015). *stl-to-voxel python library*. <https://github.com/cpederkoff/stl-to-voxel/blob/master/LICENCE.md>.
- Pellegrini, C., M. Maturo, L. Di Nardo, V. Ciciarelli, C. Gutiérrez García-Rodrigo, and M. Farnoli (2017). “Understanding the Molecular Genetics of Basal Cell Carcinoma”. In: *International Journal of Molecular Sciences* 18.11, p. 2485.
- Pence, T. J. and K. Gou (2014). “On compressible versions of the incompressible neo-Hookean material”. In: *Mathematics and Mechanics of Solids* 20.2, pp. 157–182.
- Petrofsky, J. S. (2012). “Resting blood flow in the skin: Does it exist, and what is the influence of temperature, aging, and diabetes?” In: *Journal of Diabetes Science and Technology* 6.3. Cited by: 32; All Open Access, Bronze Open Access, Green Open Access, pp. 674–685.
- Petrofsky, J. S. and L. Berk (2012). “Skin Moisture and Heat Transfer”. In: *Treatment of Dry Skin Syndrome*. Springer Berlin Heidelberg, pp. 561–580.
- Peyrounette, M., Y. Davit, M. Quintard, and S. Lorthois (2018). “Multiscale modelling of blood flow in cerebral microcirculation: Details at capillary scale control accuracy at the level of the cortex”. In: *PLOS ONE* 13.1. Ed. by J. Boltze, e0189474.
- Pfisterer, K., L. E. Shaw, D. Symmank, and W. Weninger (2021). “The Extracellular Matrix in Skin Inflammation and Infection”. In: *Frontiers in Cell and Developmental Biology* 9.
- Pittman, M., E. Iu, K. Li, M. Wang, J. Chen, N. Taneja, M. H. Jo, S. Park, W.-H. Jung, L. Liang, I. Barman, T. Ha, S. Gaitanaros, J. Liu, D. Burnette, S. Plotnikov, and Y. Chen (2022). “Membrane ruffling is a mechanosensor of extracellular fluid viscosity”. In: *Nature Physics* 18.9, pp. 1112–1121.
- Plessis, J. P. du, A. Montillet, J. Comiti, and J. Legrand (1994). “Pressure Drop Prediction for Flow Through High Porosity Metallic Foams”. In: *Chem. Eng. Sci.* 49, pp. 3545–3553.

## Bibliography

- Poffo, L., J.-M. Goujon, R. Le Page, J. Lemaitre, M. Guendouz, N. Lorrain, and D. Bosc (2014). “Laser double Doppler flowmeter”. In: *Biophotonics: Photonic Solutions for Better Health Care IV*. Ed. by J. Popp, V. V. Tuchin, D. L. Matthews, F. S. Pavone, and P. Garside. Vol. 9129. SPIE, p. 91290X.
- Pouya, A. and A. Courtois (2002a). “Definition of the permeability of fractured rock masses by homogenisation methods.” In: *Comptes Rendus Geoscience* 334.13, pp. 975–979.
- Pouya, A. and A. Courtois (2002b). “Définition de la perméabilité équivalente des massifs fracturés par des méthodes d’homogénéisation”. In: *Comptes Rendus Geoscience* 334.13, pp. 975–979.
- Proksch, E., J. M. Brandner, and J.-M. Jensen (2008). “The skin: an indispensable barrier”. In: *Experimental Dermatology* 17.12, pp. 1063–1072.
- Querleux, B., C. Cornillon, O. Jolivet, and J. Bittoun (2002). “Anatomy and physiology of subcutaneous adipose tissue by in vivo magnetic resonance imaging and spectroscopy: Relationships with sex and presence of cellulite”. In: *Skin Research and Technology* 8.2, pp. 118–124.
- Quey, R., P. Dawson, and F. Barbe (2011). “Large-scale 3D random polycrystals for the finite element method: Generation, meshing and remeshing”. In: *Computer Methods in Applied Mechanics and Engineering* 200.17-20, pp. 1729–1745.
- Altair radioss (n.d.). <https://altair.com/radioss>.
- Raveh Tilleman, T., M. Tilleman, and H. Neumann (2004). “The elastic properties of cancerous skin: Poisson’s ratio and Young’s modulus”. In: *Optimization of Incisions in Cutaneous Surgery including Mohs’ Micrographic Surgery* 105.2.
- Reswick, J. B. and J. E. Rogers (1976). “Experience at Rancho Los Amigos Hospital With Devices and Techniques to Prevent Pressure Sores”. In: *Bed Sore Biomechanics*. Macmillan Education UK, pp. 301–310.
- Ricken, T. and L. Lambers (2019). “On computational approaches of liver lobule function and perfusion simulation”. In: *GAMM-Mitteilungen* 42.4.

## Bibliography

- Rosenberry, R. and M. D. Nelson (2020). "Reactive hyperemia: a review of methods, mechanisms, and considerations". In: *American Journal of Physiology-Regulatory, Integrative and Comparative Physiology* 318.3, R605–R618.
- Rossi, M., A. Carpi, F. Galetta, F. Franzoni, and G. Santoro (2006a). "The investigation of skin blood flow motion: a new approach to study the microcirculatory impairment in vascular diseases?" In: *Biomedicine & Pharmacotherapy* 60.8, pp. 437–442.
- Rossi, M., A. Carpi, C. Di Maria, F. Galetta, and G. Santoro (2006b). "Spectral analysis of laser Doppler skin blood flow oscillations in human essential arterial hypertension". In: *Microvascular research* 72.1-2, pp. 34–41.
- Rugarli, P. (2010). *Structural analysis with finite elements*. Vol. 10. Thomas Telford London.
- Russell, N. S., B. Floot, E. van Werkhoven, M. Schriemer, R. de Jong-Korlaar, L. A. Woerdeman, F. A. Stewart, and M. Scharpfenecker (2015). "Blood and lymphatic microvessel damage in irradiated human skin: The role of TGF- $\beta$ , endoglin and macrophages". In: *Radiotherapy and Oncology* 116.3, pp. 455–461.
- Saha, M., V. Dremin, I. Rafailov, A. Dunaev, S. Sokolovski, and E. Rafailov (2020). "Wearable Laser Doppler Flowmetry Sensor: A Feasibility Study with Smoker and Non-Smoker Volunteers". In: *Biosensors* 10.12, p. 201.
- Salazar-Vázquez, B. (2011). "Blood pressure and blood viscosity are not correlated in normal healthy subjects". In: *Vascular Health and Risk Management*, p. 1.
- Samant, P. P. and M. R. Prausnitz (2018). "Mechanisms of sampling interstitial fluid from skin using a microneedle patch". In: *Proceedings of the National Academy of Sciences* 115.18, pp. 4583–4588.
- Samanta, H., B. Mandal, A. Majumder, S. R. Chowdhury, and G. Kumar (2024). *A Critical Review on Blood Flow Modeling: Relevance to Rheology, Numerical and Computational Methods*.
- Sanders, R. (1973). "Torsional elasticity of human skin in vivo". In: *Pflgers Archiv European Journal of Physiology* 342.3, pp. 255–260.

## Bibliography

- Scandelli, H., A. Ahmadi-Senichault, C. Levet, and J. Lachaud (2022). “Computation of the Permeability Tensor of Non-Periodic Anisotropic Porous Media from 3D Images”. In: *Transport in Porous Media* 142 (3), pp. 669–697.
- Schöberl, J. (1997). “NETGEN An advancing front 2D/3D-mesh generator based on abstract rules”. In: *Computing and Visualization in Science* 1.1, pp. 41–52.
- Schrader, B., S. Reboux, and I. F. Sbalzarini (2010). “Discretization correction of general integral PSE Operators for particle methods”. In: *Journal of Computational Physics* 229, pp. 4159–4182.
- Sciumè, G., D. P. Boso, W. G. Gray, C. Cobelli, and B. A. Schrefler (2014a). “A two-phase model of plantar tissue: a step toward prediction of diabetic foot ulceration”. In: *International Journal for Numerical Methods in Biomedical Engineering* 30.11, pp. 1153–1169. eprint: <https://onlinelibrary.wiley.com/doi/pdf/10.1002/cnm.2650>.
- Sciumè, G., W. G. Gray, F. Hussain, M. Ferrari, P. Decuzzi, and B. A. Schrefler (2013). “Three phase flow dynamics in tumor growth”. In: *Computational Mechanics* 53.3, pp. 465–484.
- Sciumè, G. (2021). “Mechanistic modeling of vascular tumor growth: an extension of Biot’s theory to hierarchical bi-compartment porous medium systems”. In: *Acta Mechanica* 232.4, pp. 1445–1478.
- Sciumè, G., R. Santagiuliana, M. Ferrari, P. Decuzzi, and B. Schrefler (2014b). “A tumor growth model with deformable ECM”. In: *Physical biology* 11.6, p. 065004.
- Scroggs, M. W., I. A. Baratta, C. N. Richardson, and G. N. Wells (2022a). “Basix: a runtime finite element basis evaluation library”. In: *Journal of Open Source Software* 7.73, p. 3982.
- Scroggs, M. W., J. S. Dokken, C. N. Richardson, and G. N. Wells (2022b). “Construction of Arbitrary Order Finite Element Degree-of-Freedom Maps on Polygonal and Polyhedral Cell Meshes”. In: *ACM Trans. Math. Softw.* 48.2.
- Segain, A., G. Sciume, H. Pillet, and P.-Y. Rohan (2024). “In vivo mechanical response of thigh soft tissues under compression: A two-layer model allows an improved representation of the local tissue kinematics”. In: *Journal of the Mechanical Behavior of Biomedical Materials* 156, p. 106584.

- Selvadurai, A. and A. Suvorov (2016). “Coupled hydro-mechanical effects in a poro-hyperelastic material”. In: *Journal of the Mechanics and Physics of Solids* 91, pp. 311–333.
- Settecase, F. and V. L. Rayz (2021). “Advanced vascular imaging techniques”. In: *Handbook of Clinical Neurology*. Elsevier, pp. 81–105.
- Shergold, O. A., N. A. Fleck, and D. Radford (2006). “The uniaxial stress versus strain response of pig skin and silicone rubber at low and high strain rates”. In: *International Journal of Impact Engineering* 32.9, pp. 1384–1402.
- Si, H. (2015). “TetGen, a Delaunay-Based Quality Tetrahedral Mesh Generator”. In: *ACM Transactions on Mathematical Software* 41.2, pp. 1–36.
- Siddique, J., A. Ahmed, A. Aziz, and C. Khalique (2017). “A Review of Mixture Theory for Deformable Porous Media and Applications”. In: *Applied Sciences* 7.9, p. 917.
- Simms, C. K., M. V. Loocke, and C. G. Lyons (2012). “SKELETAL MUSCLE IN COMPRESSION: MODELING APPROACHES FOR THE PASSIVE MUSCLE BULK”. In: *International Journal for Multiscale Computational Engineering* 10.2, pp. 143–154.
- Simo, J. (1988). “A framework for finite strain elastoplasticity based on maximum plastic dissipation and the multiplicative decomposition: Part I. Continuum formulation”. In: *Computer Methods in Applied Mechanics and Engineering* 66.2, pp. 199–219.
- Singh, A., I. F. Sbalzarini, and A. Obeidat (2023). “Entropically Damped Artificial Compressibility for the Discretization Corrected Particle Strength Exchange Method in Incompressible Fluid Mechanics”. In: *Computers & Fluids* 267, p. 106074.
- Sowinski, D. R., M. D. J. McGarry, E. E. W. V. Houten, S. Gordon-Wylie, J. B. Weaver, and K. D. Paulsen (2021). “Poroelasticity as a Model of Soft Tissue Structure: Hydraulic Permeability Reconstruction for Magnetic Resonance Elastography in Silico”. In: *Frontiers in Physics* 8.

## Bibliography

- Sree, V. D., M. K. Rausch, and A. B. Tepole (2019a). “Linking microvascular collapse to tissue hypoxia in a multiscale model of pressure ulcer initiation”. en. In: *Biomech. Model. Mechanobiol.* 18.6, pp. 1947–1964.
- Sree, V. D., M. K. Rausch, and A. B. Tepole (2019b). “Towards understanding pressure ulcer formation: Coupling an inflammation regulatory network to a tissue scale finite element model”. In: *Mechanics Research Communications* 97, pp. 80–88.
- Stekelenburg, A., C. W. J. Oomens, G. J. Strijkers, K. Nicolay, and D. L. Bader (2006). “Compression-induced deep tissue injury examined with magnetic resonance imaging and histology”. In: *Journal of Applied Physiology* 100.6, pp. 1946–1954.
- Strömberg, T., K. Wårdell, M. Larsson, and G. E. Salerud (2014). *Laser doppler perfusion monitoring and imaging*. Cited by: 5, pp. 435–459.
- Sutula, D., A. Elouneig, M. Sensale, F. Chouly, J. Chambert, A. Lejeune, D. Baroli, P. Hauseux, S. Bordas, and E. Jacquet (2020). “An open source pipeline for design of experiments for hyperelastic models of the skin with applications to keloids”. In: *Journal of the Mechanical Behavior of Biomedical Materials* 112, p. 103999.
- Svedman, C., G. W. Cherry, E. Strigini, and T. J. Ryan (1998). “Laser Doppler imaging of skin microcirculation.” In: *Acta dermato-venereologica* 78.2, pp. 114–118.
- Swartz, M. A. and M. E. Fleury (2007). “Interstitial Flow and Its Effects in Soft Tissues”. In: *Annual Review of Biomedical Engineering* 9.1, pp. 229–256.
- Swisher, S. L., M. C. Lin, A. Liao, E. J. Leeflang, Y. Khan, F. J. Pavinatto, K. Mann, A. Naujokas, D. Young, S. Roy, M. R. Harrison, A. C. Arias, V. Subramanian, and M. M. Maharbiz (2015). “Impedance sensing device enables early detection of pressure ulcers in vivo”. In: *Nature Communications* 6.1.
- Tang, Y., F. Xu, P. Lei, G. Li, and Z. Tan (2023). “Spectral analysis of laser speckle contrast imaging and infrared thermography to assess skin microvascular reactive hyperemia”. In: *Skin Research and Technology* 29.4.
- Téllez-Soto, C. A., M. G. Pereira Silva, L. dos Santos, T. de O. Mendes, P. Singh, S. A. Fortes, P. Favero, and A. A. Martin (2021). “In vivo determination of dermal

- water content in chronological skin aging by confocal Raman spectroscopy”. In: *Vibrational Spectroscopy* 112, p. 103196.
- Terzaghi, K. (1943). “Theoretical soil mechanics., 1943”. In: *Published Online* 19.
- Tesselaar, E., A. M. Flejmer, S. Farnebo, and A. Dasu (2017). “Changes in skin microcirculation during radiation therapy for breast cancer”. In: *Acta Oncologica* 56.8, pp. 1072–1080.
- Thimus, J.-F., Y. Abousleiman, A. H.-D. Cheng, O. Coussy, and E. Detournay, eds. (2020). *Poromechanics*. CRC Press.
- Tien, C. (1993). “Principles of Filtration”. In: *Chemical Engineering Progress* 89.8, pp. 49–58.
- Tong, P. and Y.-C. Fung (1976). “The stress-strain relationship for the skin”. In: *Journal of Biomechanics* 9.10, pp. 649–657.
- Tonge, T. K., L. S. Atlan, L. M. Voo, and T. D. Nguyen (2013). “Full-field bulge test for planar anisotropic tissues: Part I – Experimental methods applied to human skin tissue”. In: *Acta Biomaterialia* 9.4, pp. 5913–5925.
- Torres-Terán, I., M. Venczel, T. Stieler, L. Parisi, A. Kloss, and S. Klein (2023). “Prediction of subcutaneous drug absorption - Characterization of subcutaneous interstitial fluids as a basis for developing biorelevant in vitro models”. In: *International Journal of Pharmaceutics* 638, p. 122906.
- Touitou, E. (2002). “Drug delivery across the skin”. In: *Expert Opinion on Biological Therapy* 2.7, pp. 723–733.
- Traa, W. A., M. C. van Turnhout, J. L. Nelissen, G. J. Strijkers, D. L. Bader, and C. W. Oomens (2019). “There is an individual tolerance to mechanical loading in compression induced deep tissue injury”. In: *Clinical Biomechanics* 63, pp. 153–160.
- Tran, H. (2007). “Caractérisation des propriétés mécaniques de la peau humaine in vivo via l’IRM”. Theses. Université de Technologie de Compiègne.
- Tran-Minh, N. and F. Karlsen (2018). “Computational fluid dynamics approach for modeling a non-newtonian blood flow in a split and recombine micromixer”. In: vol. 63. Cited by: 1, pp. 319–323.

## Bibliography

- Treloar, L. G. (1975). *The physics of rubber elasticity*. OUP Oxford.
- Treml, B., A. Kleinsasser, K.-H. Stadlbauer, I. Steiner, W. Pajk, M. Pilch, M. Burtscher, and H. Knotzer (2018). “Cutaneous microvascular blood flow and reactivity in hypoxia”. In: *Frontiers in Physiology* 9.MAR. Cited by: 17; All Open Access, Gold Open Access, Green Open Access.
- Tsuji, S., S. Ichioka, N. Sekiya, and T. Nakatsuka (2005). “Analysis of ischemia-reperfusion injury in a microcirculatory model of pressure ulcers”. In: *Wound Repair and Regeneration* 13.2, pp. 209–215.
- Urcun, S., D. Baroli, P.-Y. Rohan, W. Skalli, V. Lubrano, S. P. Bordas, and G. Sciumè (2023). “Non-operable glioblastoma: proposition of patient-specific forecasting by image-informed poromechanical model”. In: *Brain Multiphysics*, p. 100067.
- Urcun, S., P.-Y. Rohan, G. Sciumè, and S. P. Bordas (2022). “Cortex tissue relaxation and slow to medium load rates dependency can be captured by a two-phase flow poroelastic model”. In: *Journal of the Mechanical Behavior of Biomedical Materials* 126, p. 104952.
- Urcun, S., P.-Y. Rohan, W. Skalli, P. Nassoy, S. P. A. Bordas, and G. Sciumè (2021). “Digital twinning of Cellular Capsule Technology: Emerging outcomes from the perspective of porous media mechanics”. In: *PLOS ONE* 16.7. Ed. by K. Garikipati, e0254512.
- Urevc, J., I. Zun, M. Brumen, and B. Stok (2017). “Modeling the effect of red blood cells deformability on blood flow conditions in human carotid artery bifurcation”. In: *Journal of Biomechanical Engineering* 139.1. Cited by: 16.
- Uzuner, S., G. Kuntze, L. Li, J. Ronsky, and S. Kucuk (2022). “Creep behavior of human knee joint determined with high-speed biplanar video-radiography and finite element simulation”. In: *Journal of the Mechanical Behavior of Biomedical Materials* 125, p. 104905.
- Uzuner, S., L. Li, S. Kucuk, and K. Memisoglu (2020). “Changes in Knee Joint Mechanics After Medial Meniscectomy Determined With a Poromechanical Model”. In: *Journal of Biomechanical Engineering* 142.10.
- Vaidya, A. J. and B. B. Wheatley (2020). “An experimental and computational investigation of the effects of volumetric boundary conditions on the compressive

- mechanics of passive skeletal muscle”. In: *Journal of the Mechanical Behavior of Biomedical Materials* 102, p. 103526.
- Van Loocke, M., C. Simms, and C. Lyons (2009). “Viscoelastic properties of passive skeletal muscle in compression—Cyclic behaviour”. In: *Journal of Biomechanics* 42.8, pp. 1038–1048.
- Vanderwee, K., M. Clark, C. Dealey, L. Gunningberg, and T. Defloor (2007). “Pressure ulcer prevalence in Europe: a pilot study”. In: *Journal of Evaluation in Clinical Practice* 13.2, pp. 227–235.
- Varghese, B., T. G. Van Leeuwen, and W. Steenbergen (2009). *Coherence domain path length resolved approaches in optical doppler flowmetry*. Cited by: 0, pp. 317–344.
- Vazic, B., B. Abali, H. Yang, et al. (2022). “Mechanical analysis of heterogeneous materials with higher-order parameters”. In: *Engineering with Computers* 38, pp. 5051–5067.
- Veronda, D. and R. Westmann (1970). “Mechanical characterization of skin—finite deformations”. In: *Journal of biomechanics* 3.1, pp. 111–124.
- Verruijt, A. (2013). “Theory and problems of poroelasticity”. In: *Delft University of Technology* 71.
- Volkov, M. V., D. A. Kostrova, N. B. Margaryants, I. P. Gurov, N. P. Erofeev, V. V. Dremin, E. V. Zharkikh, E. A. Zherebtsov, I. O. Kozlov, and A. V. Dunaev (2017). “Evaluation of blood microcirculation parameters by combined use of laser Doppler flowmetry and videocapillaroscopy methods”. In: *Saratov Fall Meeting 2016: Optical Technologies in Biophysics and Medicine XVIII*. Ed. by V. V. Tuchin, E. A. Genina, D. E. Postnov, and V. L. Derbov. Vol. 10336. SPIE, p. 1033607.
- Waghule, T., G. Singhvi, S. K. Dubey, M. M. Pandey, G. Gupta, M. Singh, and K. Dua (2019). “Microneedles: A smart approach and increasing potential for transdermal drug delivery system”. In: *Biomedicine & pharmacotherapy* 109, pp. 1249–1258.

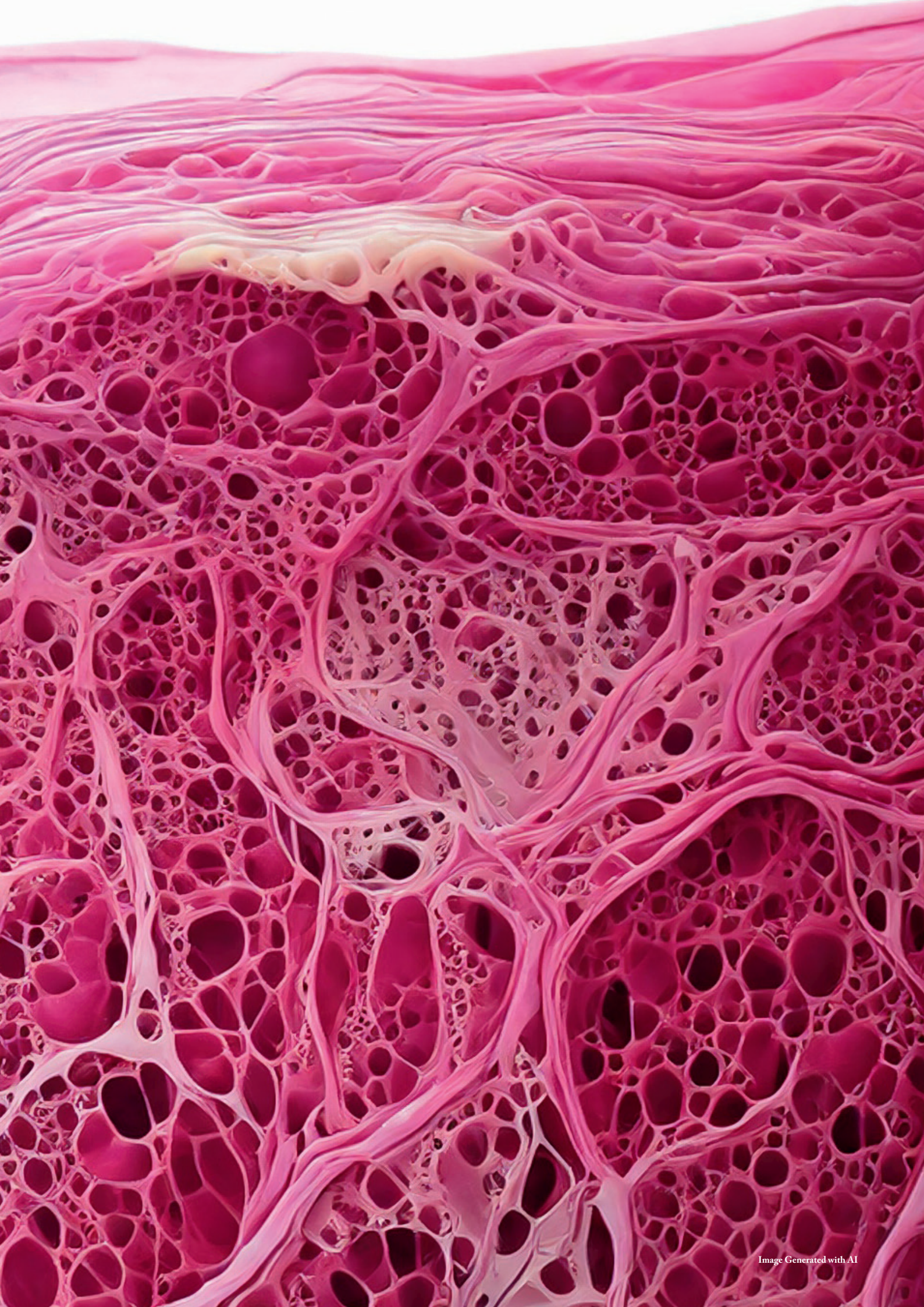
## Bibliography

- Wahlsten, A., M. Pensalfini, A. Stracuzzi, G. Restivo, R. Hopf, and E. Mazza (2019). “On the compressibility and poroelasticity of human and murine skin”. In: *Biomechanics and Modeling in Mechanobiology* 18.4, pp. 1079–1093.
- Wahlsten, A., A. Stracuzzi, I. Lüchtefeld, G. Restivo, N. Lindenblatt, C. Giampietro, A. E. Ehret, and E. Mazza (2023). “Multiscale mechanical analysis of the elastic modulus of skin”. en. In: *Acta Biomater.* 170, pp. 155–168.
- Waldman, A. and C. Schmults (2019). “Cutaneous Squamous Cell Carcinoma”. In: *Hematology/Oncology Clinics of North America* 33.1, pp. 1–12.
- Wang, M., S. Liu, Z. Xu, K. Qu, M. Li, X. Chen, Q. Xue, G. M. Genin, T. J. Lu, and F. Xu (2020). “Characterizing poroelasticity of biological tissues by spherical indentation: An improved theory for large relaxation”. In: *Journal of the Mechanics and Physics of Solids* 138, p. 103920.
- Wang, Y., R. Xu, W. He, Z. Yao, H. Li, J. Zhou, J. Tan, S. Yang, R. Zhan, G. Luo, and J. Wu (2015). “Three-Dimensional Histological Structures of the Human Dermis”. In: *Tissue Engineering Part C: Methods* 21.9, pp. 932–944.
- Wang-Evers, M., M. J. Casper, J. Glahn, T. Luo, A. E. Doyle, D. Karasik, A. C. Kim, W. Phothong, N. R. Nathan, T. Heesakker, G. Kosiratna, and D. Manstein (2021). “Assessing the impact of aging and blood pressure on dermal microvasculature by reactive hyperemia optical coherence tomography angiography”. In: *Scientific Reports* 11.1.
- Weir Weiss, M.-J., P. Shrestha, R. Basak, and B. Stoeber (2023). “Poroelastic behavior of skin tissue in response to pressure driven flow”. In: *Physics of Fluids* 35.8, p. 081902. eprint: {[https://pubs.aip.org/aip/pof/article-pdf/doi/10.1063/5.0159409/18074260/081902\\_1\\_5.0159409.pdf](https://pubs.aip.org/aip/pof/article-pdf/doi/10.1063/5.0159409/18074260/081902_1_5.0159409.pdf)}.
- Weir Weiss, M.-J., P. Shrestha, R. Basak, and B. Stoeber (2024). “Erratum: “Poroeelastic behavior of skin tissue in response to pressure driven flow” [Phys. Fluids 35, 081902 (2023)]”. In: *Physics of Fluids* 36.5.
- Weiss, J. A., B. N. Maker, and S. Govindjee (1996). “Finite element implementation of incompressible, transversely isotropic hyperelasticity”. In: *Computer Methods in Applied Mechanics and Engineering* 135.1, pp. 107–128.

## Bibliography

- Wheatley, B. B., R. B. Pietsch, T. L. H. Donahue, and L. N. Williams (2015). “Fully non-linear hyper-viscoelastic modeling of skeletal muscle in compression”. In: *Computer Methods in Biomechanics and Biomedical Engineering* 19.11, pp. 1181–1189.
- Whitaker, S. (1986). “Flow in porous media I: A theoretical derivation of Darcy’s law”. In: *Transport in Porous Media* 1 (1), pp. 3–25.
- Whitaker, S. (1998). *The method of volume averaging*. Vol. 13. Springer Science & Business Media.
- Wiig, H. and H. Noddeland (1983). “Interstitial fluid pressure in human skin measured by micropuncture and wick-in-needle”. In: *Scandinavian Journal of Clinical and Laboratory Investigation* 43.3, pp. 255–260.
- Wiig, H. and M. A. Swartz (2012). “Interstitial Fluid and Lymph Formation and Transport: Physiological Regulation and Roles in Inflammation and Cancer”. In: *Physiological Reviews* 92.3, pp. 1005–1060.
- Wong, B. J., S. J. Williams, and C. T. Minson (2006). “Minimal role for H1and H2histamine receptors in cutaneous thermal hyperemia to local heating in humans”. In: *Journal of Applied Physiology* 100.2, pp. 535–540.
- Wong, R., S. Geyer, W. Weninger, J.-C. Guimberteau, and J. K. Wong (2015). “The dynamic anatomy and patterning of skin”. In: *Experimental Dermatology* 25.2, pp. 92–98.
- Wu, J. and Y. Zhang (2016). “Hydrogels for 3D Printing: Materials and Applications”. In: *ACS Biomaterials Science & Engineering* 3.8, pp. 1599–1611.
- Xing, W., M. Yin, Q. Lv, Y. Hu, C. Liu, and J. Zhang (2014). “Oxygen Solubility, Diffusion Coefficient, and Solution Viscosity”. In: *Rotating Electrode Methods and Oxygen Reduction Electrocatalysts*. Elsevier, pp. 1–31.
- Yalcin, O., D. Ortiz, A. T. Williams, P. C. Johnson, and P. Cabrales (2015). “Perfusion pressure and blood flow determine microvascular apparent viscosity”. In: *Experimental Physiology* 100.8, pp. 977–987.
- Yazdi, S. J. M. and J. Baqersad (2022). “Mechanical modeling and characterization of human skin: A review”. In: *Journal of Biomechanics* 130, p. 110864.

- Yazdi, S. J. M., K. S. Cho, and N. Kang (2018). “Characterization of the viscoelastic model of in vivo human posterior thigh skin using ramp-relaxation indentation test”. In: *Korea-Australia Rheology Journal* 30.4, pp. 293–307.
- Zahouani, H., G. Boyer, C. Pailler-Mattei, M. Ben Tkaya, and R. Vargiolu (2011). “Effect of human ageing on skin rheology and tribology”. In: *Wear* 271.9–10, pp. 2364–2369.
- Zakaria, E. R., J. Lofthouse, and M. F. Flessner (1997). “In vivo hydraulic conductivity of muscle: effects of hydrostatic pressure”. In: *American Journal of Physiology-Heart and Circulatory Physiology* 273.6, H2774–H2782.
- Zhang, J. (2011). “Effect of Suspending Viscosity on Red Blood Cell Dynamics and Blood Flows in Microvessels”. In: *Microcirculation* 18.7, pp. 562–573.
- Zhang, M., A. R. Turner-Smith, and V. C. Roberts (1994). “The Reaction of Skin and Soft Tissue to Shear Forces Applied Externally to the Skin Surface”. In: *Proceedings of the Institution of Mechanical Engineers, Part H: Journal of Engineering in Medicine* 208.4, pp. 217–222.
- Zhou, Q. (2019). “PyMesh—Geometry processing library for Python”. In: *Software available for download at <https://github.com/PyMesh/PyMesh>.*
- Zulian, P., A. Kopaničáková, M. C. G. Nestola, A. Fink, N. Fadel, A. Rigazzi, V. Magri, T. Schneider, E. Botter, J. Mankau, and R. Krause (2016). *Utopia: A performance portable C++ library for parallel linear and nonlinear algebra. Git repository.* <https://bitbucket.org/zulianp/utopia>.
- Zulian, P., A. Kopaničáková, M. G. C. Nestola, N. Fadel, A. Fink, J. VandeVondele, and R. Krause (2021). “Large scale simulation of pressure induced phase-field fracture propagation using Utopia”. In: *CCF Transactions on High Performance Computing*. eprint: <https://doi.org/10.1007/s42514-021-00069-6>.





AFR FNR Grant N°17013182



# Biomechanical Response of Human Skin: A Hierarchical Porous Media Framework.

Thomas Jeffrey Hugo Marc LAVIGNE

**Résumé :** La peau peut être fragilisée par des pressions prolongées, entraînant des escarres et des ulcères, en particulier chez les personnes immobilisées. Une compréhension approfondie de ces lésions est essentielle pour les prévenir efficacement. Nos recherches s'appuient sur une modélisation poromécanique multicompartment, associée à des expériences, pour analyser la réponse des tissus aux contraintes. Contrairement aux modèles traditionnels qui séparent les effets mécaniques et biologiques, nous proposons une approche innovante intégrant la circulation sanguine, favorisant l'intégration des échanges biologiques. Ce cadre permet d'évaluer la capacité du modèle hiérarchique à simuler la microcirculation et d'approfondir la compréhension des phénomènes physiques impliqués lorsqu'une contrainte extérieure est appliquée à la peau.

**Mots clés :** Peau humaine, Poromécanique, Multi-compartment, microcirculation, FEniCSx

**Abstract:** The skin can be weakened by prolonged pressure, leading to pressure sores and ulcers, particularly in immobilised individuals. A thorough understanding of these lesions is crucial for their effective prevention. Our research is based on multicompartimental poromechanical modelling combined with experimental data to analyse how tissues respond to mechanical stress. Unlike traditional models that separate mechanical and biological effects, we propose an innovative approach that integrates blood circulation, enhancing the incorporation of biological exchanges. This framework allows us to assess the hierarchical model's ability to simulate microcirculation and provides a deeper understanding of the physical phenomena involved when external pressure is applied to the skin.

**Keywords:** Human skin, Poromechanics, Multi-compartment, Blood flow, FEniCSx